Universität Augsburg
Mathematisch-Naturwissenschaftliche Fakultät

AG Experimentelle Plasmaphysik

Experimental investigations on the caesium dynamics in H_2/D_2 low temperature plasmas

Dissertation zur Erlangung des Doktorgrades
an der Mathematisch-Naturwissenschaftlichen Fakultät
der Universität Augsburg

vorgelegt von
Roland Friedl
am 22. August 2013

Vorgelegt am 22. August 2013
Tag der mündlichen Prüfung: 17. Dezember 2013

Erster Gutachter: apl. Prof. Dr.-Ing. U. Fantz
Zweiter Gutachter: Prof. Dr. A. Wixforth

Contents

1 Introduction

The fusion experiment ITER requires powerful neutral beam injection (NBI) systems for plasma heating, for the current drive in the tokamak and for diagnostic purposes. Heating and current drive are provided by two heating neutral beams (HNB), which are designed to deliver each an atomic deuterium beam of 16.5 MW with a beam energy of 1 MeV for up to one hour. The high energetic neutral beam is produced via acceleration of an ion beam and subsequent neutralization of the accelerated particles. At the required beam energy only negative ions can efficiently be neutralized. To achieve the beam parameters the corresponding ion source requires an accelerated negative ion current density of 200 A/m^2 D^-. Inevitably co-extracted electrons have to be removed from the beam, which leads to heat loads of more than 10 MW/m^2 at the electron dump. Therefore, the ratio of the co-extracted electron current to the negative ion current needs to remain below unity. The diagnostic neutral beam (DNB) operates at 100 keV to minimize interference of the fusion plasma and uses atomic hydrogen. The requirements on the ion source are however more demanding: 300 A/m^2 H^- current density and a current ratio of electrons to negative ions of below 0.5 are needed. Hence, reliable sources for negative hydrogen and deuterium ions meeting the ambitious requirements have to be developed.

Negative ion sources for the ITER NBI are based on the surface production mechanism for negative ions: atomic hydrogen and positive hydrogen ions from a low temperature hydrogen plasma are converted into negative ions at a low work function surface. The required low work function is obtained via coating the converter surface with the alkali metal caesium. Due to its high chemical reactivity, the adsorbed Cs layer is susceptible to impurities from the residual gases within the ion source which leads to binding of the Cs in compounds. This degradation must be counteracted by continuous replenishment of the Cs layer, which is addressed by continuous Cs evaporation into the ion source. Consequently, the stability and reliability of a high negative ion current and a low co-extracted electron current significantly depends on the Cs dynamics in the hydrogen plasma and in the vacuum phases between the pulses.

The ITER reference source for negative hydrogen ions is the RF ion source developed at the Max-Planck-Institut für Plasmaphysik (IPP) in Garching. Investigations with short pulses ($\approx 5\,\mathrm{s}$) have already shown, that the ITER requirements can be achieved and that controlling the co-extracted electron current is the crucial issue for the source performance, further aggravated by the fact, that in deuterium more electrons are extracted than in hydrogen. Introducing Cs into the ion source leads to a mitigation of the co-extracted electron current, where it is under discussion whether this behavior arises from a direct influence of Cs on the plasma parameters of the hydrogen plasma or from an indirect influence via physical and chemical surface effects. Furthermore, at IPP the required long pulse operation of 3600 s was demonstrated with stable extracted negative ion currents but with current densities below the target parameters. Control over the Cs dynamics within the ion source, including ad- and desorption processes, was identified as one of the key issues for the reliable long pulse operation. This issue is complicated by the fact, that ion sources typically have background pressures of around $10^{-6}\,\mathrm{mbar}$, which leads to a dominance of Cs compounds rather than pure Cs. Their influence on the volume and surface dynamics, especially on the work function of the converter surface, needs to be investigated particularly.

In order to study the individual effects on a fundamental level, dedicated systematic investigations on the Cs dynamics are conducted at a flexible laboratory experiment with ion source relevant vacuum and plasma conditions. The inductively coupled plasma (ICP) setup is equipped with a comprehensive set of diagnostics: Cs fluxes, the Cs density, local and global plasma parameters, the work function of a sample surface as well as the impurity content are analyzed. Furthermore, the diagnostics are applied simultaneously in order to relate parameters from different diagnostics to the same experimental condition. The systematic investigations moreover require a reliable Cs source which is capable of stably evaporating Cs with finely adjustable evaporation rates in vacuum as well as in plasma operation. The presently used liquid Cs ovens from IPP are not suitable for the required adjustable low evaporation rates and furthermore a Cs reservoir with manageable Cs contents and a reduced susceptibility to contaminations is desirable. Thus, a new Cs source is developed within the scope of this work. The investigations are geared towards a comprehensive insight into the Cs dynamics in vacuum and during plasma operation, especially aiming at the influence of impurities, the behavior of the work function of a cesiated sample surface and the influence of Cs on the plasma parameters including isotopic differences.

2 Ion sources for negative hydrogen ions

2.1 Requirements on negative ion sources for fusion

The international fusion experiment ITER (**I**nternational **T**hermonuclear **E**xperimental **R**eactor or Latin for 'the way') is designed to demonstrate the scientific and technological feasibility of a positive energy balance by means of nuclear fusion [SCM+07]. For this purpose, a gas mixture of deuterium D_2 and tritium T_2 is heated to 10^8 K forming a thermonuclear plasma with ion temperatures[1] of about 20 keV, in which the constituents fuse to helium:

$$ {}^{2}_{1}\mathrm{D} \; + \; {}^{3}_{1}\mathrm{T} \quad \longrightarrow \quad {}^{4}_{2}\mathrm{He} \; + \; {}^{1}_{0}\mathrm{n} \; + \; 17.6\,\mathrm{MeV} \; . $$

The exothermic energy of 17.6 MeV per fusion reaction is split among the products according to the mass. The neutrons n (14.1 MeV) are absorbed within the walls of the plasma vessel and via several steps steam is produced, which drives the generators that produce electricity. The fused helium nuclei (3.5 MeV) are then considered to compensate the energy losses of the thermonuclear plasma and a 'burning plasma' is obtained, i. e. a state of a self-sustained fusion plasma.

The fusion plasma is confined against the surrounding walls by strong magnetic fields, since contact with the walls would instantaneously lead to a cooling of the plasma and to the termination of the fusion process. For ITER the Tokamak concept (Russian for 'toroidal chamber with magnetic confinement') is pursued, according to which part of the magnetic field is provided by a toroidal plasma current. This current can be driven inductively, where the plasma can be seen as

[1] It is common practice to use the temperature T as an abbreviation for the corresponding energy equivalent $k_\mathrm{B}T$ (k_B is the Boltzmann constant). In this case temperatures are given in units of eV.

the secondary winding of a transformer. However, such a fusion experiment can only be operated in pulsed mode and non-inductive current drive techniques are required for a steady-state operation.

Therefore, in total an external heating power of about 50 MW is required for heating, controlling and current drive. This is achieved by ohmic, radio frequency (RF), microwave and neutral beam injection (NBI) heating. While the former three heating mechanisms use electromagnetic fields or waves, respectively, the neutral beam heating is based on high energetic particle beams directed into the fusion plasma. Via a tangential injection into the toroidal plasma the plasma current can efficiently be driven. For the steady-state operation of ITER the NBI system has to deliver 33 MW (two beamlines) at beam energies of 1 MeV of atomic deuterium D [IAE02].

Neutral beam heating

Owing to the magnetic confinement of the fusion plasma only high energetic neutral particles can be used to heat the plasma by means of NBI, as they are not deflected by the magnetic field. This neutral beam is produced in the following way:

Ions are extracted from a low temperature deuterium plasma through apertures in one of the plasma surrounding walls. The electric field of a high voltage applied externally to this 'extraction area' reaches into the plasma vessel and ions can be extracted from the so-called 'plasma meniscus'. The extracted ions are subsequently accelerated electrostatically to produce a high energetic ion beam. The ion beam is neutralized by charge exchange collisions with a deuterium gas target and the residual ions are deflected from the beam via bending magnets onto the 'ion dump'. The produced high energetic neutral beam is directed into the fusion plasma and energy is transferred via collisions with the plasma particles. The required penetration depth of the neutral beam into the fusion plasma is one parameter among others that determines the beam energy. Detailed information on NBI systems can be found in the review article [Spe89] for instance.

A key parameter for the correlation of the required beam energy to the initial ion source parameters is the neutralization efficiency, which is shown in figure 2.1 for the different ions that can be extracted from a deuterium discharge after [BPS75]. It can be seen, that for beam energies larger than 100 keV the neutralization efficiency of positive ions decreases drastically leading to infinitesimal values at the ITER relevant energy of 1 MeV. On the contrary, the neutralization efficiency for negative ions is always above 60 %.

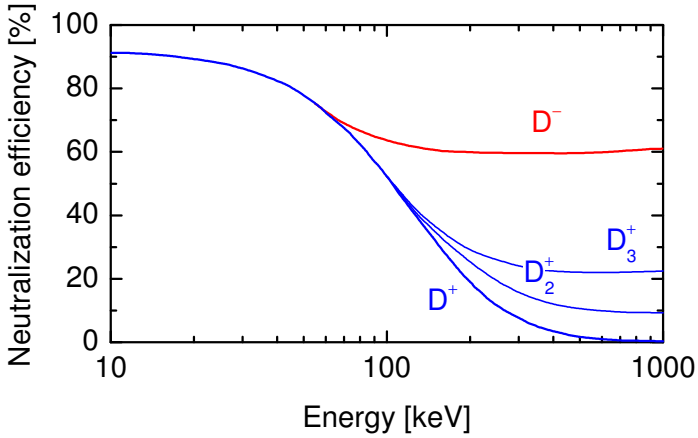

Figure 2.1: *Neutralization efficiency of ion beams traveling through a D_2 gas target at rest with optimized thickness depending on the beam energy after [BPS75].*

Therefore, the neutral beam injection system for ITER is based on negative ions (NNBI). However, the advantage of a high neutralization efficiency involves the disadvantage of a more difficile production of the negative ions, a high destruction rate due to the low binding energy of 0.75 eV [Lid05] and the implicit co-extraction of electrons from the plasma.

Requirements on NNBI [IAE02]

The required penetration depth into the fusion plasma of ITER together with the demand for an efficient current drive leads to a required beam energy of 1 MeV per D atom and the envisaged heating power per beamline is 16.5 MW. Considering the neutralization losses and further transmission losses between the ion source and the fusion plasma the required negative ion current delivered by the ion source is 40 A D^-. This is to be achieved by a current density of 200 A/m^2 and an extraction area of 0.2 m^2, which is divided into 1280 extraction apertures, each with 14 mm in diameter.

Inevitably co-extracted electrons have to be deflected from the negative ion beam, which can lead to heat loads of more than 10 MW/m^2 on the electron dump [NGH+11]. Therefore, the ratio of the co-extracted electron current density j_e to the extracted negative deuterium current density j_{D^-} must be limited: $j_e/j_{D^-} < 1$. This requirement is often more severe than the achievable current density of negative ions.

Besides the described heating neutral beam (HNB) which is based on atomic deuterium, additionally a diagnostic neutral beam (DNB) is envisaged for ITER,

which uses atomic hydrogen beams for charge exchange spectroscopy [PCI+01]. For the DNB a beam energy of 100 keV is required, whereas the corresponding ion source has to deliver a current density of 300 A/m^2 H^- with a ratio j_e/j_{H^-} of below 0.5.

The ion sources have to operate at a maximum pressure of 0.3 Pa to minimize stripping losses in the acceleration system by neutralizing collisions of negative ions with the background gas. Furthermore, for the steady-state operation of ITER the entire negative-ion-based neutral beam heating system has to deliver a homogeneous neutral beam satisfying the requirements stable for one hour. Obviously, besides the acceleration system, one of the key parts of the NNBI is the ion source itself. Ion sources for negative hydrogen and deuterium ions, which fulfill the required target parameters, especially with respect to the huge extraction area and the long pulse length, are not available at present and have to be developed.

2.2 Production and destruction of negative ions

Detailed information on the physics of production and destruction mechanisms of negative hydrogen ions can be found in the review article [Bac06]. In principle, two different processes for the formation of negative hydrogen ions exist: volume production and surface production.

Volume production

The formation of negative hydrogen ions via the volume production is based on the dissociative attachment (DA) of slow electrons to a highly vibrationally excited hydrogen molecule:

$$\begin{matrix} H_2(\nu \geq 5) \\ D_2(\nu \geq 8) \end{matrix} + e^- (T_e \leq 1\,\mathrm{eV}) \longrightarrow \begin{matrix} H^- \\ D^- \end{matrix} + \begin{matrix} H \\ D \end{matrix}, \tag{2.1}$$

where ν is the vibrational quantum number and T_e is the electron temperature. The production of $H_2(\nu \geq 5)$ or $D_2(\nu \geq 8)$ can be achieved in several ways: direct excitation of vibrational levels in collisions with electrons (requires high collision rates, i. e. high pressures), relaxation of electronically excited molecules (requires $T_e \geq 20$ eV for the excitation) and recombinative desorption from metal surfaces.

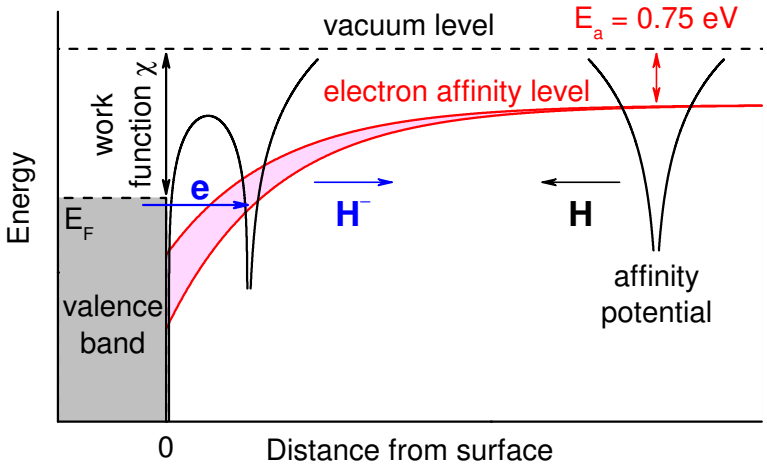

Figure 2.2: *Illustration of the surface conversion process of a hydrogen atom to a negative ion. E_F is the Fermi energy of the surface material and E_a is the electron affinity at infinite distance from the surface.*

Surface production

A surface in interaction with a hydrogen plasma can also produce negative ions directly via the surface conversion process (H can as well be replaced by D):

$$\begin{aligned} \mathrm{H} \;+\; \mathrm{e}^-_{\mathrm{surf}} \quad &\longrightarrow \quad \mathrm{H}^- \;, \\ \mathrm{H}^+_x \;+\; 2\,\mathrm{e}^-_{\mathrm{surf}} \quad &\longrightarrow \quad \mathrm{H}^- \;+\; \mathrm{H}_{x-1} \;,\; x = 1, 2, 3 \;. \end{aligned} \tag{2.2}$$

Thus, atomic and ionic hydrogen particles are converted into negative ions by obtaining one or more electrons from the surface. Impinging ions are neutralized prior to the negative ion formation via resonant electron transfer from the metal and subsequent Auger de-excitation [RWL82]. The subsequent conversion process is illustrated in figure 2.2: Approaching the surface, the electron affinity level of the hydrogen atom is lowered due to the induction of a positive image charge within the metal. This leads to electron tunneling from the conduction band of the metal into the affinity level of the hydrogen atom. The resulting finite lifetime of the electron within the atom is accompanied by a broadening of the affinity level, which in turn increases the tunneling probability [RWL82].

Obviously, the surface process depends on the work function χ of the converter surface and the negative ion yield can be parameterized by:

$$\frac{n_{\mathrm{H}^-}}{n_{\mathrm{H}}} \;\sim\; \exp\left(-\frac{\chi - E_\mathrm{a}}{C v_{H^-}}\right) \;, \tag{2.3}$$

where n_{H^-} and n_{H} are the densities of negative ionic and atomic hydrogen, $E_{\mathrm{a}} = 0.75\,\mathrm{eV}$ is the electron affinity far from the surface, v_{H^-} is the normal component of the velocity of the negative ion leaving the surface and C is a constant [RWL82]. Hence, via lowering the work function of the converter surface, the negative ion yield can be enhanced. This is utilized in negative ion sources based on surface production, where the metallic converter surface is coated with the alkali metal caesium, which significantly lowers the work function of the surface (see section 4.2.2). The increase of negative ion production due to Cs evaporation and the resulting lowering of the converter work function is shown in [BDD74, OM92, LS92, IKS92] for instance.

Destruction processes

Owing to the low binding energy of the additional electron of 0.75 eV, several destruction processes for negative hydrogen ions can occur (H can as well be replaced by D):

$$\text{Electron stripping (ES):} \quad \mathrm{e^- + H^- \longrightarrow H + 2\,e^-} \tag{2.4}$$

$$\text{Mutual neutralization (MN):} \quad \mathrm{H_x^+ + H^- \longrightarrow H + H_x}\ ,\ x = 1,2,3 \tag{2.5}$$

$$\text{Associative Detachment (AD):} \quad \mathrm{H + H^- \longrightarrow H_2 + e^-} \tag{2.6}$$

$$\text{Collisional Detachment (CD):} \quad \mathrm{H, H_2 + H^- \longrightarrow H, H_2 + H + e^-} \tag{2.7}$$

The ES process has a steep dependence on the electron temperature T_{e} and is very efficient at temperatures of several electron volts, whereas at temperatures below about 2 eV the MN process gains influence. However, in hydrogen plasmas at several Pa of absolute pressure with electron temperatures of $T_{\mathrm{e}} \lessapprox 2\,\mathrm{eV}$ and electron densities of $n_{\mathrm{e}} \lessapprox 10^{17}\,\mathrm{m}^{-3}$, the dominant processes are AD and CD due to the densities of atomic and molecular hydrogen which are typically several orders of magnitude larger than n_{e} [FFK+07]. At ion source relevant plasma parameters in front of the extraction area, the interaction of the different processes leads to survival lengths of the negative hydrogen ion of several centimeters [GWFN09, FFF+06a]. Hence, the production region of negative ions should be close to the extraction region. For ion sources based on the surface production this is managed by using the extraction area, which comprises the extraction apertures, as the converter surface.

2.3 The RF ion source for negative hydrogen ions

The negative ion source has to fulfill the requirements for the ITER NNBI system as described above, particularly a negative ion current density of 200 A/m^2 at an operating pressure of 0.3 Pa and a ratio of co-extracted electrons to negative ions of below unity. Since for the production of highly vibrationally excited molecules high pressures are beneficial and a high electron density is required for the formation of negative ions via dissociative attachment (DA) (2.1), volume production alone cannot be used for the NNBI ion sources of ITER. This was shown in [SFF+06]: at a pressure of 0.4 Pa the extracted ion current is below 50 A/m^2 and the co-extracted electron current ratio is at about 60 for a scenario in which volume production is the dominant process. However, relying on the surface process (2.2) with Cs covered converter surface, the ITER requirements can be achieved routinely [FFK+07].

Therefore, it was decided, that the ion source for the NNBI heating system of ITER is based on hydrogen/deuterium plasmas in contact with a cesiated converter surface and the official reference source is the RF ion source developed at the Max-Planck-Institut für Plasmaphysik (IPP) in Garching [HDG+09]. The concept of the ion source is described in detail in [SFF+06] and is briefly summarized hereafter.

The prototype ion source has 1/8 of the size of the ITER ion source and the CAD drawing is shown in figure 2.3 (a). It consists of three regions: The driver produces the hydrogen/deuterium discharge via inductive coupling at 1 MHz and up to 150 kW. The plasma expands into the expansion region where a magnetic filter field (5–7 mT) is used to reduce the electron temperature and density. The extraction area is a grid with multiple apertures which replaces one of the vessel walls. The plasma grid (PG) is made of molybdenum and acts as the converter surface where the interaction of the low temperature plasma with the cesiated surface produces the negative ions. The ions are subsequently extracted by the relative potential of the extraction grid (EG) of typically +9 kV and further accelerated by the relative potential of +11 kV of the grounded grid (GG). The Cs seeding to cover the PG is accomplished by the evaporation of Cs from an oven at the backplate of the expansion region, where the actual Cs source is a liquid Cs reservoir (ampoules filled with 1 g of pure Cs). Typical evaporation rates are 10 mg/h resulting in Cs densities of typically some $10^{15}\,m^{-3}$ [FW11].

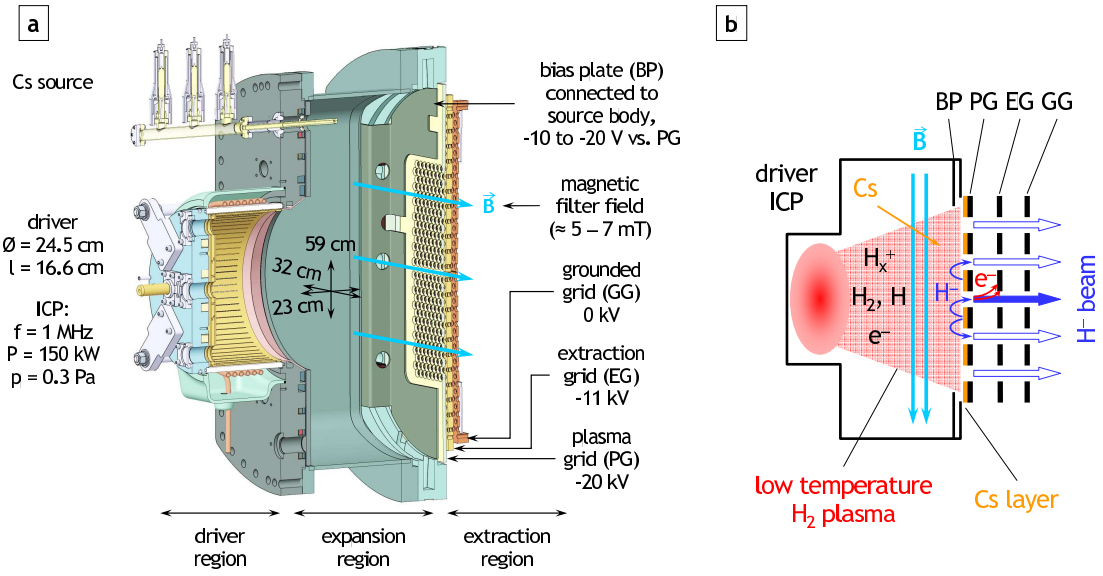

Figure 2.3: (a) *CAD drawing of the ITER NNBI prototype ion source developed at IPP Garching [SFF+06].* **(b)** *Illustration of the production of an H^- beam.*

The sketch in part (b) of figure 2.3 illustrates the processes to form the negative ion beam by means of a tandem concept: The driver produces a plasma with electron densities of $10^{18}\,\mathrm{m}^{-3}$ and temperatures of up to more than 10 eV leading to high fluxes of atomic and ionic hydrogen particles. The subsequent expansion towards the PG and the magnetization of the electrons by the filter field results in a reduced electron density and temperature of about $1\times10^{17}\,\mathrm{m}^{-3}$ and 1–2 eV, respectively. Cs evaporated from the oven mainly covers the inner walls of the expansion region, and is redistributed onto the PG due to the plasma load [GWFN11]. The resulting Cs layer on the molybdenum PG lowers its work function (see section 4.2.2). The high particle fluxes from the driver then lead to a high production rate of negative ions at the PG via the surface process (2.2) and the lowered plasma parameters in front of the PG are beneficial against the destruction of the negative ions via the ES process (2.4). Via deflection in the magnetic field and non-destructive charge exchange collisions the ions can reach the extraction apertures with a probability of about 23 % [GWFN09]. The co-extracted electron current is reduced via collecting the electrons on the PG by means of a positive bias against the so-called bias plate and thus against the source body [SFF+06].

After extraction the ions are accelerated. However, co-extracted electrons have to be removed from the beam prior to full acceleration. This is accomplished by magnets within the extraction grid (EG) which deflect the light electrons onto the EG while leaving the H^- beam virtually unaffected.

Achieved requirements

At IPP several test beds are available which are based on the prototype ion source described above. At BATMAN[2] the requirements for ITER have been achieved for short pulses of 4 s: current densities of 230 A/m^2 D^- and 330 A/m^2 H^- together with ratios of the co-extracted electron current to the negative ion current of below unity for D^- and below 0.5 for H^- have been attained at a source pressure of 0.3 Pa [FFK$^+$07]. At MANITU[3] the stable extraction of a negative deuterium ion current with $j_e/j_{D^-} \approx 1$ for 3600 s was recently achieved at 0.3 Pa [KFF$^+$12]. The current density, however, was too low to fulfill the ITER requirements.

The next step towards the full ITER NNBI ion source is the half-scale test bed ELISE[4] which has a four times larger extraction area than the prototype ion source and includes four drivers [HFF$^+$11].

Transition to laboratory experiments

The key issue for the reliable and reproducible achievement of the ITER requirements is to sustain a homogeneous and stable Cs layer on the PG, especially for long pulses. This is approached via controlling the Cs dynamics within the source during plasma pulses as well as in the vacuum phases between the pulses [GWFN11, FFW12]. For this purpose, dedicated investigations on the Cs dynamics under ion source relevant plasma and vacuum conditions are required.

Fundamental studies can be performed at a flexible laboratory setup, where the plasma parameters in front of the PG can easily be achieved: an ICP H_2 discharge at 10 Pa pressure and 250 W RF power (frequency 27.12 MHz) has electron densities of several 10^{16} m^{-3} and electron temperatures of 1–2 eV. Furthermore, investigations on the evaporation of Cs have shown, that the typically achieved caesium densities are equal to those in front of the PG in ion sources: $n_{Cs} \approx 10^{15} - 10^{16}$ m^{-3} [FGW10, FW11]. And finally, the impact of impurities on the Cs content due to residual gases is comparable due to similar background pressures of around 10^{-6} mbar.

[2] **BA**varian **T**est **MA**chine for **N**egative ions
[3] **M**ulti **A**mpere **N**egative **I**on **T**est **U**nit, decommissioned by this time
[4] **E**xtraction from a **L**arge **I**on **S**ource **E**xperiment

3 Low temperature hydrogen plasmas

3.1 Properties of low pressure low temperature plasmas

Low pressure low temperature plasmas are generated by applying an electric field to a neutral gas via internal or external electrodes, electrodeless via inductive or capacitive RF coupling or via electromagnetic waves (e. g. microwaves). Existing primary electrons respond to the electric field and are accelerated to energies sufficiently high to ionize gas particles (several eV). The produced charge carriers recombine again and in equilibrium a steady degree of ionization is achieved fulfilling *quasineutrality*: the electron density n_e within the bulk plasma equals the total ion density $\sum_s Z_s n_{\mathrm{ion},s}$, where Z_s is the ionization stage of the ion species s having an ion density $n_{\mathrm{ion},s}$. Detailed information on plasma heating mechanisms can be found in [LL05] for instance.

The electrons, which are heated by the external power supply, can transfer kinetic energy to the neutral gas or the ions via elastic collision processes. However, due to the large difference in mass this process is ineffective and high collision frequencies are required for a thermalization of the electrons and the heavy particles, i. e. the neutrals and the ions. Thus, in low pressure plasmas with low collision frequencies the heavy particle temperatures T_gas and T_ion are typically much lower ($\sim 10^{-2}$ eV) than the electron temperature T_e ($\sim$ eV) and the discharge is called a *non-thermal plasma*. Furthermore, the designation of a *temperature* in a thermodynamic meaning is only justified if an energy distribution according to the *Maxwell-Boltzmann distribution* is present. In any other case, the 'temperature' is actually an effective one and a synonym for the mean particle energy via $\langle E \rangle = \frac{3}{2} k_\mathrm{B} T^\mathrm{eff}$, where k_B is the Boltzmann constant. Furthermore, it is common practice to use the temperature T as an abbreviation for the corresponding energy equivalent $k_\mathrm{B}T$, as in this case temperatures can be given in units of eV.

The question of a temperature in a thermodynamic meaning is in particular relevant for the plasma electrons. The electrons are subject to the heating mechanisms on the one hand and to energy specific loss channels in inelastic collisions on the other hand, which can lead to an energy distribution which is not necessarily Maxwellian.

3.1.1 Electron energy distributions

An *electron energy distribution function (EEDF)* $f(E_\mathrm{e})$ describes the amount of electrons per unit energy and unit volume and is thus given in units of $[\mathrm{eV}^{-1}\mathrm{m}^{-3}]$. The integral over the electron energy E_e yields the total electron density n_e ('normalization'). In the following a brief overview over possible EEDFs in low pressure plasmas is given:

Maxwell-Boltzmann distribution This distribution represents thermodynamic equilibrium where a temperature T_e can be allocated to the electrons:

$$f_\mathrm{M}(E_\mathrm{e}) = \frac{2}{\sqrt{\pi}}\, n_\mathrm{e}\, (k_\mathrm{B}T_\mathrm{e})^{-3/2} \sqrt{E_\mathrm{e}}\, \exp\left(-\frac{E_\mathrm{e}}{k_\mathrm{B}T_\mathrm{e}}\right) . \tag{3.1}$$

Only in this case, that is also called a 'Maxwellian distribution' for short, it is valid to assign a temperature in a thermodynamic meaning.

Bi-Maxwellian distribution If there are two ensembles of electrons in the plasma which thermalize among themselves but not with the other ensemble both of them can be assigned a temperature $T_\mathrm{e,low}$ and $T_\mathrm{e,high}$. Such distinct ensembles can occur due to specific plasma heating mechanisms (refer to [LL05] for detailed information). Commonly the ensemble with the higher temperature contributes to the total electron density by the share β and the following total EEDF is obtained [GMS95]:

$$\begin{aligned} f_\mathrm{BiM}(E_\mathrm{e}) =& \frac{2}{\sqrt{\pi}}(1-\beta)\, n_\mathrm{e}\, (k_\mathrm{B}T_\mathrm{e,low})^{-3/2} \sqrt{E_\mathrm{e}}\, \exp\left(-\frac{E_\mathrm{e}}{k_\mathrm{B}T_\mathrm{e,low}}\right) \\ &+ \frac{2}{\sqrt{\pi}}\, \beta\, n_\mathrm{e}\, (k_\mathrm{B}T_\mathrm{e,high})^{-3/2} \sqrt{E_\mathrm{e}}\, \exp\left(-\frac{E_\mathrm{e}}{k_\mathrm{B}T_\mathrm{e,high}}\right) . \end{aligned} \tag{3.2}$$

Druyvesteyn distribution and ν-distribution If in the discharge energy specific loss channels exist, as for example electron impact induced excitation of electronic states or ionization, the EEDF can be underpopulated in this energy region. If such processes occur often enough that thermodynamic

equilibrium among the electrons cannot be maintained the EEDF will decrease faster than Maxwellian like. This can lead to a distribution function called *Druyvesteyn distribution* [DP40, DP41]:

$$f_{\mathrm{D}}(E_{\mathrm{e}}) = C\, n_{\mathrm{e}}\, (k_{\mathrm{B}} T_{\mathrm{e}})^{-3/2} \sqrt{E_{\mathrm{e}}}\, \exp\left(-a \left(\frac{E_{\mathrm{e}}}{k_{\mathrm{B}} T_{\mathrm{e}}}\right)^2\right) , \tag{3.3}$$

where C and a are normalization constants ($a \approx 0.24$, $C \approx 0.57$). A generalized version of this distribution function can be obtained, when the exponent of $E_{\mathrm{e}}/k_{\mathrm{B}}T_{\mathrm{e}}$ is set to an arbitrary value $\nu \geq 1$ (the constants C_ν and a_ν are then also dependent on ν). This distribution function, $f_\nu(E_{\mathrm{e}})$, is called *ν-distribution* and can be found in [BF94]. $\nu = 1$ then yields the Maxwell-Boltzmann distribution and $\nu = 2$ the Druyvesteyn distribution.

For convenience in application, an EEDF can be converted into the so-called *electron energy probability function (EEPF)* $g(E_{\mathrm{e}})$ via division by $\sqrt{E_{\mathrm{e}}}$. Its advantage is that a plot of $\ln g(E_{\mathrm{e}})$ against E_{e} yields a linear evolution if the EEDF is Maxwellian.

In summary, the following properties are inherent for each EEDF:

- The corresponding EEPF can be obtained via $g(E_{\mathrm{e}}) = f(E_{\mathrm{e}})/\sqrt{E_{\mathrm{e}}}$. (3.4)
- The EEDF is normalized to the electron density: $\int_0^\infty f(E_{\mathrm{e}})\, \mathrm{d}E_{\mathrm{e}} = n_{\mathrm{e}}$. (3.5)
- The mean electron energy is defined as $\langle E_{\mathrm{e}} \rangle = \frac{1}{n_{\mathrm{e}}} \int_0^\infty E_{\mathrm{e}} f(E_{\mathrm{e}})\, \mathrm{d}E_{\mathrm{e}}$. (3.6)
- The mean electron energy can be correlated to an effective electron temperature via $\langle E_{\mathrm{e}} \rangle = \frac{3}{2} k_{\mathrm{B}} T_{\mathrm{e}}^{\mathrm{eff}}$, whereas for the different EEDFs one has: (3.7)
  $T_{\mathrm{e,M}}^{\mathrm{eff}} \equiv T_{\mathrm{e}}, \qquad T_{\mathrm{e,BiM}}^{\mathrm{eff}} = (1-\beta) T_{\mathrm{e,low}} + \beta T_{\mathrm{e,high}}, \qquad T_{\mathrm{e,D}}^{\mathrm{eff}} = T_{\mathrm{e}}.$
  Again only for the Maxwellian EEDF T_{e} is a thermodynamic temperature.

Exemplary EEPFs with the same mean electron energy of 3 eV are presented in figure 3.1. The semi-logarithmic representation leads to the linear evolution for the Maxwellian distribution. At electron energies above about 10 eV great divergences evolve between the different cases: compared to a Maxwellian EEPF, a larger amount of high-energy electrons is present for a Bi-Maxwellian distribution whereas a Druyvesteyn distribution shows less electrons at higher energies. Electron collision processes with threshold energies in this region, like electron

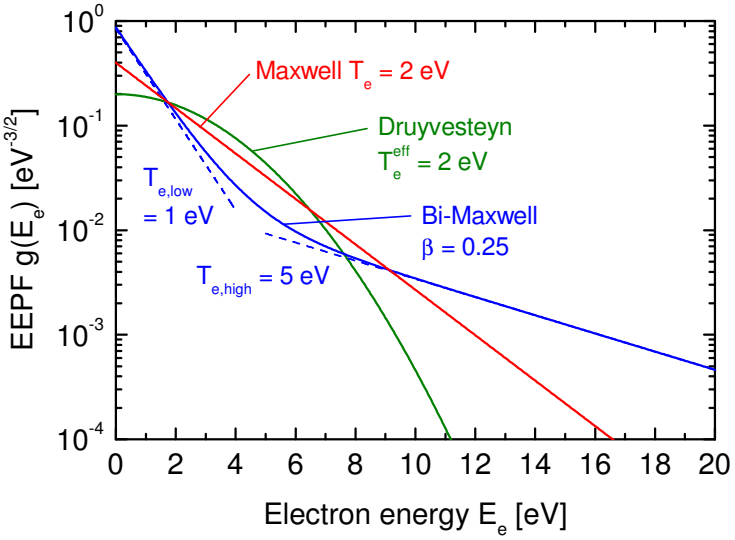

Figure 3.1: *Different electron energy probability functions, each with* $\langle E_\mathrm{e} \rangle = 3\,eV$. *The corresponding EEDFs are normalized to* $n_\mathrm{e} = 1$.

impact excitation or ionization for instance, are significantly dependent on the actual distribution function, even if the effective electron temperature for each EEDF is the same.

3.1.2 Plasma processes

Within the plasma a multitude of processes can occur where excitation, ionization and dissociation are only some examples. If each process is in balance with its reverse process ('detailed balance'), then the relations for (local) thermodynamic equilibrium can be used, e. g. the population density of excited states is determined by the Boltzmann statistics and the densities of the ionization stages are distributed after the Saha equation. However, this requires very high particle densities in order to achieve high collision rates, which is not fulfilled in low pressure low temperature plasmas. Therefore, particular processes and balance equations have to be considered for the analysis of particle densities in the present *non-equilibrium plasmas*. [SVY81]

Processes in plasmas are described in terms of *reaction rates* which constitute the number of reactions per unit volume and unit time. For two-body processes the reaction rate is parameterized by the product of the densities n_j [m^{-3}] of the two species j and the so-called *rate coefficient* $X_\mathrm{react.}(E_j, \ldots)$ [m^3/s] which is characteristic for the specific reaction and predominantly depends on the en-

ergies E_j of the involved particles. For collision processes the rate coefficient is determined by the product of the *collision cross section* $\sigma(E_{\mathrm{rel}})$ [m^2] and the relative velocity [m/s] of the two particles, both of which are directly dependent on the relative kinetic energy E_{rel} of the two particles. For electrons in collision with heavy particles the relative kinetic energy can be considered to be the electron energy E_{e}.

As described in the preceding section the electron energy is not monoenergetic but an energy distribution exists. Thus, the determination of rate coefficients for collision processes of electrons with heavy particles requires, that the electron velocity is weighted according to the EEDF $f(E_{\mathrm{e}})$ [$\mathrm{eV}^{-1}\mathrm{m}^{-3}$] [SVY81]:

$$X_{\mathrm{react.}}(\mathrm{EEDF}) = \int_0^\infty \sigma(E_{\mathrm{e}}) \sqrt{\frac{2eE_{\mathrm{e}}}{m_{\mathrm{e}}}} \frac{f(E_{\mathrm{e}})}{n_{\mathrm{e}}} \, \mathrm{d}E_{\mathrm{e}} \quad \left[\frac{\mathrm{m}^3}{\mathrm{s}}\right] , \tag{3.8}$$

where e is the elementary charge and m_{e} is the electron mass.

Reaction rates of plasma processes can now be interpreted as source and sink terms for a particular state or species j and thus a *balance rate equation* can be set up for the analysis of the density n_j [SVY81]:

$$\frac{\mathrm{d}n_j}{\mathrm{d}t} = \sum_{\mathrm{sources}} \left[\left(\prod n_{\mathrm{educt}} \right) X_{\mathrm{source}} \right] - \sum_{\mathrm{sinks}} \left[\left(\prod n_{\mathrm{reactant}} \right) n_j X_{\mathrm{sink}} \right] . \tag{3.9}$$

A set of such equations leads to *collisional radiative models (CR models)* or *dissociation* and *ionization models* where the possibly nonlinear coupled balance rate equations for excited states or dissociation and ionization products are solved simultaneously by use of a computer code. Further, for very low densities the so-called *corona equilibrium* can be valid, which results in simplified balance rate equations.

Plasma emission

Plasma particles in an electronically excited state i can relax to an energetically lower state k via spontaneous emission at the wavelength $\lambda = hc\,/(E_i - E_k)$ determined by the energies E_i and E_k of the involved states (h is the Planck constant, c is the speed of light in vacuum). The rate of the optical transition $i \rightarrow k$ is called the *emissivity* ϵ_{ik} of the transition and it is defined as the product of the density n_i [m^{-3}] of the upper state and a transition probability, the so-called

Einstein coefficient for spontaneous emission A_{ik} [s^{-1}] [TLJ99]:

$$\epsilon_{ik} = n_i A_{ik} \quad \left[\frac{1}{m^3\,s}\right] . \tag{3.10}$$

Thus, via the emission from the plasma the densities of excited states are accessible. On the other hand, these densities can be calculated using the mentioned models. The combination provides the basis for the *optical emission spectroscopy (OES)* which can be used as diagnostic for plasma parameters like particle temperatures and densities.

Ionization balance

The main source for the production of ions within low pressure low temperature plasmas is electron impact ionization, whereas the main sink is diffusion to the vessel walls and subsequent recombination [Beh91].

In the following, diffusion is approached after the review of [Möl93]. Due to quasineutrality, diffusion of ions within the plasma is always accompanied by the corresponding diffusion of electrons and vice versa. This collective behavior is called *ambipolar diffusion*. At pressures of about 10 Pa the mean free path length for ions $\lambda_{\mathrm{ion}} = (\sqrt{2}\, n_0 \sigma)^{-1}$ (where n_0 is the total density of the heavy particles and σ is the collision cross section after the hard sphere model) is much smaller than the characteristic length of the plasma (ratio of the plasma volume to the plasma surface area) which leads to a laminar motion of the ions. Therefore, diffusion of ions is described by the *laminar ambipolar diffusion* and for the diffusion time τ_{diff} it applies after [Möl93]:

$$\tau_{\mathrm{diff}} \quad \propto \quad D_{\mathrm{a}}^{-1} \quad \propto \quad \frac{T_{\mathrm{gas}}}{T_{\mathrm{e}}}\, \lambda_{\mathrm{ion}}^{-1} \sqrt{\frac{m_{\mathrm{ion}}}{k_{\mathrm{B}} T_{\mathrm{gas}}}} , \tag{3.11}$$

where D_{a} is the ambipolar diffusion coefficient and m_{ion} is the ion mass.

Thus, the ionization balance can be set up, equating electron impact ionization of the neutral species j having ground state densities $n_{j,0}$ with the laminar ambipolar diffusion of the ions s having ion densities $n_{\mathrm{ion},s}$:

$$n_{\mathrm{e}} \sum_j n_{j,0} X_{\mathrm{ion},j}(T_{\mathrm{e}}) = \sum_s \frac{n_{\mathrm{ion},s}}{\tau_{\mathrm{diff},s}} , \tag{3.12}$$

where the ionization rate coefficients $X_{\mathrm{ion},j}(T_{\mathrm{e}})$ are determined via equation (3.8) from the corresponding electron impact ionization cross sections assuming a

Maxwellian EEDF. Considering only one neutral and one ion species and using quasineutrality the ionization balance can be simplified:

$$X_{\mathrm{ion}}(T_{\mathrm{e}}) = \frac{1}{n_0 \tau_{\mathrm{diff}}} \overset{(3.11)}{\propto} \frac{\lambda_{\mathrm{ion}}}{n_0 \sqrt{m_{\mathrm{ion}}}} \,. \tag{3.13}$$

It can be seen, that with decreasing pressure and the accompanied longer mean free path of the ions the ionization rate coefficient and thus the electron temperature increases. This behavior arises from the faster diffusion of the ions to the vessel walls which has to be compensated by a higher ionization rate. On the other hand, species with a higher ion mass lead to a slower diffusion and thus a lower electron temperature is sufficient to maintain ionization balance. Finally, for particles with lower ionization potential, which is accompanied with a higher ionization rate coefficient, again a lower electron temperature is sufficient to fulfill the ionization balance.

Power balance

The external power P_{ext} that is applied to the plasma is mainly absorbed by the electrons and lost in processes like excitation, ionization or dissociation. Hence, a basic power balance for the plasma can be set up [Beh91]:

$$\begin{aligned} \frac{P_{\mathrm{ext}}}{V} = & \qquad \overbrace{\qquad}^{\text{excitation}} \qquad \overbrace{\qquad\qquad}^{\text{ionization}} \qquad \overbrace{\qquad\qquad}^{\text{dissociation}} \\ = n_{\mathrm{e}} & \left(\sum_j n_{j,0} \left(\sum_i E_{j,i} X_{j,i}(T_{\mathrm{e}}) + \sum_s E_{\mathrm{ion},j,s} X_{\mathrm{ion},j,s}(T_{\mathrm{e}}) + \sum_m E_{\mathrm{diss},j,m} X_{\mathrm{diss},j,m}(T_{\mathrm{e}}) \right) \right) \,, \end{aligned} \tag{3.14}$$

where V is the volume of the plasma, n_{e} is the electron density, $n_{j,0}$ is the density of the neutral species j, $E_{j,i}$ and $X_{j,i}$ are the excitation energy and the electron impact excitation rate coefficient for the state i of species j, $E_{\mathrm{ion},j,s}$ and $X_{\mathrm{ion},j,s}$ are the ionization potential and the electron impact ionization rate coefficient into the ionization stage s of the neutral species j and $E_{\mathrm{diss},j,m}$ and $X_{\mathrm{diss},j,m}$ are the dissociation energy and the electron impact dissociation rate coefficient for the dissociation processes m of species j (if j is molecular).

Since the energies are fixed and the rate coefficients have a steep dependence on the electron temperature, increasing the external power directly leads to an increasing electron density, as long as the pressure and thus $n_{j,0}$ and the plasma volume remain constant. Furthermore, a large amount of molecules within the

discharge leads to a large number of possible vibrational excitations, which have large rate coefficients due to their low threshold energies. Together with the possibility of dissociative processes, the share of input power, that is available for ionization processes is lessened in discharges with high amounts of molecular particles. Hence, compared to atomic discharges, molecular plasmas typically have lower electron densities. [Beh91]

3.1.3 Plasma boundaries

The following paragraphs shortly describe the development of electrostatic potentials between the plasma and an insulated object or the grounded vessel wall. Detailed information on plasma sheaths can e. g. be found in [LL05].

As described, the electron temperature in low pressure low temperature plasmas is much higher than the ion temperature whereas the densities are equal due to quasineutrality. Therefore, the electron velocity v_e and thus electron fluxes $\Gamma_\mathrm{e} = n_\mathrm{e} v_\mathrm{e}$ are much higher than ion fluxes Γ_ion in the bulk plasma.

Hence, if an electrically insulated object is placed into the plasma it will be charged negatively. This charging leads to a retarding potential for the electrons whereas ions are accelerated. In steady state the currents of electrons and ions onto the object are equal. The potential corresponding to the equality of fluxes is called the *floating potential* ϕ_fl whereas the bulk plasma has a potential which is $\phi_\mathrm{pl} - \phi_\mathrm{fl}$ greater, with the so-called *plasma potential* ϕ_pl.

Surrounding the bulk plasma with a conducting grounded wall, as is done in experiment, no charging can occur. Therefore, the high electron flux would rapidly lead to a depletion of electrons in the bulk plasma and thus to a violation of the quasineutrality condition. Hence, to confine the more mobile electrons a potential barrier will built up, where the plasma is also at a higher potential ϕ_pl compared to the vessel walls (which are at zero potential). This potential needs not necessarily equal $\phi_\mathrm{pl} - \phi_\mathrm{fl}$ which in turn means that the wall needs not to be at floating potential compared to the bulk plasma. However, in total the absolute integrated flowing electrical currents to, from or within the walls have to be balanced as well.

3.2 Molecular and atomic properties of hydrogen

The hydrogen molecule H_2 is a homonuclear molecule consisting of two protons and two electrons. Besides kinetic energy due to motion of the molecule, H_2 can store energy in a motion of the nuclei against each other (vibration), in a rotation of the molecule about an axis perpendicular to the internuclear axis and in electronic excitation of the electrons. The total internal energy of the molecule is the sum of the electronic, the vibrational and the rotational energy. Due to the large difference in mass the nuclei can be assumed to be at rest during electronic processes and thus the electronic and the nuclear motion can be treated separately, which is called the *Born-Oppenheimer approximation*.

The following paragraphs give an overview of the physical properties of the H_2 molecule, whereas further and far more detailed information on molecular physics can be found in [Her50, Ber05] for instance.

Electronic states

The electronic states of the molecule are described by the quantized orbital angular momentum and the spin of the electrons moving within the electric field of the nuclei. The angular momenta of the particular electrons couple to the total angular momenta of the molecule after the so called *Hund's coupling cases*. The electronic state of the molecule is then, among others, characterized by the projection $|L_z|$ of the total orbital angular momentum $\vec{L}$ onto the internuclear axis z and by the total spin $\vec{S}$:

$$|L_z| = \Lambda\,\hbar \qquad \text{with} \quad \Lambda \in \mathbb{N}_0\ , \tag{3.15}$$

$$\left|\vec{S}\right| = \sqrt{S(S+1)}\,\hbar \qquad \text{with} \quad S \in \{0,1\}\ . \tag{3.16}$$

Since the potential of a magnetic moment ($\propto \vec{L}$) within an electric field (nuclear field) is independent of the relative orientation, only the modulus of the projection is relevant and quantized by the quantum number Λ. Thus, each molecular state with $\Lambda > 0$ is twofold energetically degenerate. The possible absolute values of the total spin $|\vec{S}|$ are determined by the two electrons of the hydrogen molecule which can be parallel ($S = 1$) or antiparallel ($S = 0$). The coupling of the total orbital angular momentum with the total spin to the *total angular momentum of the molecule* leads to $(2S + 1)$ states for each combination of $\vec{L}$ and $\vec{S}$, where

$(2S + 1)$ is called the *multiplicity*. Molecular states with equal multiplicity are combined in multiplets, where for the hydrogen molecule a singlet ($S = 0$) and a triplet system exists ($S = 1$).

Besides the angular momenta, molecular states are additionally characterized by the symmetry of the corresponding wave function. States of diatomic molecules with $\Lambda = 0$ have wave functions which can either be *symmetric* (state denoted with '+') or *antisymmetric* ('−') under a reflection through a plane containing the internuclear axis[1]. Furthermore, for homonuclear molecules the center of the internuclear axis acts as inversion center and the wavefunction can either be *gerade* (German for 'even'; state denoted with 'g') or *ungerade* (odd; 'u') under inversion.

Hence, an electronic molecular state is described by the following term symbol:

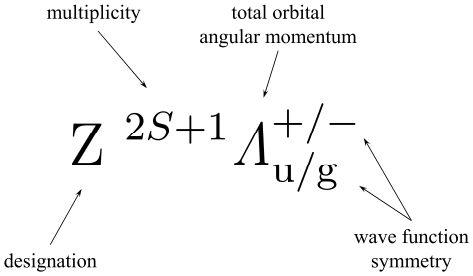

Similar to electronic states in atoms, Λ is entitled with capital Greek letters: $\Sigma, \Pi, \Delta, \ldots$ for $\Lambda = 0, 1, 2, \ldots$ For the designation of the electronic molecular states Latin letters are applied, where the ground state is labeled with 'X'. Excited states are denoted historically, where for hydrogen lower-case characters are used for the triplet system and upper-case characters for the singlet system.

Vibrational states

The nuclei can perform a vibrational motion against each other, where the corresponding potential depends on the electronic state and can in general be described by a *Morse potential* and the model of the *quantum anharmonic oscillator*. Its discretized vibrational levels are characterized by the quantum number $\nu \in \mathbb{N}_0$ and the energetic difference between adjacent vibrational levels decreases with increasing quantum number converging against the *dissociation limit* of the particular electronic state. The energy of the lowest possible vibrational state $\nu = 0$ is finite and represents the *zero-point energy* of the particular electronic state, i. e. the molecule is always vibrating.

[1]For states with $\Lambda > 0$ the wave function is a linear combination of a symmetric and an antisymmetric one and thus the symmetry is indeterminate.

Rotational states

Rotation of the molecule about a spatial axis is described by the model of the *non-rigid rotor*, which includes the elongation of the molecular bond due to the rotation (*centrifugal distortion*). The rotational motion is quantized and characterized by the rotational quantum number $J \in \mathbb{N}_0$. The always existing vibrational motion of the nuclei during the rotation leads to a dependence of the energy of a rotational level on the particular vibrational state of the molecule. Thus, each electronic state has dedicated vibrational levels, and each vibrational state has dedicated rotational levels.

Selection rules for optical transitions

Dipole transitions between different molecular states with specified electronic, vibrational and rotational levels (also called ro-vibronic states) obey quantum mechanical selection rules according to the quantum numbers of the involved states. For the homonuclear hydrogen molecule the following rules apply:

$$\Delta\Lambda = 0, \pm 1 \ , \tag{3.17}$$

$$\Delta S = 0 \ , \tag{3.18}$$

$$\Sigma^+ \leftrightarrow \Sigma^+ \text{ and } \Sigma^- \leftrightarrow \Sigma^- \ , \tag{3.19}$$

$$\mathrm{u} \leftrightarrow \mathrm{g} \ , \tag{3.20}$$

$$\Delta J = 0, \pm 1 \ , \text{ but } J = 0 \nleftrightarrow J = 0 \ , \tag{3.21}$$

$$\Delta\nu \text{ can be arbitrary} \ , \tag{3.22}$$

where equation (3.18) represents the interdiction of *intersystem crossings* and equation (3.21) denotes the *rotational branches*: P, Q and R branch for $\Delta J = -1, 0, +1$. Regarding the involved vibrational levels no restrictions exist. However, direct vibrational or rotational transitions within an electronic state are forbidden for homonuclear molecules.

The H_2 molecule

Figure 3.2 shows to the left an extract of the potential energy diagram of the hydrogen molecule after [Sha70, Sha71] including vibrational levels after [FW06a]. Rotational levels are omitted in the figure for reasons of clarity. As mentioned above, there are two multiplet systems for the hydrogen molecule: the singlet system is denoted in red and includes the ground state $\mathrm{X}\,^1\Sigma_\mathrm{g}^+$, whereas the triplet

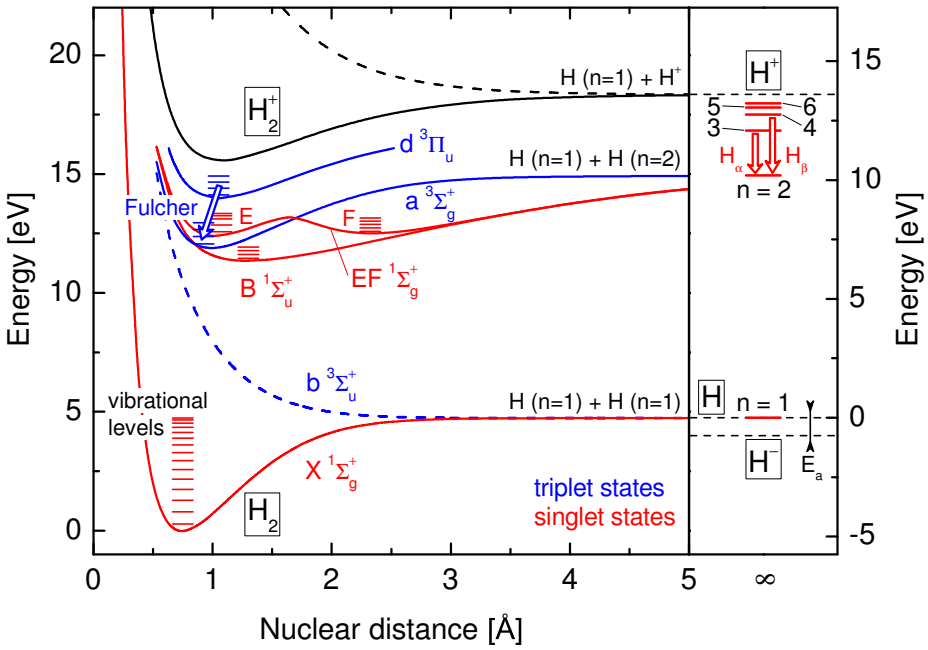

Figure 3.2: *Potential energy diagram of selected electronic states of the hydrogen molecule and its ion after [Sha70, Sha71] together with exemplary vibrational levels after [FW06a]. At the right side energy levels of the hydrogen atom are shown. The energy axis to the right is shifted to illustrate the correlation to the dissociation products of the hydrogen molecule.*

system is depicted in blue and the lowest state b $^3\Sigma_u^+$ is anti-bonding. The X and the b state dissociate into ground state hydrogen atoms. While dissociation from the ground state can occur via highly vibrational and rotational excitation (dissociation energy 4.5 eV), the repulsive b state dissociates immediately.

Among the electronically excited states the triplet states d $^3\Pi_u$ and a $^3\Sigma_g^+$ are very important, as transitions between their ro-vibronic states form the *Fulcher system*. Its transition lines between 590 and 650 nm are the most intense lines in the visible spectral range and can be used for spectroscopic diagnostics (see section 6.6.1). Further relaxation from the a state down to the repulsive b state results in a continuum emission between 160 and 600 nm and the subsequent dissociation into ground state atoms.

Within the singlet system transitions between the states EF $^1\Sigma_g^+$ and B $^1\Sigma_u^+$ lie between 700 and 900 nm and are the second most intense emission lines in low temperature hydrogen plasmas that are optically accessible. The EF state has two minima where each of them (denoted as E and F) has its particular vibrational levels. As soon as the vibrational energy is higher than the local maxima between them (which is for $\nu \geq 9$) the states E and F can no longer be separated.

Furthermore, the ground state potential of the molecular ion H_2^+ (ionization energy 15.4 eV) and its first excited state, which is also anti-bonding, are shown. Dissociation of H_2^+ results in a ground state atom and a proton (dissociation energy 2.65 eV).

Variations for the D_2 molecule Isotopic differences are restricted to vibrational and rotational levels, since the electronic structure is independent of the nuclear mass to a first approximation. In general, a higher mass leads to closer lying energy levels for both the vibrational and the rotational states as can be seen in [Die58, FSC85] for rotational and in [FW06a] for vibrational levels. This means, that the ro-vibronic transition lines are spread over a narrower wavelength range. For instance, the Fulcher system in D_2 lies between 595 and 635 nm.

Atomic hydrogen

On the right side of figure 3.2 the principal electronic energy levels of the hydrogen atom are shown. For atomic hydrogen the fine structure splitting of the energy levels due to the coupling of the orbital angular momentum and the spin of the electron is negligible. Therefore, the energy E_n of a state with principal quantum number n is degenerate for all fine structure components and can be parameterized by

$$E_n = 13.60\,\text{eV} \times \left(1 - \frac{1}{n^2}\right) \ . \tag{3.23}$$

The degree of degeneracy of each quantum state n is $2n^2$ and for $n \to \infty$ the ionization limit at 13.6 eV is reached. Furthermore, the atomic ground state with $n = 1$ has an *electron affinity* E_a of 0.75 eV which can lead to the formation of negative hydrogen ions. This is described in more detail in section 2.2.

Optical transitions are allowed between each principal energy level, where transitions terminating on $n = 1, 2$ and 3 are subsumed in the so-called *Lyman, Balmer* and *Paschen series*. The Lyman series emits in the vacuum ultraviolet spectral range, the Balmer series in the visible and the Paschen series in the near-infrared. The Balmer series in the VIS can be used for optical diagnostic purposes (see section 6.6.2) and its transition lines are summarized in table 3.1.
Due to the doubled mass of the deuterium nucleus compared to hydrogen and the associated shifted potential energy of the electron with respect to the nucleus, slight isotopic variations for the transition lines can be observed for the atomic particles.

Table 3.1: *Transition lines $i \rightarrow k$ from the Balmer series of atomic hydrogen and deuterium with the principal quantum numbers n for the upper and the lower state and the corresponding wavelengths λ.*

		Hydrogen		Deuterium	
n_i	n_k	designation	λ [nm]	designation	λ [nm]
3	2	H_α	656.3	D_α	656.1
4	2	H_β	486.1	D_β	486.0
5	2	H_γ	434.0	D_γ	433.9
6	2	H_δ	410.2	D_δ	410.1
7	2	H_ϵ	397.0	D_ϵ	396.9

Triatomic hydrogen

Besides atomic and molecular hydrogen and their positive and negative ions, the triatomic species H_3 exists. Due to a repulsive ground state potential the triatomic molecule immediately dissociates into H and H_2. However, excited states of H_3 and the molecular ion H_3^+ are stable. Especially the triatomic ion is commonly produced in hydrogen plasmas and can have a significant or even dominating share of the ion composition, as is described within the subsequent section.

3.3 Processes in hydrogen plasmas

Due to the variety of hydrogen particles and their excitation levels a multitude of possible reactions can occur in hydrogen plasmas. Collisions between the plasma particles H, H^+, H^-, H_2, H_2^+, H_3^+ and electrons lead to excitation, dissociation, ionization, charge and particle transfer, attachment and detachment, recombination and association processes. In addition, the processes can also occur in combination (e. g. dissociative recombination). A review of such collision processes in low temperature hydrogen plasmas is given in [JRS03]. Furthermore, radiative processes like emission and absorption of photons take place and diffusion of plasma particles to the vessel walls results in recombination and reformation reactions.

Vibrational excitation of molecular species can moreover have an influence on the EEDF in hydrogen plasmas leading to an underpopulation of low energy electrons ($\approx$ 2–4 eV) and an overpopulation of lowest energy electrons (below about 1 eV). The result is an EEDF, which shows the so-called 'molecular dip' in the low energy region. The actual position of the molecular dip is obviously

dependent on the vibrational excitation energies and is thus also dependent on the isotope.

The actual relevance of particular processes for a specific hydrogen discharge depends, among others, on the densities and temperatures of the plasma particles and has to be determined experimentally. For the present hydrogen plasmas with H_2 pressures of several Pa, electron densities between 10^{16} and $10^{17}\,\mathrm{m}^{-3}$, electron temperatures of 1–5 eV and gas and ion temperatures of 500–1000 K thorough analyses were performed in earlier work [Wün04, Die10] which led to collisional-radiative models for the hydrogen atom [WDF09] and the molecule [Wün04, WN11, Wün12] as well as to a dissociation and ionization model for hydrogen discharges [Wün04]. While the cited references include detailed information on the relevant plasma processes, dedicated information on particular processes are given in the following paragraphs. Furthermore, molecular excitation processes are described in section 6.6.1 and the CR model for the hydrogen atom is briefly introduced in section 6.6.2.

Dissociative excitation (DE)

Heavy particle temperatures in low temperature plasmas are far below 1 eV, whereas the dissociation energy of the hydrogen molecule is at 4.5 eV above the zero-point level $\mathrm{X}\,^1\Sigma_\mathrm{g}^+$, $\nu = 0$, $J = 0$. Therefore, dissociation via highly vibrational and rotational excitation of the molecular ground state is unlikely. However, as shown in figure 3.2, the first electronically excited state of the hydrogen molecule is anti-bonding. Therefore, electron impact excitation to this state immediately leads to dissociation of the molecule into two ground state hydrogen atoms:

$$\mathrm{e}^- + \mathrm{H}_2(\mathrm{X}\,^1\Sigma_\mathrm{g}^+) \longrightarrow \mathrm{e}^- + \mathrm{H}_2(\mathrm{b}\,^3\Sigma_\mathrm{u}^+) \longrightarrow \mathrm{e}^- + \mathrm{H}(n=1) + \mathrm{H}(n=1)\ . \quad (3.24)$$

This process is the main contribution to the overall dissociation rate in low pressure low temperature hydrogen plasmas. Further processes include dissociative excitation of higher lying electronic molecular levels resulting in excited hydrogen atoms (see section 6.6.2) or radiative de-excitation to the repulsive b state. Since these processes involve higher electronic molecular states, the corresponding dissociation cross sections are about an order of magnitude smaller than that for process (3.24) [CJL+01].

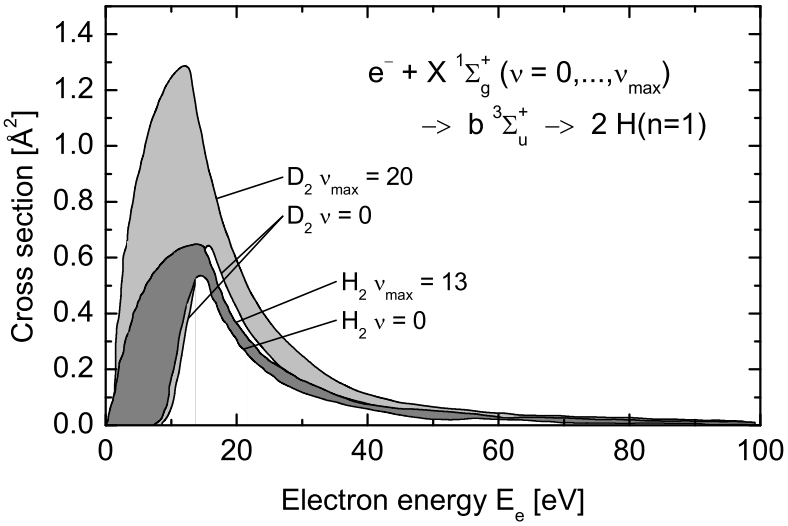

Figure 3.3: *Dissociative electron impact excitation cross sections for hydrogen and deuterium molecules after [CJL+01]. The envelopes for excitation from ground state and a highly excited vibrational state close to the dissociation limit are plotted for both isotopes. The shaded areas illustrate cross sections from initial vibrational levels in between.*

Figure 3.3 shows the cross sections for process (3.24) for hydrogen and deuterium after [CJL+01] depending on the initial vibrational quantum number of the hydrogen isotope beginning from the zero-point level $\nu = 0$. For H_2 a maximal vibrational level of $\nu_{\max} = 13$ is shown, whereas for D_2 $\nu_{\max}$ is 20. In both cases the excitation energy of the maximal vibrational level is close to the dissociation energy, where for D_2 the closer lying vibrational levels lead to higher possible quantum numbers [FW06a]. The cross sections for initial vibrational levels between $\nu = 0$ and $\nu_{\max}$ lie within the gray shaded areas.

Due to the decreasing threshold energy for the dissociative excitation process the cross section increases for increasing initial vibrational quantum number. Furthermore, it can be seen clearly, that the cross sections for the deuterium molecule are larger than for the hydrogen molecule. This leads to a higher dissociation rate in D_2 than in H_2 plasmas as long as electron temperature and density are similar.

The molecular ion H_3^+ and the mean ion mass

The molecular ion H_3^+ is produced by the reaction

$$H_2^+ + H_2 \longrightarrow H_3^+ + H\ , \tag{3.25}$$

where either a hydrogen atom or a proton is transfered. The process is exothermic by 1.7 eV and the rate coefficient at thermal energies of the colliding species is $2 \times 10^{-15}\,\mathrm{m^3/s}$ [JRS03]. This value is larger than the rate coefficient for direct electron impact excitation of the level $n = 3$ of atomic hydrogen (upper level of the H_α emission) from the atomic ground state at an electron temperature of 5 eV [WDF09]. Since the H_α line is readily seen in literally each hydrogen plasma it can be comprehended that the formation reaction (3.25) is very significant. Furthermore, the dissociation energy of H_3^+ is 4.5 eV, i. e. H_3^+ is as stable as molecular hydrogen H_2.

Therefore, the molecular ion H_3^+ constitutes a major contribution to the total ion density in hydrogen plasmas. For plasma parameters relevant to the present investigations (H_2 pressure several Pa, n_e several $10^{16}\,\mathrm{m^{-3}}$, T_e 1–3 eV) H_3^+ is the dominant ion and its density is comparable to the electron density. This was confirmed in several experiments in the literature [MGVHT06, NK07] as well as by measurement in a setup equivalent to the present experiment [Ert10] accompanied by modeling [Wün04].

Thus, the mean ion mass in low temperature hydrogen plasmas with the present plasma parameters is 3 u. This is important for the interpretation of measured ion currents and electrostatic potentials via the Langmuir probe, which is described in section 6.5. For deuterium the rate coefficient of reaction (3.25) is similar large ($1.6 \times 10^{-15}\,\mathrm{m^3/s}$ [CF72]) and thus a mean ion mass of 6 u can be used for D_2 discharges.

4 Properties of caesium

4.1 Atomic properties

Caesium is an alkali metal with an atomic mass of 132.9 u and 55 electrons with the configuration [Xe] $6s^1$ [Lid05]. This means that the single valence electron is in the 6th electron shell and the subjacent core shells are closed having the isoelectronic configuration of the rare gas xenon. The single valence electron above the stable core directly leads to a low ionization potential, in fact the lowest of all elements (3.89 eV [Lid05]), and a high chemical reactivity.

Electronically excited states of the caesium atom are described by the *spin-orbit interaction* of the valence electron: The orbital angular momentum $\vec{l}$ couples with the spin $\vec{s}$ of the electron to the total angular momentum $\vec{j} = \vec{l} + \vec{s}$. In contrast to the hydrogen atom described in section 3.2, the energy of the valence electron in Cs depends on $\vec{j}$, which is called *fine structure splitting*. Since only one valence electron is present, the angular momenta of the valence electron are equivalent to the corresponding momenta of the atom $\vec{L}$, $\vec{S}$ and $\vec{J}$. The *atomic state* is then identified by the principal quantum number n of the valence electron and the quantum numbers L, S and J:

$$\left|\vec{L}\right| = \sqrt{L(L+1)}\,\hbar \quad \text{with } L \in \{0, \ldots, n-1\} \;, \tag{4.1}$$

$$\left|\vec{S}\right| = \sqrt{S(S+1)}\,\hbar \quad \text{with } S = \frac{1}{2} \;, \tag{4.2}$$

$$\left|\vec{J}\right| = \sqrt{J(J+1)}\,\hbar \quad \text{with } J \in \{|L-S|, \ldots, L+S\} \;. \tag{4.3}$$

For each combination of $\vec{L}$ and $\vec{S}$ there are $(2S+1)$ possible values for J (as long as $L > 0$). $(2S+1)$ is called *multiplicity* and for the single valence electron system caesium $(2S+1) = 2$ which is called a doublet. Conclusively, the atomic state can be noted by the term symbol

$$n\,{}^{2S+1}L_J \;\equiv\; n\,{}^{2}L_J \text{ for Cs} \;, \tag{4.4}$$

where L is entitled with capital letters: S,P,D,... for $L = 0, 1, 2, \ldots$

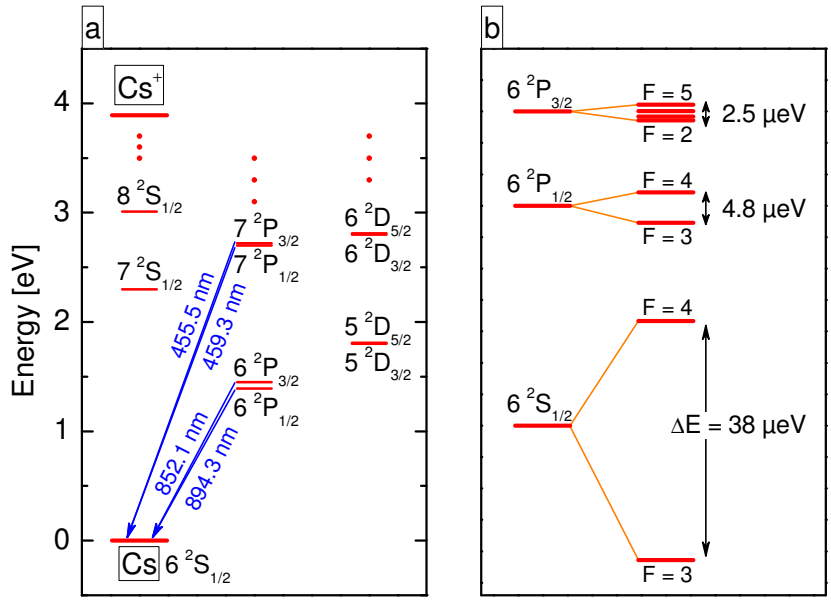

Figure 4.1: (a) *Excerpt of the energy level diagram of the caesium atom [KRRN13].* **(b)** *Illustration of the hyperfine structure splitting of the ground state and the 6 P states of Cs [Ste10].*

Optical transitions between the excited states of the single electron system Cs obey the quantum mechanical selection rules

$$\Delta L = \pm 1 \text{ and} \tag{4.5}$$

$$\Delta J = 0, \pm 1 \ , \text{ but } J = 0 \nleftrightarrow J = 0 \ . \tag{4.6}$$

The energy level diagram for caesium is shown in figure 4.1 (a) after [KRRN13] including the ground state and the first ten excited states as well as the first ionization stage. For the P and D states the doublet fine-structure splitting due to the spin-orbit interaction can be seen. Owing to the selection rule (4.5) the P states are resonant states, which means they are directly coupled to the ground state via optical transitions. The resonant lines lie in the optical spectral range and analogously to the sodium D lines the resonant lines from the 6 P levels are labeled as follows: D_1 – 894.3 nm and D_2 – 852.1 nm. The 7 P levels can additionally relax to the 7 S state and to the 5 D levels and the corresponding emission lines lie in the infrared. The mentioned transitions are used for diagnostic purposes (see section 6.2.2) where table 6.1 gives more information on the particular lines including wavelengths and transition probabilities.

Hyperfine structure of the Cs D lines

The coupling of the total angular momentum $\vec{J}$ of the electron shell with the angular momentum $\vec{I}$ of the nucleus (often called 'nuclear spin') leads to the total angular momentum of the atom $\vec{F}$:

$$\vec{F} = \vec{I} + \vec{J} \tag{4.7}$$

$$\text{with} \quad \left|\vec{F}\right| = \sqrt{F(F+1)}\,\hbar \quad \text{and} \quad F \in \{|I-J|, \ldots, I+J\}\ . \tag{4.8}$$

Again, the total angular momentum $\vec{F}$ and thus the quantum number F can have $(2J+1)$ possible values for each pair of $\vec{I}$ and $\vec{J}$. The resultant energetic splitting of the levels is called *hyperfine structure*.

The nuclear spin of the ^{133}Cs nucleus is $I = 7/2$ [Lid05]. Thus, the atomic ground state with $J = 1/2$ is subdivided due to hyperfine splitting into two levels with $F = 3$ and $F = 4$. The same splitting holds for each excited level with $J = 1/2$, whereas levels with $J = 3/2$ are split into four levels: $F = 2, 3, 4, 5$. The number of hyperfine levels corresponds to the statistical weight g of the particular fine structure state and is given additionally in table 6.1.

The energetic splitting of the ground state and the 6 P states is shown in figure 4.1 (b) after [Ste10]. It yields 38 µeV for the ground state and 4.8 and 2.5 µeV for the $6\,^2\mathrm{P}_{1/2}$ and the $6\,^2\mathrm{P}_{3/2}$ state, respectively. Optical transitions between hyperfine structure levels are allowed for

$$\Delta F = 0, \pm 1\ , \ \text{but}\ F = 0 \nleftrightarrow F = 0\ . \tag{4.9}$$

Owing to the much larger hyperfine splitting of the ground state the resulting D lines are subdivided into two groups about 20–25 pm apart. For the D_1 lines there are two lines per group (each 3 pm apart) whereas the D_2 lines are grouped by three lines each (about 0.5 pm apart). Level energies, wavelengths and relative intensities of the hyperfine split D_1 and D_2 lines can be found in appendix A.

Line profile of the caesium D_2 line

Emission or absorption lines $i \leftrightarrow k$ between atomic, ionic or molecular states are not restricted to the central wavelength λ_0 determined by the energies of the involved levels but are distributed over a finite range of wavelengths due to broadening effects [TLJ99, SVY81]. This distribution is called the line profile P_{line} and is e. g. necessary in the context of the absorption spectroscopy to

determine the caesium density. The following overview describes the broadening mechanisms considered for the determination of the profile of the transition lines of the hyperfine structure of the caesium D_2 line, i. e. natural, Doppler and collision broadening. Detailed information on these line broadening mechanisms and on further mechanisms which are not relevant to the present investigations, e. g. Stark broadening, can be found in [TLJ99, SVY81].

Natural line broadening is based on the Heisenberg uncertainty principle for energy and time. The finite lifetimes τ_i and τ_k of the states involved in the transition lead to slightly indeterminate energies of these states. Therefore the wavelength distribution of the transition is broadened giving a Lorentzian profile with a FWHM of

$$\omega_{\mathrm{nat}} = \frac{\lambda_0^2}{c}\left(\frac{1}{2\pi\tau_i} + \frac{1}{2\pi\tau_k}\right) . \tag{4.10}$$

As the lower state $6\,^2\mathrm{S}_{1/2}$ of the considered Cs line is the ground state, its lifetime is infinite. Therefore only the excited state $6\,^2\mathrm{P}_{3/2}$ contributes to this broadening. With the lifetime $\tau_{6\,^2\mathrm{P}_{3/2}} = 30.4\,\mathrm{ns}$ [Ste10] the natural line broadening yields $\omega_{\mathrm{nat}} = 0.013\,\mathrm{pm}$.

Due to the thermal motion of the emitting or absorbing particles at temperature T the transition line is subject to the Doppler effect. The undirected Maxwellian velocity distribution of the particles consequently leads to the associated *Doppler broadening* that causes a Gaussian line profile with a FWHM of

$$\omega_{\mathrm{dopp}}(T, m) = 2\lambda_0\sqrt{\frac{2k_{\mathrm{B}}T\ln 2}{mc^2}} . \tag{4.11}$$

For caesium with a mass of $m = 132.9\,\mathrm{u}$ the Doppler width of the 852.1 nm line varies from 0.9 to 1.7 pm for temperatures between 300 and 1000 K.

If the emitting or absorbing particles collide with other particles during the radiative process, the transition is disturbed which leads to a smaller effective lifetime of the involved states and thus to an additional broadening[1] of the transition line (see natural broadening). This *pressure* or *collision broadening* of the transition line yields a Lorentzian profile where the FWHM is proportional to the density n_{gas} (or pressure p) of the impinging particles and to the gas temperature T_{gas} to the power β:

$$\omega_{\mathrm{press}}\left(\begin{matrix} n_{\mathrm{gas}} \\ p \end{matrix}, T_{\mathrm{gas}}\right) = \frac{\lambda_0^2}{c}\,\gamma_n(T_0)\,n_{\mathrm{gas}}\left(\frac{T_{\mathrm{gas}}}{T_0}\right)^{\beta} = \frac{\lambda_0^2}{c}\,\gamma_p(T_0)\,p\left(\frac{T_{\mathrm{gas}}}{T_0}\right)^{\beta-1} . \tag{4.12}$$

[1] An associated shift of the transition line is neglected for Cs since the effect is typically one order of magnitude weaker than the corresponding broadening of the line [PFP10].

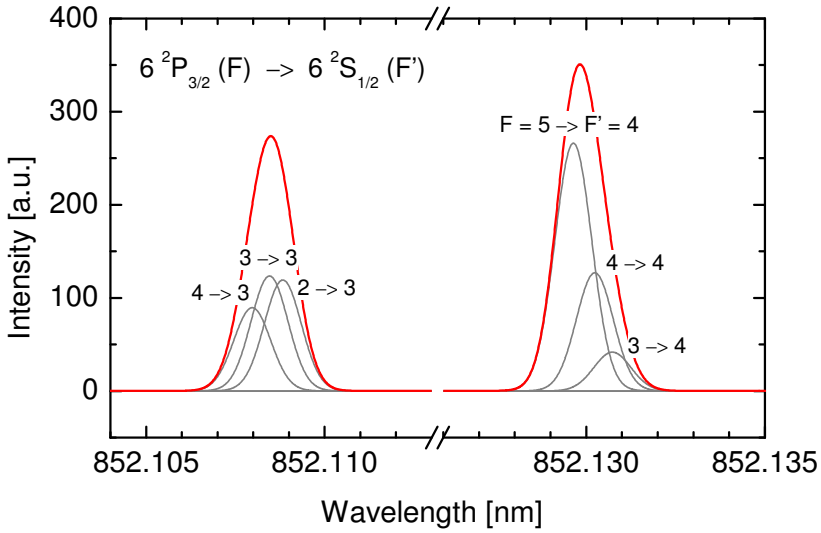

Figure 4.2: *Simulated spectrum of the hyperfine split Cs D_2 line considering natural line broadening and Doppler broadening at 525 K.*

The so-called 'broadening rate' γ_n (or γ_p) is given for a particular temperature T_0 in units of MHz/m^{-3} (or MHz/Pa) in the literature. The exponent β depends on the actual collision process between the particles and thus on the interaction potentials [TLJ99]. For Cs in collision with hydrogen molecules β is assumed to be 0.5 and the rate is $\gamma_{p,\mathrm{H_2}} = 27.13\,\frac{\mathrm{MHz}}{\mathrm{Torr}}$ at a temperature of $T_0 = 313\,\mathrm{K}$ whereas for deuterium it is $\gamma_{p,\mathrm{D_2}} = 22.84\,\frac{\mathrm{MHz}}{\mathrm{Torr}}$ [PFP10]. Thus, for a hydrogen gas pressure of 10 Pa and a gas temperature of 525 K the additional broadening due to collisions is $\omega_{\mathrm{press}} = 0.004\,\mathrm{pm}$. Broadening arising from collisions among caesium atoms can be neglected for ion source relevant conditions due to the low caesium densities involved.

The profile of the single hyperfine transition line is determined by the convolution of the particular profiles arising from the broadening mechanisms. The given values on the lifetime of the upper level and the broadening rate are assumed to be valid for each line, whereas the corresponding central wavelength is considered individually for each hyperfine structure component. The final line profile P_{line} of the Cs D_2 line is calculated as the weighted sum of the hyperfine lines, where the relative intensities are distributed according to [WE33]. Normalization of the line profile is performed after $\int_{\mathrm{line}} P_{\mathrm{line}}(\lambda)\,\mathrm{d}\lambda = 1$.

The resulting spectrum of the D_2 line is shown in figure 4.2 for an exemplary particle temperature of 525 K in vacuum. The particular hyperfine transitions are denoted and the segmentations due to the splitting of the upper and the lower level are clearly observable.

It can be seen in figure 4.2 that the grouped hyperfine lines already overlap due to Doppler broadening with temperatures common to laboratory conditions. Therefore, the single emission lines are rarely observed experimentally. However, the two groups of lines can be detected with an optical system provided the apparatus profile is narrower than about 20 pm. The spectrometers applied within this work have apparatus profiles with a FWHM of about 15 pm at 852 nm: An exemplary absorption spectrum can be seen in figure 6.3 (a) at the gray shaded background confirming the double peak structure of the hyperfine split D_2 line.

4.2 Caesium layers

4.2.1 Adsorption and desorption of Cs – vapor pressure of pure Cs

The process of adsorption of caesium onto a substrate is called *cesiation* and the characteristics of the resultant coating are discussed in the following.

If caesium atoms come in contact with a substrate an ionic bonding will develop by donating the valence electron into the solid state. The resulting dipoles of the adsorbed Cs atoms cause a repulsive interaction with dipoles in their vicinity. This leads to a decrease in the binding energy of adsorbed Cs atoms with increasing coverage of the substrate [TL33]. The Cs coverage is described by the covering fraction θ which is defined as the amount of bonding sites occupied by Cs atoms in relation to the full occupation, which corresponds to one monolayer (1 ML) of Cs. The atomic radius of the Cs atom is 265 pm and thus an area density of about 4.5×10^{18} Cs atoms per m^2 can be expected for one monolayer. However, the actual surface concentration within one monolayer of adsorbed Cs atoms depends on the crystallographic structure of the substrate surface as it defines the distribution of the bonding sites. Above the adsorption of a complete monolayer further Cs atoms are adsorbed due to the van-der-Waals interaction with the already existing Cs layer.

For an equilibrium condition the adsorption flux is in balance with the corresponding desorption flux of Cs atoms from the surface. The transition from the strong ionic bonding below one monolayer to the loose van-der-Waals bonding beyond one monolayer leads to a distinct dependence of the desorption flux on the Cs coverage θ.

For Cs coverages below one monolayer the desorption flux $\Gamma_{\mathrm{Cs}}^{\mathrm{desorp}}$ of Cs atoms from a tungsten substrate depending on the covering fraction θ is given by [ATG85]:

$$\begin{aligned}\Gamma_{\mathrm{Cs}}^{\mathrm{desorp}} = &\quad \left(6\times10^{-13}\,\mathrm{s}\right)^{-1} \quad \theta\exp\left(-\frac{3.37\,\mathrm{eV}-\theta\,2.78\,\mathrm{eV}}{k_{\mathrm{B}}T_{\mathrm{surf}}}\right) \qquad \left[\frac{\mathrm{ML}}{\mathrm{s}}\right] \\ = &\left(7.5\times10^{30}\,\mathrm{m^{-2}s^{-1}}\right)\theta\exp\left(-\frac{3.37\,\mathrm{eV}-\theta\,2.78\,\mathrm{eV}}{k_{\mathrm{B}}T_{\mathrm{surf}}}\right) \qquad \left[\frac{1}{\mathrm{m^2 s}}\right] ,\end{aligned} \tag{4.13}$$

where T_{surf} is the surface temperature and the numerator of the exponential function describes the decreasing binding energy of the adsorbed Cs atoms on the substrate with increasing covering fraction.

Above one monolayer the covering fraction has no influence and the surface physics are determined by the bulk properties of pure Cs. Thus, desorption of Cs from the surface is described by the vapor pressure, which is dependent on the surface temperature and the state of matter. The melting temperature of Cs is at 28.5 °C [Lid05] and the equilibrium caesium vapor pressure p_{Cs} above a caesium surface of temperature T_{surf} is given by [TL37]:

$$\begin{aligned} p_{\mathrm{Cs}} &= 133\,\mathrm{Pa}\times10^{(10.5460-1.00\log_{10}T_{\mathrm{surf}}/K-4150\,\mathrm{K}/T_{\mathrm{surf}})} \quad \text{for solid Cs } (T_{\mathrm{surf}}<302\,\mathrm{K}) \\ p_{\mathrm{Cs}} &= 133\,\mathrm{Pa}\times10^{(11.0531-1.35\log_{10}T_{\mathrm{surf}}/K-4041\,\mathrm{K}/T_{\mathrm{surf}})} \quad \text{for liquid Cs } (T_{\mathrm{surf}}>302\,\mathrm{K}) . \end{aligned} \tag{4.14}$$

The corresponding equilibrium flux from and thus also onto the Cs surface can be calculated via the kinetic theory of gases:

$$\Gamma_{\mathrm{Cs}}^{\mathrm{desorp}} = \frac{1}{4}n_{\mathrm{Cs}}\bar{v}_{\mathrm{Cs}} = \frac{p_{\mathrm{Cs}}(T_{\mathrm{surf}})}{\sqrt{2\pi m_{\mathrm{Cs}}k_{\mathrm{B}}T_{\mathrm{Cs}}}} , \tag{4.15}$$

where n_{Cs}, $\bar{v}_{\mathrm{Cs}}$ and T_{Cs} are the density, the mean thermal velocity and the temperature of the Cs vapor above the surface and m_{Cs} is the atomic mass of Cs.

Calculated desorption fluxes for below and beyond a complete monolayer together with the vapor pressure above a pure Cs surface are shown in figure 4.3. The desorption fluxes in part (a) show a very steep dependence on the covering fraction θ and on the surface temperature T_{surf}: for instance, increasing θ from 0.8 to 0.9 ML at a surface temperature of 150 °C leads to an increase of the desorption flux by a factor of 2000 and a temperature increase from 80 °C to 150 °C at a θ of 0.9 ML increases the flux by a factor of 100. In absolute scales $\Gamma_{\mathrm{Cs}}^{\mathrm{desorp}}$ can easily lead to the evaporation of a full monolayer of Cs per second.

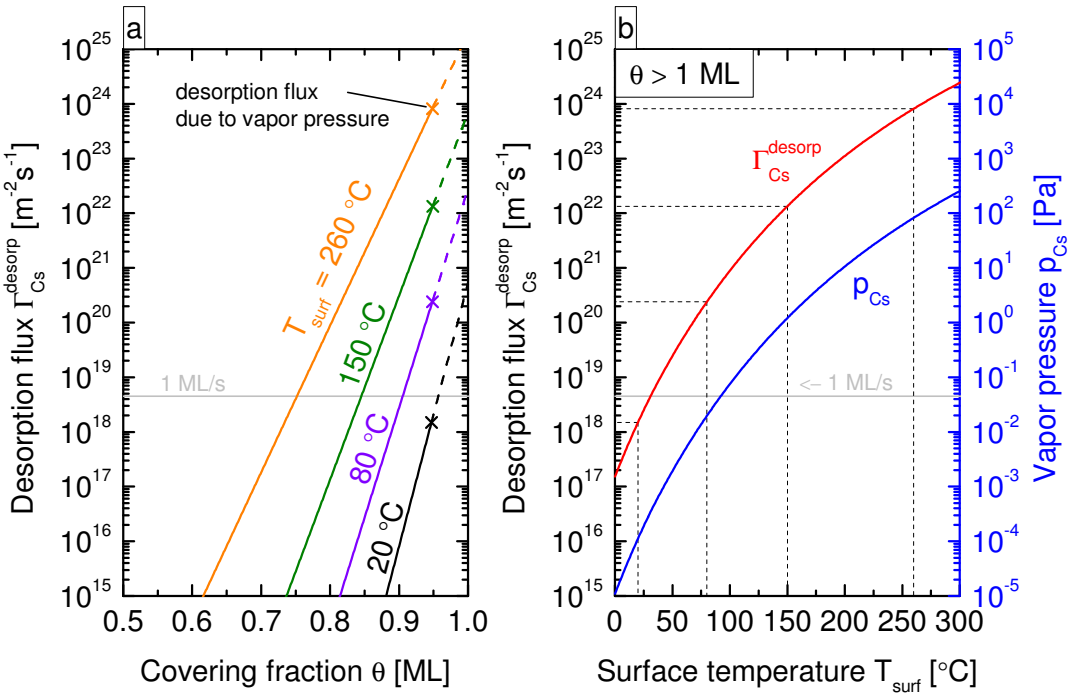

Figure 4.3: (a) *Desorption flux of Cs atoms from fractional Cs layers depending on the surface temperature after equation* (4.13) *[ATG85]. The maximum fluxes denoted by the crosses are determined by the flux arising from the vapor pressure as illustrated in part (b) by the dashed lines.* **(b)** *Equilibrium vapor pressure of Cs vapor above a pure Cs surface (equation* (4.14) *[TL37]) and the corresponding desorption flux after equation* (4.15) *for* $T_{\mathrm{Cs}} = T_{\mathrm{surf}}$*. The desorption flux corresponding to a full monolayer per second is denoted additionally in both parts.*

The desorption flux arising from the vapor pressure (part (b)) is calculated assuming thermal equilibrium between the surface and the Cs vapor: $T_{\mathrm{Cs}} = T_{\mathrm{surf}}$. The vapor pressure of caesium is the second largest of all elements after mercury [Lid05], which is the reason behind the possibility of injecting Cs into ion sources via thermal evaporation. A vapor pressure of 1 Pa is already obtained at a temperature of 146 °C and the temperature dependence is very steep: A temperature rise to 200 °C increases the vapor pressure to about 10 Pa and leads to an equally increased desorption flux by a factor of 10. Comparing the desorption fluxes for high covering fractions with the desorption flux calculated from the vapor pressure for the corresponding surface temperatures shows, that above about 0.95 monolayers the flux from the fractional Cs layer seems to be larger than determined by the vapor pressure. This behavior is physically impossible which means, that at $\theta = 0.95$ ML the Cs layer already shows properties attributable to the Cs bulk. This can be explained by the increasingly adsorption of Cs atoms

in a second layer even if the first layer is not fully occupied [TL33]. In this case deviations from the relation (4.13) are expected, since multi-layer growth is not considered.

Due to the high desorption fluxes of adsorbed Cs layers, a layer thickness of one monolayer or more can only be obtained at very high adsorption fluxes onto the substrate, which are rarely achieved in ion sources or in the laboratory experiment applied for the present investigations. Therefore, observed physical effects should predominantly be related to fractional Cs layers. However, this constraint is only existent if the properties of pure Cs layers are applicable to the system under investigation. The involvement of Cs compounds can significantly lower the desorption fluxes and thus increase the layer thickness, which is, however, consisting of Cs compounds in that case (see section 4.3.2).

4.2.2 Work function of cesiated surfaces

For metallic substrates the dipole bonding of adsorbed caesium atoms is attained by the transfer of the valence electron into the conduction band of the metal. This leads to the lowering of the electron work function of the surface. With increasing Cs coverage the work function decreases until the repulsive forces between the dipoles lead to an increasing work function again, converging to the equilibrium value of the caesium bulk. Figure 4.4 illustrates the typical dependence of the surface work function χ on the covering fraction θ.

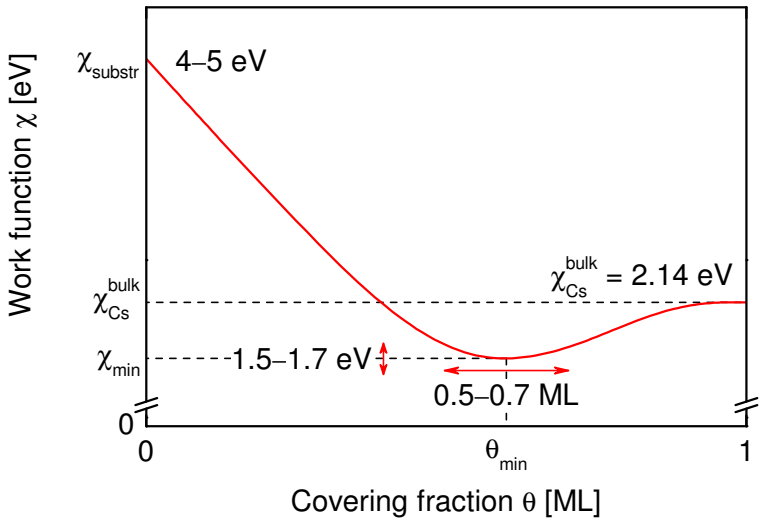

Figure 4.4: *Illustration of the work function dependence on the Cs coverage during the cesiation process of a metallic substrate.*

Typical values of the bare substrate work function χ_{substr} are between 4 and 5 eV, e. g. 4.6 eV for molybdenum or 4.55 eV for tungsten [Mic77]. The quantitative evolution of the work function due to cesiation depends on the actual substrate material and its crystallographic orientation at the surface to be covered with Cs. However, for low Cs coverage a linear dependence can be observed and the covering fraction θ_{min} for which the minimum work function χ_{min} is obtained is always at about 0.5–0.7 ML achieving an electron work function of about 1.5–1.7 eV [Wil66a, Wil66b, SS68]. At one monolayer the bulk value of a pure Cs surface of $\chi_{\mathrm{Cs}}^{\mathrm{bulk}} = 2.14\,\mathrm{eV}$ [Mic77] is attained and the work function saturates for $\theta > 1\,\mathrm{ML}$.

4.3 Chemical properties

4.3.1 Caesium compounds

The low ionization potential of the alkali metal caesium is directly linked to the highest electropositivity of all stable elements [Lid05]. Hence, caesium shows a very high chemical reactivitiy and a multitude of Cs compounds exist. Under standard conditions each of them are solid and crystallize, with the exception of the gaseous caesium dimer Cs_2. Table 4.1 summarizes some compounds together with the corresponding heat of formation and the melting point.

The enthalpies given in the table correspond to the potential energy of the synthesized compound relative to the reagents. During the actual synthesis, there my be endothermic intermediate steps. Therefore, the table gives no information, whether or not a particular compound is formed spontaneously, but in each case the product is more stable than the reactants ($\Delta_{\mathrm{f}}H^0 < 0$), except for Cs vapor and the Cs dimer. The latter is the only compound that is formed endothermally. This is because the synthesis reaction needs to be performed in gas phase and thus the liberation of the dissociation energy of the molecule ($43.9\,\mathrm{kJ/mol} = 0.45\,\mathrm{eV}$ [Lid05]) is overcompensated by the evaporation enthalpy for Cs ($2 \times 76.5\,\mathrm{kJ/mol}$).

Since any Cs compound besides the dimer is most stable in crystalline form, the reactions will most probable occur at surfaces where condensed Cs can react with adsorbed particles. Chemical reactions in gas phase will lead to chemical vapor deposition of the Cs compounds onto the surfaces. The actual occuring chemical reactions can be very complex. Figure 4.5 (a) gives a rough overview of the possible reaction paths of Cs with H_2, O_2 and H_2O. In presence of water

Table 4.1: *Caesium compounds with heats of formation $\Delta_f H^0$ for the crystalline and the gaseous form (if existent) and the melting point T_{melt} (dec. means decomposition) ([Lid05] and [1][HH13]).*

Name	Formula	$\Delta_f H^0$ [kJ/mol] crystal	gas	T_{melt} [°C]
Caesium	Cs	0	76.5	28.5
Caesium dimer[1]	Cs_2		107.4	
Caesium hydride	CsH	-54.2		$\approx$ 170 (dec.)
Caesium hydroxide	CsOH	-416.2	-256.0	342
Caesium oxide	Cs_2O	-345.8		490
Caesium superoxide	CsO_2	-286.2		432
Caesium carbonate	Cs_2CO_3	-1139.7		792
Caesium nitrate	$CsNO_3$	-506.0		414
Caesium azide	CsN_3			326

molecules each compound is converted to caesium hydroxide CsOH, where the reactions of Cs and CsH with water are very exothermic and can occur explosively. Thereby, the resultant CsOH can also be converted into gaseous form, which is also stable as can be seen in table 4.1. The possibility of caesium to react with oxygen and water is the reason behind the *getter effect* of Cs. This is utilized in environments where very low background pressures are required, i. e. in ultra high vacuum systems.

On the other hand, in environments where pure Cs is required, as in ion sources for negative hydrogen ions, the presented reactions lead to the diminishing of the caesium content. In this context, the gettering of Cs at surfaces is also called *sticking*. Impurity control and reduction is thus a key issue for the performance of negative ion sources [FFW12].

Once Cs is chemically bound at a surface, retrieval is not easily achieved. Possible options involve thermal decomposition and plasma treatment. Due to the very stable crystalline form and the low vapor pressure of most of the Cs compounds the former method is restricted to very high temperatures which are barely achieved under ion source relevant parameters. However, the caesium hydride CsH decomposes already at about 170 °C under standard conditions. In vacuum environment this can be used to effectively recover pure Cs bound in caesium hydride, as will be shown below.

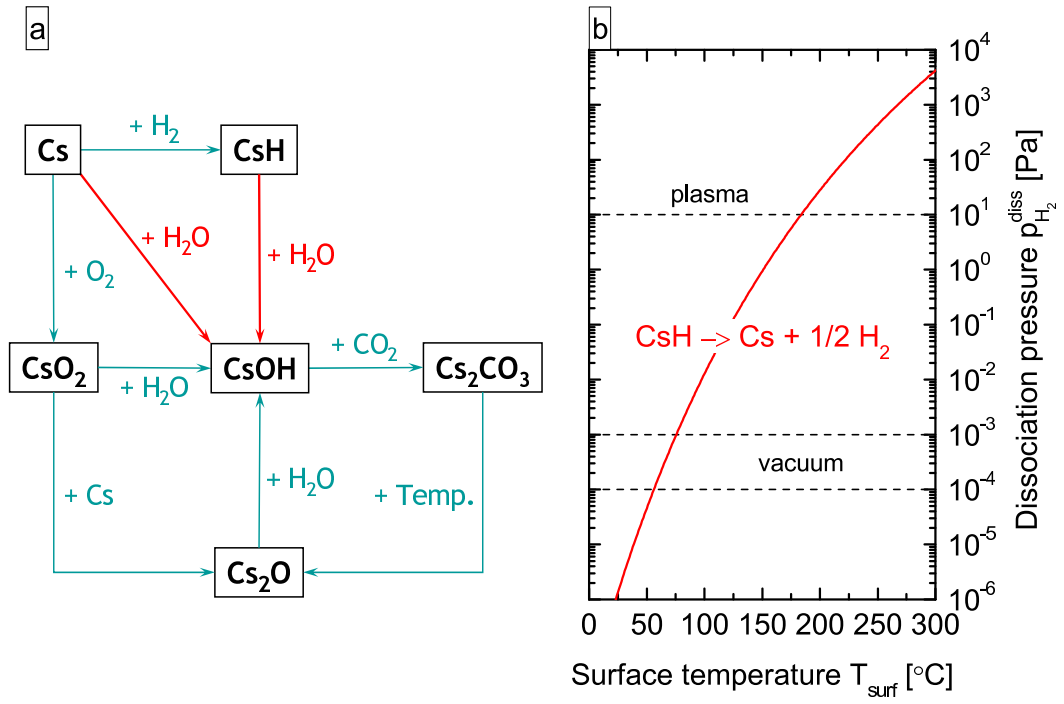

Figure 4.5: (a) *Scheme of possible reactions among Cs compounds. Red arrows denote possibly explosive reactions.* **(b)** *Dissociation pressure of CsH after equation* (4.16) *[SP94] representing the temperature dependent decomposition of the compound.*

The second possibility to regain Cs is the interaction of plasma particles with the adsorbed compounds. Due to the boundary potentials between the bulk plasma and the surrounding vessel walls, energetic ions impinge onto the Cs compound layers and Cs or Cs compounds can be released. Evaporated Cs compounds can subsequently be dissociated within the plasma. Moreover, high energetic photons from optical transitions within the discharge can assist the evaporation of particles from the surfaces due to the photoinduced breaking of chemical bonds. On the other hand, dissociation of H_2 and impurities within the plasma can introduce further reaction channels which are not accessible in vacuum or gas phase. Furthermore, the interaction of the plasma with the vessel walls can lead to an activation of adsorbed substances (generation of bonding sites) and thus to an enhanced chemical gettering of Cs. Hence, the actual influence of plasma on the pure Cs content within the vessel is not easily assessed a priori and would require sophisticated plasma and surface chemistry models.

Caesium hydride

The diatomic molecule CsH is commonly discussed in the context of the so-called *laser snow effect* [TMH75]: in a mixture of Cs vapor and hydrogen gas, particles are formed under the influence of laser light with photon energies of about 2.7 eV. The effect was explained by the resonant production of caesium hydride molecules and subsequent di- and polymerization to CsH crystals [TMH75]. The resonant character evolves from the difference in the dissociation energies of H_2 (4.5 eV [Sha70]) and CsH (1.8 eV [Lid05]) which has to be provided externally. Since both the 7 P states of Cs and the vibrational level $\nu = 6$ of the hydrogen ground state have an excitation energy of 2.7 eV [KRRN13, FW06a], the energy for the formation of the CsH molecule can be provided by the laser [TMH75]. Various studies on the 'laser snow effect' were performed leading, among others, to initial and product state resolved cross sections and rate coefficients for the underlying processes [SFLB81, VFLS83, VFDS86, LRV91] and to investigations on the molecular structure and spectroscopic properties of the caesium hydride molecule. A thorough review of the molecular data on CsH is presented in [SZY91].

For investigations in vacuum without the presence of an appropriate laser light the production of CsH molecules in the volume is thus very unlikely, although the formation enthalpy is negative. The main reason is the necessity of dissociating the hydrogen molecule prior to CsH formation. In plasma however, dissociated hydrogen atoms as well as excited hydrogen molecules and caesium atoms are present. Nevertheless, a direct reaction of Cs and H is only possible, if a third body is involved in the collision process, which absorbs part of the released dissociation energy of the CsH molecule. Otherwise, the collision partners Cs and H will exit the quasi-molecule potential without attachment [Her50].

Since three-body-collisions are very unlikely at pressures of a few pascals and dissociated hydrogen atoms are rarely present in vacuum, formation of CsH will mainly occur at the vessel surfaces for both plasma and vacuum operation.

As mentioned, the bound Cs is lost for the system and has to be retrieved either thermally or via plasma surface interaction. Due to the low vapor pressure of CsH [TMH75] thermal evaporation of the molecule as a whole is very unlikely and thermal decomposition of the compound is more significant. Since further the solubility of hydrogen in caesium is very low [SP94] the decomposition directly leads to the desorption of hydrogen from the surface accompanied by association to H_2. Thus, the temperature dependent decomposition of CsH is directly correlated to the H_2 partial pressure above the surface, which is called *dissociation pressure*

in this case. For the CsH molecule the dissociation pressure $p_{\mathrm{H_2}}^{\mathrm{diss}}$ is given by [SP94]

$$p_{\mathrm{H_2}}^{\mathrm{diss}} = 10^5\,\mathrm{Pa} \times \exp\left(\frac{-56470\,\mathrm{J/mol} + T_{\mathrm{surf}}\,85.33\,\mathrm{J/mol/K}}{1/2\,R\,T_{\mathrm{surf}}}\right)\,, \tag{4.16}$$

where T_{surf} is the temperature of the surface covered with CsH and R is the universal gas constant. The dissociation pressure of CsH depending on the surface temperature is shown in figure 4.5 (b). At a particular surface temperature the hydrogen pressure must exceed a certain value to form caesium hydride. And for a given hydrogen pressure CsH will decompose if a certain temperature is exceeded. For instance, under ion source relevant parameters the background pressure is 10^{-6}–10^{-5} mbar and thus a temperature of 80 °C is sufficient to evaporate H_2 and Cs from the compound according to their respective vapor pressures. In context of the present investigations ICP plasmas with 10 Pa H_2 are analyzed. Thus, a surface temperature of 185 °C is required for the decomposition of CsH under this condition.

In conclusion, Cs bound in caesium hydride can directly be retrieved by thermal activation, whereas for any other Cs compound (see table 4.1 or figure 4.5 (a)) recourse to plasma surface interaction has to be made.

4.3.2 Consequences for ion source relevant conditions

Ion sources as well as the present laboratory ICP experiment are operating under 'high vacuum' with background pressures of 10^{-6}–10^{-5} mbar and mean free paths much longer than the experimental dimensions. Thus, the interaction of Cs with residual gases predominantly occurs at the surfaces where moreover the influx of impurity particles is comparable with the typically achievable fluxes of Cs atoms onto the surfaces (for $n_{\mathrm{Cs}} \approx 10^{15} - 10^{16}\,\mathrm{m^{-3}}$). Therefore, the involvement of Cs compounds in the Cs dynamics of the ion source or the ICP setup is significant or even dominating.

In NNBI ion sources this chemical behavior leads to the requirement for continuous evaporation of Cs into the source to counteract the degradation of the Cs layer on the converter surface. Together with the redistribution processes due to the plasma load an equilibrium state can be reached [GWFN11]. The period to obtain this condition is called the *Cs conditioning phase* which can take several days of continuous evaporation and is severely dependent on the impurity content within the source [FFW12].

Data on characteristics of Cs vapor or Cs layers in the literature are predominantly obtained under 'ultra high vacuum' conditions (background pressure below 10^{-9} mbar) and are thus only applicable to pure Cs. Caesium compounds however, can have characteristics significantly different from that of pure Cs, e. g. most of the compounds are not metallic but ionic crystals. Hence, data from literature research need not to be relevant for ion sources and thus, detailed experimental analyses have to be performed under ion source relevant parameters.

Here, in situ diagnostics for the surface conditions would be desirable, since due to the high chemical reactivity of Cs, results from ex situ diagnostics can rarely be attributed to the surface conditions initially obtained during the investigations. For the present setup the work function measurement is used as in situ diagnostic for the surface characteristics. Further sophisticated surface analysis techniques like X-ray photoelectron spectroscopy (XPS) are not applicable due to experimental constraints. This leads to the approach to use a multitude of diagnostics for the experimental environment to deduce information about the actual surface conditions.

4.4 Hydrogen plasmas containing caesium

As described in section 2.3, the caesium layer which is applied in order to reduce the work function of the converter surface in negative ion sources is established via evaporation of Cs from an oven at the backplate of the expansion region (see figure 2.3 (a)). Furthermore, thermally released and sputtered Cs from the vessel walls and from the converter surface itself contribute to the volume Cs content. Thus, the discharge in front of the PG is a *caesium seeded hydrogen plasma*. In contrast to Cs dominated discharges or even actual Cs plasmas the Cs density in 'seeded plasmas' is much lower than the hydrogen density: $n_{\mathrm{Cs}} \ll n_{\mathrm{H_2}}, n_{\mathrm{H}}$. Nevertheless, the hydrogen plasma can significantly be influenced by the presence of caesium due to its heavy mass, low ionization potential and high chemical reactivity.

In order to separate effects of plasma and surface chemistry from those of the heavy mass and the low ionization potential of Cs, the similarity to the inert rare gas xenon can be utilized: Xe has a comparable mass to caesium and also a lower ionization energy than hydrogen, while chemical reactions can be excluded.

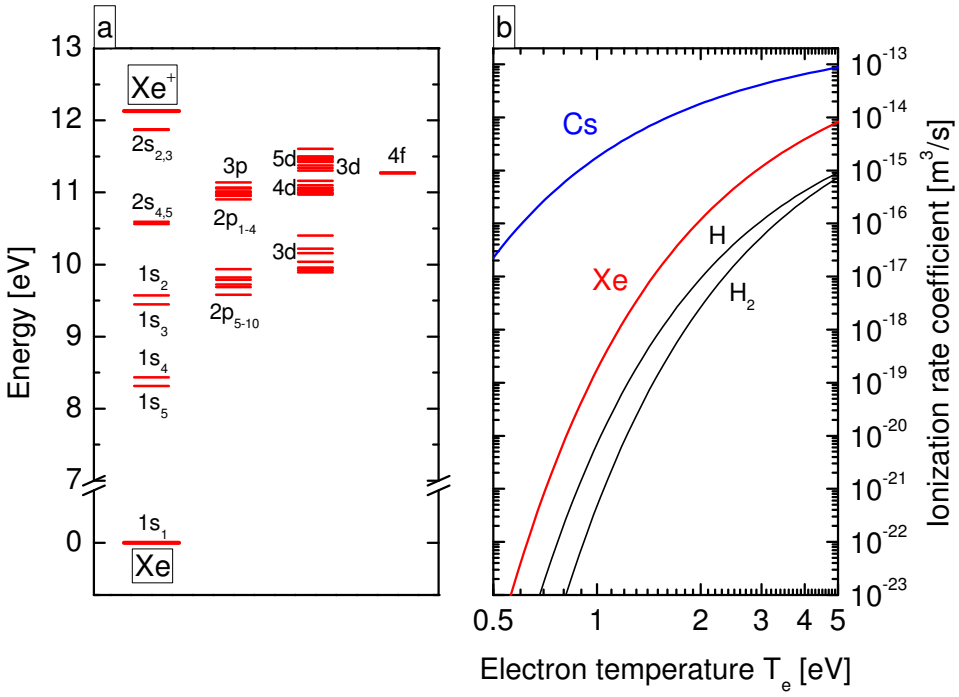

Figure 4.6: (a) *Excerpt of the energy level diagram of the xenon atom [KRRN13].* **(b)** *Electron impact ionization rate coefficients, calculated via equation* (3.8) *for a Maxwellian EEDF using the corresponding cross sections for Xe [WBHF87], Cs [Nyg68], H and H_2 [JRS03].*

4.4.1 A substitute for Cs: the rare gas Xe

Xenon has a mass of 131.3 u and an ionization potential of 12.1 eV [Lid05]. Excitation of electrons from the closed rare gas configuration is described by the so-called *jl* or *Racah coupling* [Sob92] and electronically excited states are denoted by the so-called *Paschen notation* [Pas19]. Figure 4.6 (a) shows an excerpt of the energy level diagram of the Xe atom. In Paschen notation the ground state is denoted by $1s_1$ and the first excited states are the 1s states. The levels $1s_3$ and $1s_5$ are *metastable*, i. e. relaxation via spontaneous emission to the ground state is prohibited. Owing to the Racah coupling it is possible that levels with higher principal quantum numbers lie energetically below levels with lower principal quantum numbers, e. g. part of the 4d and 5d states lie below some of the 3d states. Transitions from the 2p and the 3p levels down to the 1s states are the most prominent lines in the optical and near-infrared spectrum (3p–1s: 455–500 nm, 2p–1s: above 760 nm).

The ionization energy of Xe is higher than that of Cs, but still lower than the ionization potential of atomic and molecular hydrogen. Consequently, the ioniza-

tion rate coefficient for xenon is between that of Cs and that of H or H_2. This is shown in figure 4.6 (b). Electron impact ionization cross sections from [WBHF87] (Xe), [Nyg68] (Cs) and [JRS03] (H,H_2) are translated to rate coefficients by means of equation (3.8) using a Maxwellian EEDF. The much higher rate coefficient for ionizing Cs atoms leads to a much larger expected influence of Cs on a hydrogen plasma compared to Xe at similar admixtures. This has to be taken into account when using the substitute Xe instead of Cs for assessing the influence of a heavy particle with lower ionization potential on the hydrogen plasma.

4.4.2 Interaction of Cs with the H_2 plasma

If caesium is introduced into the hydrogen plasma it will be ionized reaching the isoelectronic configuration of Xe. Thus, the ion Cs^+ is very stable and further ionization to Cs^{2+} requires an additional ionization energy of 23.2 eV [Lid05]. Therefore, only singly ionized Cs is to be expected in the plasma and hereafter the following convention is made: n_{Cs} is the density of neutral Cs, n_{Cs^+} is the density of ionic Cs and n^*_{Cs} is the total caesium density, such that $n^*_{Cs} = n_{Cs} + n_{Cs^+}$.

Due to the presence of Cs ions the mean ion mass within the discharge is altered. However, the determination of the mean ion mass requires measurement of n_{Cs^+} which is not easily achieved. A possibility is given via optical emission spectroscopy of Cs^+ emission lines [FFF+06b]. However, Cs ion levels with emission lines in the optical spectral range have excitation energies of beyond 15.6 eV [KRRN13]. Together with a small ionization degree of the already low Cs density within the plasma, Cs ion emission is negligible in the present setup. Hence, the actual mean ion mass is unknown and the initial value of 3 u (see section 3.3) is used for the interpretation of probe measurements.

Furthermore, Cs seeding into hydrogen plasmas leads to effects related to plasma and surface chemistry. Covering the vessel surfaces with caesium leads to the lowering of the surface work function and thus to the formation of negative hydrogen ions. The enhanced negative ion density can have a great impact on the plasma dynamics, which has to be investigated experimentally. Additionally, the high chemical reactivity of Cs can significantly alter the plasma chemistry of the hydrogen discharge.

Finally, several processes between Cs and the hydrogen particles H, H^+, H^-, H_2, H_2^+, H_3^+ can occur. For the present plasmas with neutral gas and ion energies in the range of maximal 0.1 eV the occurring processes are mostly based on charge exchange collisions in which Cs is ionized due to its low ionization potential

compared to atomic or molecular hydrogen. A review of processes between H, H^+, H^- and Cs can be found in [MOSG85] while molecular ions in collision with Cs are treated in [BCP85] for instance. Collisions of the negative hydrogen ion with Cs is especially discussed in [WCD87] and in [JR78] the mutual neutralization reaction of Cs^+ with H^- is investigated.

Summarizing, the following collision processes are possible from an energetic point of view in low temperature plasmas with thermal heavy particle energies:

$$H_2(\nu \geq 10) + Cs \longrightarrow H_2(\nu = 0) + Cs^+ \tag{4.17}$$

$$H^+ + Cs \longrightarrow H + Cs^+ + 9.7\,eV \tag{4.18}$$

$$H_2^+ + Cs \longrightarrow H_2 + Cs^+ + 11.5\,eV \longrightarrow \longrightarrow \begin{cases} H_2(B\,^1\Sigma_u^+, \nu \leq 2) + Cs^+ & (4.19a) \\ H + H + Cs^+ + 7.0\,eV & (4.19b) \end{cases}$$

$$\begin{aligned} H_3^+ + Cs &\longrightarrow H_2 + H + Cs^+ + 5.5\,eV \longrightarrow \\ &\longrightarrow H + H + H + Cs^+ + 1.0\,eV \end{aligned} \tag{4.20}$$

$$\begin{aligned} H^- + Cs &\longrightarrow CsH + e^- + 1.0\,eV \longrightarrow \\ &\longrightarrow CsH(\nu \leq 11) + e^- \end{aligned} \tag{4.21}$$

$$\begin{aligned} H^- + Cs^+ &\longrightarrow H + Cs + 3.1\,eV \longrightarrow \\ &\longrightarrow H + Cs\,(\text{electronically excited}) \end{aligned} \tag{4.22}$$

The actual occurrence and relevance of the reactions is yet to be investigated experimentally. However, the compilation shows, that Cs can take influence on the plasma chemistry not only at the vessel surfaces but also within the bulk plasma.

5 Experimental setup

The laboratory setup for the fundamental studies on the Cs dynamics under ion source conditions consists of a cylindrical stainless steel vacuum vessel shown in figure 5.1 with 15 cm in diameter and 10 cm height. Via a pumping system comprising a turbomolecular pump and a rotary vane pump the system is evacuated to a background pressure of some 10^{-6} mbar. Gas supply is managed through mass flow controllers and the absolute pressure is measured by a capacitive pressure gauge. Discharges are generated by means of inductive RF coupling via an external planar coil, which is located on top of the discharge vessel and separated from it by a grounded Faraday screen and a Borosilicate glass plate as dielectric between atmosphere and vacuum. The RF generator is connected via the matching network and delivers up to 600 W power at 27.12 MHz. In the present work hydrogen and deuterium discharges are operated at 250 W between 5 and 20 Pa.

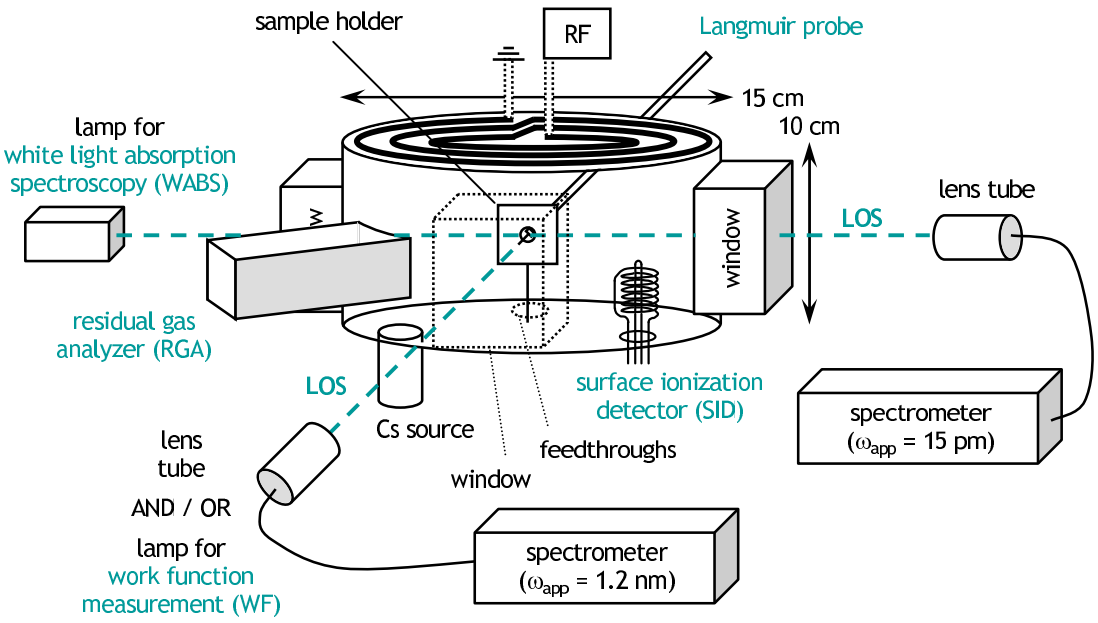

Figure 5.1: *Perspective view of the schematic experimental setup with an overview of the arrangement of the equipment.*

The vessel walls can be cooled or heated by a water circuit whose pipes are mounted round the vessel. The water temperature can be adjusted by means of a temperature control system. The obtained wall temperatures in vacuum and plasma operation depend on the operating equipment and range from about 20 °C to 65 °C.

In order to gain a comprehensive insight into the Cs dynamics in vacuum and plasma multiple diagnostics for Cs and its environment are indispensable. Therefore, Cs fluxes within the vessel are monitored by surface ionization detectors and the volume averaged Cs density is either observed with white light absorption spectroscopy or with optical emission spectroscopy. The work function of a sample surface during cesiation is traced using the photoelectric effect, where evaluation is performed after the Fowler method. A residual gas analyzer is applied to monitor the interaction of Cs with the background gases. Electrostatic potentials within the plasma as well as local and volume averaged densities and temperatures of plasma species (the 'plasma parameters' for short) are determined via a Langmuir probe and optical emission spectroscopy. Table 5.1 gives an overview of the utilized diagnostic methods, the particularly determined parameters and if they can be operated in vacuum, during plasma or in both environments. Diagnostics which are intended for vacuum operation proved to be suitable up to gas pressures of the order of 10^1 Pa.

Since the Cs chemistry at the vessel surfaces is expected to be subject to a short- and long-term behavior, the diagnostics furthermore have to be operated simultaneously to relate parameters from different diagnostics to the same experimental conditions. For this purpose the experiment vessel offers several ports and an exchangeable bottom plate with additional ports which can be used for the peripheral equipment. The basic setup is shown in the perspective figure 5.1. Three ports (at the left, right and front of the vessel) are equipped with quartz windows for the optical diagnostics and for the work function measurement, whereas the lines of sight (LOS) pass at half height diagonal through the vessel. One port is used for the Langmuir probe (backside of the vessel), another for the residual gas analyzer (half left side). The bottom plate holds a surface ionization detector (half right side), the sample holder (almost centered), several electrical feedthroughs (behind the sample holder) and the caesium source (half left side), which is basically a Cs dispenser mounted in an oven. Detailed information on the diagnostic methods can be found in chapter 6 and the Cs source is described and characterized in chapter 7.

Table 5.1: *Applied diagnostic methods including the measured quantities and the possible operation conditions.*

Diagnostic		Measured parameter (loc)al/(vol)ume averaged	Operational in (vac)uum/(pl)asma
SID	surface ionization detector	caesium flux (loc)	vac
WABS	white light absorption spectroscopy	caesium density (vol)	vac & pl
WF	work function measurement	work function (loc)	vac
RGA	residual gas analyzer	impurities (vol)	vac & pl
Langmuir probe		plasma parameters (loc)	pl
OES	optical emission spectroscopy	plasma parameters (vol) & caesium density (vol)	pl

In the following small specified pictograms of each equipment will be introduced to illustrate the particular arrangement within the experiment from a top view. These pictograms are then composed to the complete arrangement of the entire installed equipment for each experimental campaign and will always be shown at the beginning of the corresponding sections in chapters 7 through 9 to facilitate the perception of the applied equipment.

5.1 Sample holder

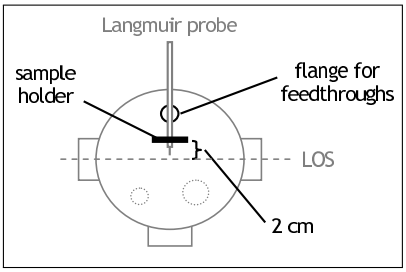

The sample holder (its pictogram is shown on the left side, a schematic is shown in figure 5.2) is mounted upright at the bottom plate electrically and thermally insulated from the grounded vessel walls by use of a teflon mount. It is located at 2 cm from the cylinder axis of the vessel and aligned parallel to the line of sight of the optical diagnostics so that the emission and absorption spectroscopy are not disturbed. It is capable of holding samples

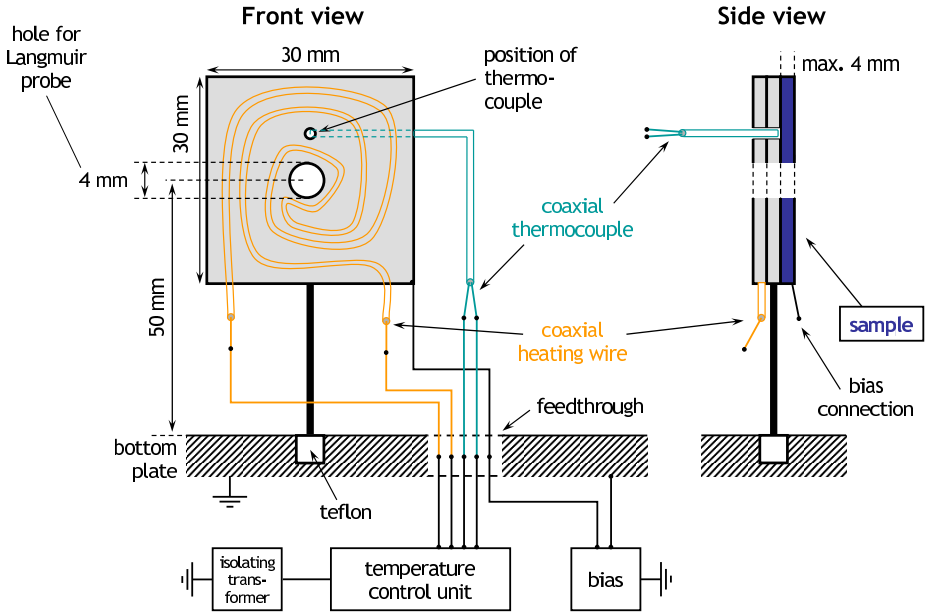

Figure 5.2: *Schematic of the sample holder in front and side view. In front view the sample is not depicted.*

of $30\times30\,\mathrm{mm}^2$ in size and up to 4 mm thickness and it is equipped with a heating wire beneath the sample and a thermocouple contacting the sample from behind, both in coaxial design. The heating wire and the thermocouple are connected to a temperature control unit via vacuum feedthroughs whereas the insulations are each left unconnected as shown in the schematic. Thus, neither the heating wire nor the thermocouple are electrically connected to the sample holder or more specific to the sample itself and electrical insulation of the sample against the vessel walls is maintained. To prevent capacitive coupling to the experimental ground via the coaxial heating wire, the temperature control unit is itself galvanically insulated against the experimental ground (which is the vessel wall). Hence, the insulation of the sample holder enables a reliable biasing of the sample against the vessel walls.

The temperature of the sample is adjusted by feedback control and the response is shown in figure 5.3. Increasing the set temperature leads to an almost instantaneous increase of the sample temperature. The nominal value is reached within 2 minutes and is maintained perfectly constant afterwards. Due to the thermal insulation from the vessel walls even sample temperatures up to 250 °C have only negligible influence on the wall temperature. On the other hand, the sample holder is not actively cooled, which leads to the delayed temperature decrease

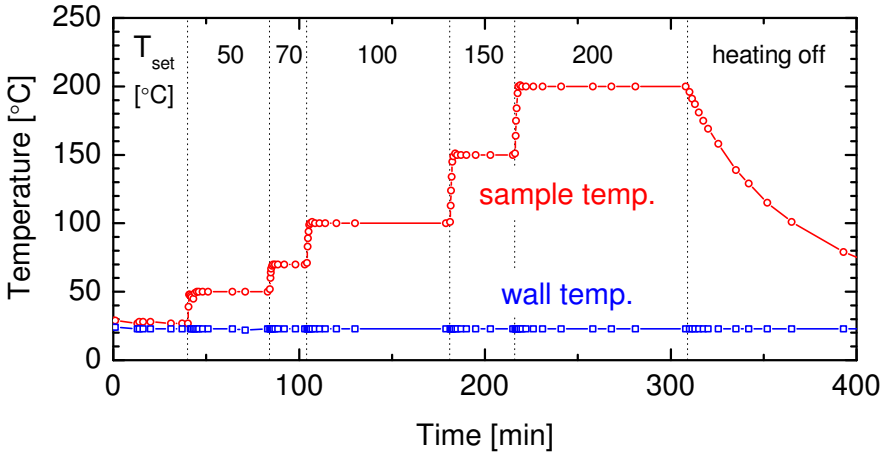

Figure 5.3: *Temperatures of the sample and the vessel wall with varying set point T_{set} of the sample temperature.*

when the heating is turned off. The resulting minimal temperature in vacuum depends on the operating equipment ranging from 20 °C to 90 °C. In plasma operation a boundary potential between the floating sample and the plasma evolves in which ions are accelerated (see section 3.1.3). The resulting energy input of the impinging ions together with the elevated gas temperature in plasma (250–300 °C) leads to intrinsic sample temperatures of about 250 °C.

Furthermore the sample holder includes a hole of 4 mm in diameter in the center. If the sample is also punched, the Langmuir probe can be fed through the sample surface (as illustrated in the pictogram and in figure 5.1). This provides the opportunity for probe measurements in the vicinity of the sample surface. Since the outer diameter of the Langmuir probe is also 4 mm and the probe tip is axially centered, the minimal distance between the probe tip and the sample surface is 2 mm.

5.2 Spectroscopic setup

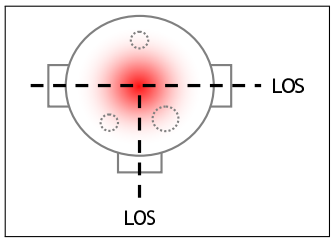

The lines of sight (LOS) for the optical diagnostics lead at half height diagonally through the plasma volume. The emitted or transmitted radiation is collected by lens tubes and transferred to the particular spectrometer by fiber optics. Within the lens tubes the entrance aperture of the fiber is positioned at the focal length (75 mm) of the quartz lens.

Table 5.2: *Data on the applied spectrometers.* ω_{app} *is the full width at half maximum (FWHM) of the Gaussian apparatus profile at 400 and 850 nm. The spectral width is the usable spectral range for a single recording at 400 and 850 nm. The survey spectrometer Plasus Emicon takes the full spectral range with one recording.*

Spectrometer	SPEX 1000M	Acton Spectra Pro	Plasus Emicon MC
Focal length	1 m	0.75 m	4.5 cm
Grating constant	1800 mm^{-1}	1800 mm^{-1}	300 mm^{-1}
⌀ Fiber	600 µm	400 µm	600 µm
Entrance slit width	50 µm	30 µm	25 µm
CCD pixels	2000×800	2500×600	2048×1
Pixel size	15×15 $µm^2$	12×26 $µm^2$	14×200 $µm^2$
ω_{app} (400 → 850 nm)	27 → 15 pm	26 → 15 pm	1.5 → 1.2 nm
Spectral width (400 → 850 nm)	8 → 5.5 nm	16 → 10 nm	entirely 200–1100 nm

Moreover an aperture stop of 10 mm is used to limit the collected solid angle. The position of the fiber together with the aperture stop ensure that only radiation parallel to the optical axis enters the optical fiber. To prevent higher diffraction orders of lower wavelengths within the spectrometers an edge filter (edge at 495 nm) is used for recording emission lines above 520 nm.

Three different spectrometers were applied within the present work, each in Czerny-Turner setup and with a Gaussian apparatus profile: a 1 m–spectrometer (SPEX 1000M), a 3/4 m–spectrometer (Princeton Instruments Acton Spectra Pro) and a survey spectrometer (Plasus Emicon MC). Data on the three spectrometers can be found in table 5.2. The shorter focal length of the Acton spectrometer is compensated by a smaller entrance slit width resulting in a similar FWHM of the apparatus profile as for the SPEX spectrometer. The drawback is a lower sensitivity resulting in a higher calibration factor, which is shown in figure 5.4. The given spectral width in the table corresponds to the spectral range that can be used for spectroscopic analyses. Beyond this range boundary effects of the CCD chip increase to a non-negligible amount. The possibility of the Plasus spectrometer to capture the entire spectral range with one recording at a reduced spectral resolution gives the opportunity for in situ monitoring of the plasma dynamics.

Quantitative emission spectroscopy and absorption spectroscopy require a sufficient wavelength resolution to separate different transition lines from each other. Therefore, the higher resolution spectrometers SPEX and Acton[1] are applied for the evaluation of optical emission spectra and for white light absorption spectroscopy and use the LOS parallel to the possible sample (from left to right in the pictogram or figure 5.1). The survey spectrometer is used to monitor the plasma emission via prominent emission lines where disturbance by close lying lines is known qualitatively and/or can be seen as negligible. The LOS opposite to the Langmuir probe is used for this purpose.

Calibration

The applied spectrometers are wavelength and intensity calibrated. Wavelength calibration can be done via recording emission lines with known transition wavelengths across the entire spectral range. This was performed in an earlier thesis [Bri11].

The intensity calibration is conducted using an Ulbricht sphere as secondary radiation standard. The diffuse and homogeneous continuum emission from the sphere is recorded with the spectroscopic system including the optical windows, possibly neutral density and edge filters, the lens tube and the corresponding optical fiber of the spectrometer. Dividing the known absolute emission from the Ulbricht sphere $\left[(\mathrm{s\,m^2\,nm})^{-1}\right]$ by the measured emission [Cts] normalized to the integration time [s] yields the *calibration factor* $C(\lambda)$ $\left[\left(\mathrm{s\,m^2\,nm\,(Cts/s)}\right)^{-1}\right]$. For the SPEX and the Acton spectrometer this was performed for the central wavelength every 10 nm and linear interpolated in between.

The calibration factors for the three spectrometers are shown in figure 5.4. The calibrated spectral range is limited at the lower end by the decreasing emission intensity of the Ulbricht sphere (around 380 nm) and the decreasing spectral sensitivity or the increasing disturbance due to etaloning at the upper end leading to 880 nm, 970 nm and 1050 nm for the SPEX, Acton and Plasus spectrometer, respectively.

[1] In the course of the work it was necessary to switch from the first to the second spectrometer due to maintenance issues.

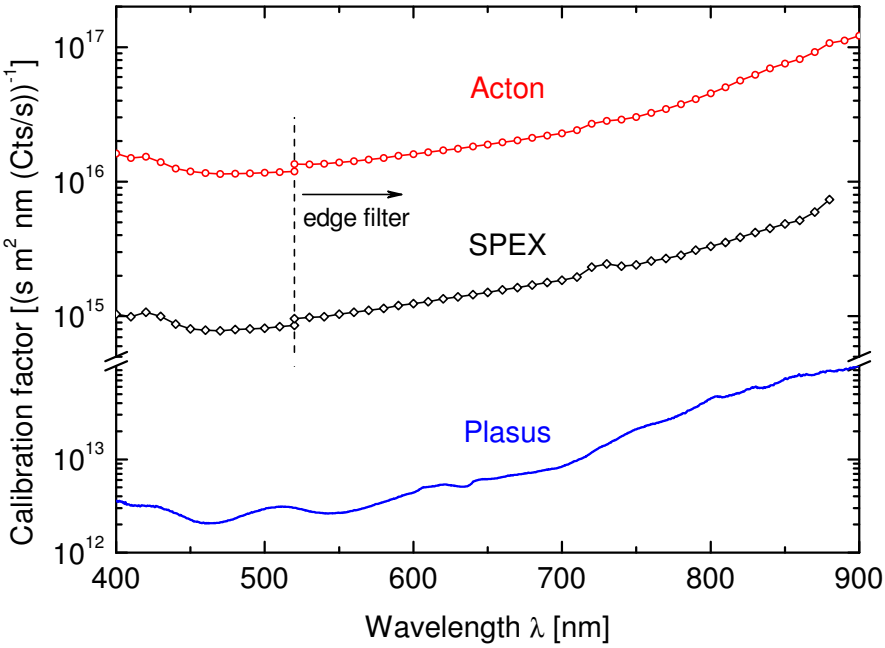

Figure 5.4: *Calibration factors of the applied spectrometers SPEX 1000M, Princeton Instruments Acton Spectra Pro and Plasus Emicon MC.*

The emissivity ϵ_{ik} of a transition line $i \rightarrow k$ is calculated from the measured spectrum $S_{\text{meas}}(\lambda)$ (normalized to the integration time) by

$$\epsilon_{ik} = \frac{1}{l_{\text{pl}}} \int_{\text{line}} S_{\text{meas}}(\lambda)\, C(\lambda)\, \mathrm{d}\lambda \qquad \left[\frac{1}{\mathrm{m^3\,s}}\right] , \tag{5.1}$$

where $l_{\text{pl}} = 15\,\text{cm}$ is the plasma length taken as the diameter of the discharge vessel. Thus, the determined value of ϵ_{ik} corresponds to the averaged value over the line of sight (line integration).

Measurement error

Taking into account the reproducibility of the single recorded spectra, the error in the determination of the measured emission from the Ulbricht sphere and the accuracy of the absolute emission of the Ulbricht sphere, the calibration itself has an error of $\pm 3.4\,\%$ for the SPEX spectrometer and $\pm 4.8\,\%$ for the Acton spectrometer. Together with an average error of the insufficient linearity of the CCD detector system on integration time, an error for the plasma length and the accuracy of determining the line integral via a fit of a Gaussian function, the determined emissivities within this work have a measurement error of $\pm 9.7\,\%$ for the SPEX spectrometer and $\pm 9.6\,\%$ for the Acton spectrometer.

6 Applied diagnostics

6.1 Caesium flux measurement

Flux measurements in alkali metal vapors can be performed using a surface ionization detector (SID), also called *Langmuir-Taylor detector* [Tay29]. Its working principle is based on the ionization of alkali atoms contacting a hot filament. If the work function of the filament is larger than the ionization potential of the alkali atom, energy can be gained by ionizing the atom and transferring the electron into the solid state. Biasing a second electrode negatively to the filament draws an ion current which is proportional to the flux of atoms onto the filament. Due to this bias the device cannot be used in plasma since a high electron current would be drawn from the discharge.

6.1.1 Probability for surface ionization

For a filament made of tungsten with a work function of $\chi_{\mathrm{W}} = 4.55\,\mathrm{eV}$ [Mic77] surface ionization can occur for potassium, rubidium and caesium which have ionization energies E_{ion} of 4.34, 4.18 and 3.89 eV [Lid05] respectively. Within the scope of this work the SID is used to measure Cs fluxes. These fluxes onto the wires can lead to Cs coating which lowers the work function of the filament significantly depending on the covering fraction θ (see section 4.2.2). The equilibrium covering fraction of caesium on a tungsten wire depending on the temperature T_{fil} of the filament and the corresponding work function $\chi(\theta)$ of the covered filament are shown in figure 6.1 (a) after [TL33]. For the calculations a Cs atom flux onto the filament surface of $\Gamma_{\mathrm{Cs}} = 7.2 \times 10^{17}\,\mathrm{m^{-2}s^{-1}}$ corresponding to a Cs density of $n_{\mathrm{Cs}} = 10^{16}\,\mathrm{m^{-3}}$ at a typical gas temperature of $T_{\mathrm{Cs}} = 250\,^{\circ}\mathrm{C}$ was used.

The ionization probability P_{ion} of Cs atoms by the partly covered tungsten filament of temperature T_{fil} having a work function $\chi\Big(\theta(T_{\mathrm{fil}})\Big)$ can be described by the Boltzmann distribution assuming thermal equilibrium during the residence

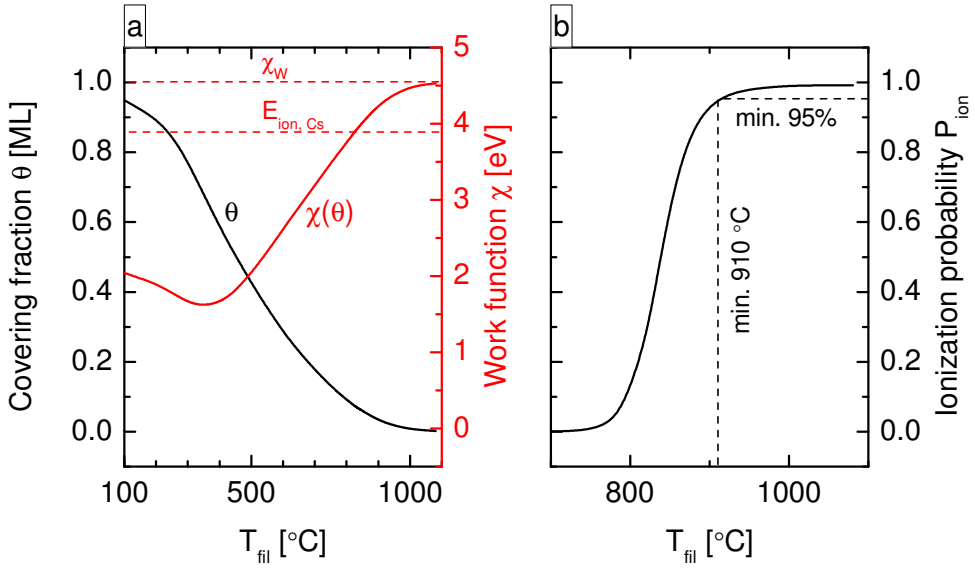

Figure 6.1: (a) *Equilibrium covering fraction of caesium on a tungsten wire and the corresponding work function for* $\Gamma_{\mathrm{Cs}} = 7.2 \times 10^{17}\,m^{-2}s^{-1}$. **(b)** *Ionization probability of Cs atoms at the covered filament.*

time of the Cs atoms at the filament (k_{B} is the Boltzmann constant):

$$P_{\mathrm{ion}} = \frac{n_{\mathrm{Cs^+}}}{n_{\mathrm{Cs^+}} + n_{\mathrm{Cs}}} = \frac{1}{1 + \frac{n_{\mathrm{Cs}}}{n_{\mathrm{Cs^+}}}} = \frac{1}{1 + \frac{g_{\mathrm{Cs}}}{g_{\mathrm{Cs^+}}} \exp\left(\frac{E_{\mathrm{ion,Cs}} - \chi(T_{\mathrm{fil}})}{k_{\mathrm{B}} T_{\mathrm{fil}}}\right)} \,. \tag{6.1}$$

Since the device is used in vacuum, atoms (n_{Cs}) and ions ($n_{\mathrm{Cs^+}}$) have to be considered only in electronic ground state where $g_{\mathrm{Cs}} = 2$ and $g_{\mathrm{Cs^+}} = 1$ are the corresponding statistical weights [KRRN13]. The ionization probability is calculated using the values of $\chi\big(\theta(T_{\mathrm{fil}})\big)$ from figure 6.1 (a) and plotted in figure 6.1 (b). Low temperatures lead to high Cs covering of the filament and thus to a low work function which in turn lowers the ionization probability. As this would result in a decreasing sensitivity of the device, coating of the ionization filament has to be prevented. In order to achieve a minimum of 95 % ionization probability at a Cs flux of $7.2 \times 10^{17}\,\mathrm{m^{-2}s^{-1}}$ the filament temperature should at least be 910 °C (corresponding to $\theta = 0.03\,\mathrm{ML}$ and $\chi = 4.27\,\mathrm{eV}$). Since the filament is made of tungsten, these temperatures can easily be achieved by ohmic heating: balancing electrical power, thermal conduction and thermal radiation, about 2 A minimal heating current is calculated for a filament diameter of 300 µm.

Due to the high reactivity of caesium, the subsequent ion current onto the ion collector would again rapidly coat the collector with caesium and caesium compounds. To ensure reliable operation without disturbing desorption or adsorption

effects from or onto the device, the ion collector is also kept at a high temperature. This can be accomplished by using likewise a tungsten wire as ion collector and heating it by an electrical current.

Measuring the ion current

The produced ions are drawn to the ion collector by the bias voltage. On the other hand, the ions lead to space charges surrounding the ionization filament which can limit the maximal current that can be drawn and lead to a dependency of the current on the bias voltage after the Child-Langmuir Law [Chi11]. Since for the SID the ion current should only depend on the varying atom flux onto the ionization filament, the voltage should be high enough to avoid this space charge limitation. An experimental approach to this issue showed, that at voltages of 40 to 50 V no saturation effect of the measured ion current was ever observed, which proves that the currents are not limited by space charges.

The measured Cs ion current I_{SID}, afterwards called 'SID signal', is then connected to the incoming Cs flux Γ_{Cs} via the following relation (e is the elementary charge):

$$\begin{aligned} I_{\mathrm{SID}} = e\ A_{\mathrm{col}}\ \Gamma^{\mathrm{col}}_{\mathrm{Cs^+}} &= e\ A_{\mathrm{col}}\ P_{\mathrm{bias}}\ \Gamma^{\mathrm{fil}}_{\mathrm{Cs^+}}\ \frac{A_{\mathrm{fil}}}{A_{\mathrm{col}}} \\ &= e\ A_{\mathrm{fil}}\ P_{\mathrm{bias}}\ P_{\mathrm{ion}}\ \Gamma_{\mathrm{Cs}}\ . \end{aligned} \tag{6.2}$$

The ion flux $\Gamma^{\mathrm{col}}_{\mathrm{Cs^+}}$ reaching the ion collector at the surface area A_{col} started as $\Gamma^{\mathrm{fil}}_{\mathrm{Cs^+}}$ from the ionization filament surface area A_{fil}, whereas only the fraction P_{bias} is directed to the ion collector by the bias voltage. Due to collisions with gas particles and/or the experiment vessel this number can be lower than unity even without space charge limitation. The ion flux $\Gamma^{\mathrm{fil}}_{\mathrm{Cs^+}}$ is in turn produced by surface ionization from the atom flux Γ_{Cs} with the probability P_{ion}. If the exact geometry of the wires and the electrical field distribution are known, the Cs flux onto the SID can in principle be calculated from the measured current. However, the electric field topology can be very complex. Thus, an experimental approach for the calibration of the SID signal is presented in section 7 and comparison with equation (6.2) is performed.

6.1.2 Surface ionization detector (SID)

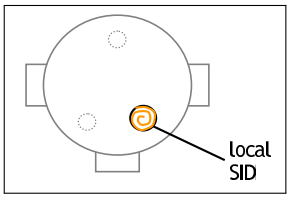

Cs fluxes are measured at two positions within the experimental setup: firstly near the bottom plate via the so-called *local SID* and secondly directly at the nozzle of the Cs source, called *oven SID*. While the first is used to monitor the caesium fluxes within the vessel, the latter is employed to measure the evaporation rate of the Cs oven and is described in chapter 7.

A schematic of the local SID is shown in figure 6.2. It comprises the two tungsten wires, the ionization filament and the ion collector, operated at heating currents of 2.8 A each. The bias voltage between the filaments is set to 40 V. Cs ion currents range from some nA up to mA. They are monitored continuously via a Keithley 602 Electrometer and values are recorded manually depending on the temporal evolution of the system (max. six times per minute, typically every five minutes).

Calibration of the SID current after equation (6.2) is not possible for the local SID due to the complex geometry. However, the SID signal in units of nA or µA is still directly proportional to the Cs flux. Therefore an absolute calibration is not necessary to observe the relative caesium re-distribution within the vessel.

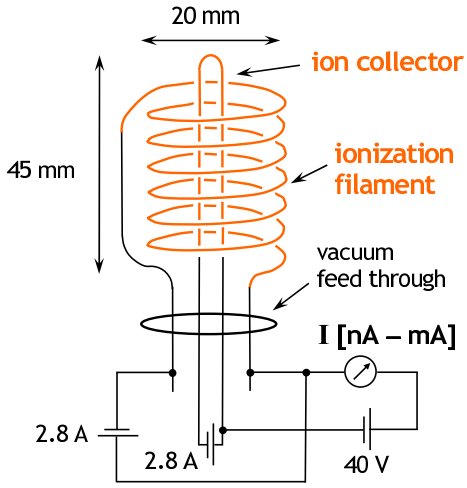

Figure 6.2: *Schematic of the local surface ionization detector (local SID).*

Measurement error

The uncertainty for one manually recorded value is taken to be half of one scale tick. Thus, the error ranges from ± 0.5 nA for SID currents of up to 100 nA to ± 50 nA for SID signals of up to 10 µA.

Contributions to the measured signal

Due to the temperature of the filaments and the bias voltage several additional effects besides surface ionization of Cs atoms can contribute to the measured signal.

The main contribution to this 'dark current' is the thermionic emission of electrons via the Edison effect. The current density $j_{\mathrm{e,th}}$ can be described by Richardson's law:

$$j_{\mathrm{e,th}} = R\, T_{\mathrm{fil}}^2\, \mathrm{e}^{\frac{-\chi(T_{\mathrm{fil}})}{k_{\mathrm{B}} T_{\mathrm{fil}}}} \quad . \tag{6.3}$$

The constant R can be approximated by the Richardson constant $4\pi m_{\mathrm{e}} k_{\mathrm{B}}^2 e/h^3 = 1.2 \times 10^6\,\mathrm{A/m^2K^2}$, where m_{e} is the electron mass, k_{B} the Boltzmann constant, e the elementary charge and h the Planck constant. Electron emission from the ionization filament can be neglected due to the retarding bias voltage, whereas emission from the ion collector leads to a measurable signal. Estimations taking account of the surface area of the ion collector give dark currents due to thermionic emission of about 5 nA. Contributions from the Schottky effect of the bias voltage (field emission) can be neglected as the electrical field strengths are of the order of $10^4\,\mathrm{V/m}$ which is too low for a significant impact.

However, the bias voltage leads to acceleration of the emitted electrons gaining energies of up to 40 eV. Therefore, background gases as well as caesium atoms can be ionized and the produced secondary electrons lead to an increasing SID signal. An avalanche breakdown after Paschen's law will not occur due to the low pressures and voltages involved. Thus, the current density due to secondary electrons should be of the order of the thermionic current density and is directly proportional to the background pressure and the caesium density.

Within the scope of this work, highly intense light sources are applied for the absorption spectroscopy and the work function measurements. Therefore, the third contribution to the dark current could be the photoelectric effect by which electrons are released from the filaments upon incidence of high energetic photons. Again only the ion collector serves as electron source and depending on the spectral intensity of the light source an increasing SID signal is expected due to incidence of light. Via the bias voltage the contribution of secondary electrons from ionized background gas particles and caesium atoms is also increased by the photoelectric effect.

6.2 Caesium density measurement

The volume averaged caesium density can be determined by white light absorption spectroscopy or by optical emission spectroscopy (OES). The Cs D_2 resonance line at 852.1 nm is used in both cases due to its high transition probabilities for absorption and emission.

Since the lower state of this transition is the ground state, absorption spectroscopy can be applied in vacuum and in plasma yielding directly the ground state density of Cs. Furthermore, the evaluation does not depend on any parameters but physical constants. However, the effect of 'apparent optical depth' may lead to an underestimation of the evaluated Cs density, which has to be corrected. This correction procedure can lead to large uncertainties of the determined density.

On the other hand, OES can only be applied in plasma and the emitted radiation is connected to the upper state of the transition. Thus, correlation with the ground state Cs density has to be performed via population models of the upper level resulting in a dependency of the density evaluation on the plasma parameters. However, emission spectroscopy holds promise for an enhanced detection limit of the Cs density due to the highly intense emission line which is readily observed under ion source relevant plasma conditions.

6.2.1 White light absorption spectroscopy on the caesium atom

If light of intensity $I(\lambda, 0)$ is lead through an absorbing medium of length l its transmitted intensity after the Beer-Lambert law is

$$I(\lambda, l) = I(\lambda, 0)\, \mathrm{e}^{-\tau(\lambda,l)} = I(\lambda, 0)\, \mathrm{e}^{-\int_0^l \alpha(\lambda,x)\,\mathrm{d}x} = I(\lambda, 0)\, \mathrm{e}^{-\alpha(\lambda)l}\ , \tag{6.4}$$

where $\tau(\lambda, l)$ is called the optical depth of the medium and $\alpha(\lambda)$ [nm^{-1}][1] is the spectral absorption coefficient which is assumed to be homogeneous over the line of sight. If the medium is gaseous or a plasma, absorption is caused by excitation of particles from the lower state k to the upper state i at the central wavelength λ_0. However, absorption of photons via this transition is not restricted to the line at λ_0 but is distributed over the line profile $P_{\mathrm{line}}(\lambda)$ [nm^{-1}], which is normalized as $\int_{\mathrm{line}} P_{\mathrm{line}}(\lambda)\,\mathrm{d}\lambda = 1$. The spectral absorption coefficient can therefore be pa-

[1] As the unit of $\alpha(\lambda)$ is nm^{-1}, l has to be given in nm as well.

rameterized by the line absorption coefficient α_{ik} [unity] which incorporates the transition specific quantities and by the line profile which determines the spectral distribution [TLJ99]:

$$\begin{aligned} \alpha(\lambda) &= \alpha_{ik} \cdot P_{\text{line}}(\lambda) \\ \Rightarrow \int_{\text{line}} \alpha(\lambda)\,\mathrm{d}\lambda &= \int_{\text{line}} \alpha_{ik} P_{\text{line}}(\lambda)\,\mathrm{d}\lambda = \alpha_{ik} \ . \end{aligned} \tag{6.5}$$

Further the line absorption coefficient depends on the density n_k of the lower state [TLJ99]:

$$\alpha_{ik} = \frac{\lambda_0^4}{8\pi c}\frac{g_i}{g_k} A_{ik} n_k \ , \tag{6.6}$$

where g_i and g_k are the statistical weights of the upper and lower state respectively and A_{ik} is the Einstein coefficient for spontaneous emission of the transition $i \to k$. Thus integrating the logarithm of equation (6.4) yields

$$\begin{aligned} \int_{\text{line}} \ln\left(\frac{I(\lambda,l)}{I(\lambda,0)}\right)\mathrm{d}\lambda &\overset{(6.5)}{=} -\alpha_{ik} l \\ \overset{(6.6)}{\Longrightarrow}\ n_k &= \frac{8\pi c}{\lambda_0^4}\frac{g_k}{g_i}\frac{1}{A_{ik} l}\int_{\text{line}} \ln\left(\frac{I(\lambda,0)}{I(\lambda,l)}\right)\mathrm{d}\lambda \ . \end{aligned} \tag{6.7}$$

To obtain the density of the lower state via white light absorption spectroscopy the signal has to be recorded with a spectrometer. This spectrometer has a finite wavelength resolution characterized by its apparatus profile, which influences the measured optical depth.

Apparent optical depth and its correction

The transmitted intensity of the broadband light source $I(\lambda, l)$ is recorded with the spectrometer where it is convolved with the apparatus profile $P_{\text{app}}(\lambda)$ resulting in the measured intensity

$$I^{\text{meas}}(\lambda, l) = I(\lambda, l) * P_{\text{app}}(\lambda) \ . \tag{6.8}$$

The initial intensity of the broadband light source without absorption $I(\lambda, 0)$ does not vary significantly over the wavelength range determined by the apparatus profile why it can be seen as constant $I_0 \equiv I(\lambda, 0)$. Therefore the apparatus profile has no influence on the initial intensity: $I^{\text{meas}}(\lambda, 0) = I(\lambda, 0) * P_{\text{app}}(\lambda) = I_0$. Since the apparatus profile is normalized as $\int P_{\text{app}}(\lambda)\,\mathrm{d}\lambda = 1$ the integral over a

wavelength range is not changed by the convolution which yields

$$\int \frac{I^{\text{meas}}(\lambda, l)}{I^{\text{meas}}(\lambda, 0)} \, \mathrm{d}\lambda = \int \frac{I(\lambda, l)}{I_0} * P_{\text{app}}(\lambda) \, \mathrm{d}\lambda = \int \frac{I(\lambda, l)}{I(\lambda, 0)} \, \mathrm{d}\lambda \; . \tag{6.9}$$

However, the integral of the logarithms as required for the evaluation of densities from white light absorption spectra after equation (6.7) does *not* profit from this equality:

$$\int \ln\left(\frac{I^{\text{meas}}(\lambda, l)}{I^{\text{meas}}(\lambda, 0)}\right) \mathrm{d}\lambda = \int \ln\left(\frac{I(\lambda, l)}{I_0} * P_{\text{app}}(\lambda)\right) \mathrm{d}\lambda \quad \neq \quad \int \ln\left(\frac{I(\lambda, l)}{I(\lambda, 0)}\right) \mathrm{d}\lambda \; .$$

In fact one has

$$-\int_{\text{line}} \ln\left(\frac{I^{\text{meas}}(\lambda, l)}{I^{\text{meas}}(\lambda, 0)}\right) \mathrm{d}\lambda \;\leq\; -\int_{\text{line}} \ln\left(\frac{I(\lambda, l)}{I(\lambda, 0)}\right) \mathrm{d}\lambda \tag{6.10}$$

$$\overset{(6.7)}{\Longrightarrow} \quad n_k^{\text{meas}} \leq n_k \; . \tag{6.11}$$

The density n_k^{meas} of the lower state which is evaluated from the measured absorption spectrum is lower than the actual density n_k. Due to the direct proportionality between the density and the optical depth of the medium, $\tau \propto n_k$, this effect is called *apparent optical depth*.

The effect of the apparent optical depth due to recording with a spectrometer can be corrected by means of a correction factor f_{corr}:

$$n_k = n_k^{\text{meas}} f_{\text{corr}} \; . \tag{6.12}$$

This correction factor can be calculated in the following way [BWF12]:

$$\begin{aligned} f_{\text{corr}} = \frac{n_k}{n_k^{\text{meas}}} \overset{(6.7)}{=} \frac{\int_{\text{line}} \ln\left(\frac{I(\lambda,0)}{I(\lambda,l)}\right) \mathrm{d}\lambda}{\int_{\text{line}} \ln\left(\frac{I^{\text{meas}}(\lambda,0)}{I^{\text{meas}}(\lambda,l)}\right) \mathrm{d}\lambda} \overset{(6.7)}{\underset{(6.8)}{=}} \frac{\alpha_{ik} l}{-\int_{\text{line}} \ln\left(\frac{I(\lambda,l)}{I_0} * P_{\text{app}}(\lambda)\right) \mathrm{d}\lambda} \\ \overset{(6.4)}{\underset{(6.5)}{=}} \frac{\alpha_{ik} l}{-\int_{\text{line}} \ln\left[\exp\left(-\alpha_{ik} P_{\text{line}}(\lambda) l\right) * P_{\text{app}}(\lambda)\right] \mathrm{d}\lambda} \; . \end{aligned} \tag{6.13}$$

Giving an actual density n_k of the lower state (and thus a line absorption coefficient α_{ik}) and an absorption length l the apparent density n_k^{meas} can be calculated using the line profile $P_{\text{line}}(\lambda)$ of the corresponding transition and the convolution with the apparatus profile $P_{\text{app}}(\lambda)$ of the applied spectrometer. A negligible effect

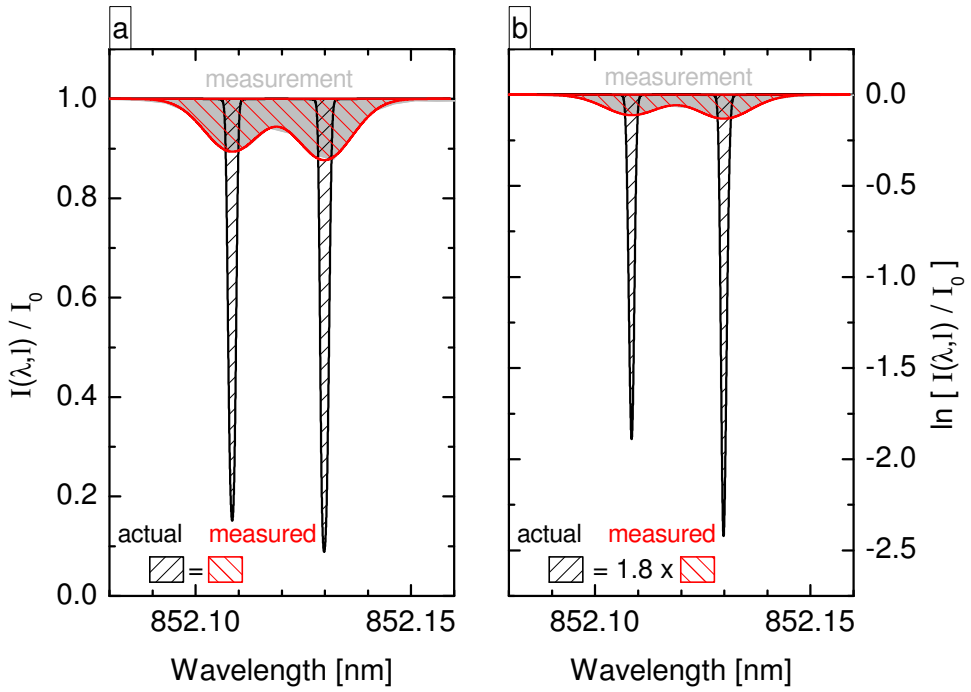

Figure 6.3: (a) *Simulation of an actual and a measured absorption signal of the caesium D_2 line at 852.1 nm and* **(b)** *its logarithms. The gray shaded background is a real measurement. Parameters for the simulation and measurement resp. are:* $T_{\mathrm{Cs}} = 525\,K$, $\omega_{\mathrm{app}} = 15\,pm$, $l = 0.15\,m$, $n_{\mathrm{Cs}} = 1 \times 10^{16}\ m^{-3}$.

of the apparatus profile can only be achieved if it is much narrower than the line profile: in this case $-\alpha_{ik} P_{\mathrm{line}}(\lambda) l$ can be seen as constant over the wavelength range determined by $P_{\mathrm{app}}(\lambda)$ which leads to $f_{\mathrm{corr}} = 1$.

Relations (6.9) and (6.10) are illustrated in figure 6.3 for the Cs resonance line at 852.1 nm by means of simulated spectra of an actual and an apparent absorption signal via equation (6.13). A caesium ground state density of $n_{\mathrm{Cs}} = 1 \times 10^{16}\,\mathrm{m}^{-3}$ and an absorption length of $l = 0.15\,\mathrm{m}$ are used and the line profile of the absorption line is calculated as presented in section 4.1 using a typical gas temperature of $T_{\mathrm{Cs}} = 525\,\mathrm{K}$. Thus, part (a) shows the simulation of a spectrum how it would look like after transmission through the caesium vapor ('actual') compared to the one measured with a spectrometer having a Gaussian apparatus profile with a full width at half maximum (FWHM) of $\omega_{\mathrm{app}} = 15\,\mathrm{pm}$. The gray shaded background is a real measurement confirming the accuracy of the simulation. The areas under the curves are equal as described by equation (6.9). In part (b) the logarithms of the signals are plotted as these are required for the determination of the Cs density. It can be seen that the area under the curve is a factor of 1.8 larger for the actual signal than for the recorded signal, which illustrates the apparent

optical depth after relation (6.10). Therefore the measured Cs density would be $n_k^{\mathrm{meas}} = 5.6 \times 10^{15}\,\mathrm{m}^{-3}$ and a correction factor of $f_{\mathrm{corr}} = 1.8$ would have to be applied in this case to obtain the actual density.

Following this procedure the correction factors for several measured Cs densities can be determined. The calculations after equation (6.13) depend on the line profile of the resonance line, for which natural, Doppler and collision broadening are considered. In section 4.1 it is shown, that the line widths of natural and pressure broadening are much smaller (in total $\approx 10^{-2}\,\mathrm{pm}$) than the width of Doppler broadening ($\approx$ pm) for parameters relevant for the present investigations. However, the former mechanisms lead to a Lorentzian profile which is much broader than the Gaussian profile of the Doppler broadening in the tails far from the central wavelength. It was shown in [BWF12] that this can lead to an influence on the calculations even if the FWHM of the Lorentzian profile is two orders of magnitude smaller than the FWHM of the Gaussian profile. For the present parameters the neglect of natural and pressure broadening can lead to an overestimation of the correction factor of 20 % at measured Cs densities of $10^{16}\,\mathrm{m}^{-3}$ and thus both Lorentzian contributions have to be considered.

Figure 6.4 shows the correction factors calculated for different Cs temperatures and hydrogen pressures for a spectrometer having a Gaussian apparatus profile with $\omega_{\mathrm{app}} = 15\,\mathrm{pm}$. The illustration shown in figure 6.3 (b) is also denoted. With increasing Cs temperature and/or hydrogen pressure the line profile is increasingly broadened which leads to a weakened effect of the convolution with the apparatus profile. Therefore, the correction factor decreases with increasing T_{Cs} and increasing $p_{\mathrm{H_2}}$. It can be seen, that the temperature has a major influence on the correction factor whereas the influence of the hydrogen gas is virtually negligible for pressures up to 10 Pa. For measured Cs densities between 10^{15} and $10^{16}\,\mathrm{m}^{-3}$ the correction factor increases from negligible values up to the order of 10 depending on the temperature. As this is the relevant range of Cs densities obtained in NNBI ion sources as well as the laboratory setup, the underestimation of the density due to the apparent optical depth can be substantial and its correction is indispensable. Hereby, the dependency of the correction factor on the Cs temperature constitutes one of the main contributions to the measurement error of Cs densities evaluated by means of white light absorption spectroscopy, since the experimental determination of the gas temperature is subject to uncertainties.

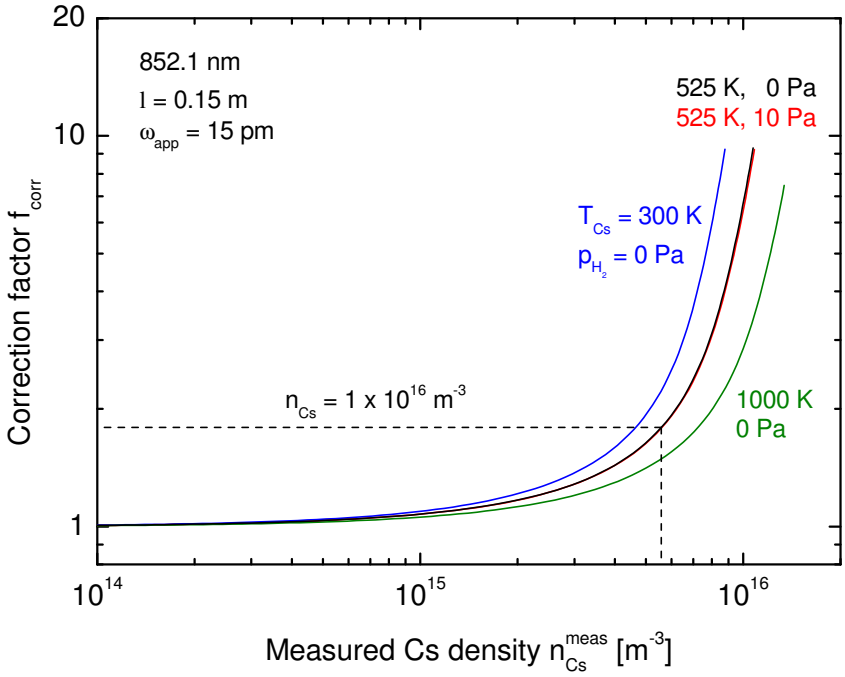

Figure 6.4: *Correction factors for the apparent optical depth of the Cs D_2 line at 852.1 nm for several Cs temperatures T_{Cs} and hydrogen pressures p_{H_2}. The absorption length is $l = 0.15\,m$ and P_{app} is Gaussian with $\omega_{app} = 15\,pm$.*

6.2.2 Optical emission spectroscopy (OES) on the caesium atom

The intensity of line emission in plasmas is directly correlated to the densities of the excited states of the plasma constituents. Thus, the determination of the Cs density via optical emission spectroscopy requires knowledge of the correlation of the ground state with the excited state. As described in section 3.1.2 the population density of excited states of particles in low pressure low temperature plasmas is modeled with so-called collisional-radiative models (CR models). The accuracy of such models is highly dependent on the input data.

For caesium the establishment of a CR model suffers from a lack of sufficient data in the literature on cross sections and/or rate coefficients for the multitude of possible plasma processes. Thus, the population of excited states is calculated using the so-called corona equilibrium according to which excitation of upper levels is assumed to be solely electron impact excitation from the ground state balanced by spontaneous emission as the only relevant depopulation channel [SVY81]. The resulting balance rate equations constitute the *corona model*, whose validity needs to be examined experimentally.

Table 6.1: *Transitions $i \rightarrow k$ for the extended corona model of caesium including statistical weights g_i and g_k, level energies E_i and E_k, wavelengths λ and transition probabilities A_{ik} [KRRN13]. Rows in bold illustrate the measured emission lines.*

Transition i $(g_i) \rightarrow k$ (g_k)	E_i [eV]	E_k [eV]	λ [nm]	A_{ik} [s^{-1}]	[Reference]
$6\,^2P_{1/2}$ (2) $\rightarrow$ $6\,^2S_{1/2}$ (2)	**1.39**	**0**	**894.3**	**2.9×10^7**	[Ste10]
$6\,^2P_{3/2}$ (4) $\rightarrow$ $6\,^2S_{1/2}$ (2)	**1.45**	**0**	**852.1**	**3.3×10^7**	[Ste10]
$7\,^2P_{1/2}$ (2) $\rightarrow$ $7\,^2S_{1/2}$ (2)	2.70	2.30	3096.1	3.6×10^6	[War68]
$7\,^2P_{1/2}$ (2) $\rightarrow$ $5\,^2D_{3/2}$ (4)	2.70	1.80	1375.9	1.3×10^6	[War68]
$7\,^2P_{1/2}$ (2) $\rightarrow$ $6\,^2S_{1/2}$ (2)	**2.70**	**0**	**459.3**	**7.9×10^5**	[VSSB02]
$7\,^2P_{3/2}$ (4) $\rightarrow$ $7\,^2S_{1/2}$ (2)	2.72	2.30	2931.8	4.0×10^6	[War68]
$7\,^2P_{3/2}$ (4) $\rightarrow$ $5\,^2D_{5/2}$ (6)	2.72	1.81	1360.3	8.3×10^5	[War68]
$7\,^2P_{3/2}$ (4) $\rightarrow$ $5\,^2D_{3/2}$ (4)	2.72	1.80	1342.4	7.5×10^4	[War68]
$7\,^2P_{3/2}$ (4) $\rightarrow$ $6\,^2S_{1/2}$ (2)	**2.72**	**0**	**455.5**	**1.8×10^6**	[VSSB02]

Applied to the first four resonance states of caesium, the 6 P and the 7 P levels, the corona model yields the following balance rate equations [SVY81]:

$$n_{\mathrm{Cs}} n_{\mathrm{e}} X_{n\mathrm{P}_J}(T_{\mathrm{e}}) = n_{n\mathrm{P}_J} \sum_{k<n\mathrm{P}_J} A_{n\mathrm{P}_J \rightarrow k} \ , \tag{6.14}$$

where $n_{n\mathrm{P}_J}$ is the density of the excited P state with main quantum number $n = 6, 7$ and total angular momentum $J = \frac{1}{2}, \frac{3}{2}$, n_{Cs} is the caesium ground state density, n_{e} the electron density, $X_{n\mathrm{P}_J}$ the rate coefficient for electron impact excitation from the ground state into the state $n\mathrm{P}_J$ which depends on the electron temperature T_{e} and $A_{n\mathrm{P}_J \rightarrow k}$ the Einstein coefficients for spontaneous emission to all lower states k. In table 6.1 the properties of the transitions from the 6 P and 7 P levels are summarized and an energy level diagram can be found in figure 4.1 (a).

The rate coefficient $X_{n\mathrm{P}_J}$ is calculated after equation (3.8) via the cross section $\sigma_{n\mathrm{P}_J}(E_{\mathrm{e}})$ for electron impact excitation from the ground state into the state $n\mathrm{P}_J$ and the electron energy distribution function (EEDF) $f(E_{\mathrm{e}})$. As a first approximation a Maxwellian EEDF is assumed hereafter and thus the rate coefficient $X_{n\mathrm{P}_J}(T_{\mathrm{e}})$ can be given in dependence of the electron temperature T_{e}.

Equation (6.14) illustrates the correlation of the caesium density n_{Cs} on the left-hand side with the emission from the 6 P and 7 P levels on the right-hand side, which is the basis for the Cs density measurement via OES. However, in order to evaluate the Cs density the transition probabilities $A_{n\mathrm{P}_J \rightarrow k}$ and the cross sections $\sigma_{n\mathrm{P}_J}(E_{\mathrm{e}})$ are required which can be found in the literature.

Transition probabilities

Calculated values for each considered transition of Cs are given by Warner [War68], recently measured values for the resonance lines originating from the 7 P levels are available in [VSSB02] and in [Ste10] the latest transition probabilities for the lines emitting from the 6 P states are reviewed. Thereby, the calculated values in [War68] for the transitions $6\,^2\mathrm{P}_J \rightarrow 6\,^2\mathrm{S}_{1/2}$ are in agreement with the reviewed ones from [Ste10] (within an accuracy of 1 %). Thus, the latest measured [VSSB02] and reviewed [Ste10] transition probabilities are taken for the resonance transitions in the present model (these are e. g. also used in [KRRN13]) whereas for the other emission lines from the 7 P states the calculated values by [War68] are used. Table 6.1 summarizes the utilized Einstein coefficients and the corresponding references.

Cross sections

Basically, electron impact excitation cross sections for Cs are only available in the literature for the combined levels 6p and 7p, respectively, and not for the fine structure resolved states $6\,^2\mathrm{P}_J$ and $7\,^2\mathrm{P}_J$. Thereby, theoretically calculated cross sections for excitation from the ground state can be found in [Gan82] for both combined levels, whereas only for the combined 6p level additionally a measured cross section is given in [CG78]. The latter furthermore includes population via spontaneous emission from higher lying levels (so-called cascades), which contribute by about 7 % to the total population.

In figure 6.5 (a) the measured and the calculated cross sections for the combined 6p level are shown, together with another cross section explained below. It can be seen, that below electron energies of 300 eV the calculated cross section from [Gan82], which was computed via the Born approximation [SVY81], shows an overestimation of typically a factor of 2–3 (factor 5 in maximum near the threshold around 1.5 eV). This deviation is to be expected as the Born approximation only holds for high energies of the impinging particles [SVY81]. However, since the mean electron energy in low temperature plasmas is at 1–5 eV exactly the low-energy part of the electron impact excitation cross section is decisive for the absolute value of the corresponding excitation rate coefficient. This can be seen in figure 6.5 (c) where the rate coefficients calculated from the cross sections after equation (3.8) are plotted: the Born cross section results in a rate coefficient about a factor of 2–4 higher than the one resulting from the measured cross section.

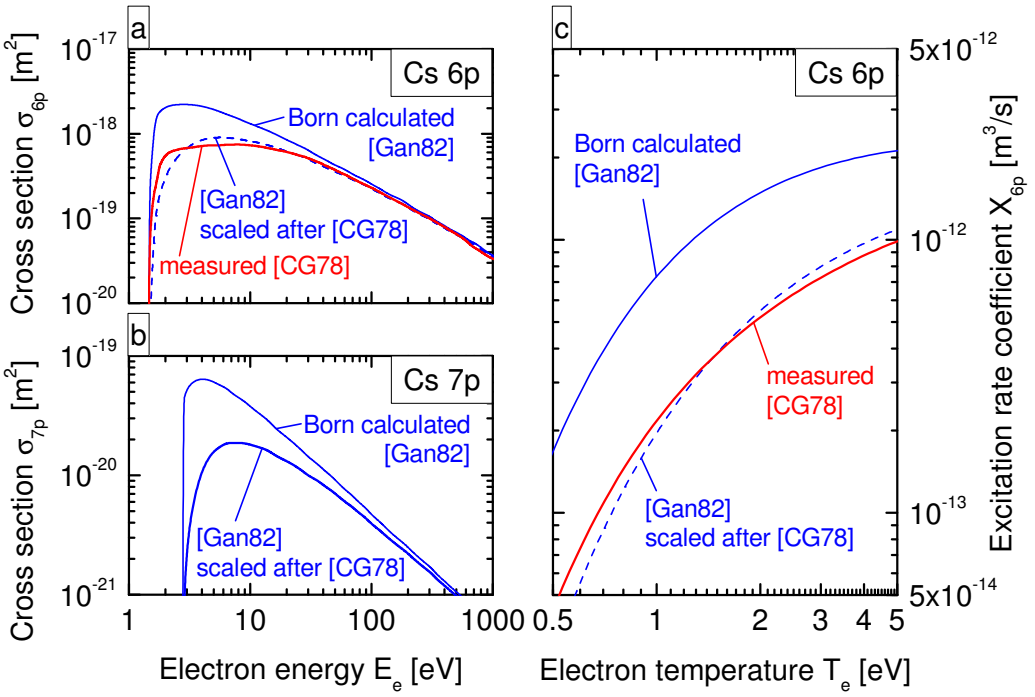

Figure 6.5: (a) *Electron impact excitation of the Cs 6p level from the ground state: measured cross section from [CG78], calculated cross section via the Born approximation from [Gan82] and the same cross section scaled after [CG78].* **(b)** *Excitation of Cs 7p: calculated Born cross section from [Gan82] and scaled after [CG78].* **(c)** *Excitation rate coefficients for the level 6p calculated via equation* (3.8) *using the cross sections from part (a) and a Maxwellian EEDF.*

Thus, also for the combined 7p level, for which no measured cross section exists, the applicability of the calculated cross section in [Gan82] is questionable. In [CG78] this discrepancy between their measurement and Born calculations is also revealed for the 6p level and an analytical correction is suggested with which Born cross sections can be brought near the measured cross sections. This scaling is examined in the following.

The cross section for the combined 6p level calculated via the Born approximation from [Gan82] and scaled after [CG78] is plotted additionally in figure 6.5 (a) showing much better accordance with the measurement in both magnitude and in the location of the maximum. The rate coefficient based on this scaled cross section is also plotted in part (c) of the figure. The remaining deviation of the scaled cross section to the measured one leads to uncertainties of the rate coefficient of only about 10 % in the relevant range $1\,\mathrm{eV} \leq T_\mathrm{e} \leq 5\,\mathrm{eV}$. Since on the other hand the uncertainty of OES measurements is itself about 10 %, this discrepancy is acceptable for the present diagnostic purpose. Therefore, also the electron im-

pact excitation cross section of the combined level 7p calculated by [Gan82] is scaled after [CG78] and plotted in figure 6.5 (b).

Summarizing, the following cross sections are applied for the present model:

Level 6p: the measured cross section from [CG78].

Level 7p: the calculated cross section from [Gan82] scaled after [CG78].

Extension of the corona model

Since cross sections for the excitation of the fine split levels of caesium are not available in the literature the simple corona model of equation (6.14) has to be extended. Excitation to the combined levels np has to be balanced by the spontaneous emissions from both fine structure components J and J' leading to the *extended corona model*

$$n_{\mathrm{Cs}} n_{\mathrm{e}} X_{n\mathrm{p}}(T_{\mathrm{e}}) = n_{n\mathrm{P}_J} \sum_{k<n\mathrm{P}_J} A_{n\mathrm{P}_J \to k} \; + \; n_{n\mathrm{P}_{J'}} \sum_{l<n\mathrm{P}_{J'}} A_{n\mathrm{P}_{J'} \to l} \; , \tag{6.15}$$

where $X_{n\mathrm{p}}$ is the rate coefficient for electron impact excitation from the ground state into the combined level np. The evaluation of the equilibrium density $n_{n\mathrm{P}_J}$ is now coupled to the density of the other fine structure level. Defining their density ratio $\eta_J = n_{n\mathrm{P}_{J'}}/n_{n\mathrm{P}_J}$ yields

$$n_{\mathrm{Cs}} n_{\mathrm{e}} X_{n\mathrm{p}}(T_{\mathrm{e}}) = n_{n\mathrm{P}_J} \left(\sum_{k<n\mathrm{P}_J} A_{n\mathrm{P}_J \to k} \; + \; \eta_J \sum_{l<n\mathrm{P}_{J'}} A_{n\mathrm{P}_{J'} \to l} \right) \; . \tag{6.16}$$

For the density ratio η_J it seems natural to use the Boltzmann distribution. However, its validity needs to be examined: the energy gap $|E_{n\mathrm{P}_{J'}} - E_{n\mathrm{P}_J}|$ between the fine structure levels is less than 0.07 eV for both cases (see table 6.1) which is much smaller than T_{e}; and the probability of transitions within the levels induced by heavy particle collisions is infinitesimal, as the collision frequency f_{coll} is much smaller (10^0–$10^1\,\mathrm{s}^{-1}$)[2] than the transition probabilities for spontaneous emission (10^6–$10^7\,\mathrm{s}^{-1}$). According to these two considerations it is justified to approximate the density ratio by the Boltzmann relation where the appropriate temperature should be the electron temperature (for which applies $k_{\mathrm{B}} T_{\mathrm{e}} \gg |E_{n\mathrm{P}_{J'}} - E_{n\mathrm{P}_J}|$):

$$\eta_J = \frac{n_{n\mathrm{P}_{J'}}}{n_{n\mathrm{P}_J}} = \frac{g_{n\mathrm{P}_{J'}}}{g_{n\mathrm{P}_J}} \; \exp\left(-\frac{E_{n\mathrm{P}_{J'}} - E_{n\mathrm{P}_J}}{k_{\mathrm{B}} T_{\mathrm{e}}} \right) \; . \tag{6.17}$$

[2] Calculated after the hard sphere model for the collision cross section σ_{coll} and the thermal velocity v_{th}: $f_{\mathrm{coll}} \propto n_{\mathrm{Cs}} \sigma_{\mathrm{coll}} v_{\mathrm{th}}$.

Using equations (3.10), (6.16) and (6.17), the emission from each fine structure level $n\mathrm{P}_J$ can now be calculated depending on the Cs density, the electron density and the electron temperature. If n_e and T_e are known from another diagnostic, the measured emission can thus be used as diagnostic for the Cs density.

For this purpose the resonance lines are applied, since they lie in the optical spectral range and are thus accessible with the applied spectrometers. In conclusion, the resonance emission $\epsilon_{n\mathrm{P}_J\to 6s}$ from each fine structure level $n\mathrm{P}_J$ is determined by

$$\epsilon_{n\mathrm{P}_J\to 6s} = n_{n\mathrm{P}_J} A_{n\mathrm{P}_J\to 6s} = \overset{(6.16)}{\underset{(6.17)}{=}} n_\mathrm{e} n_\mathrm{Cs}\; X_{n\mathrm{p}}(T_\mathrm{e}) \frac{A_{n\mathrm{P}_J\to 6s}}{\sum\limits_{k<n\mathrm{P}_J} A_{n\mathrm{P}_J\to k} + \frac{g_{n\mathrm{P}_{J'}}}{g_{n\mathrm{P}_J}} \exp\left(-\frac{E_{n\mathrm{P}_{J'}} - E_{n\mathrm{P}_J}}{k_\mathrm{B} T_\mathrm{e}}\right) \sum\limits_{l<n\mathrm{P}_{J'}} A_{n\mathrm{P}_{J'}\to l}} \tag{6.18}$$

$$=: n_\mathrm{e} n_\mathrm{Cs}\; X_{\mathrm{em},n\mathrm{P}_J\to 6s}(T_\mathrm{e})\ , \tag{6.19}$$

where in the last line the so-called *emission rate coefficient* $X_{\mathrm{em},n\mathrm{P}_J\to 6s}$ for resonance radiation from the fine structure state $n\mathrm{P}_J$ is introduced. The Cs density can then be evaluated using the measured resonance emission, the electron density from probe measurements (section 6.5) and the electron temperature from OES on the hydrogen atom (section 6.6.2):

$$n_\mathrm{Cs} = \frac{\epsilon_{n\mathrm{P}_J\to 6s}}{n_\mathrm{e} X_{\mathrm{em},n\mathrm{P}_J\to 6s}(T_\mathrm{e})}\ . \tag{6.20}$$

The emission rate coefficients for the four caesium resonance lines are shown in figure 6.6 (a). Part (b) of that figure shows the line ratio of the more intense lines of both p levels (at 852.1 nm and 455.5 nm). After equation (6.19) this line ratio equals the ratio of the corresponding emission rate coefficients and is independent of the electron density and the Cs ground state density.

The emission rate coefficient for the Cs D_2 line at 852.1 nm is largest which is directly connected to the most intense emission among the resonance lines. Therefore, using this transition as diagnostic line for the Cs density holds promise for the highest sensitivity and the lowest detection limit. However, the extended corona model has to be benchmarked first, to ensure the validity of the corona equilibrium. This is performed in section 9.2.3 by comparing measured and calculated emissions from all four resonance lines, where the Cs density determined by white light absorption spectroscopy is applied for the calculations.

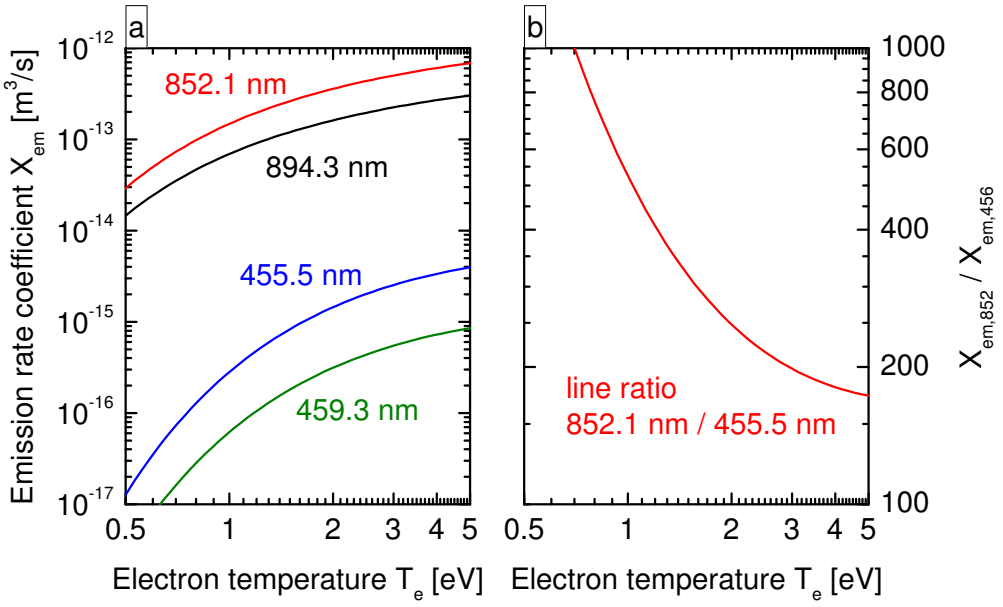

Figure 6.6: **(a)** *Emission rate coefficients for the resonances lines of Cs, calculated after equation* (6.18). **(b)** *Line ratio of the Cs lines at 852.1 nm and 455.5 nm.*

6.2.3 Setup for white light absorption and optical emission spectroscopy

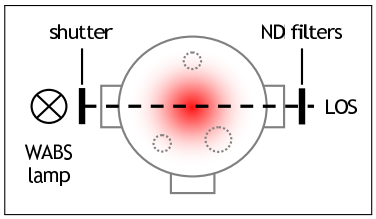

For the determination of the Cs density the spectrometers with higher resolution (SPEX and Acton) are applied and thus the LOS parallel to the possible sample is used. For the white light absorption spectroscopy a stabilized xenon high pressure lamp (250 W) is used as light source (WABS lamp) and placed opposite to the lens tube. Care has been taken that the plasma emission is not reflected back from internal mirrors of the xenon lamp into the LOS. The highly intense continuum emission has to be mitigated before entering the fiber optics to prevent damage to the fiber. Therefore neutral density filters are used with a total transmission between 0.6 and 1.9 % depending on the wavelength. For recording of the Cs emission, the filters are removed and a shutter is applied between the WABS lamp and the discharge vessel. The emission is also required for the absorption spectroscopy, since the plasma emission has to be subtracted from the transmitted intensity to obtain the pure absorption signal.

With the applied equipment a detection limit for the absorption spectroscopy of $n_{Cs} \gtrapprox 3\text{–}4\times10^{14}\,\mathrm{m}^{-3}$ is achieved, taking the vessel diameter of 15 cm as absorption

length. The detection limit for the Cs density measurement via OES depends on the electron density and temperature. However, for the resonance emission at 852.1 nm a detection limit of $\epsilon_{852} \gtrapprox 7 \times 10^{16}\,\mathrm{m^{-3}s^{-1}}$ can be stated.

Absorption and emission spectra for monitoring the Cs density are taken typically every five minutes (max. four times per minute) depending on the temporal evolution of the system.

Measurement errors

Contributions to the error for the absorption spectroscopy arise from the fit procedure to obtain the absorption signal (Bi-Gaussian in the case of the Cs resonance line), the absorption length and the correction factor, which in turn depends on the absorption length, the gas temperature and pressure and the apparatus profile of the spectrometer. For densities close to the detection limit the accuracy of the fitting routine is decisive whereas at high densities uncertainties of the correction factor are the main source of error. In total the analysis leads to an accuracy of about $\pm\,50\,\%$ at densities of some $10^{14}\,\mathrm{m^{-3}}$ (45 percentage points of which arise from the fit) and $\pm\,22\,\%$ at densities of $1 \times 10^{16}\,\mathrm{m^{-3}}$ (19 percentage points arise due to the correction factor).

The error for the Cs density measurement via OES consists of the 10 % uncertainty for the determination of the emissivity and the errors for the electron density and temperature. Taking the electron density from probe measurements (typical error $\pm\,6.5\,\%$) and the electron temperature from emission spectroscopy on the hydrogen atom (typical error $\leq 0.1\,\mathrm{eV}$ at an exemplary electron temperature of 2 eV) an uncertainty of about $\pm\,22\,\%$ can be stated for n_{Cs}.

6.3 Work function measurement

The work function of a surface can be determined using the outer photoelectric effect after which photoelectrons are released from a solid state if photons with energies $h\nu$ larger than the electron work function χ of the solid state incide on its surface. The photoextracted electrons have a maximal kinetic energy of $E_{\mathrm{kin,e}}^{\mathrm{max}} = h\nu - \chi$. Increasing the photon energy yields higher maximal kinetic energies, whereas increasing the amount of the inciding photons per unit time (increasing the intensity of the applied light source) increases the number of emitted electrons per unit time.

For the so-called *Fowler method* [Fow31] this general comprehension of the photoelectric effect is enhanced by taking into account the electron energy distribution within the solid state. This leads to the concept that increasing the photon energy also results in an increasing amount of photoemitted electrons and the work function of the surface is a parameter that describes this correlation.

For experimental application the surface under investigation is biased negatively against a secondary electrode and the photocurrent is measured. Thus, the work function of the surface can be determined via measuring the photocurrents due to incidence of varying photon energies and evaluating the signals by means of the Fowler method. Because of this bias voltage the method can only be applied in vacuum, as in plasma a high electron current from the discharge would disturb the measurement.

6.3.1 Density of photoelectrically releasable electrons

Electrons in the valence band of a solid state obey the Fermi-Dirac statistics:

$$N_i = \frac{1}{1 + \exp\left(\frac{E_i - \mu}{k_\mathrm{B} T}\right)} \,, \tag{6.21}$$

where N_i is the probability for an electron to occupy state i having an energy E_i, μ is the chemical potential and T the absolute temperature of the solid state. The chemical potential itself is temperature dependent but can be approximated by the Fermi energy E_F for temperatures T far below the Fermi temperature, which is fulfilled in the context of this work. Fermi-Dirac distributions for temperatures of 300 K, 600 K and 1200 K are shown in figure 6.7 together with an illustration of the process of electron photoemission. Electrons in the valence band of a solid state with a work function χ that have energies E_e higher than $E_\mathrm{F} + \chi - h\nu$ can be transferred beyond the vacuum level $E_\mathrm{F} + \chi$ by absorbing the photon energy $h\nu$. The excess energy is converted to kinetic energy of the free electron $E_\mathrm{kin,e}$. As can be seen readily, with higher photon energy more electrons can be extracted. On the other hand, the temperature of the solid state should have only a minor effect on the electron emission.

Multiplying equation (6.21) by the density of states for free electrons in a Fermi gas gives the number of electrons per unit volume and unit energy. Integrating this quantity over the appropriate energy range determines the density of electrons $n_\mathrm{e,ph}$ which can be released photoelectrically, hereafter called 'available electrons'. Fowler's conception of the photoinduced emission process is that only

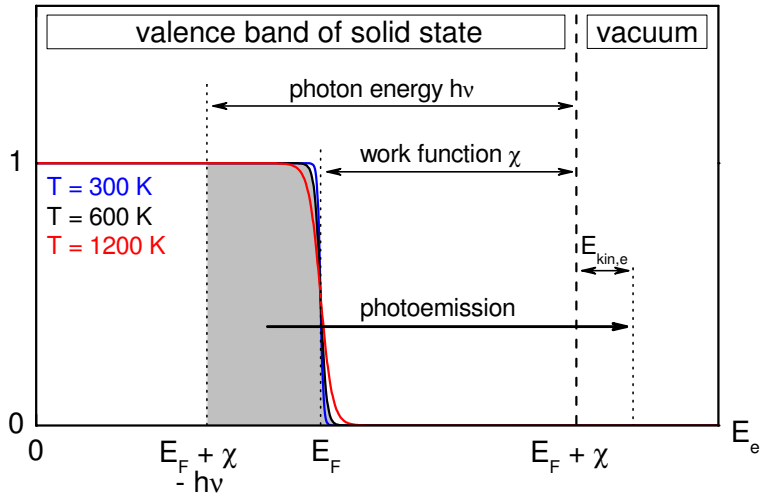

Figure 6.7: *Illustration of photoemission from a solid state with Fermi energy E_F and work function χ due to absorption of the photon energy $h\nu$ for different temperatures of the solid state.*

those electrons can escape the solid state, whose *kinetic energy $E_{\mathrm{e},\perp}$ attributed to a motion perpendicular to the surface* is raised beyond the vacuum level due to the absorption of the photon energy $h\nu$ [Fow31]. Evaluating this one-dimensional approach yields

$$n_\mathrm{e,ph} = C \cdot T^{3/2} \cdot \int_{E_\mathrm{F}+\chi-h\nu}^{\infty} \frac{1}{\sqrt{E_{\mathrm{e},\perp}/k_\mathrm{B}T}} \frac{1}{k_\mathrm{B}T} \ln\left(1 + \mathrm{e}^{\frac{-E_{\mathrm{e},\perp}+E_\mathrm{F}}{k_\mathrm{B}T}}\right) \mathrm{d}E_{\mathrm{e},\perp} \,, \qquad (6.22)$$

$$\text{with } E_\mathrm{F} + \chi - h\nu > 0 \,,$$

where C consists solely of physical constants ($C \approx 1.4 \times 10^{21}\,\mathrm{m^{-3}K^{-3/2}}$). This integral cannot be solved analytically and approximations have to be made.

Assuming photon energies greater than but close to the work function, $h\nu \gtrapprox \chi$, the integration range is very narrow around E_F since the integrand decreases very fast at energies above E_F for relevant temperatures. Therefore the square root in the denominator of the integral does not vary much over the integration interval and can be taken as constant in front of the integral with $E_{\mathrm{e},\perp} = E_\mathrm{F} + \chi - h\nu > 0$:

$$n_\mathrm{e,ph} \overset{h\nu \gtrapprox \chi}{\approx} C \cdot T^{3/2} \cdot \frac{1}{\sqrt{E_\mathrm{F}+\chi-h\nu/k_\mathrm{B}T}} \cdot \int_{E_\mathrm{F}+\chi-h\nu}^{\infty} \frac{1}{k_\mathrm{B}T} \ln\left(1 + \mathrm{e}^{\frac{-E_{\mathrm{e},\perp}+E_\mathrm{F}}{k_\mathrm{B}T}}\right) \mathrm{d}E_{\mathrm{e},\perp} \,. \qquad (6.23)$$

Further simplification can be made when considering the experimental application

of the Fowler method where the photon energy is varied. If for the range of variation $h\nu \approx \chi$ is still valid the denominator of the square root can additionally be assumed to be constant ($1/\sqrt{E_\mathrm{F} + \chi - h\nu} = C'$):

$$n_{\mathrm{e,ph}} \overset{h\nu \approx \chi}{\approx} C \cdot T^{3/2} \cdot C' \cdot \sqrt{k_\mathrm{B} T} \cdot \int_{E_\mathrm{F}+\chi-h\nu}^{\infty} \frac{1}{k_\mathrm{B} T} \ln\left(1 + \mathrm{e}^{\frac{-E_{\mathrm{e},\perp}+E_\mathrm{F}}{k_\mathrm{B} T}}\right) \mathrm{d}E_{\mathrm{e},\perp} \ . \quad (6.24)$$

This equation represents the 'Fowler case' for the density of electrons which can be released photoelectrically [Fow31].

The remaining integral can be solved analytically for the two cases $h\nu \leq \chi$ and for $h\nu \geq \chi$, whereas only the latter one is relevant to experimental application. The result is

$$\int_{E_\mathrm{F}+\chi-h\nu}^{\infty} \frac{1}{k_\mathrm{B} T} \ln\left(1 + \mathrm{e}^{\frac{-E_{\mathrm{e},\perp}+E_\mathrm{F}}{k_\mathrm{B} T}}\right) \mathrm{d}E_{\mathrm{e},\perp} =$$

$$\overset{h\nu \geq \chi}{=} \frac{\pi^2}{6} + \frac{1}{2}\kappa^2 - \left[\mathrm{e}^{-\kappa} - \frac{\mathrm{e}^{-2\kappa}}{2^2} + \frac{\mathrm{e}^{-3\kappa}}{3^2} - \cdots\right] =: f(\kappa) \ , \quad (6.25)$$

$$\text{with } \kappa = \frac{h\nu - \chi}{k_\mathrm{B} T} \geq 0 \ .$$

Thus, the density of available electrons can be determined for arbitrary values of χ and $h\nu$. This is the basis for the evaluation of the work function χ using the photocurrents induced by various photon energies $h\nu$.

6.3.2 The Fowler method for evaluating work functions

The actual number of electrons which are photoelectrically extracted from the surface due to incidence of photons with a given photon energy $h\nu$ is directly proportional to the density of available electrons $n_{\mathrm{e,ph}}$ and to the number of absorbed photons at this frequency $\#ph_{\mathrm{abs}}(h\nu)$. The latter is in turn proportional to the number of photons inciding onto the sample at this frequency $\#ph_{\mathrm{inc}}(h\nu)$. This quantity can be normalized to an absolute intensity $\#ph^*_{\mathrm{inc}}$ yielding a frequency dependent relative intensity of the applied light source $F(h\nu)$, with the result that $\#ph_{\mathrm{inc}}(h\nu) = \#ph^*_{\mathrm{inc}} \cdot F(h\nu)$. Assuming a frequency independent absorption coefficient for the narrow energy range $h\nu \approx \chi$, also the direct proportionality $\#ph_{\mathrm{abs}}(h\nu) \propto \#ph^*_{\mathrm{inc}} \cdot F(h\nu)$ applies [Fow31].

Via a bias voltage subsequently a photocurrent $I_{\mathrm{ph}}(h\nu)$ is drawn which is in turn directly proportional to the number of photoextracted electrons and thus

$$I_{\mathrm{ph}}(h\nu) \;\propto\; n_{\mathrm{e,ph}} \cdot \#ph_{\mathrm{abs}}(h\nu) \;\propto\; n_{\mathrm{e,ph}} \cdot \left[\#ph^{*}_{\mathrm{inc}} \cdot F(h\nu)\right] . \tag{6.26}$$

For the former proportionality to be valid, the bias should be high enough to work without space charge limitation.

Using equations (6.24) and (6.25) the following relation can be established for the photocurrent at frequency ν per absorbed photon (A_1, A_2 and A_3 are proportionality constants and $T = T_{\mathrm{spl}}$ is the temperature of the sample):

$$\begin{aligned} & \frac{I_{\mathrm{ph}}(h\nu)}{\#ph_{\mathrm{abs}}(h\nu)} && = A_1\; n_{\mathrm{e,ph}} = A_2\; T_{\mathrm{spl}}^2\; f(\kappa) \\ \Longleftrightarrow \quad & \frac{I_{\mathrm{ph}}(h\nu)}{F(h\nu)} && = A_3\; T_{\mathrm{spl}}^2\; f\left(\frac{h\nu-\chi}{k_{\mathrm{B}}T_{\mathrm{spl}}}\right)\;,\; h\nu \geq \chi\;. \end{aligned} \tag{6.27}$$

Thus, the relative values of the photocurrents corresponding to different photon energies depend on a function which is mainly determined by the work function of the surface.

The evaluation of measurements is done by dividing the measured photocurrents by the corresponding relative intensity of the light source and the squared temperature of the sample and plotting its logarithm against $h\nu/k_{\mathrm{B}}T_{\mathrm{spl}}$:

$$\ln\left[\frac{I_{\mathrm{ph}}(h\nu)/F(h\nu)}{T_{\mathrm{spl}}^2}\right] = A + \ln\left[f\left(\frac{h\nu}{k_{\mathrm{B}}T_{\mathrm{spl}}} - \frac{\chi}{k_{\mathrm{B}}T_{\mathrm{spl}}}\right)\right] . \tag{6.28}$$

Fitting this so-called *Fowler plot* of the measured signals by the Fowler function $A + \ln\left[f\big(\kappa(\chi)\big)\right]$ yields the work function χ and a constant A.

In figure 6.8 (a) the photocurrent calculated after equation (6.27) is shown for a sample temperature of 300 K (for $F = A_3 = 1$) depending on the difference of the applied photon energy $h\nu$ to the surface work function χ. The axes to the right and to the top pertain to the corresponding Fowler plot after equation (6.28). The expected behavior referring to figure 6.7 can clearly be seen: The photocurrent drastically increases with increasing photon energy or decreas-

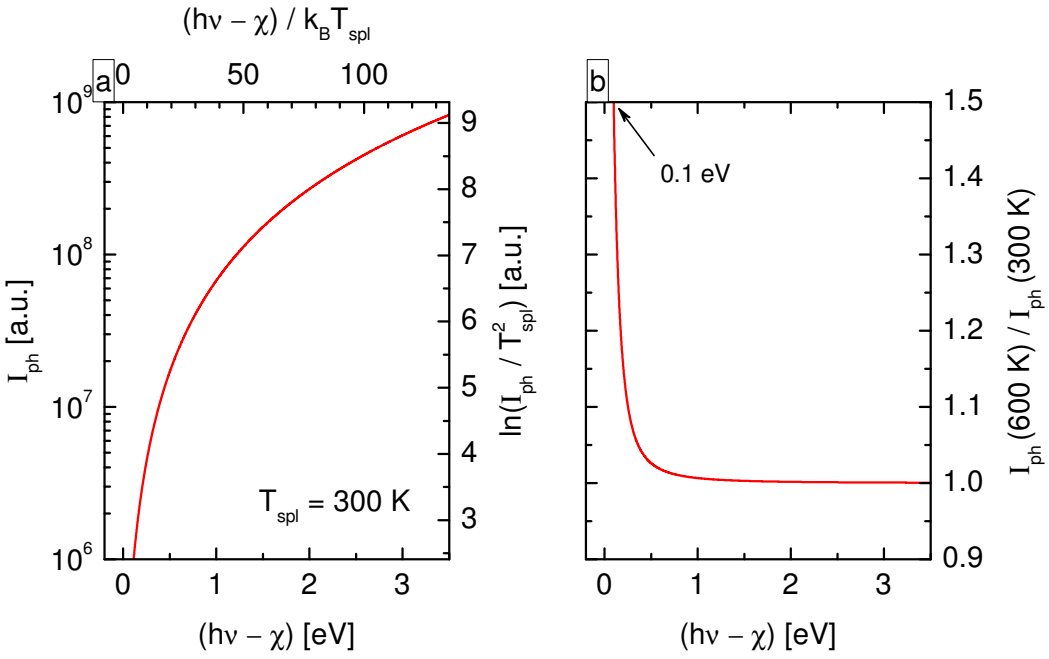

Figure 6.8: **(a)** *Photocurrent after equation* (6.27) *for* $T_{\mathrm{spl}} = 300\,K$ *using* $F = A_3 = 1$. *The right and top axis belong to the corresponding Fowler plot.* **(b)** *Photocurrent for a temperature of 600 K related to the current for 300 K.*

ing work function and the threshold is at $h\nu \approx \chi$. The closer the photon energy is to the work function, the steeper is the Fowler function and thus, the more sensitive is the evaluation of work functions via the Fowler method which results in smaller uncertainties of the evaluation.

The temperature dependence of the photocurrent is shown in figure 6.8 (b) where the ratio of the photocurrent for 600 K to that for 300 K is plotted. As already expected from the temperature dependence of the Fermi-Dirac distribution in figure 6.7, an influence of the temperature on the photocurrent can only be seen near the threshold around the Fermi energy. However, even at $h\nu - \chi = 0.1\,\mathrm{eV}$ the temperature rise by a factor of two only leads to a 50 % increase of the photocurrent. For higher photon energies compared to the work function the quadratic temperature dependence identifiable in equation (6.27) is compensated by the reciprocal quadratic temperature dependence of $f(\kappa)$, shown in equation (6.25) (for increasing values of $h\nu - \chi$ the exponential series loses relevance against κ^2). Thus, only for photon energies close to the work function of the sample, a slight temperature dependence of the photocurrent is to be expected.

6.3.3 Applied work function setup

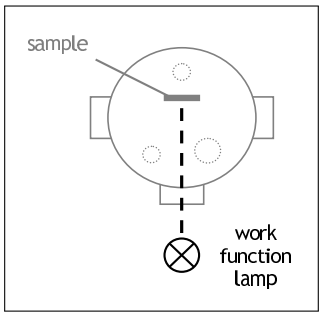

The optimal realization of the Fowler method is using a laser with continuously variable frequency as light source. Another possibility, applied in this work, is to use a filter system for a light source emitting broadband. The setup is shown in figure 6.9. The highly intense UV emission from a high pressure mercury lamp (100 W) is led through an interference filter, two quartz lenses and the quartz window onto the sample surface mounted on the sample holder. The size of the spot on the sample is adjusted via lens 2 for maximal photocurrent (compromise between power density on the sample and absolutely absorbed power) having about 1.5 cm in diameter in the present setup. The subsequently photoemitted electrons are drawn to the vessel wall due to the bias of 30 V. The photocurrent depending on the incident wavelength is measured with a Keithley 602 Electrometer.

Different wavelengths are obtained via the filter wheel that can house six interference filters and is directly mounted at the Hg lamp. Properties of the available filters are summarized in table 6.2.

For the evaluation of the measured photocurrents after equation (6.28), the relative intensity $F(h\nu)$ of the work function lamp inciding onto the sample and the mean photon energy as the corresponding value of '$h\nu$' for each fil-

Table 6.2: *Wavelength range of the transmitted spectrum, corresponding energy range and mean photon energy of the available interference filters for the work function measurements.*

Filter label	Wavelength range	Energy range	Mean photon energy
239 nm	236 – 253 nm	4.9 – 5.3 eV	5.04 eV
254 nm	244 – 253 nm	4.9 – 5.1 eV	4.96 eV
270 nm	269 – 284 nm	4.4 – 4.6 eV	4.49 eV
280 nm	274 – 305 nm	4.1 – 4.5 eV	4.31 eV
289 nm	280 – 316 nm[1]	3.9 – 4.4 eV	4.18 eV
300 nm	289 – 322 nm	3.9 – 4.3 eV	4.07 eV
313 nm	296 – 335 nm	3.7 – 4.2 eV	3.94 eV
334 nm	330 – 344 nm	3.6 – 3.8 eV	3.69 eV
365 nm	358 – 375 nm	3.3 – 3.5 eV	3.39 eV
405 nm	397 – 416 nm	3.0 – 3.1 eV	3.05 eV

[1] further emissions at 365 nm

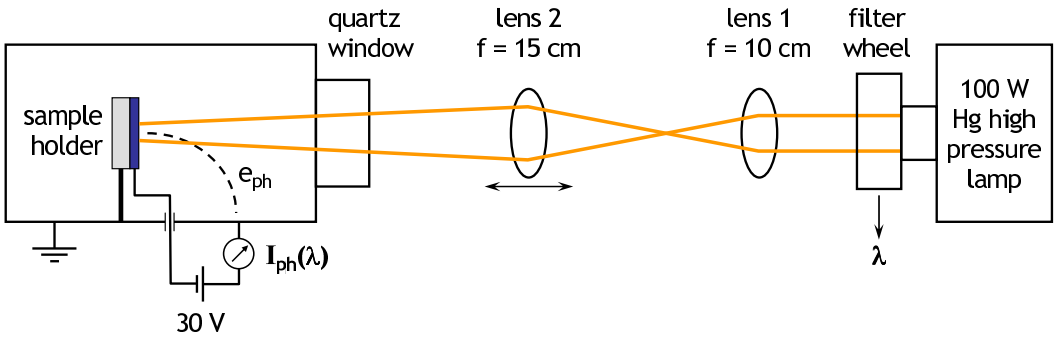

Figure 6.9: *Schematic of the setup to measure the work function after the Fowler method. Shown is a side view of the vessel, the quartz window is the front window in figure 5.1.*

ter have to be taken into account. Therefore, the entire setup was separated from the experiment vessel and a lens tube connected to an absolutely calibrated spectrometer was positioned at the place where the sample surface would be. The measured transmission spectra of each filter (always including the lenses and the quartz window) are assembled in appendix C, whereas the wavelength ranges are summarized in table 6.2. Converting the transmitted spectrum $S(\lambda)$ on the x-axis to a spectrum $S(E_{\mathrm{ph}})$ depending on the photon energy E_{ph}, the mean photon energy $\langle E_{\mathrm{ph}} \rangle$ can be calculated via the mathematical expectation: $\langle E_{\mathrm{ph}} \rangle = \int E_{\mathrm{ph}} S(E_{\mathrm{ph}}) \mathrm{d}E_{\mathrm{ph}} \; / \; \int S(E_{\mathrm{ph}}) \mathrm{d}E_{\mathrm{ph}}$. The values are also given in table 6.2.

Integrating the absolutely calibrated spectrum $S(\lambda)$ and normalizing it to the integral of the spectrum of the 280 nm filter yields the relative intensity factor $F(h\nu)$ for the corresponding filter. These are shown in figure 6.10. Y-errors in the figure originate from the reproducibility of the measured spectrum and denote the maximal and minimal value of the intensity. The x-errors correspond to the energy range of the transmitted photons, as listed in table 6.2.

To obtain one value of work function, the photocurrents of at least five filters are recorded, where the 270 nm filter is not applied during this work due to its low transmission. The repetition time for work function measurements is about three minutes in minimum, whereas typically measurements are taken every 15 minutes.

Measurement error

The error for the single determined value of work function is the standard error of the performed Fowler fit (typically ± 0.05 eV). Errors of the particular recorded photocurrents are not considered in the fitting routine: For photon energies near

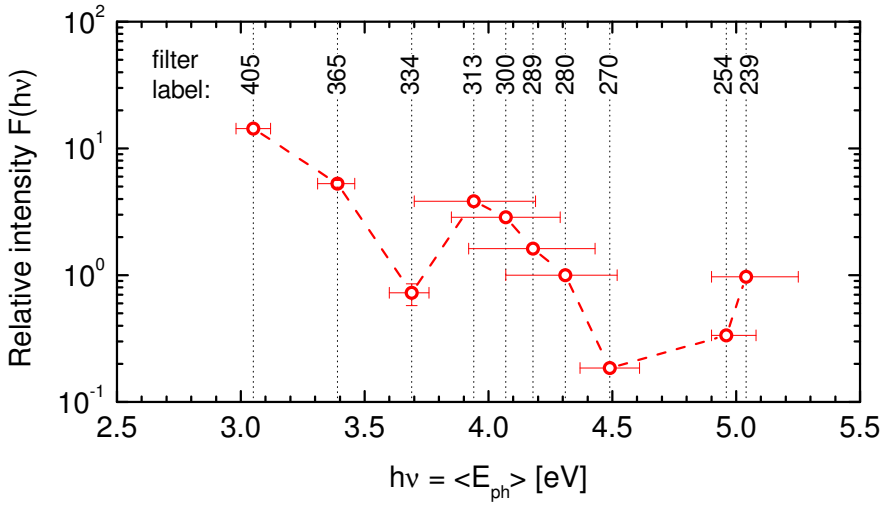

Figure 6.10: *Relative intensities of the work function lamp for the particular available filters over the corresponding mean photon energy.*

the work function the currents are very low leading to large errors. However, due to the vicinity to the threshold $h\nu \approx \chi$ precisely these currents are crucial for the evaluation of an accurate work function value. Therefore, assigning those currents a lower weight for the Fowler fit would be counterproductive.

6.3.4 Limits of applicability

The approximations leading to the Fowler equation (6.24) and thus to the introduced evaluation method are only valid for $h\nu \approx \chi$. However, for the experimental determination of the work function at least five interference filters are used, which leads to a distance of the highest applied photon energy to the work function of at least 0.6 eV (see table 6.2). Furthermore, cesiation of the surface under investigation can lead to a variation of the work function by several electron volts (see section 4.2.2), whereas the applied photon energies are fixed (as long as the filters are not exchanged). Thus, it is very likely to happen, that the applied photon energies are far from the actual work function of the surface.

Hence, the validity of the Fowler method beyond '$h\nu \approx \chi$' has to be analyzed and possible consequences have to be revealed. In the following, equation (6.22) is regarded as the 'realistic solution' (**case I**), since approximations were not yet performed; equation (6.23) is referred to as **case II**; and equation (6.24) is the 'Fowler case' (**case III**).

Analysis of the approximations

The successive approximations applied to derive the Fowler case equation (6.24) are analyzed by evaluating the corresponding densities of equations (6.22) through (6.24) by numerical means. The calculations are performed for $T = 300\,\mathrm{K}$ and are plotted in figure 6.11 depending on $h\nu - \chi$ for different Fermi energies[3], whereas for the Fowler case (III) the constant C' is taken as $C' = 1/\sqrt{E_\mathrm{F}}$.

Basically, the tendencies already observed in figure 6.8 (a) are confirmed: the density of available electrons increases with higher photon energies or lower work functions, whereas the threshold is at $h\nu \approx \chi$. Furthermore, it can be seen that decreasing Fermi energies lead to increasing densities and to a steeper evolution of $n_\mathrm{e,ph}$ over $h\nu - \chi$. Near the threshold each case yields virtually the same density. However, departing from $h\nu \approx \chi$ deviations between the cases evolve.

The approximation made for case II leads to an overestimation of the density of available electrons compared to the realistic solution of case I. This can be attributed to the square root taken in front of the integral in equation (6.23) whose value is always determined by the lower integral limit. Compared to its varying value within the integral this case yields too high densities. As the energy dependence of the square root is steeper at lower energies, the deviation is greater for larger values of $h\nu - \chi$ and lower values of E_F and diverges approaching the limit $E_\mathrm{F} + \chi - h\nu \longrightarrow 0$.

Due to the further simplification, by which the Fowler case (III) is obtained, this singularity is canceled out, since the reciprocal square root taken in front of the integral is now solely determined by E_F. However, the value of the reciprocal square root is lower than the corresponding value within the integral (for the relevant cases $h\nu - \chi > 0$). Hence, the Fowler case shows a slight underestimation of the density of available electrons compared to the realistic solution. As with case II, the deviation to the realistic case I increases with decreasing lower integral limit and thus with increasing photon energies compared to the work function and decreasing Fermi energies.

Moreover, the integral in equations (6.23) and (6.24) is invariant under shifts of the entire energy axis. Hence, the integral, taken by itself, is independent of the Fermi energy. Together with the further simplification $E_\mathrm{F} + \chi - h\nu = \mathrm{const.}$ for equation (6.24), the only remaining E_F dependence of the Fowler case is concentrated in the prefactor C'. However, this prefactor has no influence on the

[3]The choice of odd 2.1 eV for the lowest Fermi energy has solely mathematical reasons avoiding singularities, which can arise due to the reciprocal square roots in the equations.

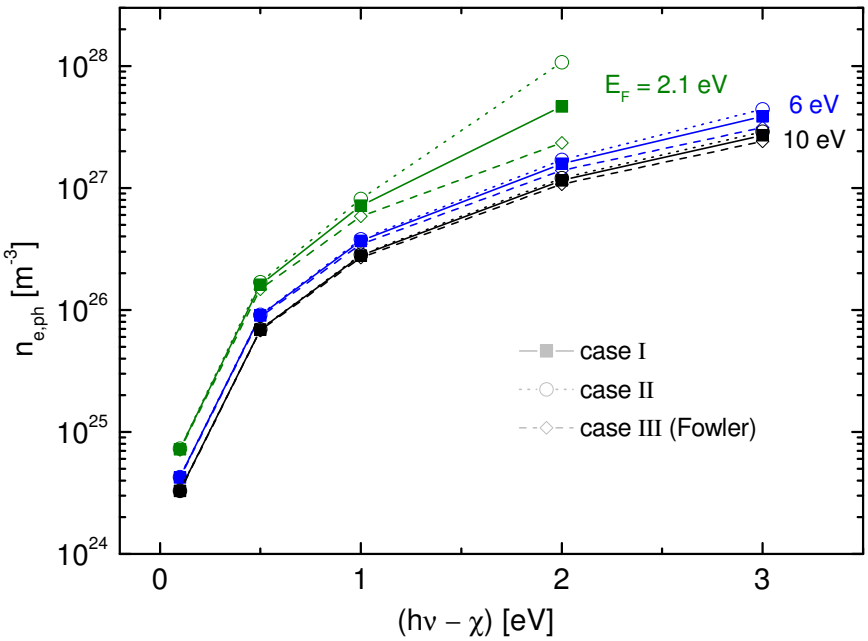

Figure 6.11: *Density of photoelectrically releasable electrons calculated for different cases of approximation, each for three different Fermi energies and for* $T = 300\,K$.

relative behavior of $n_{\mathrm{e,ph}}$ over $h\nu - \chi$ and thus the increasing slope of the realistic case with decreasing E_{F} cannot be reproduced by the Fowler case.

Hence, the simplifications performed to obtain the Fowler case lead to an underestimation of the density of photoelectrically releasable electrons for photon energies beyond the validity of $h\nu \approx \chi$ and to an independence of the slope of the density $n_{\mathrm{e,ph}}(h\nu - \chi)$ from the Fermi energy.

Consequences

The result of the simplifications is, that in experimental application where photocurrents are measured for different photon energies, the currents of the highest photon energies are larger than predicted by the Fowler theory and the deviation is more severe at lower Fermi energies. This means that the fitting routine will fit a steeper Fowler function $A + \ln\left[f\left(\kappa(\chi)\right)\right]$ to match the measurements which is accompanied by the evaluation of a higher work function.

The effect is much less pronounced or even negligible if at least for one frequency the condition $h\nu \approx \chi$ is fulfilled, as this photon energy determines the threshold of the Fowler function and therefore the work function. Thus, the set of interference

filters for the application of the Fowler method should include at least one filter with a mean photon energy close to the work function. However, even if the set of frequencies is initially appropriate, two incidents can yet occur if the sample surface is subject to modifications:

- If the work function of the surface decreases at constant Fermi energy, also the lowest applied photon energy gradually diverges from the actual work function. This can then again lead to the evaluation of overestimated work functions.

- If the Fermi energy decreases at constant work function, the overestimation effect is aggravated. Thus, an increasing work function can be evaluated, even if the actual work function is unaffected.

In both cases, the constant A from the Fowler fit can be used as a control parameter: if the evaluated work function is overestimated, the measured photocurrents are too high for this particular work function and therefore the fitting routine gives an increased value for A in order to compensate for that effect.

Summarizing, evaluated work functions via the Fowler method are always upper limits, whereas the accuracy of the work function can be assessed qualitatively via the constant A.

A method for the quantitative assessment of the overestimation including a possible correction of the wrongly determined work function is presented in the next paragraphs.

Identification and correction of overestimated work functions

Consider a sample whose current work function is χ_0 together with a fixed set of photon energies used for the measurement of the work function and let $h\tilde{\nu}$ be a particular photon energy for which applies $h\tilde{\nu} \approx \chi_0$. Then the measured photocurrent at the particular photon energy is $I_{\mathrm{ph},0}^{\mathrm{meas}}(h\tilde{\nu})$ and the evaluation of the current work function via the Fowler method should yield a value $\chi_0^{\mathrm{meas}} \approx \chi_0$. If the work function decreases to a value χ (which is actually unknown), a modified value χ^{meas} is determined by the fixed set of photon energies, where the corresponding photocurrent due to incidence of $h\tilde{\nu}$ is $I_{\mathrm{ph}}^{\mathrm{meas}}(h\tilde{\nu})$. However, besides the *measurement*, the expected photocurrent for the work function χ^{meas}, $I_{\mathrm{ph}}^{\mathrm{Fowler}}(h\tilde{\nu}, \chi^{\mathrm{meas}})$, can be *calculated* using the Fowler theory and the ratio to the

initially measured photocurrent:

$$\begin{aligned} I_{\mathrm{ph}}^{\mathrm{Fowler}}(h\tilde{\nu},\chi^{\mathrm{meas}}) &\overset{(6.27)}{=} I_{\mathrm{ph},0}^{\mathrm{meas}}(h\tilde{\nu})\,\frac{T_{\mathrm{spl}}^2\,f(\chi^{\mathrm{meas}},T_{\mathrm{spl}})}{T_{\mathrm{spl},0}^2\,f(\chi_0,T_{\mathrm{spl},0})} \;= \\ &= I_{\mathrm{ph},0}^{\mathrm{meas}}(h\tilde{\nu})\left(\frac{T_{\mathrm{spl}}}{T_{\mathrm{spl},0}}\right)^2\left(\frac{f(\kappa^{\mathrm{meas}})}{f(\kappa_0)}\right)\,, \end{aligned} \tag{6.29}$$

where $T_{\mathrm{spl},0}$ and T_{spl} are the initial and current temperature of the sample. On the other hand, the expected photocurrent corresponding to the currently evaluated work function χ^{meas} can also be calculated using case II. If the procedure performed for the Fowler case in section 6.3.2 is performed for case II, simply the square root taken in front of the integral in equation (6.23) has to be taken into account additionally. Therefore, considering an assumed variation of the Fermi energy from initially $E_{\mathrm{F},0}$ to currently E_{F}, the calculated photocurrent is

$$I_{\mathrm{ph}}^{\mathrm{case\,II}}(h\tilde{\nu},\chi^{\mathrm{meas}},E_{\mathrm{F}}) = I_{\mathrm{ph},0}^{\mathrm{meas}}(h\tilde{\nu})\sqrt{\frac{E_{\mathrm{F},0}+\chi_0-h\tilde{\nu}}{E_{\mathrm{F}}+\chi^{\mathrm{meas}}-h\tilde{\nu}}}\left(\frac{T_{\mathrm{spl}}}{T_{\mathrm{spl},0}}\right)^2\left(\frac{f(\kappa^{\mathrm{meas}})}{f(\kappa_0)}\right)\,. \tag{6.30}$$

As shown in figure 6.11, for constant E_{F} the actual solution (case I) lies between the Fowler case and case II. Thus, the following relation should apply for the actually measured photocurrent $I_{\mathrm{ph}}^{\mathrm{meas}}(h\tilde{\nu})$ at this work function:

$$I_{\mathrm{ph}}^{\mathrm{Fowler}}(h\tilde{\nu},\chi^{\mathrm{meas}}) \;\le\; I_{\mathrm{ph}}^{\mathrm{meas}}(h\tilde{\nu}) \;\le\; I_{\mathrm{ph}}^{\mathrm{case\,II}}(h\tilde{\nu},\chi^{\mathrm{meas}},E_{\mathrm{F}}) \quad \text{for } E_{\mathrm{F}}=E_{\mathrm{F},0}\,. \tag{6.31}$$

As the Fermi energy of the sample is actually unknown, an upper limit for the right hand side of relation (6.31) can be given by using the lowest possible value for the Fermi energy within physically reasonable limits[4]. Like this the maximal range of validity can be achieved.

A graphic representation of these equations and relations is shown in figure 6.12. For a set of photon energies (4.0 eV, 4.1 eV, 5.0 eV) the photocurrents are numerically calculated for different work functions and Fermi energies (see also figure 6.11, case I). For each case the calculated currents are subsequently used to simulate measured work functions χ^{meas} after the Fowler method. In figure 6.12 the single photocurrents arising from the particular photon energy $h\tilde{\nu}=4.1\,\mathrm{eV}$ relative to its value at $\chi_0 = 4\,\mathrm{eV}$ and $E_{\mathrm{F},0} = 6\,\mathrm{eV}$ are plotted as squares. Thereby, the abscissae for the full squares represent the evaluated χ^{meas}

[4]This value depends on the material of the sample under investigation including possible modifications.

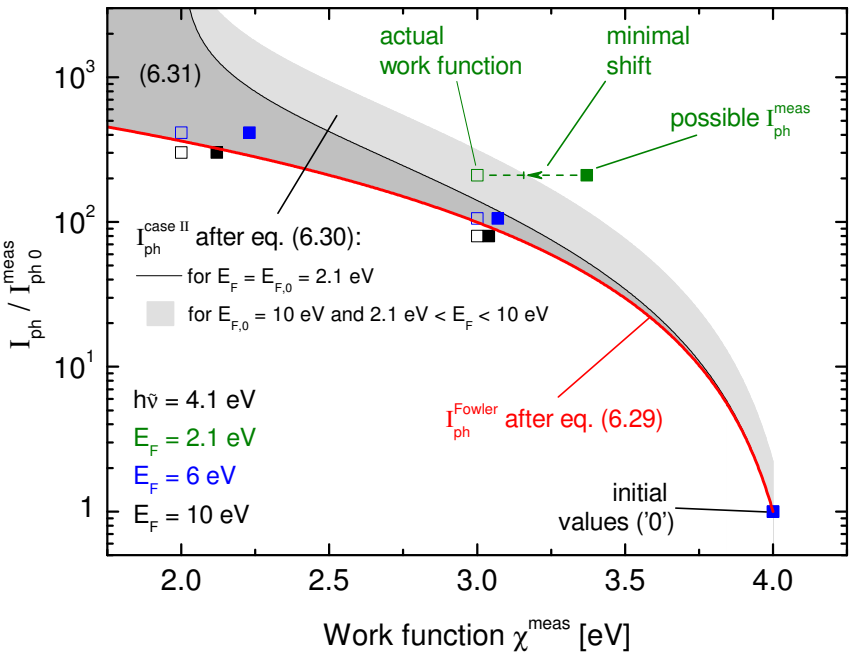

Figure 6.12: *Photocurrents for $h\tilde{\nu} = 4.1\,eV$ calculated for different Fermi energies and work functions (open squares) as well as the same photocurrents plotted over simulated measured work functions (full squares). Lines and shaded areas correspond to calculations after different approaches. Each value is related to the photocurrent at $\chi_0 = 4\,eV$ and the sample temperature is constantly 300 K.*

whereas the x-coordinates for the open squares correspond to the actual work functions originally used to calculate the photocurrents. The increasing deviation between actual and evaluated work functions for increasing difference between photon energy and work function and for decreasing Fermi energy can be observed. At the initial point '0' both values are the same as expected from the explanations above: $h\tilde{\nu} \approx \chi_0 \Rightarrow \chi_0^{\mathrm{meas}} \approx \chi_0 = 4\,\mathrm{eV}$.

In the presented plot, a decreasing Fermi energy of the sample surface generally leads to a vertical shift of the photocurrents in positive y-direction (vice versa for increasing E_F) whereas a wrongly determined work function due to inappropriate photon energies leads to a horizontal shift in positive x-direction.

Now the theoretical photocurrents $I_\mathrm{ph}^{\mathrm{Fowler}}(h\tilde{\nu}, \chi^{\mathrm{meas}})$ after equation (6.29) ($T_\mathrm{spl} = T_{\mathrm{spl},0} = 300\,\mathrm{K}$) are calculated and plotted as the red curve and the currents $I_\mathrm{ph}^{\mathrm{case\,II}}(h\tilde{\nu}, \chi^{\mathrm{meas}}, E_\mathrm{F})$ are calculated after equation (6.30) and plotted as the black curve. The required Fermi energy for the latter one is actually unknown in experimental application and therefore in order to delimit the maximal possible range the minimal value of $E_\mathrm{F} = E_{\mathrm{F},0} = 2.1\,\mathrm{eV}$ is taken here. The dark gray shaded area between these two curves represents relation (6.31) and it can be seen that

the photocurrents for a constant Fermi energy ($E_\mathrm{F} = 6\,\mathrm{eV}$, blue squares) indeed comply with the inequality.

Photocurrents beyond the validity of relation (6.31) (dark gray shaded area) are to be ascribed to a modified Fermi energy. A decrease in E_F yields photocurrents above the black curve (e. g. for $E_\mathrm{F} = 2.1\,\mathrm{eV}$, olive squares), whereas values below the red curve arise from an increased Fermi energy (e. g. for $E_\mathrm{F} = 10\,\mathrm{eV}$, black squares). For the former case, relation (6.31) can be extended, as it applies also for $E_\mathrm{F} < E_{\mathrm{F},0}$, which can readily be seen at figure 6.11. Hence, the upper limit for the influence of a possibly decreased Fermi energy can be assessed by using the highest possible value for $E_{\mathrm{F},0}$ and the lowest possible one[5] for E_F in equation (6.30). In figure 6.12 this was performed for $E_{\mathrm{F},0} = 10\,\mathrm{eV}$ and $E_\mathrm{F} = 2.1\,\mathrm{eV}$, which limits the light gray shaded area above the black curve.

Thus, any measured photocurrent arising from the particular photon energy $h\tilde{\nu} = 4.1\,\mathrm{eV}$, that lies within the gray shaded areas can be explained by a decreased Fermi energy of the investigated sample surface. Furthermore, since relation (6.31) with the extension to $E_\mathrm{F} \leq E_{\mathrm{F},0}$ has to be fulfilled for each measured photocurrent, values above the light gray shaded area have to be connected to a wrongly determined work function χ^meas at this point. In figure 6.12 this would be the case for the photocurrent for $E_\mathrm{F} = 2.1\,\mathrm{eV}$ for which a work function of $3.37\,\mathrm{eV}$ was simulated by the set of photon energies defined above. Using the extended relation (6.31), the work function can be corrected to attain the new maximal value of $3.17\,\mathrm{eV}$ which is 50 % closer to the actual value of $3.0\,\mathrm{eV}$.

For an increased Fermi energy (measured photocurrent below the red curve), such an approach cannot be made. However, as an increasing E_F is accompanied by decreasing errors in the determination of the work function, this issue has less significance.

Finally, as the evaluation of the work function χ^meas is always performed after the Fowler method using the fixed set of photon energies (see equation (6.28)), any deviation between $I_\mathrm{ph}^\mathrm{meas}(h\tilde{\nu})$ and $I_\mathrm{ph}^\mathrm{Fowler}(h\tilde{\nu}, \chi^\mathrm{meas})$ has to be compensated by the constant A, and within the accuracy of the Fowler fit applies

$$I_\mathrm{ph}^\mathrm{meas}(h\tilde{\nu}) \overset{(6.28)}{\approx} I_{\mathrm{ph},0}^\mathrm{meas}(h\tilde{\nu})\ \frac{\mathrm{e}^A}{\mathrm{e}^{A_0}} \left(\frac{T_\mathrm{spl}}{T_{\mathrm{spl},0}}\right)^2 \left(\frac{f(\kappa^\mathrm{meas})}{f(\kappa_0)}\right) \overset{(6.29)}{=} \frac{\mathrm{e}^A}{\mathrm{e}^{A_0}}\ I_\mathrm{ph}^\mathrm{Fowler}(h\tilde{\nu}, \chi^\mathrm{meas})\ , \tag{6.32}$$

whereas $A = A_0$ should apply after the Fowler theory. In other words, a non-

[5] Again, these values depend on the material of the used sample including possible modifications and are to be chosen within reasonable physical limits.

constant value of A implies that the currently measured photocurrent is incompatible with the currently evaluated work function after the Fowler method. This confirms the applicability of A as an control parameter.

For $A > A_0$ either the determined work function is wrong ($\chi^{\mathrm{meas}} > \chi$) due to a set of photon energies which is not appropriate any more or the Fermi energy has decreased which cannot be taken into account by the Fowler theory. The latter cause can be examined as done in figure 6.12 (shaded areas) whereas the former cause can be corrected to some extent if a certain degree of deviation is reached (beyond the shaded areas). For $A < A_0$ the Fermi energy must have increased. However, if an increased Fermi energy occurs together with a wrongly determined work function a value of A equal to A_0 can be produced. Therefore, a constant value of A does not necessarily imply that the determined work function is correct. This can be seen in figure 6.12 at the black full square, where E_{F} is increased from 6 to 10 eV and χ^{meas} is determined to 2.12 eV compared to the actual value of 2.0 eV. The measured photocurrent assigned to the wrong work function is almost identical to the photocurrent calculated after the Fowler theory for this work function and the Fowler fit would yield $A \approx A_0$ even if the work function is wrong.

In conclusion, the implication due to the limited validity of the Fowler theory remains: An evaluated work function after the Fowler method is always an upper limit for the actual one. However, the assessment of evaluated work functions via the plot presented in figure 6.12 gives the opportunity for correcting overestimated work functions.

6.4 Monitoring of background gases

The high chemical reactivity of caesium requires surveillance of the impurity gases within the system. This gives the opportunity to possibly relate potential unexpected behaviors of the caesium content to variations of the impurity content. On the other hand, the influence of caesium on the background gases can give an insight into the chemical behavior of caesium. Therefore, a residual gas analyzer (RGA) is applied.

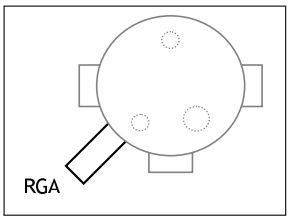

The RGA (Pfeiffer Vacuum PrismaPlus QMG 220) is connected to the discharge vessel via a 300 µm orifice and pumped differentially. It is capable of detecting masses from 1 to 200 u with either a Faraday cup or a secondary electron multiplier for higher sensitivity.

To prevent accumulation of caesium in the RGA system, especially at the orifice, it is heated to about 80 ℃. Nevertheless, for caesium the probability of reaching the detector is infinitesimal due to the high affinity for chemical or physical adsorption at the walls. In fact, caesium can only be detected if no orifice is present. However, in this case the applicability of the RGA is limited to operation in vacuum since the pumping rate of the RGA system is too high to maintain sufficient absolute pressure within the main vessel.

Thus, for the main campaigns the orifice is installed and the system is running in continuous mode to track the time traces of the background gases.

6.5 Determination of local plasma parameters with a Langmuir probe

The *Langmuir probe* is an electrostatic probe which is led to the bulk plasma electrically insulated from the vessel walls. Applying a voltage between the probe tip and the vessel walls draws a current from which several plasma parameters can be evaluated, which characterize the discharge locally at the place of the probe tip [MSL26]. To minimize interferences of the plasma, the probe tip consists of a wire of only some 100 µm in diameter and is made of tungsten for sustained stability.

6.5.1 Current-voltage characteristic

The probe bias V_p applied against the grounded vessel wall leads to an electrical current I_p consisting of an electron current I_e and an ion current[6] I_ion: $I_\mathrm{p} = I_\mathrm{e} - I_\mathrm{ion}$. A standard current-voltage characteristic ($I - V$ curve) can be seen in figure 6.13.

As described in section 3.1.3, the plasma is at a potential ϕ_pl above ground. Thus, for $V_\mathrm{p} = \phi_\mathrm{pl}$ the probe behaves as part of the plasma: quasineutrality and the much higher temperature and thus velocity of the electrons lead to much higher electron than ion fluxes and the probe current is almost exclusively carried by electrons. At voltages higher than the plasma potential solely electrons can reach the probe why this region is called *electron saturation*. Due to the cylindrical probe geometry an actual saturation is not reached as the volume from which

[6] Actually the ion current is electron current from the probe into the plasma why it is considered negatively.

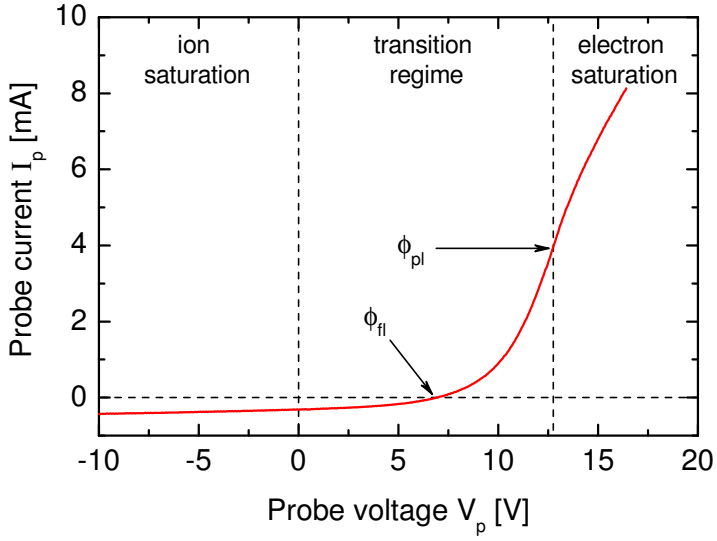

Figure 6.13: *Exemplary current-voltage characteristic of a Langmuir probe with associated current regimes and denoted floating and plasma potential.*

electrons can be collected rises with voltage.

Decreasing the voltage below the plasma potential builds up a retarding field for electrons (and an accelerating one for ions) and the probe current decreases consequently. This region is called *transition regime* and the electron current I_e reacts exponentially on the potential barrier if a Maxwellian EEDF is assumed. When the electron and ion fluxes are balanced the probe current is zero and the floating potential ϕ_{fl} is reached: a floating body in the plasma is not able to carry current and would charge to this potential with respect to the plasma (see section 3.1.3).

At voltages sufficiently below the floating potential virtually no electrons can reach the probe and the *ion saturation* region is reached. Due to the high mass of ions compared to electrons the ion saturation current is much smaller than the electron saturation current and again an increasing collection volume around the cylindrical probe wire prohibits an actual saturation.

Another interesting point to mention is, that at zero voltage where the probe is at the same potential as the vessel wall still a current flows, which is negative in the exemplary case in figure 6.13. This current can at least partly be ascribed to a profile of the plasma potential within the bulk plasma: The local plasma potential at the position of the probe tip is not necessarily the same as the plasma potential in vicinity of the vessel walls. Thus, if the probe and the wall are short-circuited, the potential drop from the plasma to the probe differs from the potential drop

to the vessel walls, which leads to unbalanced electron and ion currents. This discrepancy is compensated by a nonzero probe current whereas its value depends on the actual topology of the plasma profiles of the particular experiment. [LL05]

Negative ions and ion-ion plasmas

In hydrogen plasmas negative hydrogen ions H^- can be produced, especially at cesiated surfaces (see section 2.2). The negative ions have thermal velocities of the order of the velocity of positive ions, which is about two orders of magnitude smaller than the electron velocity. Hence, the contribution of negative ions to the current of negative charges is not significant until the density ratio of negative ions to electrons, $n_{\mathrm{ion}^-}/n_\mathrm{e}$, is of the order of 10^2. Thus, below this density ratio, negative ions do not have to be considered in the evaluation of the $I-V$ curve.

But another effect can be observed in Langmuir probe characteristics at much lower negative ion densities. Consider a standard positive-ion–electron plasma with constant total density of positive ions. Then, since quasineutrality has to be fulfilled, an increasing negative ion density directly leads to a decreasing electron density and thus to a decreasing electron current onto the probe [WMA75], even if or precisely because the contribution of negative ions to the measured current is still negligible. In conclusion, this can yield an apparently symmetric $I-V$ curve (with respect to the floating potential) even if electrons are still the major negative charge carrier [WMA75].

However, increasing the density ratio $n_{\mathrm{ion}^-}/n_\mathrm{e}$ further to values of the order of 10^4 can in fact lead to a plasma in which electrons are the minor charge carriers and can be neglected. This state is called *ion-ion plasma* and is characterized by a symmetric $I-V$ curve [WPL73]. In NNBI ion sources such conditions can be achieved near the cesiated plasma grid [MS10, TNK$^+$12]. For the laboratory experiment, this effect can, if ever, only occur directly at the vessel surfaces, whereas in the plasma volume an ion-ion plasma will never be achieved due to the permanent ionization processes.

6.5.2 Determination of plasma parameters

Information on processing probe characteristics is widespread in the literature and can e. g. be found in [MSL26], [LL05], [Che03] or [Her89]. The following paragraphs are just an outline on how $I-V$ curves are evaluated in the present work to determine plasma parameters.

Potentials

The floating potential ϕ_{fl} is easily determined as $I_{\mathrm{p}}(\phi_{\mathrm{fl}}) = 0$ (see figure 6.13). Assuming a Maxwellian EEDF, the electron current for $V_{\mathrm{p}} \leq \phi_{\mathrm{pl}}$ can be approximated by

$$I_{\mathrm{e}}(V_{\mathrm{p}}) = \frac{1}{4} e n_{\mathrm{e}} \bar{v_{\mathrm{e}}} A_{\mathrm{p}}\, \mathrm{e}^{-\frac{e\,(\phi_{\mathrm{pl}} - V_{\mathrm{p}})}{k_{\mathrm{B}} T_{\mathrm{e}}}} \ , \text{ with } \bar{v_{\mathrm{e}}} = \sqrt{\frac{8 k_{\mathrm{B}} T_{\mathrm{e}}}{\pi m_{\mathrm{e}}}} \ , \tag{6.33}$$

where $\bar{v_{\mathrm{e}}}$ is the mean electron velocity and A_{p} the probe surface area. Thus, the slope of the electron current reaches its maximum at $V_{\mathrm{p}} = \phi_{\mathrm{pl}}$ whereas at higher probe voltages saturation begins and the slope starts to decrease. Hence, at the plasma potential, where the ion current can be neglected, the first derivative of $I_{\mathrm{p}}(V_{\mathrm{p}})$ is maximal. This correlates with the inflection point and therefore ϕ_{pl} is determined via the root of the second derivative of the probe characteristic. This is illustrated in figure 6.14 (a).

The potential drop $\phi_{\mathrm{pl}} - \phi_{\mathrm{fl}}$ between the plasma and a floating sample at the place of the probe tip can also be determined by equating the electron and the ion flux in the transition regime. After [LL05] this yields

$$\phi_{\mathrm{pl}} - \phi_{\mathrm{fl}} = \frac{k_{\mathrm{B}} T_{\mathrm{e}}}{e} \left(\frac{1}{2} + \ln \sqrt{\frac{m_{\mathrm{ion}}}{2\pi m_{\mathrm{e}}}} \right) \ , \tag{6.34}$$

with the ion mass m_{ion}. Thus, for constant ion mass the potential drop solely depends on the electron temperature, in fact directly proportional.

Electron density

If the probe is at the same potential as the plasma, no sheath between the probe and the plasma exists and the measured probe current $I_{\mathrm{p}}(\phi_{\mathrm{pl}})$ can be approximated by the sole electron current $I_{\mathrm{e}}(\phi_{\mathrm{pl}})$. Referring to equation (6.33), the electron density n_{e} can thus be determined from the probe current at the plasma potential if the electron temperature is known:

$$n_{\mathrm{e}} = \frac{4 I_{\mathrm{p}}(\phi_{\mathrm{pl}})}{e A_{\mathrm{p}}} \sqrt{\frac{\pi m_{\mathrm{e}}}{8 k_{\mathrm{B}} T_{\mathrm{e}}}} \ . \tag{6.35}$$

Electron temperature and EEDF

The determination of the electron temperature from probe measurements can basically be performed via two different methods. Both of them arise from the decreasing electron current with increasing difference of the probe bias from the

plasma potential.

If a Maxwellian EEDF can be assumed, then the electron current between flux equilibrium and density equilibrium is described by equation (6.33) and it applies:

$$\ln I_\mathrm{e}(V_\mathrm{p}) \propto \frac{eV_\mathrm{p}}{k_\mathrm{B}T_\mathrm{e}} \ , \ \text{for } \phi_\mathrm{fl} \leq V_\mathrm{p} \leq \phi_\mathrm{pl} \ . \tag{6.36}$$

Thus, a linear fit of the logarithmic electron current yields the electron temperature as the inverse slope. However, at least near the floating potential the ion current is a major contribution to the probe current, why it cannot be neglected and has to be subtracted from the measured probe current in order to obtain the pure electron current. For this, the progression of the ion current with the probe bias needs to be known, which is not easily determined (see section 'Ion density' below).

A more general approach, which is not based on the absolutely measured probe current and is furthermore independent from a specific EEDF is described in the following: Starting from the plasma potential, decreasing probe voltages lead to an increasing potential barrier for the electrons. Thus, the minimum energy of those electrons that can contribute to the measured current increases with decreasing V_p. This leads to the conception that by varying the probe bias the *electron energy distribution function (EEDF)* $f(E_\mathrm{e})$ is scanned. The correlation via the second derivative of the probe current was derived by Druyvesteyn [Dru30] and is reproduced here after [LL05]:

$$\begin{aligned} f(E_\mathrm{e}) &= \frac{\sqrt{8m_\mathrm{e}E_\mathrm{e}}}{e^3A_\mathrm{p}} \cdot \frac{\mathrm{d}^2I_\mathrm{p}}{\mathrm{d}V_\mathrm{p}^2} \ , \ \text{for } [E_\mathrm{e}] = \mathrm{J} \ \longrightarrow \ \Big[f(E_\mathrm{e})\Big] = \mathrm{J}^{-1}\mathrm{m}^{-3} \\ f(E_\mathrm{e}) &= \frac{\sqrt{8m_\mathrm{e}E_\mathrm{e}}}{e^{3/2}A_\mathrm{p}} \cdot \frac{\mathrm{d}^2I_\mathrm{p}}{\mathrm{d}V_\mathrm{p}^2} \ , \ \text{for } [E_\mathrm{e}] = \mathrm{eV} \longrightarrow \ \Big[f(E_\mathrm{e})\Big] = \mathrm{eV}^{-1}\mathrm{m}^{-3} \ , \end{aligned} \tag{6.37}$$

where $E_\mathrm{e} = e\,(\phi_\mathrm{pl} - V_\mathrm{p})$ is the electron energy in J or eV respectively[7] with $V_\mathrm{p} \leq \phi_\mathrm{pl}$. The determined EEDF complies with the general properties of EEDFs (equations (3.4) to (3.7)) and can in particular be transfered to the electron energy probability function (EEPF) $g(E_\mathrm{e})$:

$$g(E_\mathrm{e}) = \frac{f(E_\mathrm{e})}{\sqrt{E_\mathrm{e}}} = \frac{\sqrt{8m_\mathrm{e}}}{e^{3/2}A_\mathrm{p}} \cdot \frac{\mathrm{d}^2I_\mathrm{p}}{\mathrm{d}V_\mathrm{p}^2} \ , \qquad \Big[g(E_\mathrm{e})\Big] = \mathrm{eV}^{-3/2}\mathrm{m}^{-3} \ . \tag{6.38}$$

[7] Strictly speaking, the change from J to eV corresponds to a change of the used system of natural units. However, for convenience SI units are used for all quantities but the electron energy. This leads to the correction factor $e^{3/2}$ compared to the equation where J is used for E_e.

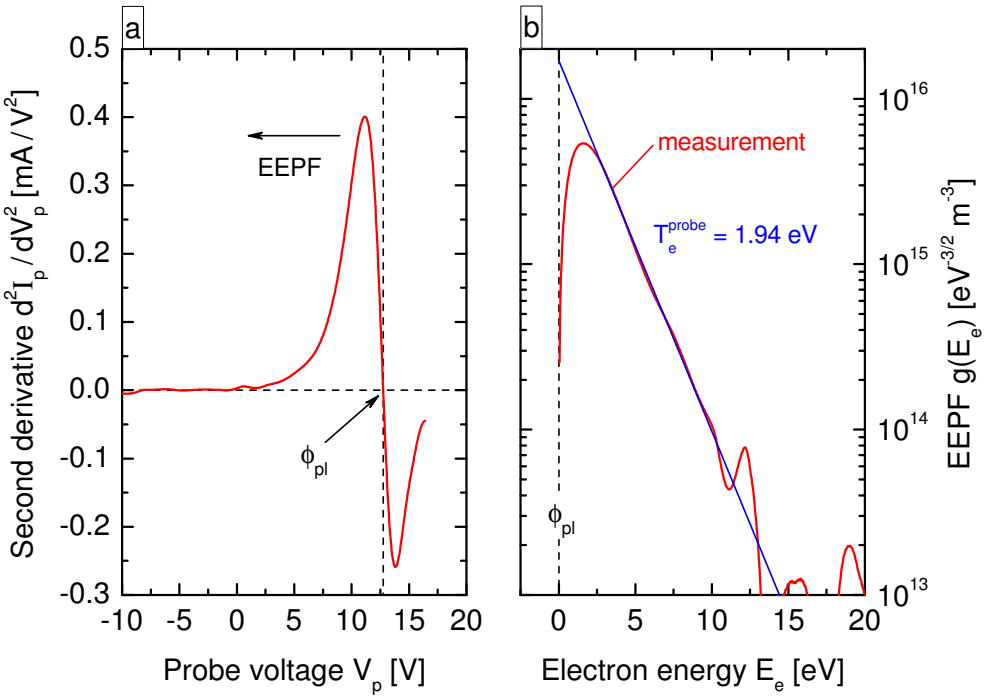

Figure 6.14: (a) *Second derivative of the probe characteristic of figure 6.13 illustrating the determination of the plasma potential and the position of the EEPF.* **(b)** *Determination of $T_{e,p}$ from a measured EEPF, which is calculated after equation* (6.38).

Hence, the second derivative of the measured probe current is directly proportional to the EEPF. This is illustrated in figure 6.14 (a).

For a Maxwellian distribution the logarithm of the EEPF is directly proportional to the inverse electron temperature (see equation (3.1)): $\ln g_M(E_e) \propto -E_e/k_B T_e$. Therefore, using equation (6.38) an electron temperature can be determined from the measured Langmuir probe characteristic via a linear fit to the logarithm of the second derivative of the $I-V$ curve:

$$k_B T_e = -\left(\frac{d}{dE_e} \ln g_M(E_e)\right)^{-1} \Longrightarrow \qquad k_B T_e^{probe} = -\left(\frac{d}{dE_e} \ln \frac{d^2 I_p}{dV_p^2}\right)^{-1} . \quad (6.39)$$

This is demonstrated in figure 6.14 (b) where for the probe characteristic from figure 6.13 an electron temperature of about 2 eV is evaluated.

It has to be kept in mind that T_e^{probe} can only be seen as thermodynamic temperature, if the measured EEPF resembles a Maxwellian evolution. For the present case this is valid for $2.5\,eV \leq E_e \leq 10\,eV$. For lower and higher energies the measured EEPF differs from the linear regression. Besides the possibility,

that the EEPF actually behaves nonlinear (see section 3.1.1 or section 3.3 for the 'molecular dip' in the low energy region), metrological causes can be quoted for this behavior: while the high energy part can simply be explained by the low probe currents at these voltages (below the floating potential) and therefore by a low signal-to-noise ratio, a variety of influences can affect the low energy part including inappropriate probe dimensions, contaminations of the probe tip, inadequate probe circuits and RF noise [GPA92]. In experimental application the range of electron energies for which the measured EEPF can be seen as reliable has to be assessed by experienced judgment.

Besides the electron temperature, further quantities can be evaluated from the measured EEPF. After equation (3.5) the EEDF can be used for an alternative way to determine the electron density and via equation (3.6) a mean electron energy can be obtained. However, in both cases the lack of measured low energy electrons can influence the evaluation: n_e is possibly underestimated and $\langle E_\mathrm{e} \rangle$ is most likely overestimated.

Therefore, in this work the second derivative of the probe characteristic is only used for the determination of the EEPF and the electron temperature (together with ϕ_pl as shown above).

Ion density

Since quasineutrality has to be fulfilled, $n_\mathrm{ion} = n_\mathrm{e}$ can be used for the determination of the ion density. Nevertheless, it can also be evaluated from the ion saturation region of the $I-V$ curve. Several theories exist in the literature about the ion current onto a cylindrical probe differing in the conception of the motion of the particles (straight or orbital) and whether or not a sheath around the probe is considered. A summary is given in table 6.3. However, all of them assume a collisionless collection of ions by the probe and thus the ion current is only approximated. A review on the different approximations including assessments of the applicability can be found in [Che03] for instance.

A crucial issue common to all theories is the ion mass, which has to be known for the evaluation of the ion density. If several ion species are present in the plasma (for a hydrogen plasma there are H^+, H_2^+ and H_3^+) even the ion composition is required to determine a mean ion mass $\overline{m}_\mathrm{ion}$. This issue is further complicated when heavy ions are introduced into the plasma (as xenon or caesium in the present case), because here already very little shares to the total ion density can lead to significant variations of $\overline{m}_\mathrm{ion}$.

Table 6.3: *Overview of the different theories in the literature for the ion current onto a cylindrical probe.*

Theory		Considered effect orbiting	sheath	Reference
Floating potential method based on Child-Langmuir Law	FP/CL	–	–	[Chi11, CEA02]
Orbital Motion Limited	OML	+	–	[MSL26]
Allen-Boyd-Reynolds	ABR	–	+	[ABR57, Che65]
Bernstein-Rabinowitz-Laframboise	BRL	+	+	[BR59, Laf66]

For pure hydrogen (deuterium) plasmas it was pointed out in section 3.3, that H_3^+ (D_3^+) is the predominant ion for the present plasma parameters and thus a mean ion mass of 3 u (6 u) can be used. Furthermore, it was determined experimentally, that by applying the BRL theory to a hydrogen plasma at 10 Pa and 250 W RF power, the evaluated ion density was closest to the corresponding electron density: n_{ion} was about 20 % higher than n_{e}. The tendency of the BRL theory to commonly overestimate ion densities is also described in [Che03]. Thus, for the present investigations, the BRL theory is applied with a mean ion mass of 3 u (6 u).

For discharges with admixtures of xenon or caesium the mean ion mass is a priori unknown due to the lack of a diagnostic for the ion composition. Thus, the evaluation of the absolute ion density loses relevance. However, via a variation of $\overline{m}_{\mathrm{ion}}$ the ion density evaluated after the BRL theory can be fitted to the electron density. Like this, a rough estimation of the mean ion mass can be obtained which gives an insight into the ion composition.

6.5.3 Applied Langmuir probe system

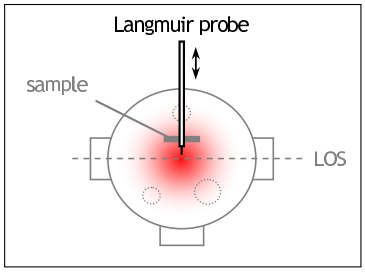

The applied Langmuir probe consists of a stainless steel rod in a quartz tube with a narrow nozzle through which the actual probe tip (tungsten wire, diameter 100 µm, length 1 cm) is led to the plasma. If the sample holder is installed, it is also possible to lead the probe through the sample surface as described in section 5.1. The actual position of the probe tip in horizontal direction

is variable (illustrated by the double arrow in the pictogram). However, in pure plasma operation without a sample it is centered axially and radially within the discharge vessel. The current-voltage characteristic ($I-V$ curve) is recorded by electronics and transfered to a PC via fiber-optic cables for galvanic insulation. The Langmuir probe system is described in detail in [MDCK$^+$09].

The software used to control the electronics is also capable of automatically evaluating the plasma parameters after the procedures described above. The determination of the second derivative of the measured $I-V$ curve is very sensitive to high frequency noise. Therefore, a smoothing technique is applied where the smoothing interval is chosen to be 1 V, which was experimentally determined as the compromise between evaluable probe characteristics and negligible influence on the evaluation of plasma parameters. Details on the smoothing procedure can be found in [MDCK$^+$09].

In plasmas containing caesium, accumulation of Cs on the probe tip can lead to the production of negative hydrogen ions at the probe surface and thus to an alteration of the flux balance within the boundary between the probe and the plasma. In this case the evaluated plasma parameters do no longer reflect the undisturbed properties of the bulk plasma. Thus, Cs accumulation has to be prevented which is accomplished by heating the probe tip to red heat each time before an $I-V$ curve is recorded. This is attained by a high positive probe voltage drawing a large electron current.

For each measurement about ten $I-V$ curves are taken within one minute and the evaluated plasma parameters are averaged afterwards.

Measurement errors

The standard deviation of the averaged value of the multiple measurements serves as a part of the measurement error. Another contribution is the mean error of the single determined values themselves. A thoroughly performed analysis yields the following errors:

Plasma parameter	Single measurement	Typical standard deviation	Typical error
ϕ_{fl}, ϕ_{pl}	$\pm 0.05\,\mathrm{V}$	$\pm 0.02\,\mathrm{V}$	$\pm 0.07\,\mathrm{V}$
T_{e}	$\pm 0.1\,\mathrm{eV}$	$\pm 0.02\,\mathrm{eV}$	$\pm 0.12\,\mathrm{eV}$
n_{e}	$\pm 6\,\%$ (+ 10 %)	$\pm 0.5\,\%$	$\pm 6.5\,\%$
n_{ion}	dep. on $\overline{m}_{\mathrm{ion}}$	$\pm 1\,\%$	$\gg \pm 1\,\%$

The above given errors from a single measurement are taken as constants throughout the present work whereas the standard deviation from the multiple recordings of $I-V$ curves is considered separately in each case (typical values given in the table). The accuracy of the determined ion density for a given ion current theory mainly depends on the unknown, but possibly varying, mean ion mass. Therefore its error is not assessable, but the standard deviation of several measurements is about 1 % on average. For the electron and the ion density an additional error of $\pm 10\,\%$ for the probe surface area can be considered. However, this contribution only shifts each determined value, why it is not taken into account for the resultant error bars hereafter.

6.6 Determination of global plasma parameters by means of OES

Optical emission spectroscopy is a non-invasive diagnostic by which the emitted radiation from the plasma is used to evaluate line-of-sight integrated plasma parameters (also called 'global' or 'volume averaged'). In section 6.2.2 OES is already applied to determine the Cs density from the Cs emission. Presented in the following, the emission from molecular and atomic hydrogen is used to evaluate global parameters which are characteristic for the plasma environment of caesium, like the gas and electron temperature. The hydrogen plasma is moreover characterized by the densities of the hydrogen species, among which mainly H, H_2^+ and H^- are accessible via OES.

6.6.1 Molecular spectroscopy on the hydrogen molecule

The internal energy of the hydrogen molecule is determined by the electronic state, the vibrational state ν within the electronic state (summarizingly labeled 'vibronic state') and the rotational level J within the vibronic state ('ro-vibronic levels'). Among the resultant multitude of optical transitions the prominent *Fulcher system* of the hydrogen/deuterium molecule between 590 and 650 nm is spectroscopically accessible. Its ro-vibronic transition lines $(\mathrm{d}\,^3\Pi_\mathrm{u}, \nu', J') \rightarrow (\mathrm{a}\,^3\Sigma_\mathrm{g}^+, \nu'', J'')$ can be used to determine the gas temperature, the vibrational temperature of the ground state and the integrated emission from the entire Fulcher system.

Excitation of ro-vibronic levels and emission intensity

The energy difference between vibrational and rotational levels of the ground state $\mathrm{X}\,^1\Sigma_\mathrm{g}^+$ of the hydrogen or deuterium molecule is of the order of 0.1 eV and 0.01 eV, respectively [HH13]. Since $T_\mathrm{gas} \sim 600\,\mathrm{K} \sim 0.05\,\mathrm{eV} \ll T_\mathrm{e} \sim \mathrm{eV}$, the vibrational population in the ground state can be redistributed via collisions with heavy particles and electrons whereas rotational states are predominantly repopulated by heavy particle collisions. Thus, the population distribution of rotational states can be described by the energy distribution of the heavy particles (T_gas) [OOR+89] whereas for the vibrational population electrons and heavy particles have to be considered.

The total population distribution $\{\nu, J\}_\mathrm{X}$ of the ground state can be transfered to an excited electronic state i by electron impact excitation after the *Franck-Condon principle* [Her50]. Accordingly the excitation process occurs in such small time scales that the internuclear distance does not change during the excitation ('vertical excitation' in a potential curve diagram) and the probability that the molecule is excited from the lower vibrational state ν to the upper vibrational state ν' is described by the so-called *Franck-Condon factors (FCF)* $q_{\mathrm{X}i}^{\nu\nu'}$. These are determined by the overlap integral of the corresponding vibrational wave functions in the lower and upper electronic state. On the other hand, the rotational distribution of the lower state is projected directly into the upper state as the light electrons are not able to change the angular momentum of the molecule strongly (more precisely the rotational quantum number).

The population distribution in the upper state $\{\nu', J'\}_i$ subsequently relaxes to a lower electronic state via spontaneous emission and is thus spectroscopically accessible. The emissivity $\epsilon_{\mathrm{d}\,^3\Pi_\mathrm{u}\;\mathrm{a}\,^3\Sigma_\mathrm{g}^+}^{\nu'\nu''J'J''}$ ($\epsilon_{\mathrm{d\,a}}^{\nu'\nu''J'J''}$ for short) of a single ro-vibronic transition line $(\mathrm{d}\,^3\Pi_\mathrm{u}, \nu', J') \rightarrow (\mathrm{a}\,^3\Sigma_\mathrm{g}^+, \nu'', J'')$ from the Fulcher system can be parameterized after [Ber05]:

$$\epsilon_{\mathrm{d}\,^3\Pi_\mathrm{u}\;\mathrm{a}\,^3\Sigma_\mathrm{g}^+}^{\nu'\nu''J'J''} \equiv \epsilon_{\mathrm{d\,a}}^{\nu'\nu''J'J''} \;\propto\; n_{\mathrm{d}\,\nu'J'}\,\frac{S_\mathrm{P,Q,R}(J')}{2J'+1}\,A_{\mathrm{d\,a}}^{\nu'\nu''}\;, \tag{6.40}$$

where $n_{\mathrm{d}\,\nu'J'}$ is the absolute density in the upper ro-vibronic state, $S_\mathrm{P,Q,R}(J')$ is the so-called *Hönl-London factor (HLF)* for the rotational line which depends on the rotational branch of the electronic transition and $A_{\mathrm{d\,a}}^{\nu'\nu''}$ is the vibronic transition probability which is defined like in [FW06a] for instance as the overlap integral of the vibrational wave functions of the involved states weighted with the electronic transition dipole moment.

Rotational temperatures and the gas temperature

After [OOR+89] a Boltzmann distribution among the rotational states of the upper Fulcher level can be assumed if the gas temperature T_{gas} complies with the condition $k_{\mathrm{B}}T_{\mathrm{gas}} \gg B^{\mathrm{X}}_{\nu=0}$, where $B^{\mathrm{X}}_{\nu=0}$ is the rotational constant[8] of the vibrational ground state. For gas temperatures of typically about 600 K in low pressure low temperature plasmas and the rotational constants $B^{\mathrm{X,H_2}}_{\nu=0} = 59.3\,\mathrm{cm}^{-1}$ for hydrogen and $B^{\mathrm{X,D_2}}_{\nu=0} = 29.9\,\mathrm{cm}^{-1}$ for deuterium (see appendix B.1) this condition is well fulfilled. Therefore the population density ratio $n_{\mathrm{d}\,\nu' J'}/n_{\mathrm{d}\,\nu' J'=1}$ can be parameterized as

$$\frac{n_{\mathrm{d}\,\nu' J'}}{n_{\mathrm{d}\,\nu' J'=1}} \;\propto\; g_I(J')\,(2J'+1)\exp\left(-\frac{\Delta E_{\mathrm{rot}}(J')}{k_{\mathrm{B}}T^{\mathrm{d}\,\nu'}_{\mathrm{rot}}}\right)\,, \tag{6.41}$$

with the rotational temperature $T^{\mathrm{d}\,\nu'}_{\mathrm{rot}}$ of the vibrational state ν' of the upper Fulcher level, the energy gap $\Delta E_{\mathrm{rot}}(J')$ of the rotational state J' relative to the state $J'=1$ and a statistical factor $g_I(J')$ which is connected to the nuclear spin I [Her50]. Thus, using equation (6.40) the intensity distribution of the rotational lines within a vibronic transition ensues the proportionality

$$\epsilon^{\nu'\nu''J'J''}_{\mathrm{d\,a}} \;\propto\; g_I(J')\,S_{\mathrm{P,Q,R}}(J')\exp\left(-\frac{\Delta E_{\mathrm{rot}}(J')}{k_{\mathrm{B}}T^{\mathrm{d}\,\nu'}_{\mathrm{rot}}}\right)\,. \tag{6.42}$$

Hence, plotting the logarithm of $\left[\epsilon^{\nu'\nu''J'J''}_{\mathrm{d\,a}}/\Big(g_I(J')S_{\mathrm{P,Q,R}}(J')\Big)\right]$ against $\Delta E_{\mathrm{rot}}(J')$ yields the rotational temperature $T^{\mathrm{d}\,\nu'}_{\mathrm{rot}}$ via the slope of the linear regression. In the present work the rotational lines J'=1,...,5 $\rightarrow$ J''=J' (Q1 to Q5) from the Q branches of the diagonal vibronic transitions ν'= 0,...,3 $\rightarrow$ ν''=ν' are analyzed, since they are the most intense lines in the Fulcher spectrum. Information on the corresponding values of $g_I(J')$ and $S_{\mathrm{P,Q,R}}(J')$ is given in appendix B.2 and the values of $\Delta E_{\mathrm{rot}}(J')$ can be found in [Cro72] for hydrogen and in [LU08] for deuterium.

As described above the rotational distribution of the upper Fulcher state was projected from the ground state X via an electron induced excitation process. Thus, the determined $T^{\mathrm{d}\,\nu'}_{\mathrm{rot}}$ can be transferred to the ground state rotational temperature $T^{\mathrm{X}\,\nu=0}_{\mathrm{rot}} \equiv T^{\mathrm{X}}_{\mathrm{rot}}$ whereas the differing energy spreads of the rotational levels has to be taken into account via the rotational constants [OOR+89]:

$$T^{\mathrm{X}}_{\mathrm{rot}} = T^{\mathrm{d}\,\nu'}_{\mathrm{rot}}\,\frac{B^{\mathrm{X}}_{\nu=0}}{B^{\mathrm{d}}_{\nu'}}\,, \tag{6.43}$$

[8] In the first approximation, the energy of the rotational level J is given by $B^{\mathrm{X}}_{\nu=0}J(J+1)$.

where the rotational constants of the ground state $B^{\mathrm{X}}_{\nu=0}$ and of the excited states $B^{\mathrm{d}}_{\nu'}$ can be found in appendix B.1 for hydrogen and deuterium after [HH13]. According to [OOR+89] a slight variation in the angular momentum of the molecule can occur during electron excitation processes of light molecules like hydrogen and deuterium. Therefore, the translation of rotational temperatures after equation (6.43) does not necessarily yield the same value of $T^{\mathrm{X}}_{\mathrm{rot}}$ for each vibronic level (d,ν'). However, the temperature $T^{\mathrm{X}}_{\mathrm{rot}}$ should be similar to the gas temperature T_{gas} in accordance with the population via heavy particles. It was determined experimentally that for hydrogen the rotational temperature derived from $T^{\mathrm{d}\,\nu'=2}_{\mathrm{rot}}$ matches the gas temperature most accurate and for deuterium the one from $T^{\mathrm{d}\,\nu'=1}_{\mathrm{rot}}$ [Fan04, Die10].

Vibrational temperature of the ground state

Knowing the rotational temperatures of the vibronic levels (d,ν') allows for the calculation of the entire emission from the vibronic bands $(\mathrm{d}\,^3\Pi_{\mathrm{u}}, \nu') \rightarrow (\mathrm{a}\,^3\Sigma^+_{\mathrm{g}}, \nu'')$ using the relative rotational transition intensities after equation (6.42):

$$\epsilon^{\nu'\nu''}_{\mathrm{d\,a}} = \sum_{J'J''} \epsilon^{\nu'\nu''J'J''}_{\mathrm{d\,a}} = \epsilon^{\nu'\nu''Q1}_{\mathrm{d\,a}} \sum_{J'J''} \frac{\epsilon^{\nu'\nu''J'J''}_{\mathrm{d\,a}}}{\epsilon^{\nu'\nu''Q1}_{\mathrm{d\,a}}}$$

$$\overset{(6.42)}{=} \epsilon^{\nu'\nu''Q1}_{\mathrm{d\,a}} \sum_{J'J''} \frac{g_I(J')\, S_{\mathrm{P,Q,R}}(J') \exp\left(-\frac{\Delta E_{\mathrm{rot}}(J')}{k_{\mathrm{B}} T^{\mathrm{d}\,\nu'}_{\mathrm{rot}}}\right)}{g_I(J'=1)\, S_{\mathrm{Q}}(J'=1)} \,. \tag{6.44}$$

Thus, the measured emission of the most intense rotational line, the Q1 line ($J'=1 \rightarrow J''=1$), of the corresponding vibronic transition $\nu' \rightarrow \nu''$ is scaled by a factor which is determined by the rotational temperature of the upper vibronic state. For deuterium the reference of the sum is the Q2 line as it is the most intense line in that case. Furthermore, for deuterium another factor is required in the denominator, $\exp\left(-\frac{\Delta E_{\mathrm{rot}}(J'=2)}{k_{\mathrm{B}} T^{\mathrm{d}\,\nu'}_{\mathrm{rot}}}\right)$, since $\Delta E_{\mathrm{rot}}(J'=2) \neq 0$. As a side note the sum over both J' and J'' is equivalent to a sum over J' for the three branches P, Q and R.

Using equations (6.40) and (3.10) the vibronic emissions $\epsilon^{\nu'\nu''}_{\mathrm{d\,a}}$ can now be related to the vibronic population densities $n_{\mathrm{d}\,\nu'}$ via the vibronic transition probabilities $A^{\nu'\nu''}_{\mathrm{d\,a}}$:

$$n_{\mathrm{d}\,\nu'} = \sum_{J'} n_{\mathrm{d}\,\nu'J'} = \frac{\epsilon^{\nu'\nu''}_{\mathrm{d\,a}}}{A^{\nu'\nu''}_{\mathrm{d\,a}}} \,. \tag{6.45}$$

In the present work this analysis is performed via the diagonal vibronic transi-

tions $\nu'=0,\ldots,3 \rightarrow \nu''=\nu'$ of the Fulcher system, since they are the most intense bands. The corresponding Einstein coefficients $A_{\mathrm{d\,a}}^{\nu'\nu''}$ can be found in [FW06a] for hydrogen and deuterium.

The determined vibrational population distribution $\{n_{\mathrm{d}\,\nu'}\}$ of the upper Fulcher state is associated with the corresponding distribution $\{n_{\mathrm{X}\,\nu}\}$ of the ground state if solely population via electron impact excitation is assumed, as mentioned. Calculating the ground state population distribution and transferring it according to Franck-Condon factors and vibrationally resolved relative rate coefficients for electron impact excitation into the upper state allows for a comparison with the measured distribution. For comparable plasma parameters to the present investigations it was estimated in [FH98] that the ground state vibrational distribution can be determined by Boltzmann statistics and thus, it can be characterized by a vibrational temperature T_{vib}. Hence, matching calculated vibrational distributions in the upper Fulcher state to measured ones yields the vibrational temperature of the ground state. Mind, that due to the electron impact excitation this fitting routine is also dependent on the electron temperature T_{e}. The principles behind this diagnostic method including the determination of vibrationally resolved excitation cross sections is described in detail in [FH98]. For the present work more up to date data on FCFs and cross sections are used from [FW06a] and [Die10] respectively.

Entire Fulcher emission

Using the determined vibrational temperature of the ground state T_{vib}, the Franck-Condon factors $q_{\mathrm{Xd}}^{\nu\nu'}$ and vibrationally resolved relative rate coefficients for electron impact excitation of the upper level $\mathrm{d}\,^3\Pi_{\mathrm{u}}$ together with vibrationally resolved transition probabilities $A_{\mathrm{d\,a}}^{\nu'\nu''}$ for spontaneous emission to the lower level $\mathrm{a}\,^3\Sigma_{\mathrm{g}}^+$ the entire, but relative, emission of the Fulcher system $\epsilon_{\mathrm{Ful}}^{\mathrm{rel}}$ can be calculated. Taking the sum over the first four diagonal bands $(\mathrm{d}\,^3\Pi_{\mathrm{u}}, \nu') \rightarrow (\mathrm{a}\,^3\Sigma_{\mathrm{g}}^+, \nu'' = \nu')$ as the reference for the relative Fulcher emission yields a factor $f_{\mathrm{Ful}}(T_{\mathrm{vib}})$ for the extrapolation of measured emissions to the absolute Fulcher emission:

$$\epsilon_{\mathrm{Ful}} = \left(\sum_{\substack{\nu'=0,1,2,3 \\ \nu''=\nu'}} \epsilon_{\mathrm{d\,a}}^{\nu'\nu''} \right) \cdot f_{\mathrm{Ful}}(T_{\mathrm{vib}}) \ . \tag{6.46}$$

The particular emissivity $\epsilon_{\mathrm{d\,a}}^{\nu'\nu''}$ is thereby determined after equation (6.44) from the Q1 line (Q2 for deuterium) of the corresponding vibronic band using the

rotational temperature $T_{\mathrm{rot}}^{\mathrm{d}\,\nu'}$ which in turn is determined after equation (6.42) from the appropriate first five Q lines. The applied scaling factors $f_{\mathrm{Ful}}(T_{\mathrm{vib}})$ in this work for hydrogen and deuterium can be found in appendix B.3 after [Die10].

6.6.2 Collisional-radiative model for atomic hydrogen

The emission of atomic hydrogen can be used to determine the electron temperature and the densities of particular hydrogen species. The latter possibility arises from collision processes of these species with electrons or other species, which result in electronically excited hydrogen atoms. The evaluated electron temperature is referred to as '$T_{\mathrm{e}}^{\mathrm{OES}}$' to distinguish it from '$T_{\mathrm{e}}^{\mathrm{probe}}$': since the excitation energies of electronic levels of the hydrogen atom are higher (above 10 eV) than the typical electron energy range that is accessible via probe measurements (below 10 eV), $T_{\mathrm{e}}^{\mathrm{OES}}$ describes the high energy part of the EEDF and thus it does not necessarily coincide with $T_{\mathrm{e}}^{\mathrm{probe}}$.

For modeling the population densities of the excited states of the hydrogen atom the collisional radiative model *Yacora H* [WDF09] with latest extensions by [Wün12] is applied. The CR model solves the coupled non-linear balance rate equations for the electronic states of atomic hydrogen with principal quantum numbers $n = 1, \ldots, 40$ ($\equiv$ state i) and calculates so-called *population coefficients* $R_{\mathrm{s}i}$. These relate the density of the excited state i to the electron density n_e and the density n_{s} of a particular species s and are, among others, dependent on the electron temperature and density. The equilibrium density n_i is thus determined by

$$n_i = n_{\mathrm{e}} \sum_{\mathrm{s}} n_{\mathrm{s}}\, R_{\mathrm{s}i}(T_{\mathrm{e}}, n_{\mathrm{e}}, \ldots) \; . \tag{6.47}$$

In the CR model Yacora H basically each hydrogen species is considered for the determination of the population densities of the atomic states, i. e. atomic hydrogen H, molecular hydrogen H_2, the hydrogen ions H^+, H_2^+ and H_3^+ and the negative ion H^-. In table 6.4 the integrated excitation and de-excitation channels are compiled. Information on the corresponding cross sections or rate coefficients can be found in [WDF09, Wün12, ESOS95] and in [BF00] for the reabsorption (4) of resonance emission in the Lyman series. The main extension to the model described in [WDF09] is the implementation of separate reactions (12) and (13) for the mutual neutralization of negative ions with H^+ and H_2^+, respectively [Wün12, ESOS95].

Table 6.4: *Population and de-population channels for the excited states of atomic hydrogen (principal quantum number parameterized by i, k) considered in the CR model Yacora H [WDF09, Wün12].*

Electron impact excitation	$\mathrm{H}(k) + \mathrm{e}^- \longrightarrow \mathrm{H}(i>k) + \mathrm{e}^-$		(1)
Electron impact de-excitation	$\mathrm{H}(i) + \mathrm{e}^- \longrightarrow \mathrm{H}(k<i) + \mathrm{e}^-$		(2)
Spontaneous emission	$\mathrm{H}(i) \longrightarrow \mathrm{H}(k<i) + \mathrm{h}\nu$		(3)
Reabsorption	$\mathrm{H}(1) + \mathrm{h}\nu \longrightarrow \mathrm{H}(i)$		(4)
Ionization	$\mathrm{H}(i) + \mathrm{e}^- \longrightarrow \mathrm{H}^+ + 2\mathrm{e}^-$		(5)
Three-body recombination	$\mathrm{H}^+ + 2\mathrm{e}^- \longrightarrow \mathrm{H}(i) + \mathrm{e}^-$		(6)
Radiative recombination	$\mathrm{H}^+ + \mathrm{e}^- \longrightarrow \mathrm{H}(i) + \mathrm{h}\nu$		(7)
Dissociative excitation	$\mathrm{H}_2 + \mathrm{e}^- \longrightarrow \mathrm{H}(i) + \mathrm{H}(1) + \mathrm{e}^-$		(8)
Dissociative excitation	$\mathrm{H}_2^+ + \mathrm{e}^- \longrightarrow \mathrm{H}(i) + \mathrm{H}^+ + \mathrm{e}^-$		(9)
Dissociative recombination	$\mathrm{H}_2^+ + \mathrm{e}^- \longrightarrow \mathrm{H}(i) + \mathrm{H}(1)$		(10)
Dissociative recombination	$\mathrm{H}_3^+ + \mathrm{e}^- \longrightarrow \mathrm{H}(2) + \mathrm{H}_2$		(11)
Mutual neutralization	$\mathrm{H}^- + \mathrm{H}^+ \longrightarrow \mathrm{H}(i) + \mathrm{H}(1)$		(12)
Mutual neutralization	$\mathrm{H}^- + \mathrm{H}_2^+ \longrightarrow \mathrm{H}(i) + \mathrm{H}_2$		(13)

The population coefficient for the heavy particle collisions, i. e. the mutual neutralization reactions (12) & (13), can be separated from the sum in equation (6.47) and converted into a form R'_{si} which then allows to evaluate the population density of the excited state i with the additional dependence of both the heavy particle densities involved in the heavy particle collisions [Wün12]:

$$n_i \;=\; n_\mathrm{e} \sum_{\mathrm{s} \neq \mathrm{H}^-} n_\mathrm{s}\, R_{\mathrm{s}i} \;+\; n_{\mathrm{H}^-} \left(n_{\mathrm{H}^+} R'_{\mathrm{H}^- i} + n_{\mathrm{H}_2^+} R''_{\mathrm{H}^- i} \right) \;. \tag{6.48}$$

The emissivity of the transition $i \to k$ can then be calculated via equation (3.10) with the transition probabilities given in [KRRN13]. Analogously to the emission rate coefficient of the (extended) corona model, equation (6.19), an *effective* emission rate coefficient $X^{\mathrm{eff}}_{\mathrm{em},ik}$ can now be defined which, besides the electron temperature, is also depending on the electron density and the density of all the species (and in general additionally on their temperatures):

$$\epsilon_{ik} = n_i A_{ik} \overset{(6.48)}{=:} n_\mathrm{e} n_\mathrm{H} X^{\mathrm{eff}}_{\mathrm{em},ik}(T_\mathrm{e}, n_\mathrm{e}, \{n_\mathrm{s}\}, \ldots) \;. \tag{6.49}$$

Hence, the atomic hydrogen emission on the left-hand side can be used as diagnostic for the plasma parameters n_e, T_e and n_H on the right-hand side as well as for an assessment of the densities $\{n_\mathrm{s}\}$. Among the transition series of the hydrogen atom the Balmer series is spectroscopically accessible and is thus used for this

purpose: the modeled emission from the Balmer lines H_α to H_δ as well as their paired line ratios H_α/H_β, H_β/H_γ and H_γ/H_δ are matched to the measurements by varying the plasma parameters and the densities of the hydrogen species. Therefore, the electron density n_e is taken from probe measurements and the evaluation of the atomic hydrogen density n_H is described in the succeeding section 6.6.3. Thus, the parameter space which is to be solved consists of T_e, n_{H^+}, $n_{H_2^+}$, $n_{H_3^+}$ and n_{H^-}. To facilitate this multi-dimensional problem, the influence of particular species on the emission of the Balmer series is analyzed in the following.

In figure 6.15 the population coefficients for the state $n = 3$ (part (a)) and the corresponding effective emission rate coefficient for the H_α line ($n = 3 \rightarrow n = 2$) (part (b)) are shown exemplarily. For the latter the particular contributions from the specific species, which arise from the sum in equation (6.48) inserted in equa-

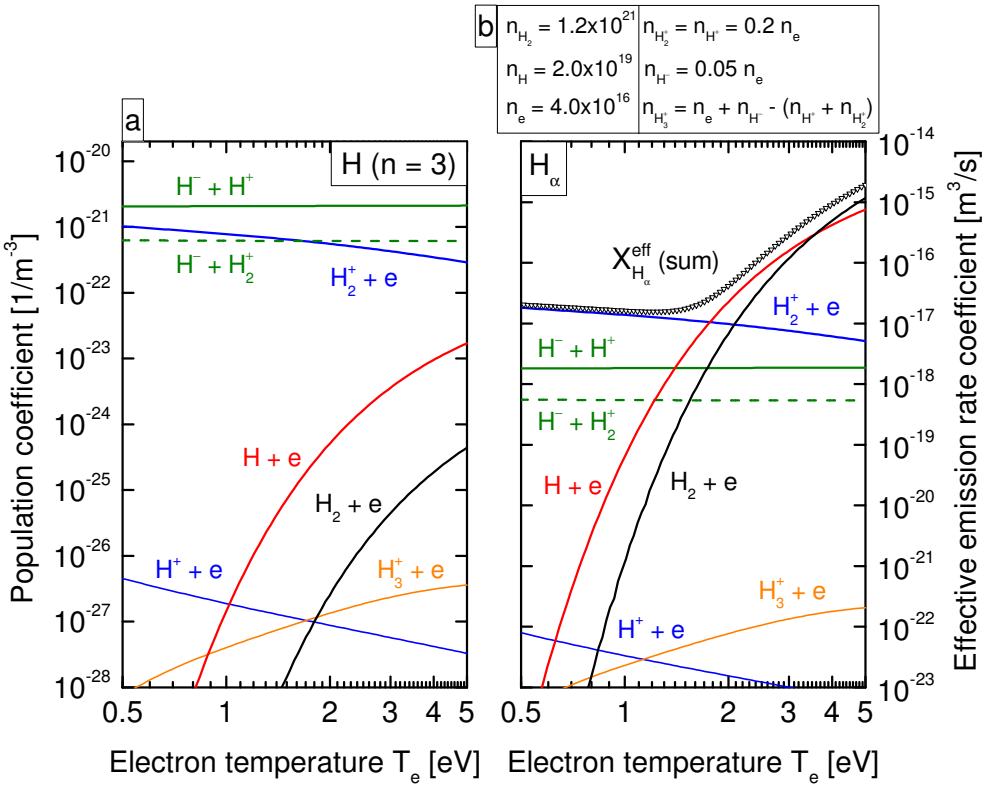

Figure 6.15: (a) *Population coefficients (in the conception of equation* (6.48)*) for the state $n = 3$ of atomic hydrogen calculated with the CR model Yacora H [WDF09, Wün12] for an electron density of 4×10^{16} m^{-3}.* **(b)** *Corresponding effective emission rate coefficients for the H_α line after equation* (6.49) *for the denoted particle densities on top of the figure, given in units of m^{-3}. $X^{\mathrm{eff}}_{H_\alpha}$ is the sum of the particular contributions.*

tion (6.49), are itemized additionally. The densities required for the calculation of the effective emission rate coefficients denoted on top of part (b) are representative values for the present investigations.

It can be seen that despite the large population coefficients of the mutual neutralization processes (12) & (13) their relevance for the absolute emission is diminished due to the low particle densities involved. Hence, dissociative recombination of H_2^+ (10) is the decisive reaction at low electron temperatures (dissociative excitation of H_2^+ (9) is less relevant due to the low T_e), whereas dissociative excitation of H_2 (8) and the processes coupled to atomic hydrogen (1)–(5) show a steep dependence on the electron temperature and are the crucial population channels at higher T_e. Radiative or three-body recombination of H^+ (6) & (7) as well as dissociative recombination of H_3^+ (11) can be neglected as contributions to the H_α line. These general observations on the relevance of the different population channels can in principle also be transferred to the other lines of the Balmer series.

Hence, the density of H^+ is only relevant if also negative ions are present in the discharge and the density $n_{H_3^+}$ can already be omitted from the set of parameters to be solved, as its value has no influence on the Balmer emission. Instead, $n_{H_3^+}$ can be used to fulfill quasineutrality.

Influence of the molecular ion H_2^+

Figure 6.16 (a) shows the effective emission rate coefficients for the Balmer series at $T_e = 2\,\mathrm{eV}$ considering only the processes coupled to the hydrogen atom and to the molecular ion H_2^+. With increasing molecular ion density the emission coefficient and thus the emission increases, where the influence increases with higher principal quantum number. In part (b) the paired ratios of the emission rate coefficients are shown, which after equation (6.49) equal the corresponding line ratios. The differing impact on different principal quantum numbers leads to decreasing line ratios with increasing molecular ion density whereas obviously H_α/H_β is affected most. This steep dependence can be used in the course of matching modeled and measured values, since slight variations of $n_{H_2^+}$ have a large influence on H_α/H_β but only a slight influence on the absolute emission compared to a variation of the electron temperature (around $T_e = 2\,\mathrm{eV}$, which is the relevant range for the laboratory setup).

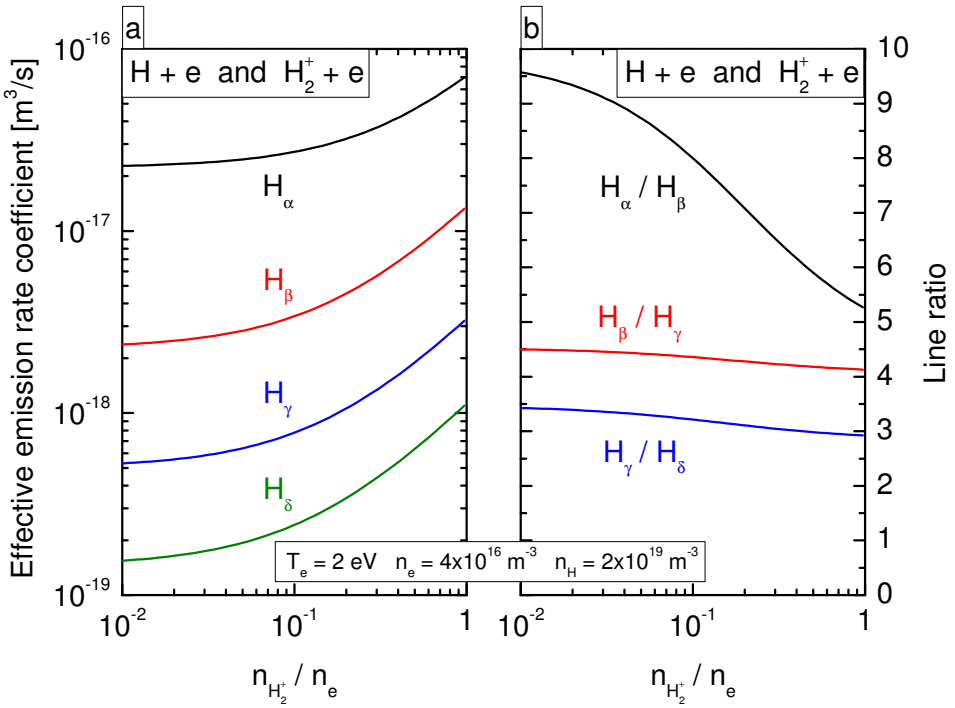

Figure 6.16: (a) *Effective emission rate coefficients for the first four Balmer lines depending on the ratio of the molecular ion density to the electron density. Only processes coupled to H and H_2^+ are taken into account.* **(b)** *Ratios of the rate coefficients of part (a).*

Influence of negative ions H^-

The effects of negative ions within the discharge on the line ratios can be seen in figure 6.17. Part (a) shows the line ratios determined from coupling to the hydrogen atom and to negative ions for both mutual neutralization (MN) reactions with increasing negative ion density. The charge exchange with the hydrogen ion H^+ (solid lines) only influences the line ratio H_α/H_β yielding higher values as predominantly the state $n = 3$ is populated via this reaction [ESOS95]. Considering the neutralization of H^- with the molecular ion H_2^+ (dashed lines) leads to decreasing line ratios for H_α/H_β and H_β/H_γ whereas H_γ/H_δ is again virtually unaffected. This behavior arises from the increasing population of states with higher principal quantum numbers via the MN reaction with H_2^+ [ESOS95].

Conclusively, the influence of negative ions on the line ratios depends on the composition of the positive ions. This is shown in part (b) of figure 6.17 where for a constant negative ion density of $n_{H^-}/n_e = 0.05$ the density ratio $n_{H^+}/n_{H_2^+}$ is varied (whereas the sum $n_{H^+} + n_{H_2^+}$ is held constant). The left end of the x-axis corresponds to the case of MN with H_2^+ only whereas the right end represents

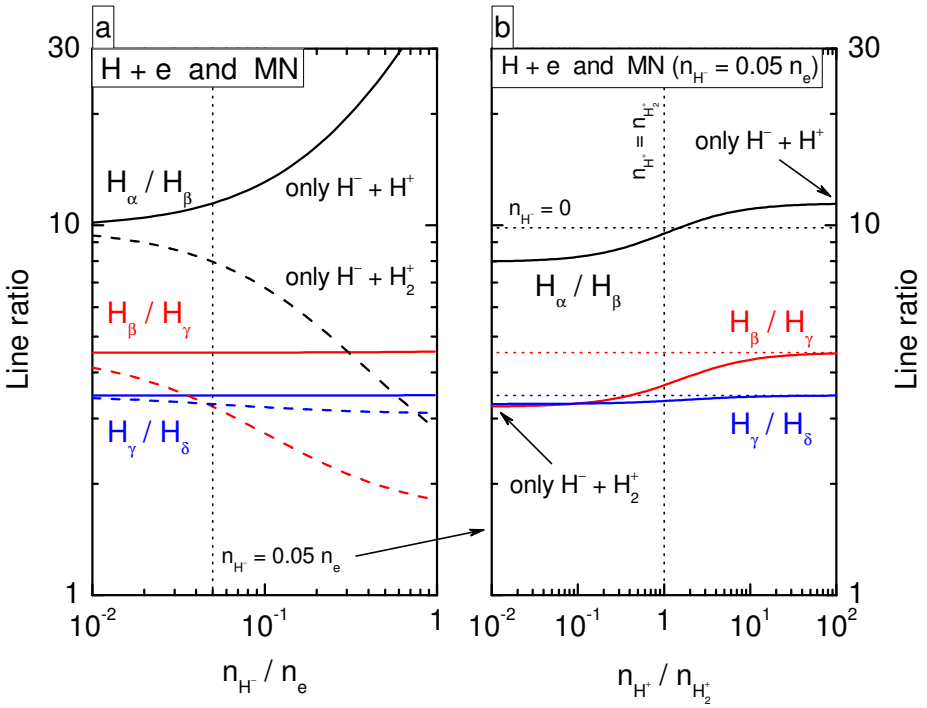

Figure 6.17: **(a)** *Line ratios influenced by the mutual neutralization reactions (MN with H^+: solid lines; MN with H_2^+: dashed lines) with increasing ratio of the negative ion density to the electron density. T_e, n_e and n_H as in figure 6.16, n_{H^+} and $n_{H_2^+}$ equal 0.4 n_e, respectively.* **(b)** *Influence of MN on the line ratios at varying positive ion composition for constant $n_{H^-} = 0.05\,n_e$ and $n_{H^+} + n_{H_2^+} = 0.4\,n_e$.*

MN with solely H^+. Additionally the line ratios for negligible negative ion density are illustrated with dotted horizontal lines. H_γ/H_δ is almost unaffected by the presence of negative ions, independently of the positive ion composition. H_β/H_γ shows an interference by negative ions only at low values of $n_{H^+}/n_{H_2^+}$. For H_α/H_β a variation of the positive ion composition yields a transition from a decreasing to an increasing line ratio as consequence of negative ions. This behavior arises from the different influences of the two MN reactions resulting in contrary trends of the line ratio. For $n_{H^+} = n_{H_2^+}$ the line ratio H_α/H_β is almost unaffected and the value for infinitesimal negative ion density is obtained.

Hence, if H^+ is the dominant positive ion, only the line ratio H_α/H_β is influenced by negative ions. Since in this case also the influence of dissociative recombination or excitation of H_2^+ is less pronounced, H_α/H_β can be used as diagnostic for the negative hydrogen ion density. This approach is described in detail in [FW06b].

On the other hand, if the densities of H^+ and H_2^+ are comparable, the MN reactions only affect the line ratio H_β/H_γ. Hence, like the correlation of the

molecular ion density $n_{H_2^+}$ with the line ratio H_α/H_β, the modeled line ratio of H_β/H_γ can be matched to the measurement, if $n_{H^+} \approx n_{H_2^+}$ is assumed and the negative ion density n_{H^-} is varied.

Determination of plasma parameters by means of Yacora H using the Balmer series

Summarizing, the species H, H_2, H^+, H_2^+ and H^- can have an influence on the Balmer emission, whereas $n_{H_3^+}$ can be used to fulfill quasineutrality. The density of the hydrogen gas n_{H_2} is calculated from the absolute pressure and the gas composition of the discharge using the gas temperature from molecular spectroscopy (see section 6.6.1) and n_H is determined as described in section 6.6.3. Furthermore, the ratio $n_{H^+}/n_{H_2^+}$ needs to be known for the assessment of the influence of negative ions on the emission. The ratio is accessible via ion mass spectrometry or has to be assessed via dissociation and ionization models. From measurements in a setup equivalent to the present experiment [Ert10] accompanied by modeling [Wün04], $n_{H^+} \approx n_{H_2^+}$ can be assumed for the present plasma parameters. Hence, the following scheme can be pursued:

- The electron density n_e is taken from the probe measurements and kept constant.
- Taking n_{H_2}, n_H and T_{gas} as described above and setting $n_{H^+} = n_{H_2^+} = n_{H^-} = 0$, a preliminary electron temperature T_e^{OES} is determined from the measured emissivities of the Balmer lines H_α to H_δ after equation (6.49).
- Via increasing the **molecular ion density** $n_{H_2^+}$ the line ratio H_α/H_β is matched without influencing the other line ratios.
- $n_{H^+} = n_{H_2^+}$ can be applied without consequences, since the density of H^+ has no influence on the Balmer emission as long as $n_{H^-} = 0$.
- Via increasing the **negative ion density** n_{H^-} the line ratio H_β/H_γ can be matched without influencing the already determined line ratio H_α/H_β. The line ratio H_γ/H_δ should still be virtually unaffected.
- $n_{H_3^+}$ is adapted to fulfill quasineutrality, since it has no influence on the Balmer emission.
- Finally, the **electron temperature** needs to be readjusted and the procedure is performed iteratively.

Applicability for D_2 plasmas

Since the CR model is designed for the hydrogen atom H [WDF09, Wün12], some remarks have to be made, if application to deuterium discharges is intended.

The slight variations of the atomic energy levels, which lead to the shifted wavelengths of the Balmer series for deuterium compared to hydrogen, are not expected to have a significant impact on the electronic excitation processes. Furthermore, the probabilities for optical transitions are virtually equal [KRRN13]. Thus, the processes coupled to the atomic ground state (H + e) can be transferred directly to deuterium. In contrast, the energies of vibrational and rotational states of molecules are dependent on the nuclear masses. Therefore, cross sections or rate coefficients for molecular processes as well as for processes coupled to molecular ions might vary among the isotopes. However, since the cross sections or rate coefficients are not always available for D_2 in the literature and furthermore no substantial modifications to the data for H_2 are to be expected, no separate model for deuterium is established yet. Nevertheless, some remarks have to be made for particular reactions:

Dissociative excitation from H_2/D_2 The cross sections for excitation of the Balmer series due to electron impact on molecular hydrogen and deuterium can be found in [MHL77] showing lower cross sections for deuterium over the entire electron energy range. Therefore applying the present CR model to deuterium leads to an overestimation of the dissociative excitation (DE) channel. In general this could lead to the determination of too low electron temperatures or too low particle densities of other species. The absolute error depends on the actual share of DE for the population of excited states.

Dissociative recombination from H_2^+/D_2^+ Comparative cross sections for this population channel can be found in [NTN87, Tak02]. The given cross sections are resolved for the initial vibrational level of the molecular ion. However, if the effective cross sections are estimated[9] almost no dependency on the isotope can be observed. Hence, the error of applying the hydrogen input data of this channel for deuterium should be negligible.

Mutual neutralization with H_2^+/D_2^+ No information on isotopic differences of this reaction are available in the literature why the uncertainty of using the hydrogen data for deuterium cannot be assessed.

[9] The weighted sum of the vibrationally resolved cross sections is calculated using an exemplary vibrational population distribution according to a vibrational temperature of 4000 K.

6.6.3 Determination of the H/H_2 density ratio

The combination of a collisional radiative model for the electronic states of molecular hydrogen, Yacora H_2 [Wün04, WN11, Wün12], and the CR model Yacora H is used to determine the density ratio n_H/n_{H_2} of atomic and molecular hydrogen. While the former model is used to calculate the absolute density n_d of the upper state of the Fulcher transition, the latter computes the population densities n_i of the atomic excited states:

$$n_i = n_e n_H R_{Hi} \tag{6.50a}$$

$$\text{and} \quad n_d = n_e n_{H_2} R_{H_2d} \ , \tag{6.50b}$$

where R_{H_2d} is the population coefficient of the upper state $d\,^3\Pi_u$ of the Fulcher emission coupled to the hydrogen molecule and R_{Hi} is the population coefficient of the excited atomic state i coupled to the hydrogen atom. For the current diagnostic purpose, the coupling to other species (H_2, H^+, H_2^+, H_3^+ and H^-) and reabsorption of the resonance lines is neglected at first to minimize the number of unknown parameters.

Using equation (3.10), the atom-to-molecule density ratio n_H/n_{H_2} can be determined via the measured emission of the Fulcher system ϵ_{Ful} and a specific Balmer line ϵ_{Bal}:

$$\frac{\epsilon_{Bal}}{\epsilon_{Ful}} = \frac{n_i A_{Bal}}{n_d A^{eff}_{Ful}} \quad \overset{(6.50)}{\Longrightarrow} \quad \frac{n_H}{n_{H_2}} = \frac{\epsilon_{Bal}}{\epsilon_{Ful}} \left(\frac{R_{Hi} A_{Bal}}{R_{H_2d} A^{eff}_{Ful}} \right)^{-1} = \frac{\epsilon_{Bal}}{\epsilon_{Ful}} \left(\frac{X^{eff}_{Bal}}{X^{eff}_{Ful}} \right)^{-1} \ , \tag{6.51}$$

where A_{Bal} and A^{eff}_{Ful} are the corresponding transition probabilities (for the Fulcher system an effective value has to be used which is determined as a weighted sum of the vibrationally resolved values [FW06a]), X^{eff}_{Bal} is the effective emission rate coefficient of the particular Balmer line as defined in equation (6.49) and X^{eff}_{Ful} is the effective emission rate coefficient for the Fulcher transition, which is analogously connected to the population coefficient R_{H_2d}. The measured absolute emission of the Fulcher system is thereby determined after equation (6.46) and the values for the A_{Bal} and A^{eff}_{Ful} can be found in [KRRN13] and [FW06a], respectively.

For this evaluation simply the measured emissions of molecular and atomic hydrogen would be required. However, as presented in section 6.6.2, the atomic states are influenced by further excitation channels which were initially neglected for equation (6.51). Their influences are discussed in the following.

Reabsorption of the resonance Lyman series leads to enhanced population of the upper levels of the Balmer series [BF00]. This effect, which is called opacity, is

dependent on the atomic hydrogen density. Since this is the value to be obtained from the present diagnostic, its influence cannot be assessed a priori and a Balmer line has to be chosen which is not strongly affected. The impact of opacity on the population density of the atomic hydrogen levels decreases with increasing principal quantum number. On the other hand, the population density as well as the transition probability decreases with increasing quantum number. Therefore, usually the H_γ line is used as it constitutes the compromise between emission intensity and interference by opacity. [BF00]

Furthermore, the species H_2, H^+, H_2^+ and H^- can be relevant for the population density of the upper Balmer level. However, the actual influence on the Balmer emission is assessed with the CR model Yacora H, for which the atomic hydrogen density is to be used as input parameter. Thus, as mentioned, the coupling with theses species is neglected at first and the potential impact on n_H is determined afterwards. Via an iterative procedure, a consistent picture can be gained. However, it turned out, that the recursive influence on the determined value of n_H is mostly negligible.

Figure 6.18 shows the ratio of the effective emission rate coefficients for the H_γ line and the Fulcher system calculated with the corresponding CR models Yacora H and H_2 considering only the coupling to the corresponding ground states H and H_2. The ratio is almost independent of electron temperature and density in the relevant parameter space of the present investigations and lies between

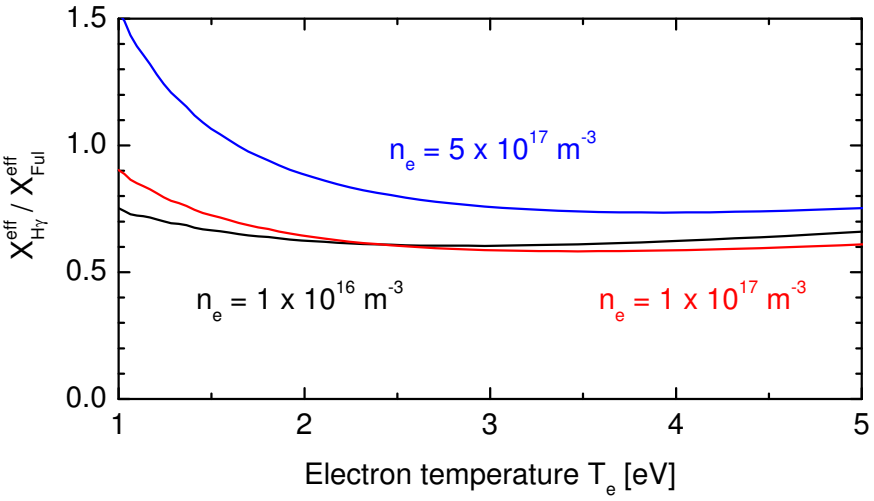

Figure 6.18: *Ratio of the effective emission rate coefficients for the H_γ line and the Fulcher system calculated with the corresponding CR models Yacora H [WDF09] and H_2 [Wün04, WN11, Wün12] for different electron densities n_e.*

0.6 and 0.7 for $10^{16}\,\mathrm{m}^{-3} \leq n_\mathrm{e} \leq 10^{17}\,\mathrm{m}^{-3}$. Thus, the atomic hydrogen density can easily be determined via equation (6.51) and serves as input parameter for the analysis of the Balmer series with the CR model Yacora H.

6.6.4 Parameters for OES measurements

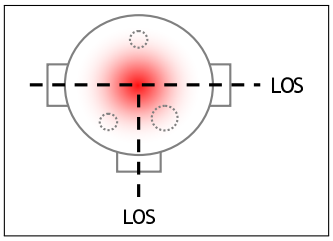

Quantitative spectroscopy for the determination of plasma parameters is performed by means of the spectrometers with higher resolution (SPEX and Acton, horizontal LOS). Each time the full set of emission lines is recorded including the Balmer series (H_α–H_δ) and the 20 required ro-vibronic transition lines from the Fulcher system (Q1–Q5 for $\nu' = 0, 1, 2, 3 \rightarrow \nu'' = \nu'$). Recording the entire set takes about five minutes, whereas typically measurements are taken every half an hour.

Furthermore, the plasma emission is monitored by means of the survey spectrometer (Plasus, vertical LOS), which records the following time traces at a recording interval of 500 ms: the Balmer series of the hydrogen atom, the Fulcher emission of the hydrogen molecule and the D_2 line of the caesium atom or particluar lines of the $2p \rightarrow 1s$ system of the xenon atom.

Measurement errors

As described in section 5.2, the uncertainty for the determination of emissivities with the present spectrometers is about 10 %. Together with the uncertainties of the evaluation of rotational temperatures via linear regressions (equation (6.42), $\pm\,10\,\mathrm{K}$) and of the evaluation of the vibrational temperature ($\pm\,500\,\mathrm{K}$) a typical error for the extrapolated entire Fulcher emission of about $\pm\,13\,\%$ can be estimated. The gas temperature can be given to $\pm\,20\,\mathrm{K}$.

Taking the effective emission rate coefficients in equation (6.51) for granted, the uncertainty of the H/H_2 density ratio can be estimated to $\pm\,23\%$. However, the consideration of coupling to further species can introduce further uncertainties, which cannot be assessed from a theoretical point of view.

The accuracy of the analysis of the Balmer series by means of the CR model Yacora H cannot be assessed either due to the multitude of input parameters, their interactions and the iterative evaluation. However, taking the evaluated densities for granted, the determined electron temperature has an uncertainty of maximal $\pm\,0.1\,\mathrm{eV}$ at an absolute T_e value of 2 eV.

6.7 Overview of the procedure to evaluate plasma parameters

Summarizing, figure 6.19 illustrates the interaction of the different diagnostics in plasma operation to obtain the plasma parameters. The direct input parameters are shaded in bright blue, i. e. the probe characteristic, the emissivities and the absorption signal. The major parameters that are evaluated by this scheme are shaded in orange. Dashed lines represent paths, that are only rarely pursued or which have only limited influence on the target diagnostic.

The recording of all the input parameters takes about 10 minutes in maximum. Thus, for Cs seeded hydrogen and deuterium plasmas the plasma conditions need to be constant at least over this time period. Therefore, a stable Cs source and a well-conditioned experiment are indispensable. Via the survey spectrometer the plasma emission is monitored and the appropriate moment to start the measurements can be identified.

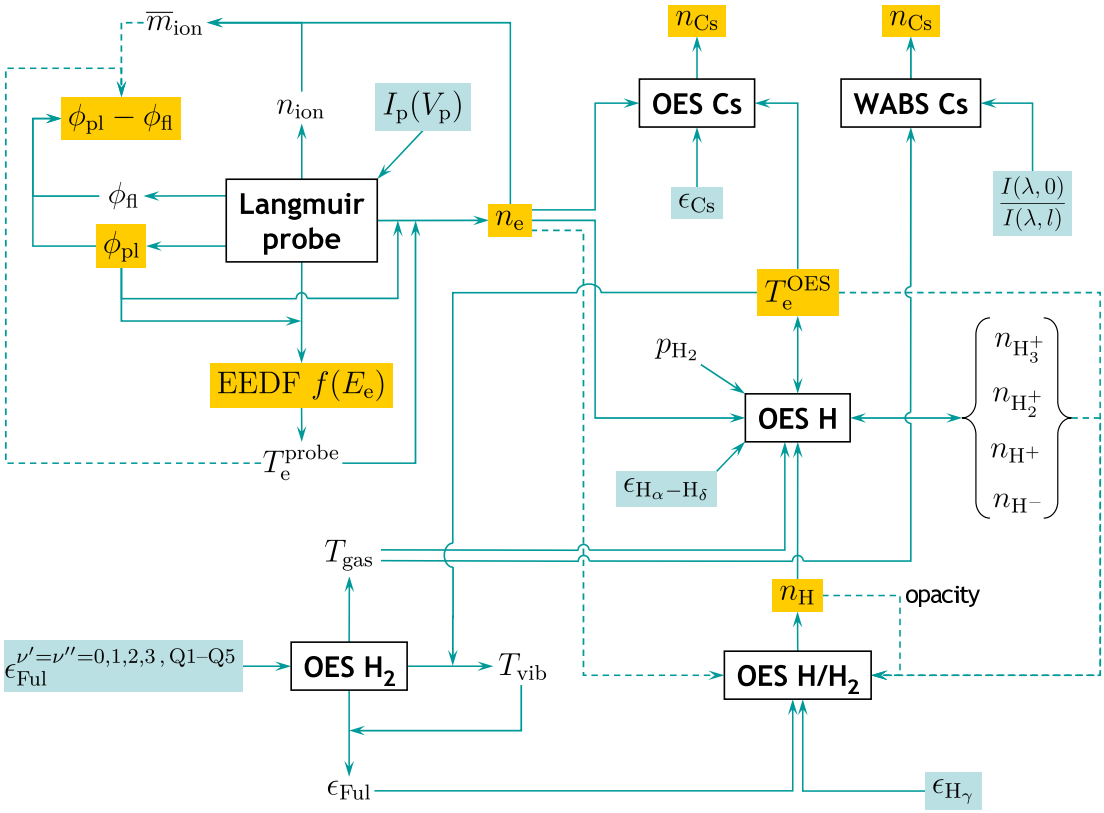

Figure 6.19: *Scheme of the procedure to evaluate plasma parameters using the interplay of the Langmuir probe and the optical emission and absorption spectroscopy.*

7 The caesium source: Cs dispenser oven

Systematic investigations on the Cs dynamics require a reliable Cs source which is capable of a stable and adjustable evaporation of caesium for several hours. In order to investigate transient phenomena as well as conditions similar to negative ion sources the target parameters are reliably adjustable evaporation rates between some µg/h and more than 10 mg/h generating Cs densities of up to $10^{16}\,\mathrm{m}^{-3}$ in vacuum as well as in plasma operation.

At the IPP NNBI ion sources, Cs ovens are used, which are based on the thermal evaporation of pure caesium [SFF+06, FGW10]. Glass ampules filled with 1 g of liquid caesium serve as the Cs reservoir. However, application of these ovens is unfavorable for the present investigations: Firstly, the evaporation rate is solely adjustable via the temperature of the oven, which results in limited controllability of the evaporation rate due to the thermal inertia. However, investigation of transient phenomena, e. g. the beginning layer growth on a sample surface, requires finely adjustable evaporation rates. Moreover, a device for measuring the actual evaporation rate is desirable. Secondly, the pure Cs reservoir is very susceptible to contamination by impurities due to the high chemical reactivity of Cs. The resulting formation of Cs compounds might result in uncontrollable evaporation, which has to be prevented to obtain stable conditions. Thirdly, the laboratory setup needs to be vented regularly to install or exchange equipment. Contact with ambient air would rapidly corrupt the Cs reservoir and the remaining Cs content would be lost. Thus, the system could only be vented, if most of the Cs is already evaporated and chemically bound at the vessel walls. Assuming a mean evaporation rate of 1 mg/h and a daily evaporation of 7 hours, depletion of the Cs reservoir would take more than half a year, which is unacceptable for the envisaged flexibility of the laboratory setup. Furthermore, great efforts considering the safety would have to be made, if a system with 1 g of pure Cs would be in use in the laboratory.

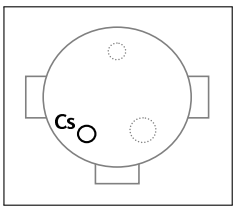

Hence, within the framework of this thesis a Cs source is developed, which is based on an alloy dispenser from Alvatec as Cs reservoir [Alv10] integrated in an oven with an all-metal blocking valve and a surface ionization detector at the oven nozzle to measure the evaporation rate. The oven design is described in detail in [FFF12] and is shown in figure 7.1. The oven is flanged to the main vessel from below via a port of the bottom plate, the nozzle of the oven being about 2 cm above the bottom plate.

The dispenser, a photograph of which is also shown in figure 7.1, is the actual caesium source. It consists of a stainless steel sleeve filled with a caesium-bismuth alloy (Bi_2Cs) which is chemically stable at room temperature and thus, it can be handled safely and is not susceptible to contamination by impurities. Both ends of the sleeve are crimped and at the side of the sleeve a small slit serves as caesium outlet. Argon is filled up as buffer gas and indium serves as sealing of the dispenser. If the dispenser is heated to about 160 °C, e. g. by ohmic heating using a current of 3 A flowing through the dispenser, the indium sealing melts and the buffer gas is released ('activation process'), which can be monitored with the RGA, as shown in figure 7.5. Further heating of the dispenser leads to decomposition of the alloy and the evaporation of pure caesium (5–10 A). The evaporation rate is then finely adjustable via the heating current and thus the evaporation rate of the Cs source can be regulated separately from the oven temperature.

For the present investigations dispensers with a content of 100 mg caesium are used, which is a compromise between a sufficiently long evaporation time and a manageable Cs content within the system. Within the present investigations the dispenser needed to be exchanged once a month for pure vacuum operation and once a week for pure plasma operation, which gives the opportunity for systematic investigations without breaking the vacuum on the one hand, and precludes excessive amounts of Cs within the system on the other hand.

The dispenser is mounted via metallic luster terminals at the electrical vacuum feedthrough serving as the 'back flange' of the oven. Thus, the dispenser is positioned in the 'body' of the oven. Evaporation of caesium into the experiment is conducted through the valve and the duct. Therefore, the oven has to be held at elevated and homogeneous temperatures, to prevent adsorption of Cs at the oven surfaces as far as possible. Furthermore, large temperature gradients would lead to excessive accumulation of caesium at cold spots followed by uncontrolled evaporation, which has to be prevented for a reliable operation. This is achieved

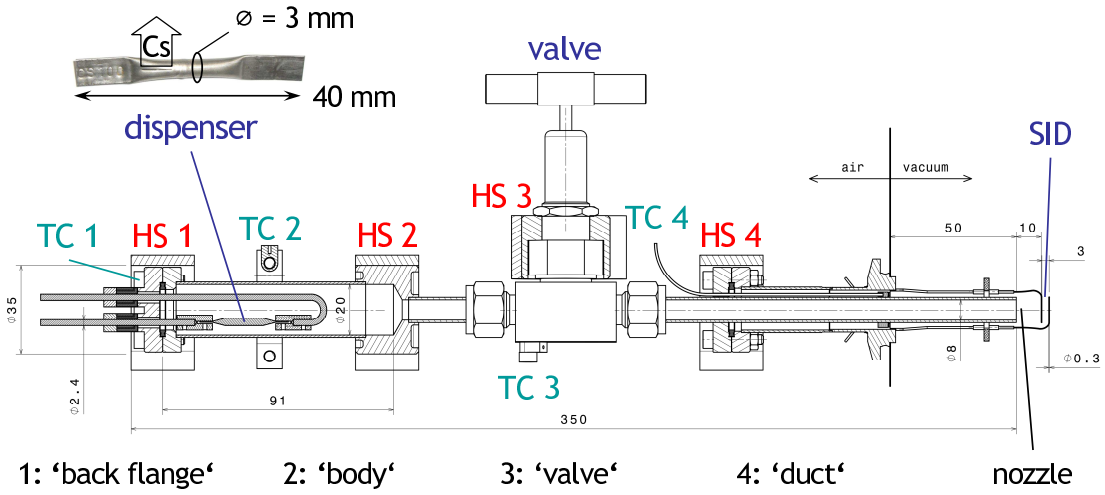

Figure 7.1: *Drawing of the dispenser oven including dimensions in mm and a photograph of the dispenser. The numbered heating sleeves ('HS') and thermocouples ('TC') are called as denoted beneath the drawing throughout the work.*

by the all-metal construction of the oven and four heating sleeves (denoted as 'HS' in the figure). The temperature distribution is measured with thermocouples (denoted as 'TC') at four positions along the oven (TC 4 is actually located at the vacuum flange denoted with 'air/vacuum'). Via feedback control it is possible to maintain a temperature deviation of less than 5 °C at absolute temperatures of typically 260 °C.

The integrated valve (available commercially) performs three functions. Once the dispenser is activated it is sensitive to contamination by impurities. Therefore, the valve can firstly be used to separate the body of the oven from the main experiment vessel if it is necessary to vent the vessel for maintenance or changes of the equipment. Secondly, the valve gives the opportunity for an instantaneous shutdown of the evaporation and an equally fast recovery. Precisely the latter would not be possible if the evaporation is stopped via turning off the heating current. Thirdly, if the dispenser has to be exchanged, closing the valve gives the opportunity for maintaining the vacuum and thus the Cs conditioning of the main experiment vessel. The latter describes the covering of the vessel surfaces by chemically bound Cs and can be altered due to Cs evaporation, plasma treatment and impurity exposition for instance. The condition of the vessel walls can have a direct influence on the vacuum and plasma dynamics via its influence on adsorption and desorption processes of Cs. Thus, measurements are only comparable if they are obtained under the same Cs conditioning, why it is beneficial to maintain its state as far as possible.

7.1 The oven SID

At the oven nozzle a surface ionization detector (SID) is mounted for in situ measurements of the evaporation rate. The basic functionality of SIDs is described in section 6.1 whereas the instrumentation of the so-called *oven SID* is shown in figure 7.2. Heating currents of 3 A and a bias of 50 V are used for this SID. The Cs ion current is measured via a Keithley 6487 Picoammeter and recorded continuously by a dedicated LabView program with a temporal resolution of about 4 s.

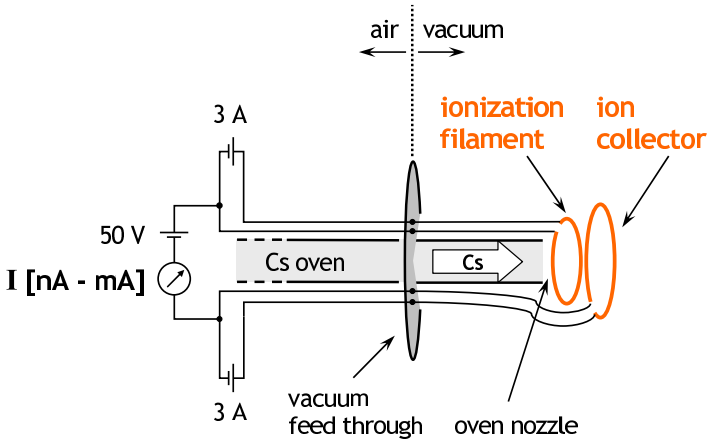

Figure 7.2: *Instrumentation of the oven SID.*

After equation (6.2) the measured SID signal in [A] can be calibrated to the actual Cs flux onto the device in $[m^{-2}s^{-1}]$. Due to the position of the oven SID, this value can furthermore be connected to the evaporation rate of the oven in [mg/h]:

Assuming a homogeneous evaporation out of the oven after the cosine law, the share of the total Cs flux reaching the ionization filament can be calculated considering conservation of mass and the geometry of the SID relative to the oven nozzle. Further, an ionization probability of $P_{\text{ion}} = 1$ can be expected, as the heating current of 3 A leads to filament temperatures exceeding 1100 °C, and the probability for the ions to reach the ion collector can be assumed to be $P_{\text{bias}} = 1$, since the electrical field between the two wires can be seen as a simple dipole field. Hence, using equation (6.2), a calibration value of 0.13 (mg/h)/µA can be determined. However, the motion of the Cs ions from the ionization filament to the ion collector is likely to be interrupted by collisions with gas particles or the vessel walls, which leads to a value of P_{bias} of below unity. The determined calibration value is thus most probably a lower limit.

Additionally, another approach to the calibration can be done empirically using the direct proportionality between the measured SID signal and the incoming/evaporated Cs flux. Knowing the total amount of evaporated caesium, e. g. via weighing the dispenser before and after use, and integrating the entire SID current over time, the cumulated value in units of [µA h] corresponds to the evaporated mass of caesium in [mg]. This was performed after depleting a dispenser with a Cs content of 100 mg leading to a calibration value of 0.24 (mg/h)/µA. For this approach it is assumed that the entire evaporated Cs from the dispenser actually left the oven and was measured by the oven SID, i. e. no caesium remained within the oven parts. However, as will be shown in section 7.3 (figure 7.7), uniform Cs layers build up within the oven during operation. Thus, the determined calibration value should be an upper limit. On the other hand, contributions to the SID signal during calibration that were not caused by evaporated caesium from the oven, but by redistributed Cs within the vessel for instance, would lead to an underestimation of the calibration value. Another issue is the determination of the evaporated amount of caesium via weighing. Further material can possibly be evaporated (e. g. indium) and, since weighing has to be performed outside the vacuum vessel, Cs compounds can be formed on the depleted dispenser when it is brought into contact with ambient air. Errors arising from these aspects (leading to contrary directions) cannot be assessed but have to be kept in mind when interpreting SID signals with absolute evaporation rates.

The differently determined calibration values of 0.13 and 0.24 (mg/h)/µA are very similar being aware of the underlying assumptions. By slight variations of these assumptions considering the discussions above both values can be brought into agreement. Therefore it is reasonable to use an average value of

$$C_{\mathrm{ovenSID}} \equiv \frac{\text{evaporation rate}}{\text{SID signal}} = 0.19 \pm 0.05 \ \frac{\mathrm{mg/h}}{\mu\mathrm{A}} \ . \tag{7.1}$$

Throughout the presented investigations, the measured SID signals of the oven SID are calibrated after equation (7.1). This gives the opportunity to correlate analyzed effects to the absolutely quantified evaporation rate of the Cs source. Furthermore, the evaporated amount of Cs can be assessed and thus estimations on the Cs coverage of the vessel surfaces or the sample surface can be performed.

7.2 Evaporation characteristics of the dispenser

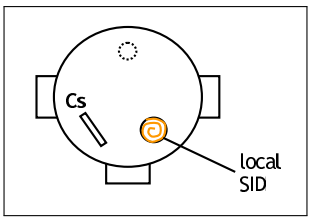

Prior to application within the dispenser oven the characteristics of the Alvatec dispenser [Alv10] itself need to be investigated. Therefore the dispenser is positioned directly in the experiment vessel and the evaporation is measured with the local SID using the data acquisition equipment later used for the oven SID.

Decision for using Alvatec dispensers

Basically, two types of dispensers can be used for the dispenser oven: the presented one from Alvatec and another one from SAES Getters [SAE10]. The latter was used in earlier work, e. g. in [FGW10], and it is presented here, why it is not used for the present purposes.

Dispensers from SAES use a caesium chromate as reagent and several reducing agents for the thermally activated decomposition and evaporation of Cs. The required heating currents for these dispenser types strongly depend on the embedded amount of caesium, being around 7 A for the typically used 10 mg dispensers. Figure 7.3 shows a typical evaporation curve of an SAES dispenser compared to two curves representing the Alvatec dispensers (two particular dispensers with equal properties) operated at different heating currents.

It is to mention, that the behavior of the onset of the evaporation cannot be compared in this context as for the Alvatec dispensers only an excerpt of a much longer operation is presented (shifted on the time axis), whereas for the SAES dispenser the entire evaporation curve is shown. It can be seen, that despite a constant dispenser heating current, the Cs flux from the SAES dispenser varies almost by a factor of 2 and already declines after 20 minutes of evaporation due to depletion of the Cs content. On the contrary, the Alvatec dispensers constantly evaporate even after one hour. This gives the opportunity for adjustments of the evaporation during investigations, including shutdown (shown in the lower curve) and recovery. Certainly, this argument could be addressed by using larger contents of caesium also for the SAES dispensers. However, because of the nonmetallic chromate this would lead to the necessity of much higher heating currents (several 10 A up to 100 A) which cannot be handled easily. Due to the metallic compound used in the Alvatec dispenser the heating current has almost no dependency on the Cs content why the use of favorable 100 mg dispensers is

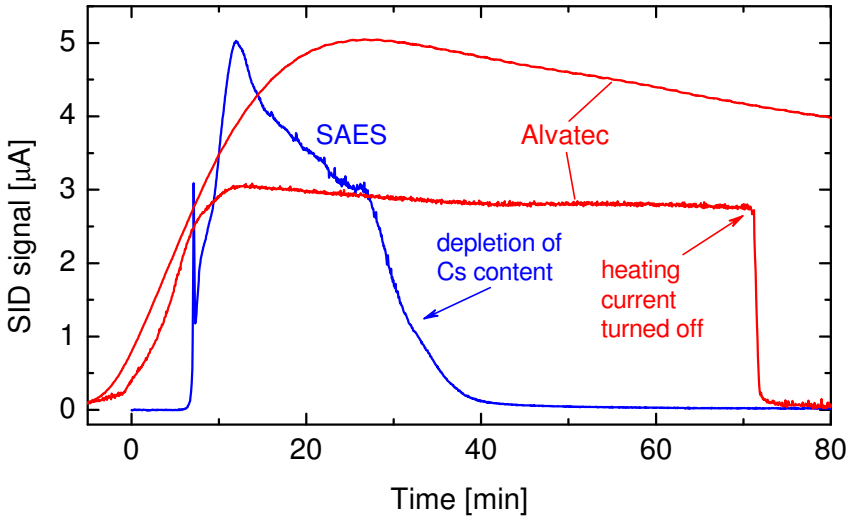

Figure 7.3: *Evaporation curves from SAES (10 mg) [SAE10] and Alvatec (100 mg) [Alv10] dispensers. Heating currents: SAES 7 A, Alvatec upper curve 6.5 A, Alvatec lower curve 7 A.*

unproblematic. Thus, by using the dispensers from Alvatec a longer and much more stable evaporation of caesium is guaranteed. The higher evaporation rate from the dispenser operated at lower heating current can be explained by an aging effect discussed below.

Another disadvantage of SAES dispensers is the high temperature required for evaporation, which is around 800 °C (red heat). For the application in the dispenser oven, this high temperature represents a further influencing factor for the overall temperature distribution and it can furthermore disturb the feedback control of the oven temperature. Hence, the envisaged separation of oven temperature and dispenser evaporation would be repealed.

Therefore, only the alloy dispensers from Alvatec [Alv10] are used for the present investigations.

Adjustability of the evaporation

The dependency of the evaporation rate of the Alvatec dispenser on the dispenser current is shown in figure 7.4 (a) where on the left axis the raw SID current is shown and the corresponding calibrated[1] evaporation rate on the right axis. It is to mention, that the given absolute values of the evaporation rate describe the

[1] A calibration via the accumulated amount, as described in section 7.1, was performed for the local SID for this particular campaign.

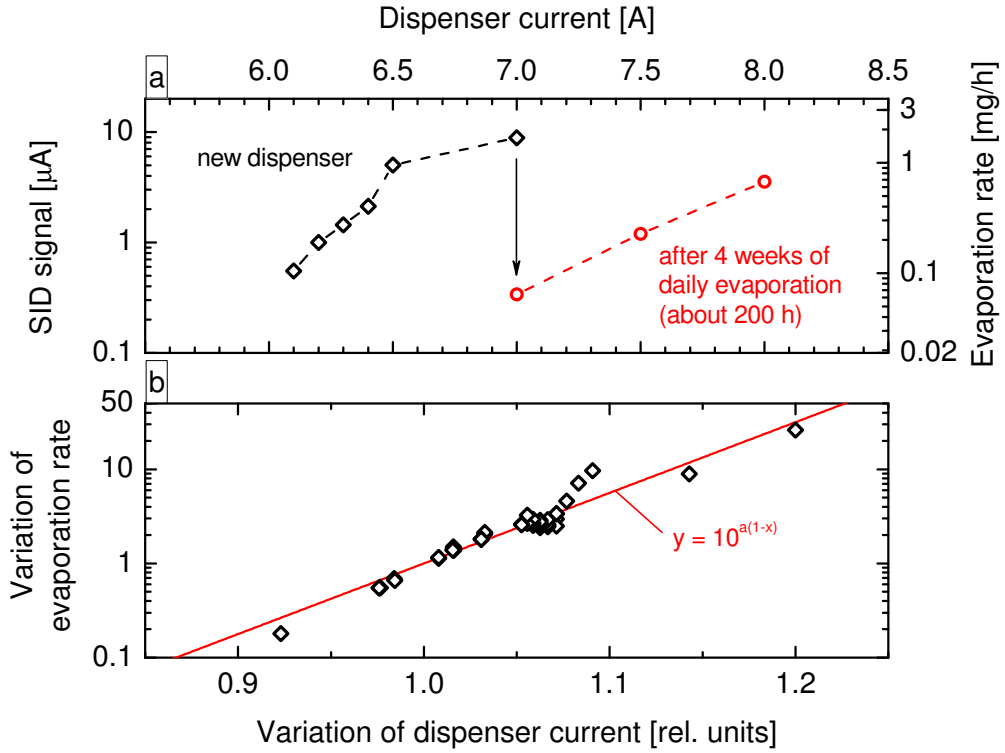

Figure 7.4: **(a)** *SID current and corresponding evaporation rate depending on the dispenser current from a new dispenser and after ∼200 h of evaporation.* **(b)** *Relative variation of the evaporation rate due to the variation of the dispenser current and an appropriate exponential fit.*

evaporation of the dispenser seen individually and a connection to the achievable evaporation rates of the entire Cs source, if the dispenser is installed in the oven, is not easily made. However, the basic behavior and tendencies of the evaporation rate can be analyzed.

As expected, higher dispenser currents yield higher evaporation rates. However, the evaporation rate at constant dispenser current decreases with evaporation time. This can be ascribed to the depletion of particular parts of the dispenser associated with the specific temperature profile at this heating current. Thus, for maintaining a constant evaporation rate, the dispenser current has to be readjusted. Since the depletion takes place on very long time scales and increasing the evaporation rate can easily be addressed via the heating current, this effect had no adverse influence throughout the investigations of this work. On the other hand, this behavior illustrates the importance of an in situ measurement of the evaporation rate, which is given by means of the oven SID.

In figure 7.4 (b) the relative variation of the evaporation rate due to a variation

of the dispenser current (depicted in relative units) can be seen, showing an exponential dependency. An exemplary variation of the heating current from 7 to 7.3 A results in a doubled evaporation rate from the dispenser. This proves the adjustability of the evaporation rate resulting in a controllable flux of pure caesium using Alvatec dispensers.

Activation procedure

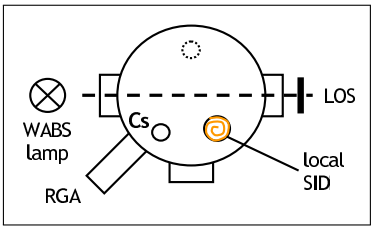

The activation procedure of the Alvatec dispenser, demonstrated in figure 7.5, is monitored while it is already installed in the dispenser oven. Thus, the diagnostics which will be standard in the next sections are already in operation, namely the integral oven SID, the local SID, the residual gas analyzer (RGA) to monitor the impurities and the white light absorption spectroscopy to monitor the Cs density.

The oven temperature is held constant at 150 °C (compared to the standard value of 260 °C) to prevent premature activation. When the dispenser current is set to 3 A, a sudden increase in the RGA signal for argon is observed whereas the other parameters, the RGA signals for water, nitrogen and oxygen, the SID signals from the oven and the local SID as well as the signal from the absorption

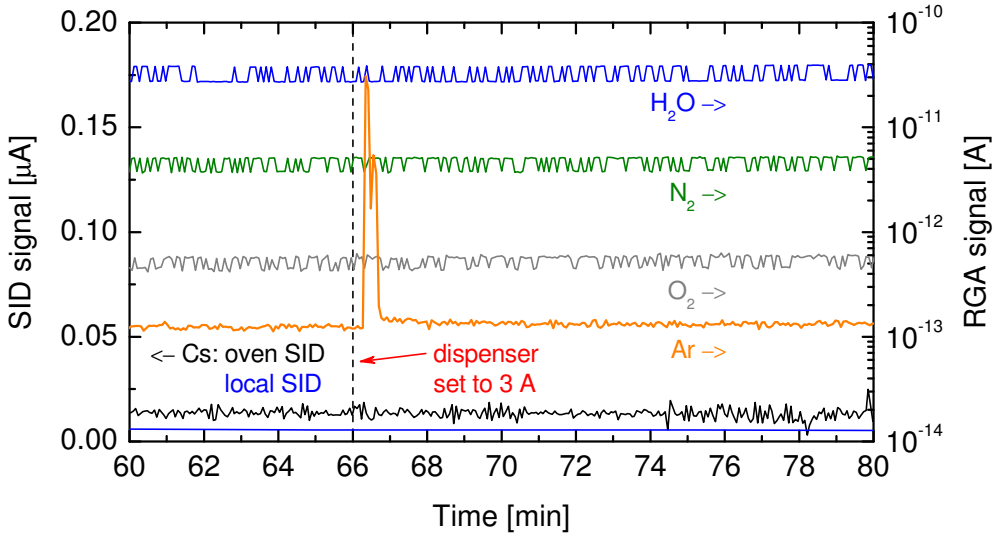

Figure 7.5: *Demonstration of the activation procedure for Alvatec dispensers at 3 A dispenser current, monitored by signals from both SIDs (the blue curve at the bottom corresponds to the local SID) and pertinent RGA signals. The oven temperature is constant at 150 °C.*

spectroscopy of caesium (not shown), are not influenced. This demonstrates the clean activation process without accompanied evaporation of caesium. Within one minute the buffer gas is pumped down accompanied by the decrease of the Ar signal to the background level and the signals from the RGA and the SIDs remain constant afterwards.

It should be noted, that for both SIDs the raw ion currents are presented here demonstrating the low dark currents of about 15 nA for the oven SID and 5 nA for the local SID. For the latter it is moreover to mention, that the current measurement equipment for the local SID (Keithley 602 Electrometer) uses an analog meter, which introduces an inert response on noise. Together with the manual recording (read off from the meter), which additionally leads to a limited resolution of ± 0.5 nA, a very low dark current noise is achieved and the apparently straight line of the local SID signal in figure 7.5 is obtained.

7.3 Operation under vacuum conditions

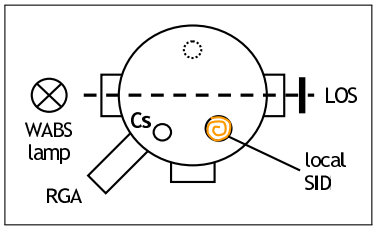

Prior to the application for systematic measurements on the caesium dynamics, the Cs dispenser oven is tested for stability, controllability and reliability of the caesium evaporation in vacuum and in hydrogen plasmas (section 7.4). Some of the findings presented here are also published in [FFF12].

In figure 7.6 the three standard diagnostics, namely the oven SID, the local SID and the white light absorption spectroscopy (WABS) monitor exemplarily an intentionally varied evaporation of the oven. The actual background of the variation and its absolute values are subordinate in this case. The signal from the local SID is scaled to get quantities that can be depicted together with the evaporation rates from the oven SID (the unit is 2 µA per mg/h) and the axis for the absorption signal is scaled to match the signal from the oven SID.

It can be seen that the oven SID signal and the absorption signal follow each other whereas the local SID signal shows a much lower dynamic. The direct correlation of the former both over more than eight hours clearly demonstrates the functionality of the oven SID without potential saturation effects or delayed response due to Cs coating of the wires. The latter can be seen in particular at the instantaneous reaction of both signals on the shutdown of the dispenser heating

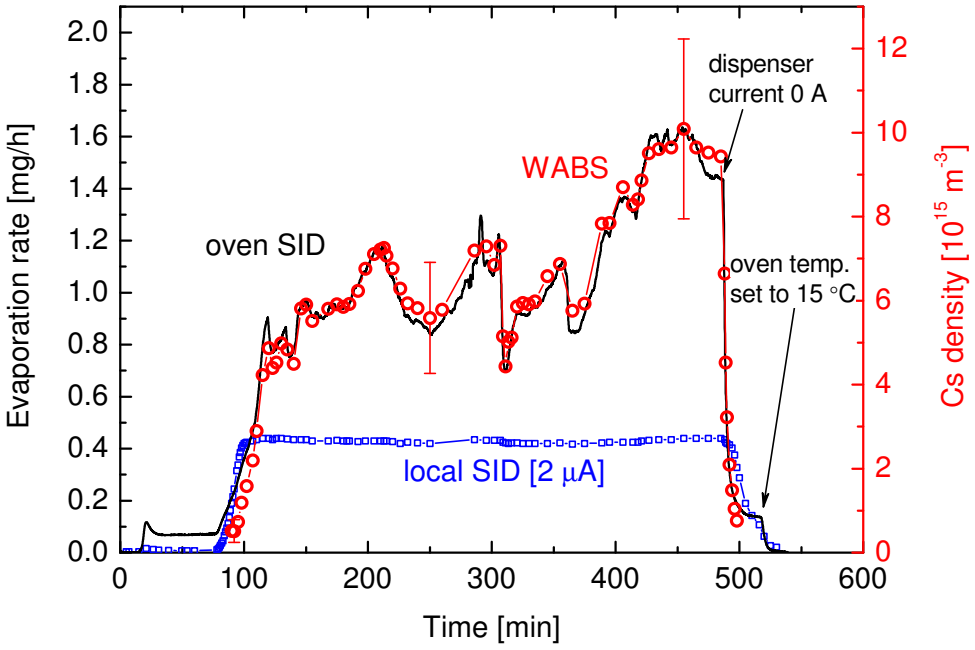

Figure 7.6: *Comparison of the signals from the oven SID, the local SID and the white light absorption spectroscopy at dynamical behavior of the dispenser oven. The oven temperature is set to 260 °C, the dispenser heating current is 7 A.*

current or the oven heating[2]. The error bars of the absorption signal show the increasing absolute errors due to the increasing correction factors. Here the correlation with the oven SID signal serves as indication, that the actual determined values show the correct dynamical behavior despite the large metrological errors, i. e. the relative progression of the Cs density is reliable and only the absolute values are subject to the measurement error.

The comparison with the signal from the local SID shows several important aspects for the investigation of the dispenser oven: Since the local SID is positioned at the bottom of the experiment and evaporation is directed upwards, caesium can reach the local SID solely via multiple adsorption and desorption processes at the vessel walls. This redistribution within the vessel leads to a much lower sensitivity of the local SID on the actual behavior of the evaporation which leads to the virtually constant signal. It should be noted, that the measured constancy of the signal is not attributable to a saturation effect, since higher signals can easily be measured at higher evaporation rates. Thus, the signal of the local SID represents the volume averaged conditions within the experiment vessel without

[2]Setting the oven temperature to 15 °C is equivalent to switching off the heating, since the room temperature at 20 °C is the minimal obtainable value.

interference of possible variations in the actual evaporation rate. On the contrary, the LOS of the absorption spectroscopy passes some centimeters above the oven nozzle and thus the comprehensive oven dynamic can be monitored.

In conclusion, using the equivalent signals from the oven SID and the absorption spectroscopy together with the signal from the local SID, both the behavior of the oven evaporation and its effects on the vessel volume can be investigated simultaneously. However, since the direct proportionality of Cs density and evaporation rate certainly also depends on the condition of the vessel wall surfaces, the exact correlation between absorption spectroscopy and oven SID signal (expressed by the scaling of the absorption axis) needs not to stay constant during the following investigations.

Conditioning of the dispenser oven – the background evaporation

The commissioning of the dispenser oven includes the activation of the dispenser (see figure 7.5) and the conditioning of the inner oven surfaces. The latter is shown in figure 7.7 (a). Beginning from a cold oven, the oven is heated to its working temperature of 260 °C accompanied by a slight increase of the oven SID signal. Setting the dispenser current to a value between 5 and 10 A (here 7–8.5 A) evaporation of caesium starts. Turning the dispenser heating current off after a certain time leads to the rapidly decreasing evaporation. However, if the evaporation time was sufficiently long (here about 2 hours) a background evaporation of about 0.05 mg/h remains from the hot oven. Two possible causes for such an evaporation can be envisaged: on the one hand, an insufficiently homogeneous temperature profile of the oven can lead to accumulation of Cs at certain cold spots and on the other hand, uniform caesium layers (or caesium compounds) can build up at the inner surfaces of the dispenser oven. In the former case redistribution processes between different temporary local cold spots would take place if the temperature of the oven is varied, accompanied by uncontrolled evaporation from the oven. Since no such unexpected evaporation was ever observed during the whole experimental campaigns over more than one year, it can be stated that the background evaporation arises from uniform caesium layers at the inner oven surfaces. The resultant background evaporation from the hot oven (260 °C) is very stable and its absolute value ranges from 0.04 mg/h to 0.08 mg/h.

The behavior of the background evaporation can be seen in figure 7.7 (b) where additionally to the signal from the oven SID the temperatures from the body and the duct of the oven are plotted. The oven is heated to 260 °C (set temperature)

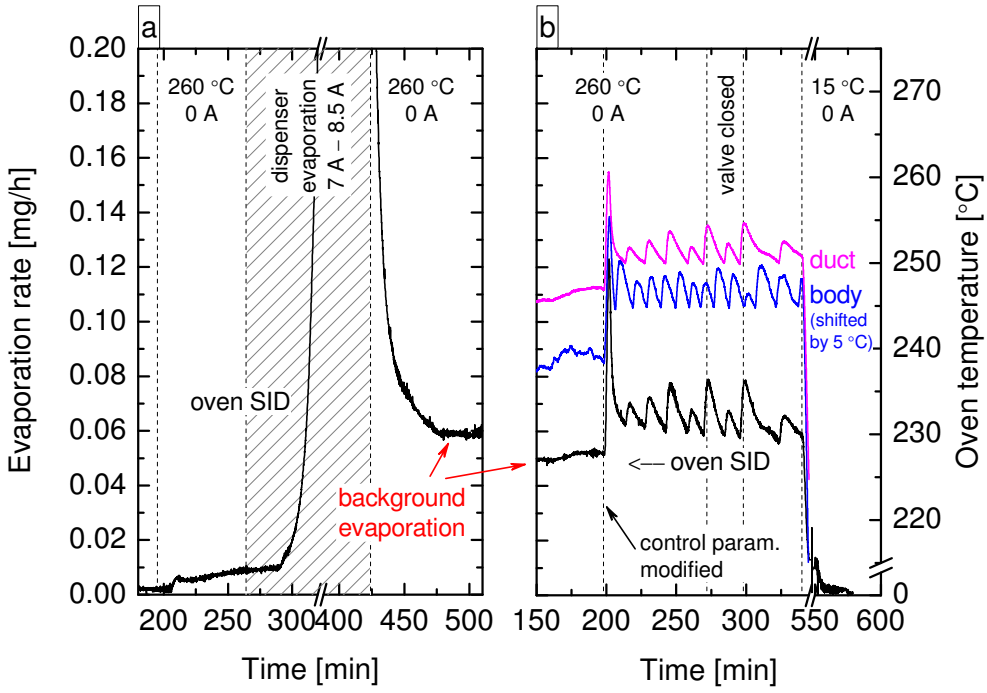

Figure 7.7: (a) *Demonstration of the emergence of the background evaporation monitored by the oven SID.* **(b)** *Dependency of the background evaporation on the oven temperatures (the body temperature is shifted by –5 °C for clarity) and the position of the valve. The scale for the evaporation rate is the same as for part (a).*

and no dispenser current is driven. At time mark 200 min the control parameters of the feedback control system are varied leading to oscillating oven temperatures and an oscillatory background evaporation. Comparing the temporal behavior of the evaporation to the oven temperatures reveals that the duct temperature is the determining factor. Furthermore, the evaporation is not influenced by the position of the valve which leads to the conclusion, that the front part of the oven, namely the duct, is the decisive part for the background evaporation. Cooling the oven down leads to the instantaneous decline of the residual evaporation.

However, the dependency of the background evaporation on the measured oven temperatures shows a steeper correlation than expected from the corresponding vapor pressure of pure caesium (see figure 4.3 (b)). Therefore it can be stated, that either the determining temperature is much lower than the measured ones (roughly around 150 °C) or that the measured caesium originates from caesium compounds that were thermally decomposed with a steeper temperature dependence.

While this background evaporation is ubiquitous when the oven is heated, its resultant evaporation rate is negligible if the dispenser is also evaporating. Therefore, the dispenser is still the major source of evaporation from the oven. Moreover, as can be seen in figure 7.6 at the beginning, the background evaporation is not detectable by the local SID, neither by absorption spectroscopy.

Temperature dependence of the evaporation rate

In figure 7.8 an example for the evaporation from the oven arising from the dispenser is shown, together with the oven temperatures of the body and the duct. After the oven is heated to working temperature and the background evaporation can be observed, the dispenser current is set to 6 A. The resultant evaporation rate of about 0.3 mg/h varies within $\pm$ 0.1 mg/h, although the adjusted parameters for the evaporation are kept constant. On the other hand, the local SID shows that the averaged caesium content in the vessel volume is not influenced. However, caesium condensation on a sample surface is also to be investigated and the sample holder is further upwards within the experiment compared to the local SID. Therefore, direct evaporation from the oven onto the sample surface can occur why stabilization of the evaporation rate is indispensable.

Comparison of the oven SID signal with the progression of the oven temperatures suggests a connection between them, which is frequently observed: a variation of the oven temperatures of about 5 °C can lead to a variation of the evaporation rate of about 40 %, which clearly contradicts the envisaged separation of oven temperature and evaporation rate. The cause for the strong dependency can be given by considering ad- and desorption processes within the oven: Evaporated caesium from the dispenser collides multiple times with the oven surfaces before leaving the oven through the nozzle. If the temperature dependent desorption fluxes from the oven surfaces are smaller than the evaporation flux from the dispenser itself, the oven temperature can be the determining factor for the final evaporation rate of the oven. However, the observed variations in figure 7.8 can again not be described by the vapor pressure of pure Cs using the measured temperatures: colder temperatures must be determinant or chemical compounds must be involved.

Nevertheless, the dependency of the evaporation rate on the oven temperature can still be reduced significantly if the temperature of the oven is increased further since the desorption flux has a steep dependence on temperature. However, due to the elastomer seal at the connection between the oven and the bottom plate of

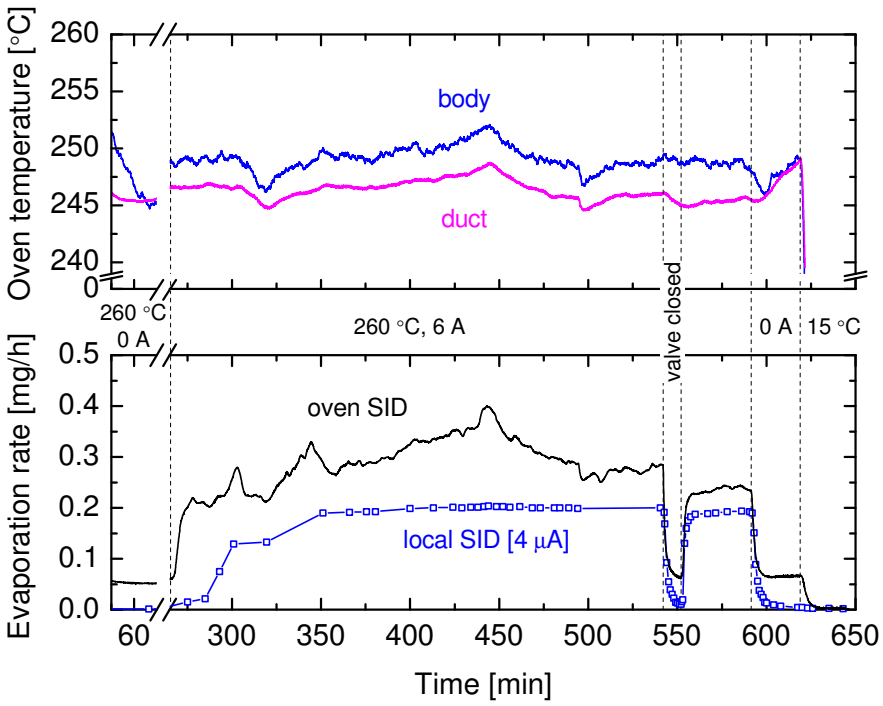

Figure 7.8: *Example for the evaporation from the dispenser oven illustrating the correlation with the oven temperature. Functionality of the valve is demonstrated additionally.*

the experiment, this is not possible in the present setup. Therefore, the solution for stable evaporation is to keep the oven temperature virtually constant which was achieved by systematic investigations on the appropriate tuning of the control parameters of the feedback system and by thermal insulation of the oven against ambient air and cooling draughts. However, the alternative solution by using a temperature stable sealing should be kept in mind for future investigations.

Furthermore, figure 7.8 clearly demonstrates the functioning of the valve. Closing the valve instantaneously leads to a decline of the evaporation rate to the background level, which is in turn independent of the position of the valve as shown in figure 7.7 (b). When the valve is opened again, the evaporation rate is regained. Finally, turning off the dispenser heating current shows the analogy to closing the valve and cooling down the oven rapidly yields a vanishing evaporation.

The observed gradual increase of the evaporation rate after opening the valve without overshoot again indicates the involvement of chemical de- and adsorption processes at the oven surfaces: While the valve is closed, the constant oven temperature and dispenser current lead to an increased vapor pressure of Cs within

the oven body. Thus, if the evaporation of the oven would be determined by the vapor pressure of pure Cs, an increased evaporation would be expected after opening the valve (overshoot) followed by a gradual decrease down to the evaporation rate prior to closing the valve. This is not observed and the behavior can be explained by the consideration of Cs compounds: While the valve is closed, Cs is evaporated out of Cs compounds at the oven surfaces (background evaporation) leaving free bonding sites. Hence, when the valve is opened again the excess of Cs vapor pressure is gettered at the oven surfaces and the evaporation from the oven increases only gradually until the oven surfaces are saturated again.

Stable evaporation and adjustment

Adjusting the control parameters of the feedback system for the oven temperatures leads to a very stable evaporation for several hours. In figure 7.9 the controlled evaporation from the oven is demonstrated for standard conditions, i. e. after a certain time of operation without venting the system. Therefore, oven and vessel surfaces are conditioned and the amount of impurities within the experiment is low (background pressure 1.6×10^{-6} mbar). In the upper part of the figure additionally the signals from the RGA for oxygen, nitrogen and water and the background pressure of the experiment are shown.

Heating the oven to working temperature (set temperature 260 °C) is accompanied by the emergence of the background evaporation and an increase of the background pressure up to 1.1×10^{-5} mbar due to evaporation of adsorbed particles and/or thermally decomposed caesium compounds from the oven surfaces. A slight increase in the water signal from the RGA can also be observed whereas no nitrogen or oxygen is desorbed from the oven at this state of conditioning.

After about $2\frac{1}{2}$ hours the dispenser heating current is turned on and with beginning evaporation a slight decrease of the background pressure can be observed due to the getter effect of caesium. Subsequently, increasing the dispenser current leads to an increasing evaporation rate which is always virtually constant for more than one hour. After exceeding the detection limit of the white light absorption spectroscopy of $n_{\mathrm{Cs}} \gtrapprox 3\text{–}4 \times 10^{14}\,\mathrm{m}^{-3}$ this stable behavior can also be monitored at the caesium density. At 9 A heating current the evaporation rate of about 1.7 mg/h and a caesium density of about $2 \times 10^{15}\,\mathrm{m}^{-3}$ can be maintained for over 6 hours. The amount of the background gases oxygen, nitrogen and water show no dependency on the evaporation rate whereas the background pressure gradually decreases.

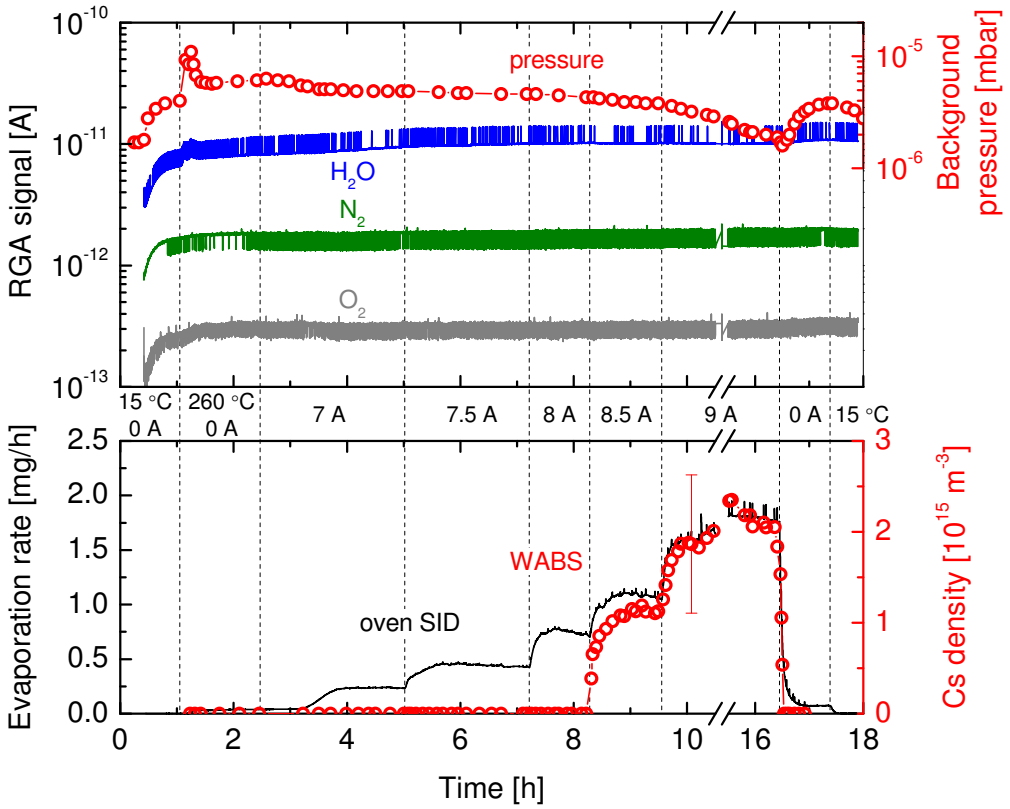

Figure 7.9: *Demonstration of adjustable stable evaporation of the dispenser oven monitored with the oven SID and white light absorption spectroscopy and its influence on the background gases and the total background pressure.*

Turning off the dispenser heating current leads to the instantaneous decrease of the evaporation rate down to the background level and below the detection limit of the white light absorption spectroscopy. The lack of caesium evaporation can also clearly be seen at the increasing background pressure, since the getter effect of caesium is missing. Observing the water signal more precisely also shows a slight increase. Cooling the oven down results in the vanishing evaporation and a decreasing background pressure again.

In conclusion, the dispenser oven can be used for stable and controllable evaporation of pure caesium leading to an adjustable Cs density in the required range, while the oven SID is an excellent tool for monitoring the evaporation.

Heating the oven after vacuum break The above shown signals are typical for conditions after several days of operation and evaporation. However, directly after venting the entire experiment vessel including the front part of the dispenser oven (valve closed), much more dynamic can be observed in the signals. During aeration times water and oxygen from ambient air can be embedded into the layers of caesium and caesium compounds. Heating the oven in vacuum afterwards releases large amounts of water and oxygen leading to an increase of the corresponding RGA signals to values of 10^{-9} and several 10^{-12} A, respectively. This can yield an immense pressure increase up to several 10^{-3} mbar. Comparing these values with those of the standard scenario in figure 7.9 shows the significance of conditioning the dispenser oven.

Concluding, the evaporation of particles from the oven mainly depends on the experimental history and can be used to assess the purity of the system.

7.4 Operation in plasma

Influence of plasma on the Cs evaporation

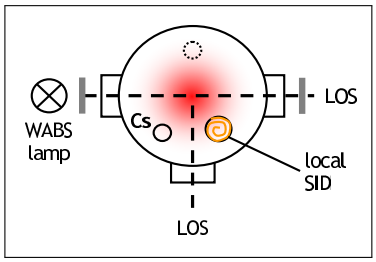

Figure 7.10 shows the effect of igniting a plasma while evaporating caesium. Since the SIDs cannot be used in plasma operation, optical emission spectroscopy is applied to monitor the Cs dynamics in plasma via continuously recording the Cs D_2 resonance line with the survey spectrometer. Apart from the biases, the SID wires are still permanently heated during plasma to counteract Cs accumulation. Like this it is guaranteed, that the SIDs can be used again directly after plasma operation. Besides some minor RF noise on the SID heating currents and a slight offset for the measured oven temperatures (some °C), the components of the oven, in principle, showed no interferences by the RF fields.

In figure 7.10 the oven is heated to working temperature and the dispenser current is set to 8.5 A leading to an evaporation rate of about 6 mg/h and a Cs density of 7–8×10^{16} m^{-3} in 10 Pa hydrogen gas. Turning on the RF (250 W power) leads to a drastic decrease of the signal from the absorption spectroscopy which can also be observed with the OES. Within 20 minutes the Cs density decreases below the detection limit of the white light absorption spectroscopy. The subsequent increase of the dispenser heating current leads to increasing caesium

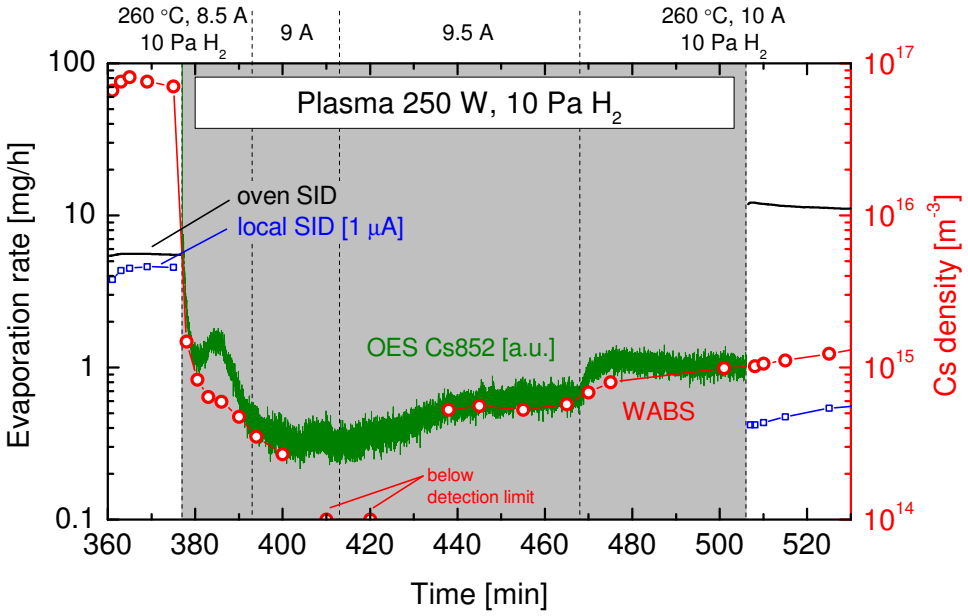

Figure 7.10: *Influence of a hydrogen plasma at 10 Pa and 250 W on the evaporation of caesium from the dispenser oven. The hydrogen pressure of 10 Pa is maintained throughout the shown period of time.*

emission and the Cs density rises to about $1 \times 10^{15}\,\mathrm{m}^{-3}$. Switching off the RF again has no influence on the caesium density monitored with the absorption signal. Restarting the SIDs shows an increased evaporation rate by a factor of two (oven SID) whereas the caesium content within the volume is diminished by a factor of ten (local SID).

Since the increased dispenser heating current actually led to an increased evaporation rate, as can be seen at the oven SID signal after turning off the plasma, the decreased caesium density within the vessel due to the discharge has to be ascribed to an aggravation of existing sinks and/or the emergence of further sinks for caesium. During plasma caesium is ionized and reactions with plasma particles can occur (see section 4.4.2). Both channels would lead to a rapid decrease of the neutral caesium density and thus of the absorption signal, as caesium ions are not accessible via absorption spectroscopy at this transition line. On the other hand, these reactions should instantaneously disappear if the RF is switched off again, directly yielding increased caesium densities. As this is not the case, processes within the plasma volume can be neglected here.

However, the Cs density in the volume is determined by ad- and desorption processes at the vessel surfaces. Therefore, surface effects have to be considered. The electrostatic potential of the bulk plasma lies more than 10 V above the

grounded vessel walls (see section 9.2). This leads to a flux of energetic ions (H^+, H_2^+, H_3^+, Cs^+) onto the vessel and oven surfaces with energies of about 10 eV, which can lead to an activation of already existing caesium compound layers. Together with the hydrogenation of the walls by atomic hydrogen dissociated in the plasma, an enhanced chemical gettering of caesium can be expected leading to a rapid decrease of the Cs density in the plasma. As these effects also persist after switching off the RF the caesium density does not recover directly after plasma treatment, which can be observed in the signals of the absorption spectroscopy and the local SID. Recovery of the Cs content will not occur until the additional sinks are saturated, the time scale being about an hour depending on the plasma exposure time.

Summarizing, it can be stated, that the oven can be applied in plasma environment. However, in order to achieve comparable caesium densities the evaporation rate should be higher than in vacuum to compensate for the additional Cs sinks.

Heating the oven in plasma

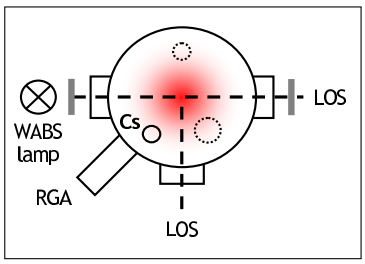

The standard scenario for evaporating caesium into hydrogen plasmas includes igniting the discharge, waiting for the system to establish stable conditions (by monitoring the temperatures and the RGA and OES signals) and subsequently heating the oven. Thereby, the oven heating is accompanied by several effects which can be monitored with the RGA and the OES, shown in figure 7.11.

In the bottom part of the figure the emissions of atomic and molecular hydrogen (H_α line, Fulcher system), of the hydroxyl molecule OH (A–X transition, 305–320 nm) and of casium (D_2 resonance line Cs852) together with the Cs density are depicted, whereas the upper part shows the RGA signals of oxygen, nitrogen, water and atomic and molecular hydrogen. The latter both are separated and shifted against each other to emphasize analogies and differences among them. On top of the figure the temperatures of the body, the duct and the valve of the oven are shown.

In an anticipated summary, the evolution of the signals when heating the oven up to working temperature of 260 °C can be explained by the fact, that adsorbed particles together with Cs and/or caesium compounds are evaporated from the oven surfaces and dissociated in the plasma. The particular effects are described in the next paragraphs.

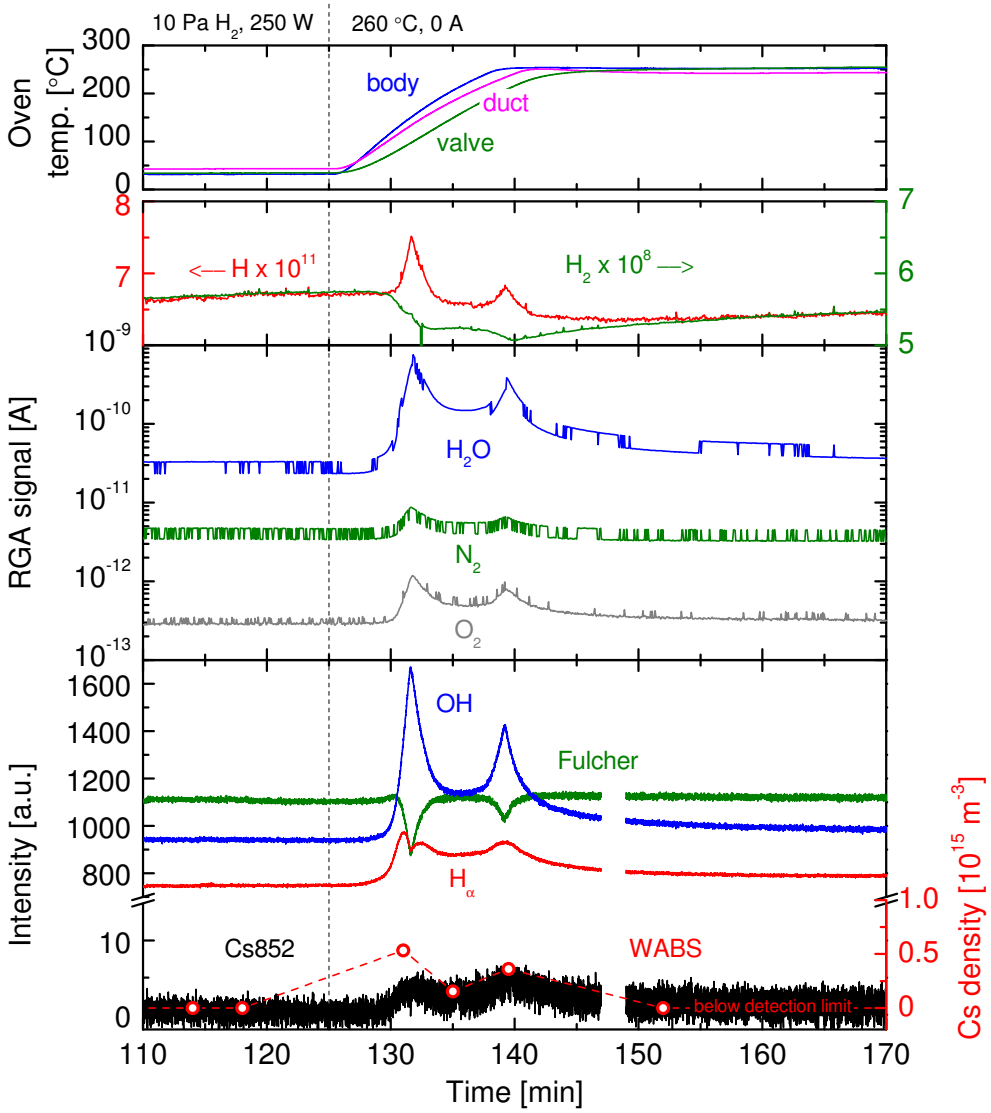

Figure 7.11: *Effects of heating the oven in plasma (10 Pa H_2, 250 W) monitored with RGA, emission and absorption spectroscopy.*

Observable at the RGA signals, H_2O, N_2 and O_2 are evaporated from the oven, either directly as desorption of adsorbed particles or from thermal decomposition of Cs compounds at the oven surfaces or as dissociation products of evaporated Cs compounds in the plasma. The analogous double peak structure in each signal, which is consistently observed when the oven is heated, indicates, that different parts of the oven are heated at different rates yielding a varying temperature profile of the oven. This can be seen at the differing progression of the oven temperatures, which can e. g. result in a temperature difference between the body and the valve of more than 50 °C. Thus, the same particles can be evaporated from the oven at different times originating from different oven parts.

Dissociation of the rising water content in the plasma directly leads to the related parallel behavior of the OH and the H_α emission, respectively. Furthermore, Cs is evaporated from layers of Cs and/or Cs compounds within the oven, as can be seen at the emission and the absorption signal. The getter effect of Cs consequently leads to a decreasing H_2 signal in the RGA and a reduced Fulcher emission. As the emission from atomic hydrogen, in principle, arises from dissociative excitation of molecular hydrogen as well as direct excitation from dissociated hydrogen atoms (see section 6.6.2), the getter effect for H_2 and H can be seen additionally at the small dip in the first peak of the H_α emission, superimposing the effect of the dissociation of water.

Considering the RGA signal for atomic hydrogen, it is to mention that it arises solely as dissociation product within the detector since atomic hydrogen from dissociation within the plasma cannot reach the RGA detector. This was observed in another campaign, in which the atom-to-molecule density ratio in a plasma of constant total hydrogen pressure was varied whereas the RGA signal for H stayed constant. Therefore, atomic hydrogen measured by the RGA is to be ascribed to the dissociation of molecular hydrogen or water within the detector. This conception is strengthened by the identical relative progression of the RGA signals of H and H_2 at the left and right end of the time axis in figure 7.11. Therefore, the peaks in the RGA signal for H arise from the additional dissociation of water evaporated from the oven, whereas the declining base line corresponds to the decreasing molecular hydrogen content due to the gettering by Cs.

Furthermore it can be seen, that the background evaporation from the hot oven, which was observed in vacuum with the oven SID (see figure 7.7), is not detectable in emission.

Heating the oven in plasma after vacuum break As already described in section 7.3, venting the system can lead to the incorporation of ambient air into the compound layers at the oven surfaces and an associated excessive evaporation of water, nitrogen and oxygen from the oven. In plasma this can lead to an increase of the working pressure by several Pa. This pressure increase is additionally accompanied by an influence on the plasma parameters and therefore on the emissions. Furthermore, it was observed that the temperature of a sample surface within the plasma increases from about 250 °C to about 280 °C if large amounts of heavy particles (mainly water) are evaporated from the oven. The definite cause could not be determined but the most probable explanation is a rising temperature of the heavy particles in the plasma due to varied plasma parameters.

Again, the effects when heating the oven can be used as indicators for the purity of the system, and systematic investigations cannot be performed until stable conditions have established after this transition regime.

Stable evaporation and adjustment in plasma

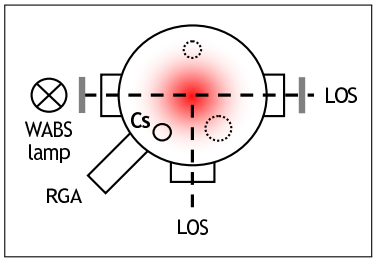

After heating the oven to working temperature caesium can be evaporated, which is shown in figure 7.12 for a hydrogen plasma at 10 Pa and 250 W. Signals from emission and absorption spectroscopy are shown at the bottom together with the RGA signals from the background gases H_2O, N_2 and O_2 at the top. Further emission signals are omitted here as these are subject to the investigations presented in section 9.2.

It can be seen that emission and absorption spectroscopy show the identical behavior demonstrating that emission from the caesium D_2 resonance line at 852.1 nm is an excellent tool for monitoring the caesium dynamics in plasma, like is the oven SID for vacuum (see figure 7.9). The axis for the absorption signal is scaled to match the signal from the OES and it is to mention, that the observed correlation of emission and absorption spectroscopy is of course dependent on the plasma parameters (electron temperature and density). However, in this case the influence of n_e and T_e is negligible as will be shown in section 9.2. Thus, increasing the dispenser current leads to increasing emission, which is directly related to an increasing caesium density. The Cs density is always maintained virtually constant for about half an hour giving the opportunity for systematic

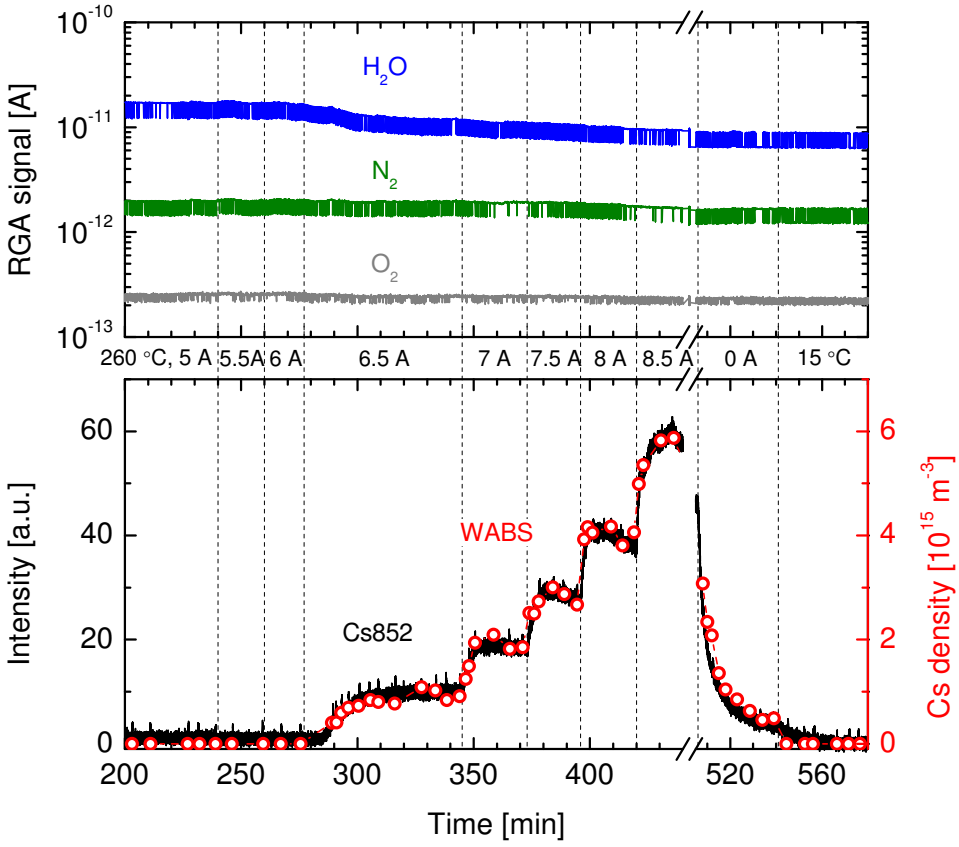

Figure 7.12: *Demonstration of stable and adjustable evaporation of caesium into a hydrogen plasma at 10 Pa and 250 W monitored by emission and absorption spectroscopy and the RGA.*

investigations. Switching off the dispenser heating current leads to a rapidly decreasing caesium content within the plasma.

Considering the RGA signals, it can be stated that evaporation of caesium has no effect on the contents of nitrogen and oxygen in the experiment which confirms the observations under vacuum atmosphere in figure 7.9. On the other hand, at the RGA signal for H_2O the getter effect of caesium can clearly be seen leading to a decreasing water content.

Furthermore the functionality of the valve was tested in plasma (not shown here) yielding similar response times as in vacuum, shown in figure 7.8.

In conclusion, the dispenser oven can be used for stable and controllable evaporation of caesium into hydrogen plasmas generating adjustable caesium densities in the required range.

8 Investigation of the Cs dynamics under vacuum conditions

8.1 Influence of background gases on the Cs content

Background gases, including rare gases, impurity gases and the working gas hydrogen, can have several effects on the caesium content within the vessel. Thereby, the evaporation from the Cs oven can be affected as well as the redistribution within the vessel. The principle possible influences are summarized in table 8.1 together with the expected effect on the evaporation rate and/or the caesium content within the vessel.

Table 8.1: *Possible influences of background gases on the evaporation rate of the dispenser oven and on the Cs content within the experiment vessel, whereas obviously the former also influences the latter.*

Possible Influence		Caused by	Consequence
(i)	Chemical reactions (see section 4.3)	O_2, H_2O, H_2, less with N_2	decreasing evaporation rate and decreasing Cs content, dependent on partial pressure
(ii)	Decreasing oven temperature	some Pa of absolute press.	decreasing evaporation rate, dependent on absolute pressure
(iii)	Hindered expansion of Cs out of the oven	some Pa of absolute press.	decreasing evaporation rate, dependent on absolute pressure
(iv)	Hindered diffusion to the vessel walls	some Pa of absolute press.	increasing Cs content, dependent on absolute pressure

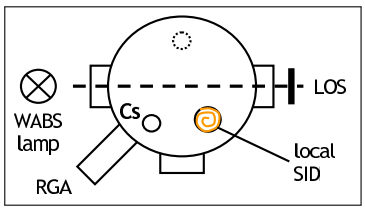

The resulting conjoint influence of a particular gas cannot be assessed a priori and has to be determined experimentally. Furthermore, using the diagnostic set of the oven SID, the local SID and the white light absorption spectroscopy, the distinct effects on the evaporation rate on the one hand, and on the Cs content on the other hand, can be separated. However, it should be mentioned, that the background gas itself can have a direct influence on the SID measurements, besides effects correlated with caesium. As described in section 6.1.2, thermionically emitted electrons from the SID filaments that are accelerated by the bias voltage can ionize the background gas and lead to secondary electrons which are measured as SID signal. An estimation of this contribution using the thermionic electron current density after Richardson (equation (6.3)) and a typical ionization cross section of 1 Å^2 leads to an additional SID signal of about 100 nA for 10 Pa background pressure, depending linearly on pressure and cross section. This has to be taken into account in the interpretations of possibly rising SID signals.

8.1.1 Rare gases: He, Ar

In order to omit possible chemical reactions in a first step, the inert rare gases helium and argon are used to examine the influence of an increasing background pressure on the Cs content within the experiment vessel.

In figure 8.1 the admixture of the gas **helium** is shown, monitored by the oven and the local SID as well as the oven temperatures. The oven was operated at 260 °C set temperature and 9.5 A dispenser heating current leading to an evaporation rate of 0.6–0.7 mg/h. Increasing the background pressure of helium leads to a decreasing duct temperature due to conductive cooling, where higher absolute pressures yield a stronger temperature decrease, as expected. The temperature of the oven body is not influenced since it is further away from the main vessel where gas conductive cooling has only a minor influence.

The oven SID signal shows that increasing the background pressure leads to decreasing evaporation rates, whereas the actual influence of 1.6 Pa He can be seen at disabling the gas supply towards the end. Referring to table 8.1 the observed influences can be explained by the decreasing oven temperature (ii) and/or by a possibly hindered expansion out of the oven (iii). The latter should result in an instantaneous reaction, which is not observed. On the other hand, the temporal behavior of the evaporation rate is very similar to the progression of the oven

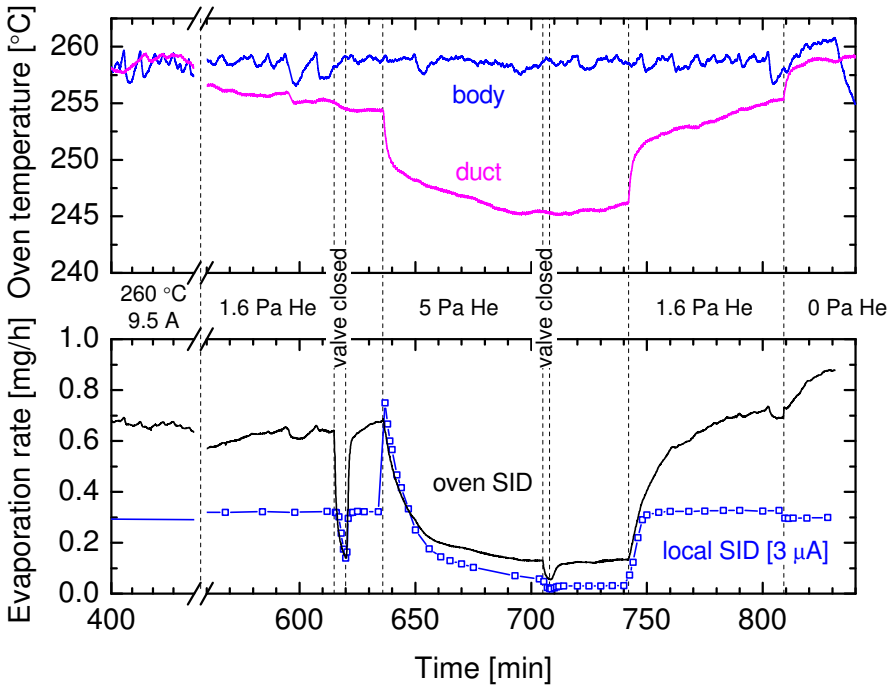

Figure 8.1: *Influence of helium on the oven temperatures, the evaporation rate of the oven (oven SID) and the volume averaged Cs content (local SID) at varying absolute He pressure.*

temperature, which suggests that the decisive effect should be the decreasing oven temperature.

Hence, the unaffected evaporation rate of the oven at 1.6 Pa He after opening the gas supply must be explained by a slightly increased evaporation rate of the dispenser itself which compensates the reduced transfer of the evaporated caesium through the oven nozzle due to the decreased duct temperature. Since the latter effect disappears with closing the helium supply the increased dispenser evaporation can be observed at the right end of the time axis. At 5 Pa He the evaporation rate from the oven decreases to about 0.13 mg/h. However, the quantitative correlation between the temperature decrease and the decreased evaporation rate cannot be described by the vapor pressure of pure caesium, unless much lower temperatures are considered. This again confirms the corresponding observations made in section 7.3.

The local SID now shows the consequences for the Cs content in the vessel volume. At 1.6 Pa He the unaffected evaporation rate of the oven together with the hindered diffusion of the evaporated caesium to the vessel walls (item (iv) in table 8.1) leads to a slight increase of the Cs content in the volume of about

80 nA. It is to mention, that this increase in the SID signal cannot be attributed to the ionization effect, as the ionization cross section for He [WBHF87] and the pressure are about a factor of five and six, respectively, lower than for the estimation above, yielding an impact of only 3 nA. Therefore, this effect can be neglected here. Further increasing the He pressure to 5 Pa initially yields an instantaneously increased volume averaged Cs content by a factor of 2.3 due to the further hindered diffusion. However, the decreasing evaporation from the oven subsequently leads to a decreasing Cs content down to 90 nA. Furthermore, the influence of the valve is maintained throughout the variations of the He pressure proving that the dispenser always remains the source of evaporation.

Similar behavior was observed using **argon** as background gas, whereas the pressure was increased up to 41 Pa (not shown). As with helium the duct temperature decreases at constant body temperature resulting in a decreasing evaporation rate from the oven and consequently in a decreasing caesium content within the vessel volume. The additional influence of a possibly hindered expansion out of the oven cannot be ruled out either at these high pressures. However, when the gas supply is disabled the conditions prior to Ar feeding are regained proving that even at 41 Pa background pressure no irreversible effects occur.

Summarizing, the inert rare gases helium and argon show the expected reversible influences of an increasing background pressure on the Cs content within the vessel (see items (ii)–(iv) in table 8.1): decreasing oven temperature, hindered expansion out of the oven and hindered diffusion to the vessel walls. The effects are dependent on the absolute pressure where in the range of some Pa the impact increases from a virtually negligible influence to a substantial reduction of the evaporation rate. The latter prevails the hindered diffusion to the vessel walls at higher pressure and thus it can be stated, that an increasing background pressure will always lead to a diminished caesium content. However, as this can mainly be ascribed to the decreasing oven temperature, simple readjustment of the temperature can mitigate that effect.

8.1.2 Impurity gases: N_2, O_2, H_2O

Nitrogen and Oxygen

The impurity gases nitrogen and oxygen can have a major impact on the Cs content even in very low dosages due to the possibility of chemical reactions, by which the crystalline compounds caesium superoxide CsO_2, caesium oxide Cs_2O,

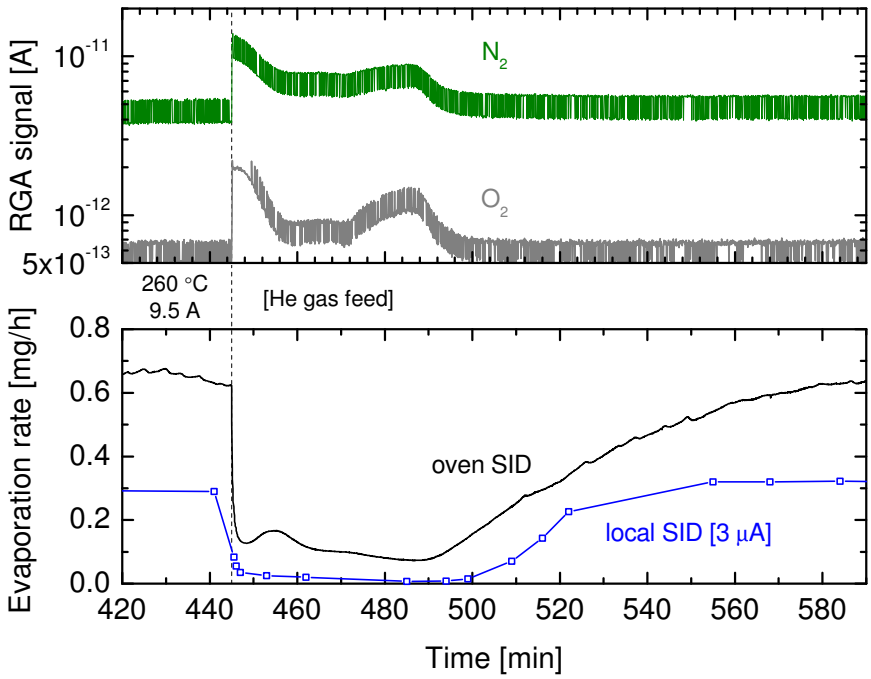

Figure 8.2: *Influence of oxygen and nitrogen on the evaporation rate of the oven (oven SID) and the volume averaged Cs content (local SID). O_2 and N_2 are intrinsic admixtures to the helium feeding via the gas supply system.*

caesium nitrate $CsNO_3$ and caesium azide CsN_3 can be formed (see section 4.3). Furthermore, feeding of gases via the gas supply system (He, Ar, H_2) is always accompanied by the influx of small quantities of nitrogen and oxygen. These small amounts accumulate within the gas supply system during downtimes and are pumped via the experiment vessel if a gas flow is set. Therefore, the influences of the impurities N_2 and O_2 can be investigated using these intrinsic amounts via the gas feed.

Figure 8.2 shows the influence of nitrogen and oxygen on the evaporation rate and on the Cs content within the experiment. Helium feeding was used in this case and the flow rate was maintained constant at 10 sccm (yielding 1.6 Pa absolute pressure): the oxygen and nitrogen background is increased by a factor of 4 and 2.5, respectively. A rough estimate of the corresponding partial pressure using the mass dependent sensitivity of the residual gas analyzer gives values of the order of 10^{-5} mbar in maximum for both impurities. Despite these low partial pressures, the evaporation rate instantaneously decreases from 0.6 mg/h down to about 0.1 mg/h and the Cs content within the vessel is diminished.

Effects (ii)–(iv) in table 8.1 can be neglected in this case and the main determining effect is the possibility for chemical reactions. These can occur at the

inner oven surfaces leading to the decreased evaporation rate as well as at the vessel surfaces leading to increased chemical gettering of the evaporated caesium and in turn to the decreased signal from the local SID. It can be observed, that the minima of the evaporation rate coincide with the maxima of the RGA signals for O_2 and N_2. After about an hour the impurities are pumped down and the evaporation as well as the Cs content within the volume recover. Since the cause for the decrease were chemical reactions at the surfaces, the recovery occurs gradually and it takes about 100 minutes until the equilibrium is regained.

However, further investigations have shown, that nitrogen plays only a minor role in surface chemistry leading to the getter effect: Even larger amounts of nitrogen (intrinsically via the gas feed) have virtually no influence on the Cs content within the vessel as long as oxygen or water are not involved. Furthermore it is often observed that heating the oven leads to substantial evaporation of water and oxygen from the oven, while the nitrogen content is almost unaffected. However, if the oven with already conditioned inner surfaces (uniform Cs layers) is brought into contact with ambient air, nitrogen is also released when the oven is heated in vacuum afterwards. This suggests, that chemical reactions of Cs with N_2 do occur, but that the kinetics of the reactions are much slower than those of reactions with O_2 or H_2O. Thus, the small background partial pressure of nitrogen in vacuum is too low to induce significant reactions with the Cs layers within the oven, whereas oxygen and water can be embedded considerably.

Therefore, it can be stated, that also in figure 8.2 the increased **oxygen** content is the decisive cause and that the accompanied increased **nitrogen** amount is negligible for the chemical influence on the Cs content.

Water

It was observed that heating the vessel walls by the temperature control system for the cooling water circuit leads to substantial evaporation of water from the walls. Thus, the impurity H_2O can be introduced into the vessel and its influence on the Cs content can be investigated by use of the heating system for the vessel walls. Substantial influence is expected due to the multitude of possible reactions of Cs and Cs compounds with H_2O by which predominantly the salt caesium hydroxide CsOH is formed, as illustrated in figure 4.5 (a).

Figure 8.3 shows the correlation of wall temperature and water content in the upper part, whereas the lower part illustrates the influence of the increased water vapor pressure on the evaporation from the oven (oven SID) and the volume

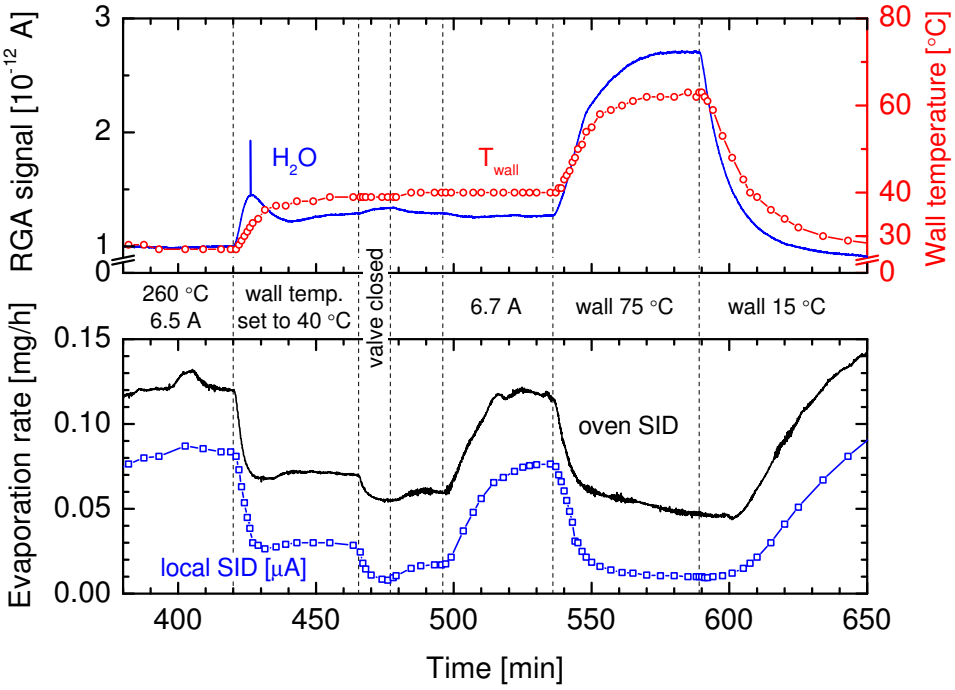

Figure 8.3: *Influence of water vapor, induced by heating the vessel walls, on the Cs evaporation (oven SID) and on the Cs content within the vessel (local SID).*

averaged Cs content within the vessel (local SID). The oven was operated at 260 °C and a dispenser current of 6.5 A. Setting the temperature of the cooling water circuit to 40 °C leads to the correlated increase of the water content corresponding to an estimated partial pressure of the order of 10^{-4} mbar. Due to the related increased chemical gettering of caesium within the oven the evaporation rate decreases from 0.12 mg/h to 0.07 mg/h. Closing the valve demonstrates, that the dispenser is still evaporating and via increasing the dispenser heating current the evaporation rate can be regained. Further heating the vessel walls to 63 °C (set temperature 75 °C) again yields a decreasing evaporation rate due to the further increased H_2O vapor pressure of about 10^{-3} mbar. The subsequent decrease of the wall temperature leads to condensation of the water at the vessel walls and consequently to a recovery of the evaporation, which ends in a higher evaporation rate than at the beginning due to the increased dispenser current.

In contrast to the decreasing evaporation rate, elevated vessel wall temperatures should lead to decreased sticking of caesium at the vessel walls due to a lower occupation with impurities and due to a higher desorption flux. Thus, an increased volume averaged caesium content would be expected, which should be measurable via the local SID. However, as the evaporation rate from the oven

is substantially influenced by the increased water vapor pressure, the Cs content within the vessel and thus the local SID signal behave similar to the oven SID signal.

Furthermore it was observed, that the background evaporation from the oven is not influenced by an increased water vapor pressure (not shown). As described in section 7.3, the background evaporation originates from the front part of the oven (duct) compared to evaporation from the dispenser which is located in the oven body. Hence, the background evaporation is much less susceptible to chemical gettering at the oven surfaces and thus an increased water vapor pressure has only limited influence. In this case, the elevated vessel wall temperatures could lead to an increased volume averaged Cs content. However, as described in section 7.3, the local SID is not sensitive enough to detect the background evaporation and thus, the effect cannot be observed experimentally.

Summary

Among the main impurity gases N_2, O_2 and H_2O, nitrogen can be seen as virtually inert. A chemical influence on the caesium content within the experiment vessel (item (i) in table 8.1) is only expected after very long interaction times or at very high partial pressures due to the slow kinetics of chemical reactions with nitrogen. Further, at high pressures the effects observed with the rare gases (items (ii)–(iv)) can have an additional impact.

On the other hand, the impurities oxygen and water have a major influence on the evaporation rate and thus on the Cs content within the vessel due to chemical reactions with fast kinetics (item (i), see figure 4.5 (a)). However, the possibility of the recovery of the evaporation, the maintained functioning of the valve and the response of the evaporation rate on the dispenser heating current suggest, that the increased partial pressure of the impurity has no irreversible effect on the dispenser itself. Instead, it can be stated that just the transfer of the evaporated caesium through the oven is obstructed leading to the decreased evaporation rate: The increased partial pressure within the experiment yields higher fluxes of O_2 and/or H_2O onto the oven surfaces. As caesium is conveyed through the oven via multiple ad- and desorption processes this increased influx of impurities leads to a higher sticking probability, which consequently yields a modified equilibrium for the correlation of the dispenser heating current with the resulting evaporation rate from the oven. If the source of the increased impurity partial pressure is eradicated, the initial equilibrium is regained and thus the

evaporation rate increases again. The observed negligible effect of an increased water vapor pressure on the background evaporation from the oven reinforces this explanation as in this case much less ad- and desorption processes are performed before leaving the oven.

8.1.3 Working gas H_2

Since hydrogen can chemically react with caesium forming CsH (see section 4.3.1) and is introduced into the experiment not only as impurity with low partial pressure but as working gas with some Pa absolute pressure, each effect listed in table 8.1 has to be considered as influence on the Cs content within the vessel.

Figure 8.4 shows the effect of hydrogen feeding on the caesium content monitored by absorption spectroscopy, the SIDs, the oven temperatures and the RGA. The oven is operated at the working temperature of 260 °C and the dispenser heating current is set to the maximal value of 10 A. The evaporation rate from the oven prior to introducing hydrogen into the vessel is 0.1 mg/h. This low value can be explained by the depleted dispenser: As can be seen in the inlet towards the end of the operational day, turning off the dispenser heating current (at 621 minutes) has no effect on the evaporation rate. Therefore, the dispenser is already almost empty at the beginning of the investigations. However, it is to mention, that the following effect of hydrogen feeding also occurs with a newly activated dispenser (see e. g. figure 8.5) and cannot be ascribed to the depleted dispenser in this particular measurement.

The 'H_2 effect'

Feeding hydrogen gas into the experiment (at 483 minutes) results in an effect which was not expected and is not fully understood up to now: Despite the 4.5 Pa of possibly reactive hydrogen gas leading to chemical gettering and a decreasing duct temperature and despite an accompanied increasing partial pressure of H_2O, the signals from oven SID, local SID and absorption spectroscopy instantaneously increase strongly. This effect is hereafter called the *'H_2 effect'*. The substantially decreasing duct temperature from 254 °C down to 240 °C should normally lead to a decreasing evaporation rate, as was shown in section 7.3 and additionally in figure 8.1. Furthermore, the water vapor pressure is increased by about a factor of two, possibly as admixture to the hydrogen feeding via the gas supply system as was already observed for nitrogen and oxygen with He feeding in figure 8.2.

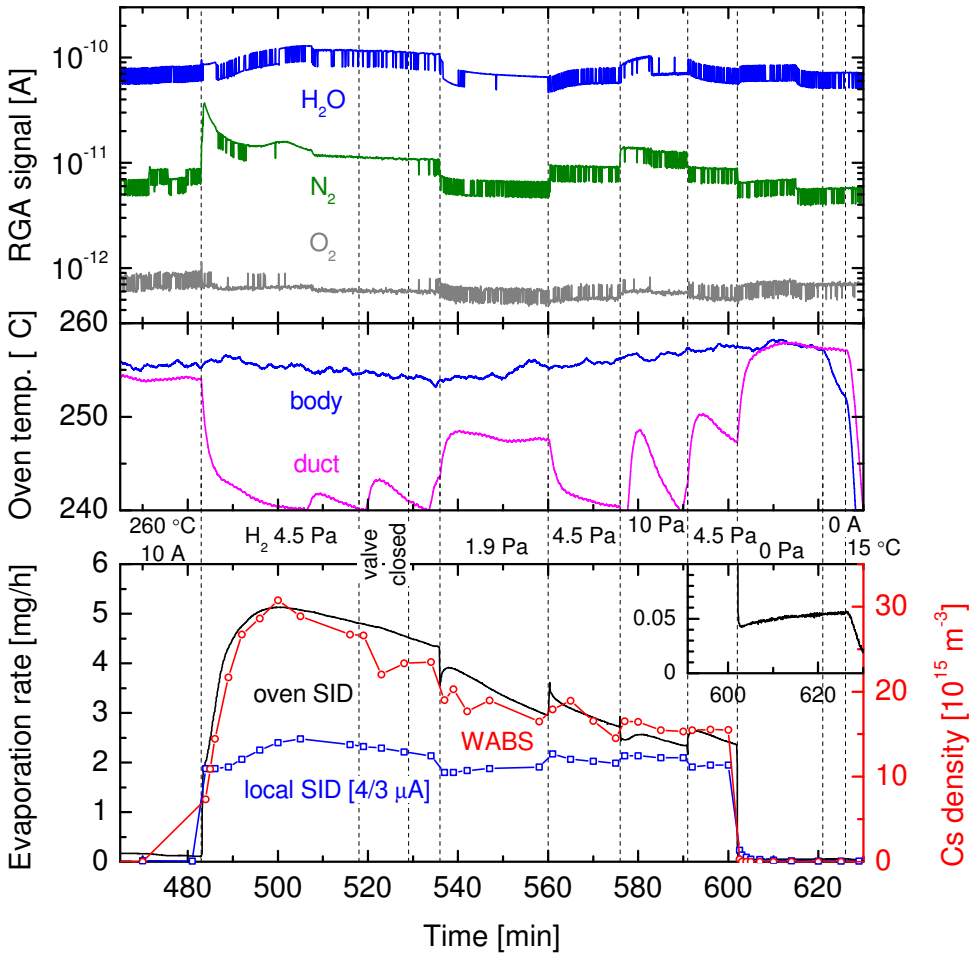

Figure 8.4: *Influence of hydrogen gas on the Cs content within the vessel at different hydrogen pressures. The inlet illustrates the depleted dispenser towards the end of the investigations.*

This increased water content should also yield a decreasing caesium content, as illustrated in figure 8.3. Additionally, hydrogen can react chemically with caesium and the pressure of 4.5 Pa can possibly hinder the expansion out of the oven. Nevertheless, the signal from the oven SID is increased by a factor of 50, the signal from the local SID by a factor of 100 and the measured caesium density increases from below the detection limit ($n_{\mathrm{Cs}} \lessapprox 3\text{–}4 \times 10^{14}\,\mathrm{m}^{-3}$) up to $3 \times 10^{16}\,\mathrm{m}^{-3}$ in maximum. For the local SID it is to mention, that the increased signal can again not be explained by the ionization effect, as this should contribute only about 50 nA (4.5 Pa, cross section 1 Å^2 [JRS03]).

Therefore, the hydrogen effect has a fundamental influence on the caesium content as it not only compensates the above described effects but moreover increases the Cs content by about two orders of magnitude.

Some observations on the H_2 effect can be made:

- The onset of the effect is instantaneous but the maximum is reached only after 15 minutes.
- Closing the valve has no function any more, which means that the dispenser can obviously no longer be the Cs source. Mind, that the described effects also occur with a not-depleted dispenser.
- The new source seems to be subject to depletion, since the Cs signals decrease.
- The oven temperatures, in particular the duct temperature, have only very limited influence on the evaporation.
- The oven SID and the absorption spectroscopy respond more sensitive on the Cs content than the local SID as can be seen at the different relative temporal behaviors of the signals.

The observations indicate that the increased Cs content originates from the front part of the oven. This location is also the source of the background evaporation which arises from caesium bound in the established uniform layers of caesium compounds at the oven surfaces (see section 7.3). Therefore, it seems obvious to consider chemical reactions of hydrogen with these caesium compounds as possible reagents for the increased caesium evaporation. Further, if the evaporation would originate from the main vessel, the local SID should respond more sensitive to it. Evaporation from the oven however is detected by the local SID with decreased sensitivity compared to the oven SID or the absorption spectroscopy, which was described at figures 7.6 and 7.8. The possibility of gas phase reactions between evaporated Cs compounds and the H_2 gas can be ruled out, since in this case the maximal effect should also be obtained instantaneously and not after 15 minutes. Therefore, the underlying reactions should occur at the oven surfaces. The observed decrease of the Cs content, ascribed to a possible depletion, can then be explained by a very high rate of decomposition of the caesium compounds at the oven surfaces due to the presence of H_2. The integrated evaporation of the oven SID signal in figure 8.4 yields a released amount of caesium of about 7.3 mg. Compared to the background evaporation, where the thermal decomposition of the compounds yields evaporation rates of about 0.05 mg/h (to be seen in the inlet in figure 8.4 for instance), the evaporation due to hydrogen gas is a factor of 100 higher. Even if about 10 % of the Cs content of the 100 mg dispenser remains within the oven bound at the surfaces, the reservoir would rapidly be depleted at these decomposition/evaporation rates.

On the other hand, the virtual independence of the evaporation from the duct temperature suggests, that either the decomposition process itself is only slightly dependent on temperature or that the source is not located in the oven duct. Apart from the possibly unknown location of the caesium reservoir, the appropriate chemical reaction(s) between hydrogen and caesium compounds that corroborate the assumed release of caesium are unknown and have to be investigated from a chemical point of view.

Furthermore, considering the signal of the oven SID **the H_2 effect seems to be pressure dependent**: Decreasing the absolute H_2 pressure from 4.5 Pa to 1.9 Pa leads to a decrease in the Cs evaporation. This behavior would be expected after the above described assumption of chemically released Cs, as a decreasing H_2 pressure results in a decreasing decomposition rate. On the other hand, an increase from 4.5 Pa to 10 Pa absolute pressure also yields a decline of the evaporation rate. This can then be ascribed to a non-negligible interference of the expansion out of the oven due to the high pressure. Considering the signal from the local SID, the increasingly hindered diffusion to the vessel walls with increasing pressure can be seen. While the dependence of the oven SID signal on the H_2 pressure confirms an evaporation out of the oven, the progression of the local SID signal can as well be ascribed to a reservoir within the main vessel.

Therefore, **the first conclusion** on the increased Cs content due to H_2 would be an unknown chemical reaction with existing Cs compounds at an unknown location, whereas more indications suggest the oven duct as the reservoir.

Further investigations

The H_2 effect is further examined, shown in figure 8.5. The oven is operated at 260 °C and 5 A heating current yielding an evaporation rate of about 1.7 mg/h. Opening the gas supply for hydrogen leads to the already observed increasing Cs signal in each diagnostic, namely both the SIDs and the absorption spectroscopy. This confirms that the observations in figure 8.4 cannot be ascribed to effects resulting from the depleted dispenser, such as evaporation of substances besides caesium due to the high heating current of 10 A. Furthermore, it can be seen in figure 8.5 that the increasing oxygen content accompanied with the gas feed, briefly leads to a decrease in the Cs evaporation. After O_2 is pumped down the H_2 effect can develop. Additionally, the RGA signal for nitrogen in figure 8.4 is more than twice as large as in figure 8.5. Hence, if nitrogen had a contribution to the decreasing signals in figure 8.5 the influence in figure 8.4 should be substantial,

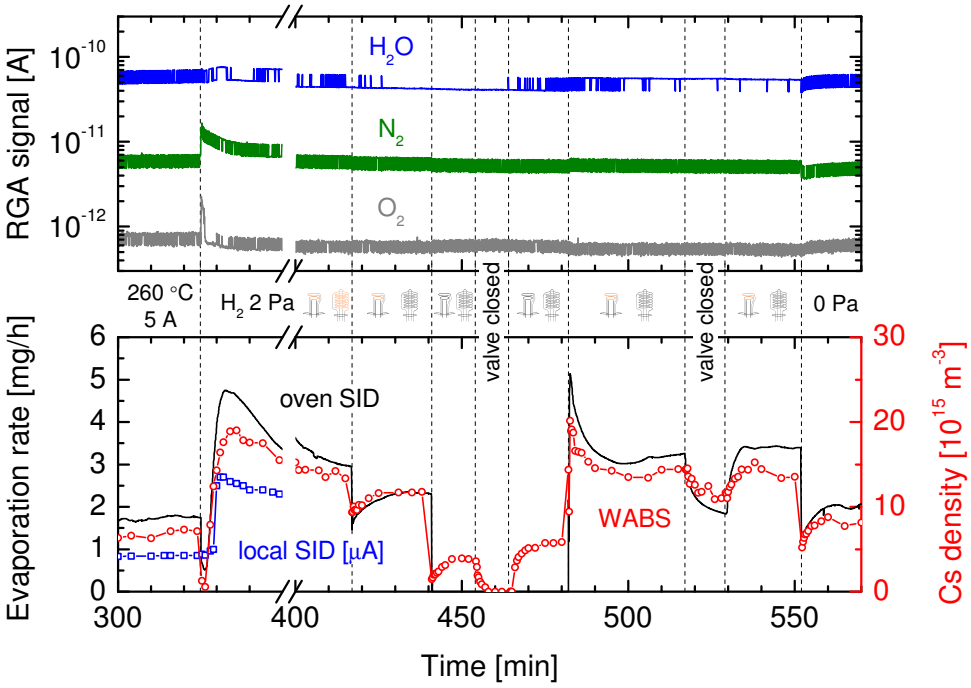

Figure 8.5: *Influence of hydrogen gas on the Cs content within the vessel for 2 Pa absolute pressure depending on the state of the heating currents for the SID wires (on/off).*

which is not observed. These two observations on O_2 and N_2 confirm the results obtained in section 8.1.2. Apart from these slight variations at the beginning in figure 8.5, the RGA signals maintain constant throughout the investigations.

In the following two possible bases of the H_2 effect are examined. Since each known chemical reaction of caesium with H_2, O_2 or H_2O occurs exothermically (see table 4.1) and the reverse processes to release Cs are consequently endothermic, a catalyzed chemical reaction is anticipated. Thereby it can be thought of a *photo-catalysis* due to the high intense broadband light source for the white light absorption spectroscopy on the one hand, and of a *thermally activated catalysis* via the red-hot filaments of the SIDs on the other hand.

It was shown, that the intense white light had no influence on the measured signals of the SIDs, regardless of whether hydrogen is present or not. However, the influences of the red-hot filaments can be seen in figure 8.5. At time mark 417 minutes the heating currents for the wires of the local SID are switched off. This leads to an instantaneous decrease in the measured signals from the oven SID as well as in the evaluated Cs density. Additionally switching off the heating currents of the oven SID wires leads to a further decrease of the Cs density. In this

state, the valve functions properly, confirming that the dispenser is the Cs source. Switching on the heating current for the oven SID wires again yields the increased Cs density, whereas now the dispenser is no longer the only source of caesium, as can be seen when the valve is closed. Shutting down the gas supply consequently leads to the decrease in the Cs signals, yielding comparable evaporation rates and Cs densities as prior to the gas feeding. In the following it can be observed (not shown in the figure), that without hydrogen the red-hot filaments have no influence on the Cs density within the vessel.

Therefore, it can be stated, that the increased Cs content due to hydrogen can only develop, if filaments with a temperature of the order of 1000 °C are present. These can act as catalytic converter for instance and therefore chemical reactions are accessible which would have to be omitted for reactions in thermal equilibrium with the environment. The partly preserved functionality of the valve compared to its ineffectiveness in figure 8.4 can be explained by the lower hydrogen pressure, which corroborates the pressure dependence of the H_2 effect.

Furthermore it can be observed that without the red-hot filaments a decreased Cs density is detected if hydrogen gas is present than compared to the vacuum state. This is the expected behavior considering the possible chemical reactions of H_2 with Cs and the decreasing duct temperature due to gas-conductive cooling by the absolute pressure of 2 Pa and due to the loss of the red-hot oven SID wires as additional heating channel.

Summary

It can be concluded, that hydrogen feeding can lead to a substantial increase of the Cs content within the experiment, if red-hot filaments are present. Thermally catalyzed chemical reactions of the hydrogen gas with already existing caesium compounds yielding an increased release of the bound Cs is suggested as possible explanatory approach. Cs compound layers at the surfaces of the duct of the dispenser oven are proposed as reservoir for this novel Cs source. The decomposition rate of this process is about two orders of magnitude larger than the background evaporation from the oven. The H_2 effect is shown to be pressure dependent, whereas around 5 Pa the maximal Cs content can be achieved. In this case, the Cs dispenser can be neglected as Cs source. Additionally it is to mention, that this effect does not occur in plasma operation, i. e. whether or not the SID wires are heated in plasma has no influence on the Cs density within the vessel. This indicates, that either the impact of the red-hot filaments is replaced by plasma processes or that the effect cannot occur in plasma environment.

8.2 Work function of a cesiated surface

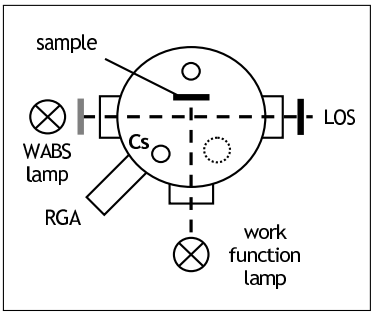

As described in section 4.2.2 coating a surface with caesium decreases its work function. However, for ion source relevant parameters (e. g. 10^{-6}–10^{-5} mbar background pressure) the behavior of pure Cs layers, illustrated in figure 4.4, is not expected due to the involvement of Cs compounds, as is already pointed out in section 4.3.2. Therefore, the dependencies of the work function of a cesiated surface under ion source relevant conditions has to be investigated particularly. Since the highly intense xenon lamp for the white light absorption spectroscopy (WABS lamp) significantly affects the work function measurements due to its broadband spectrum, the shutter in front of the WABS lamp has to be closed during work function measurements.

In NNBI ion sources the converter surface is typically made of molybdenum and the inner walls are made from copper [SFF$^+$06], whereas the vessel of the laboratory setup is made of stainless steel. Cs can react chemically with copper forming caesium oxycuprate $CsCuO_2$ [PTVZ09] and thus, the effects of a growing Cs layer could not be observed undisturbed using a copper sample. Molybdenum and stainless steel do not show this possibility for a chemical adsorption. However, the former would represent another material within the laboratory setup and thus, a stainless steel sample surface is investigated in a first step. Like this, the results on the work function of this dedicated sample surface, mounted on the sample holder in the center of the experiment vessel, can also be transfered to the vessel walls assisting the interpretations of observed effects in plasma (section 9.3).

Figure 8.6 illustrates the determination of the work function after the Fowler method. For two states of the sample surface ((1) high work function, low sample temperature and (2) low work function, high sample temperature) the photocurrents due to incidence of photons with different energies are shown in the top part. The x-error bars correspond to the transmitted energy range of the particular interference filters for the broad band emitting work function lamp. The photocurrents on the y-axis are divided by the corresponding relative intensity of the light source and the y-errors include the measurement error of the photocurrents as well as the error of the relative intensity of the work function lamp.

It can be seen that, as expected, for each case the photocurrents increase with increasing photon energy. If the work function is decreased ((1)→(2)) the applied set of filters is changed in order to fulfill the advisements in section 6.3.4, i. e. the

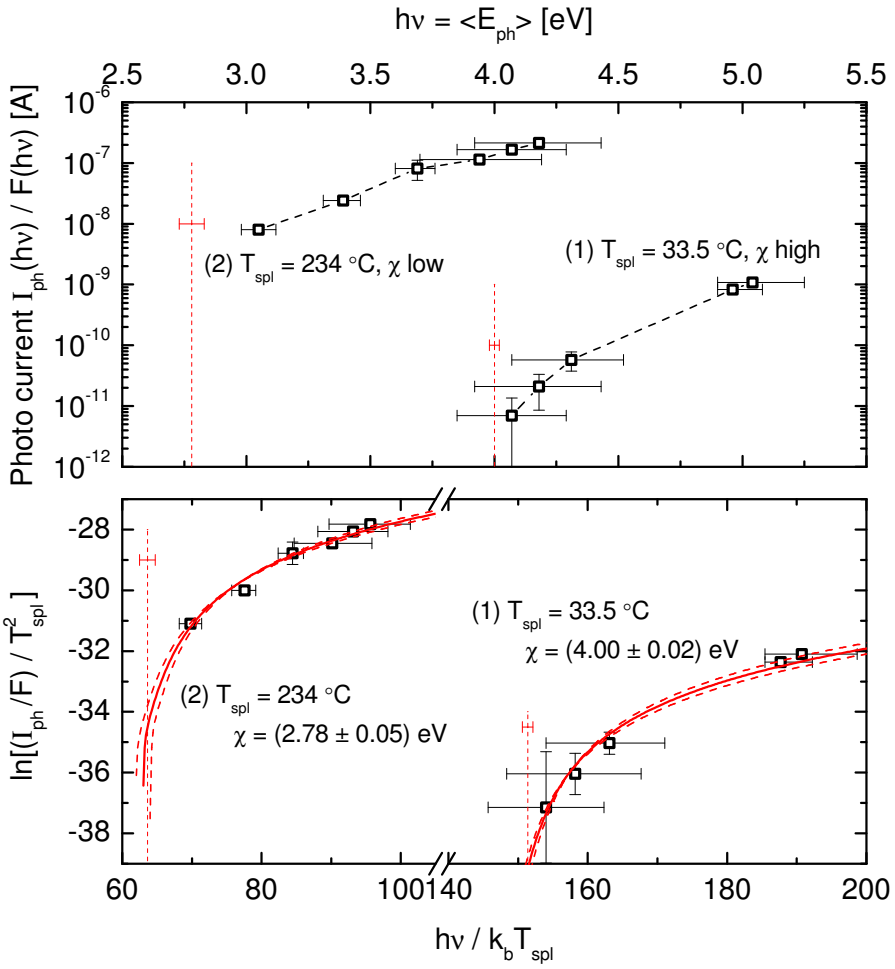

Figure 8.6: *Photocurrents depending on the mean photon energy measured for two different states of the sample (top part) and the corresponding Fowler plots for the determination of the work function including the fitted Fowler functions (bottom part). The evaluated work functions are depicted as thresholds in both parts.*

lowest possible photon energy should be close to the work function and the highest applied photon energy should not be too far from the work function. As expected, the decreased work function leads to increased photocurrents.

The determination of the work functions χ is shown in the bottom part of figure 8.6, where the Fowler plots of the measured signals from the top part are shown (see equation (6.28)). The resultant fitted Fowler functions are plotted as full lines together with the error margins as dashed lines. The determined work functions are plotted as vertical lines in both parts of the figure illustrating the threshold. It can be seen, that for case (2) the error of the evaluated work function is larger than for case (1). This can be attributed to the fact, that for case (1) the lowest photon energy (4.07 eV) is closer to the work function (4.00 eV)

than for case (2) (3.05 eV vs. 2.78 eV). Therefore the threshold at $\langle E_{\mathrm{ph}} \rangle \approx \chi$ is less pronounced for case (2) which leads to a larger error in the evaluation of χ as the dependency of the photocurrents on the photon energy gets flatter with increasing distance from the actual work function which reduces the sensitivity of the Fowler fit. Throughout the investigations on work functions the shown error bars represent this uncertainty of the performed Fowler fit.

8.2.1 Temperature dependence of the work function

Figure 8.7 shows the work function of the stainless steel sample depending on the temperature of the sample. The sample was cleaned mechanically and chemically before it was mounted on the sample holder. However, it was in contact with ambient air until installation in the vessel and evacuation could be conducted. Therefore adsorption of nitrogen, oxygen and water on the sample surface are to be expected. In the top part of the figure the temporal progression of the background pressure and the RGA signals for N_2, O_2 and H_2O during the heating process are shown supplementally.

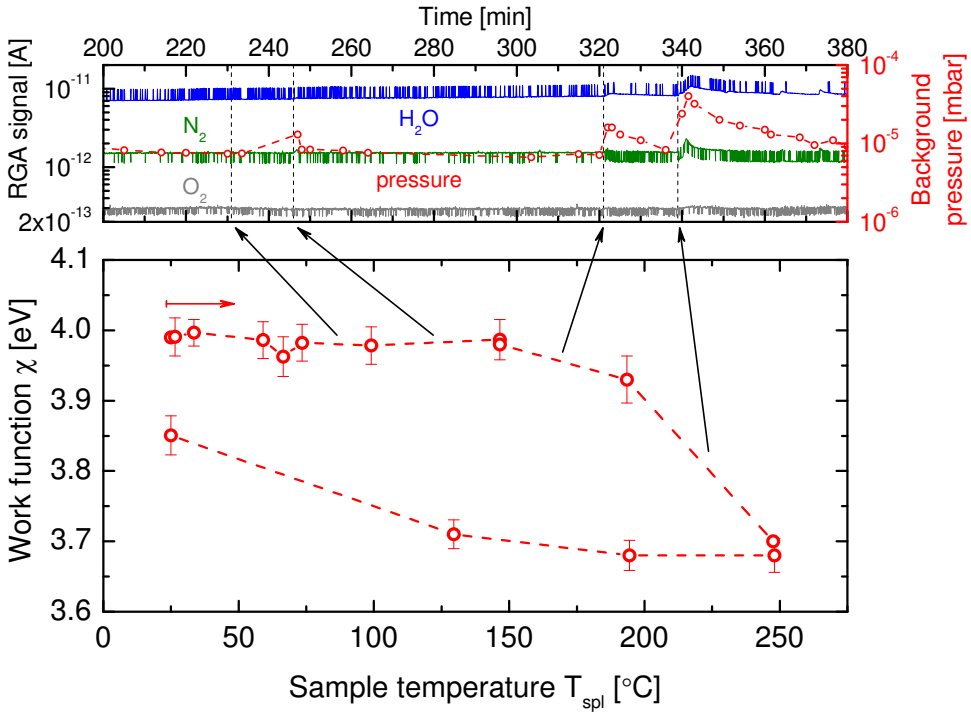

Figure 8.7: *Work function of the stainless steel sample depending on the sample temperature (bottom part) and the evolution of the background pressure and the RGA signals monitoring the heating process (top part).*

The initial stainless steel sample at 25 °C has a work function of about 4.0 eV. Up to sample temperatures of 100 °C no variation in χ can be observed, neither in the signals from the background pressure or the RGA. Heating the sample to 150 °C shows a slight and temporary increase of the background pressure whereas the RGA signals and the work function still remain unaffected. Further increasing the temperature to about 200 °C and subsequently to 250 °C leads to a further increasing background pressure and slightly increasing RGA signals. The observed evaporation of adsorbed particles from the sample surface is accompanied by a decreasing work function down to 3.9 eV and 3.7 eV, respectively. With decreasing sample temperature the adsorption of background particles is augmented again and the work function gradually increases up to 3.85 eV.

Referring to figure 6.8 (b), a direct impact of the temperature on the photoinduced emission of electrons from the surface is not expected, since even the lowest photon energy used for these measurements (4.07 eV) is about 0.4 eV greater than the work function at 250 °C (3.7 eV), i. e. $(h\nu - \chi) > 0.4$. Furthermore, if the decrease of χ would solely arise from a direct influence of the sample temperature, cooling the sample should yield an equivalent increase of χ. As this is not observed, the reduction of χ is to be attributed to a cleaning effect of the surface which can be subject to a hysteresis.

8.2.2 Cesiation of the sample surface

In figure 8.8 (a) the work function of the stainless steel sample with increasing caesium evaporation is shown together with the photocurrent resulting from the interference filter for 313 nm ($\langle E_{\mathrm{ph}} \rangle = 3.94$ eV). The sample is baked out at 250 °C prior to the investigations and it is left to cool down to 22 °C afterwards. During the measurements the heating circuit is switched off, but due to the intrinsic heating by the red-hot SID wires an equilibrium temperature of about 80 °C is reached after 200 minutes.

As already mentioned, the light source for the absorption spectroscopy (WABS lamp) disturbs the work function measurements, why the shutter has to be closed during the measurements of the photocurrents. Certainly, for measuring the Cs density, the shutter has to be opened again. This repetitive opening and closing leads to the spikes observable in the SID signal in figure 8.8 (a). The reasons for the increased SID current due to incidence of highly intense high energetic photons involve photo ionization of Cs on the one hand and photo emission of electrons from the vessel surfaces and the SID wires on the other hand. The

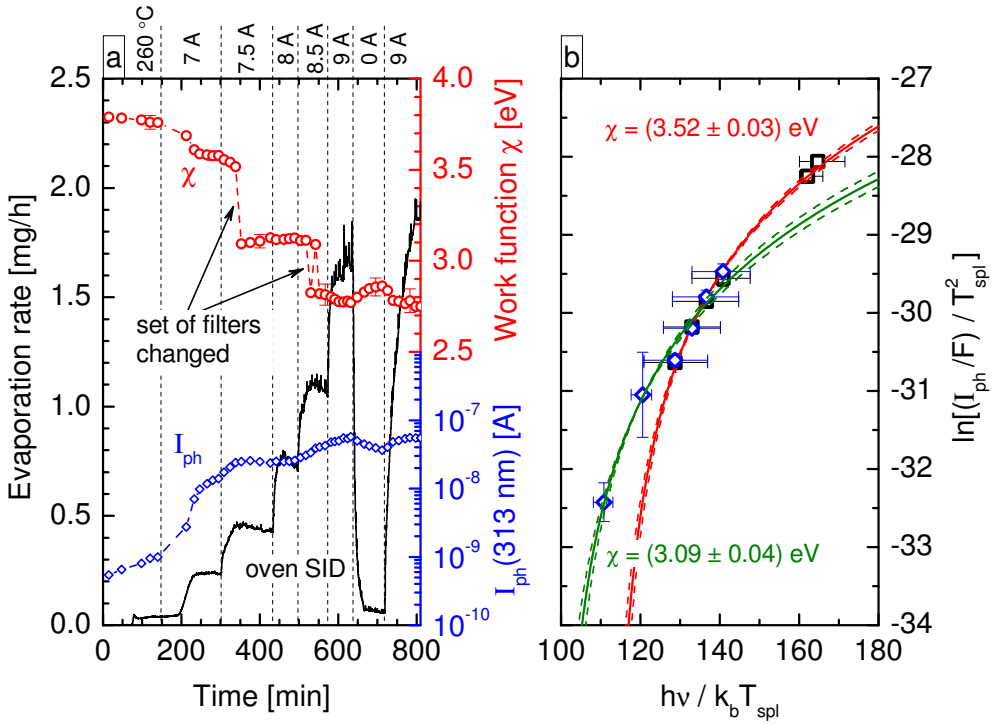

Figure 8.8: (a) *Increasing Cs evaporation from the oven and its influence on the work function of a stainless steel sample together with the photocurrent arising from the 313 nm filter.* **(b)** *Fowler plots before and after the first filter exchange.*

latter are accelerated due to the biases of the oven SID and the work function measurement and are subsequently capable of ionizing the background gas and the caesium vapor. Therefore, the influence of the WABS lamp increases with increasing Cs evaporation. However, the disturbance remains below 5 % and thus it is unproblematic for the monitoring of the cesiation process.

Basically, the increasing caesium evaporation of up to 1.6 mg/h (dispenser heating current 7–9 A) leads to cesiation of the sample surface accompanied by a decrease of the work function from initially 3.8 eV down to 2.75 eV. However, it can be seen, that the required change of the applied set of interference filters causes jumps in the determined work function. As this is not expected from a physical point of view and the jumps are not observed in the corresponding photocurrent, the explanation should be connected to the evaluation of χ itself.

Figure 8.8 (b) shows the two Fowler plots before (black squares) and after (blue diamonds) the first jump in the work function, which is caused by exchanging the filters for 239 nm and 254 nm by the filters for 334 nm and 365 nm. At the four photocurrents in between it can be seen, that the measurement of the currents is very reproducible. However, the currents arising from the high energetic photons

due to the filters for 239 nm and 254 nm lead to the fitting of a much steeper Fowler function (depicted in red) accompanied by the evaluation of an overestimated work function of 3.52 eV. On the other hand, the currents due to the low energetic photons at 334 nm and 365 nm pronounce the actual threshold and the corresponding Fowler function is much flatter (green curve). Hence, a more realistic work function of 3.09 eV is determined and it can clearly be recognized that the photocurrents from high energetic photons are underestimated by the Fowler theory. This behavior illustrates the importance of using the appropriate set of filters for the determination of work functions after the Fowler theory and is described in detail in section 6.3.4.

The second jump to be seen in figure 8.8 (a) is to be ascribed to exchanging[1] the 270 nm filter by the 405 nm filter ($\langle E_{\mathrm{ph}} \rangle = 3.05\,\mathrm{eV}$) which decreases the evaluated work function from about 3.1 eV down to about 2.8 eV. Here, too, the explanations from the preceding paragraph can be applied. However, an alternative explanatory approach can be given additionally: If 3.1 eV would be the correct work function, then an inciding photon energy of 3.05 eV would not be capable of inducing a measurable photocurrent. Therefore, the work function must be below 3.05 eV.

Correction of erroneous work functions

Since it can be stated, that only the work functions evaluated after the second filter exchange in figure 8.8 (a) are close to the actual work function of the sample, the beforehand determined values have to be corrected. This is demonstrated in figure 8.9.

The procedure for correcting work functions is performed following section 6.3.4. Accordingly, the measured photocurrents $I_{\mathrm{ph}}^{\mathrm{meas}}$ arising from the particular filter for 313 nm are plotted against the evaluated work functions and compared with the theoretical curves derived via the Fowler theory (equation (6.29), red line $I_{\mathrm{ph}}^{\mathrm{Fowler}}$) and via another case of approximation (case II, equation (6.30), gray shaded area $I_{\mathrm{ph}}^{\mathrm{case\,II}}$). For the '0' value, for which $\langle E_{\mathrm{ph}} \rangle \approx \chi$ should apply, the first measured work function $\chi_0 = 3.79\,\mathrm{eV}$ is taken and the curve after the Fowler theory is calculated for $T_{\mathrm{spl}} = T_{\mathrm{spl},0} = 22.5\,^{\circ}\mathrm{C}$. For case II, Fermi energies have to be considered additionally. The Fermi energy of the stainless steel sample is approximated by the Fermi energy of iron: $E_{\mathrm{F}}^{\mathrm{Fe}} = 11.1\,\mathrm{eV}$ [Lid05]. And the bulk value of the Fermi energy for caesium is $E_{\mathrm{F}}^{\mathrm{Cs}} = 1.6\,\mathrm{eV}$ [Lid05]. For the present

[1] Actually this exchange was done twice to verify the observed effect.

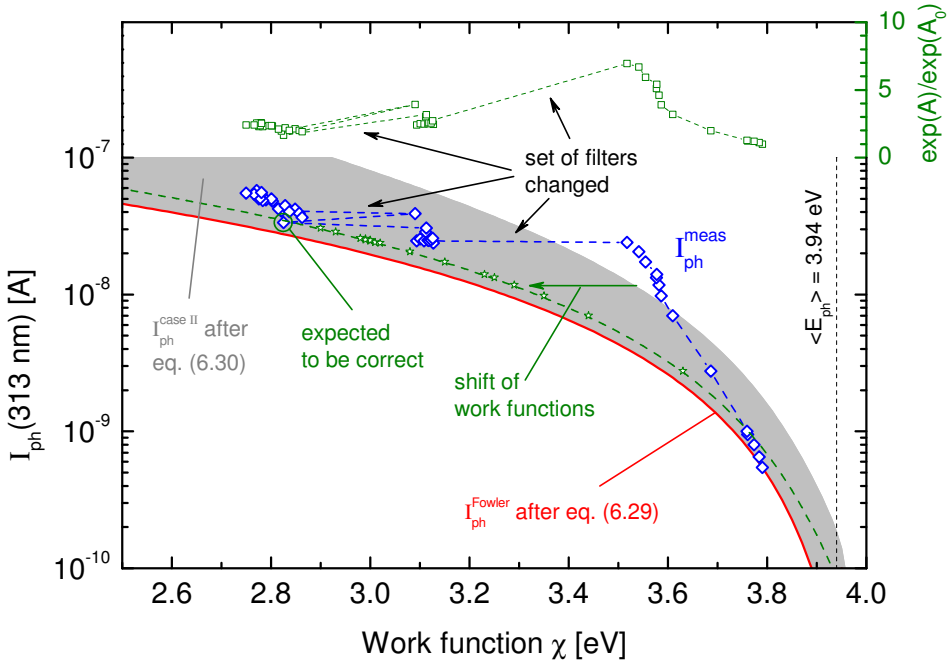

Figure 8.9: *Measured photocurrents arising from the 313 nm filter plotted against the evaluated work functions (see figure 8.8 (a)) and compared to two theoretical curves. The procedure for correcting the work functions is illustrated. The top part shows the fitting constant A of the Fowler fit in a relative representation.*

analysis it is now assumed that covering the stainless steel sample with caesium leads to a monotonous decrease of the Fermi energy from initially 11.1 eV down to 1.6 eV. Thus, for the calculation of the theoretical photocurrent after case II the following parameters are used: $T_{\mathrm{spl}} = 250\,^{\circ}\mathrm{C}$, $E_{\mathrm{F},0} = 11.1\,\mathrm{eV}$, $E_{\mathrm{F}} = 1.6\,\mathrm{eV}$. By using the lowest sample temperature of 22.5 °C for the Fowler case and the highest value of 250 °C for case II the maximal scope of this approach is obtained.

For illustration the mean photon energy of the photons transmitted by the 313 nm filter for 3.94 eV is depicted additionally in figure 8.9 and in the top part of the figure the relative variation of the constant A from the fitting routine after Fowler (see equation (6.28)) is plotted.

It can now be observed, that with decreasing work function, the measured photocurrents $I_{\mathrm{ph}}^{\mathrm{meas}}$ deviate more and more from the theoretical curve after Fowler $I_{\mathrm{ph}}^{\mathrm{Fowler}}$ and the constant A rises. This is the expected behavior described in section 6.3.4 and constitutes the erroneously evaluation of work functions. The latter is substantiated by the effect of changing the applied set of filters: By decreasing the minimally applied photon energy, work functions can be determined which are very close to the theoretical values. This is also accompanied by a

drastic decrease of the fitting constant A. Further decreasing the minimal photon energy by the second exchange of interference filters leads to the evaluation of further decreased work functions and even smaller values of the constant A. Thus, for the present purpose the first evaluated work function after the second filter exchange is considered to be realistic.

In section 6.3.4 a procedure for correcting work functions is introduced. It is based on the (extended) relation (6.31) after which each value $I_{\mathrm{ph}}^{\mathrm{meas}}(\chi^{\mathrm{meas}})$ must lie within the gray shaded area. For the present case in figure 8.9 this would lead to a correction of the work functions just for the seven data points above the gray shaded area. For instance, the uppermost value of 3.52 eV would be corrected to a work function of 3.37 eV. However, the change of the filter set shows, that the actual work function is even lower (3.09 eV in the example). Thus, the correction procedure can be extended in this particular case: The first evaluated work function after the second filter exchange is considered to be realistic, as mentioned above, and each work function prior to this value is corrected in a way, that a continuous transition is achieved from the first values of work functions to the more realistic work functions determined with the more adequate set of filters. The corresponding theoretical curve (green dashed line) is obtained by using the case II equation (6.30) and a fictional Fermi energy of $E_{\mathrm{F}} = 8\,\mathrm{eV}$. It should be noted, that this Fermi energy has no physical meaning as it is just used to obtain the postulated continuous transition. The correction of one of the work functions is illustrated by the green arrow. It can be seen, that with this approach also the values determined after the first exchange of filters are corrected. This can be seen as the proper behavior, as otherwise the second filter exchange should have a much less pronounced impact.

Interpretation of the evolution of the work function

The corrected values of the work functions, χ_{corr}, compared to the initially determined ones, χ, are shown in figure 8.10 (a). It can be seen, that due to the correction a continuous decrease of the work function without non-physical jumps is achieved. Owing to the correction procedure, the corrected work functions now show a very similar evolution to the photocurrents plotted in figure 8.8 (a).

Part (b) of figure 8.10 shows the (corrected) work functions of the stainless steel sample depending on the Cs evaporation rate (top part) and thus depending on the Cs flux onto the sample. The scale of the χ-axis is the same as in part (a) to facilitate the reference to the corresponding time dependent values. In the bottom

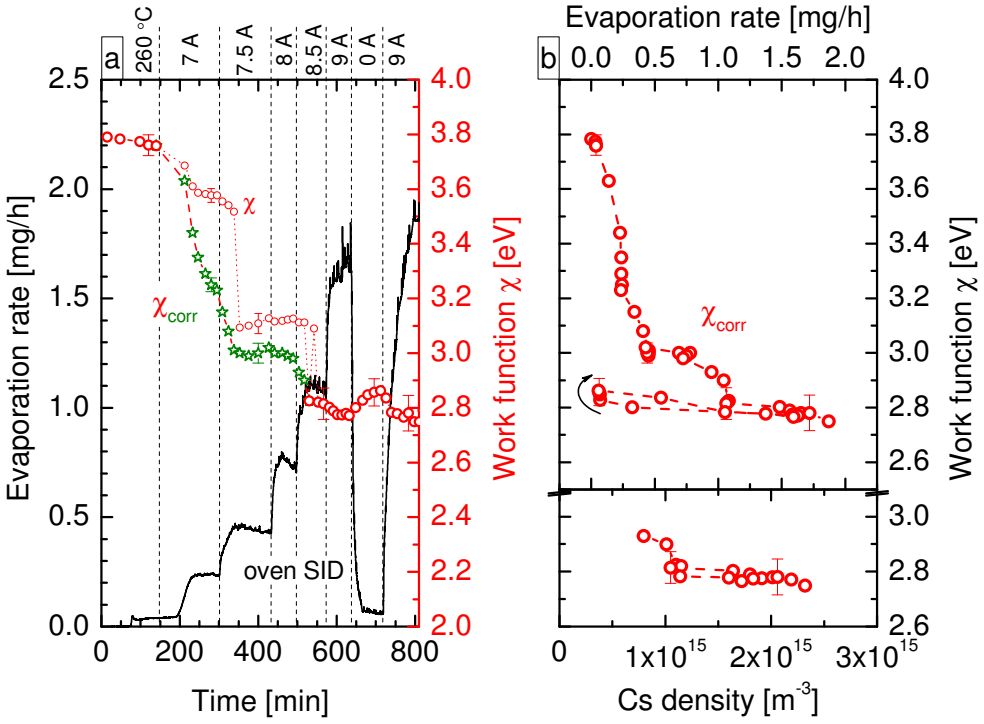

Figure 8.10: **(a)** *Measured and corrected work functions of the stainless steel sample with increasing evaporation.* **(b)** *Work functions depending on the evaporation rate (top, same χ-axis scale as for part a) and on the Cs density (bottom).*

part the same work functions are plotted against the corresponding Cs densities, as soon as the detection limit for the absorption spectroscopy is exceeded. As a side note, the correlation of evaporation rate and Cs density is shown in figure 7.9.

Introducing the cesiation process leads to a steep decrease of the work function from initially 3.8 eV down to 3.0 eV at an evaporation rate of 0.45 mg/h. An increase of the evaporation rate up to 0.75 mg/h has virtually no influence on the work function of the sample at this state. Only a further increase of the Cs evaporation to 1.1 mg/h and subsequently to 1.65 mg/h yields a further decreasing work function down to 2.75 eV.

The temporary saturation of the work function at 3.0 eV could possibly be explained by a non-homogeneous covering of the surface, which is homogenized by increasing the Cs flux onto the sample. At the highest evaporation rate the work function of the sample seems to saturate at a minimum value of 2.75 eV, as even a constant flux of Cs over about 40 minutes does not lead to a further decrease of the work function. Stopping the Cs evaporation leads to an increasing work function whereas via re-engaging the Cs flux onto the sample the work function of 2.75 eV can be regained.

In figure 8.10 (b) it can be seen clearly, that the work function of the cesiated stainless steel sample saturates at values just below 2.8 eV. An increase of the evaporation rate by a factor of two, which is directly correlated to the doubling of the Cs density and thus of the Cs flux onto the sample surface, has virtually no influence. In order to address this effect, the actual thickness of the Cs layer on the sample surface is estimated via balancing adsorption and desorption fluxes: the desorption flux is taken from equation (4.13) and the adsorption flux is calculated from the Cs density assuming a sticking coefficient of unity. For a sample temperature of 80 ℃ and a Cs density of $1 \times 10^{15}\,\mathrm{m}^{-3}$ (produced by an evaporation rate of 1 mg/h) an equilibrium coverage of about 0.85 monolayers is determined, increasing to only 0.86 monolayers with doubled Cs density. This negligible influence is correlated to the desorption flux, which has a very steep dependence on the coverage (see figure 4.3 (a)). Thus, the saturation of the work function could be ascribed to the independence of the Cs layer on the sample surface from the Cs flux onto the surface. However, the estimation also shows, that for the given conditions the adsorption of pure Cs would lead to a layer 'thickness' of less than a full monolayer. Referring to figure 4.4 this should yield a work function of slightly below the theoretical bulk value for caesium of 2.14 eV [Mic77], whereas the measured work function is about 0.6 eV higher. As pointed out in section 6.3.4, it has to be kept in mind that the measured values are always an upper limit for the actual work function. However, figure 8.9 gives no indication for a required correction of the lowest work functions of this order of magnitude and thus the deviation of 0.6 eV seems to be too large to be reduced to the uncertainty of the Fowler method.

Thus, it can be concluded that the work function of the cesiated sample surface is not determined by a pure Cs layer. Due to the equal (or even higher) fluxes of background particles onto the surface it is more likely to consider the growth of Cs compound layers which obviously have higher work functions due to their non-metallic nature.

8.2.3 Impact of elevated temperatures on the Cs layer

As already shown in figure 8.7 heating the sample leads to a cleaning effect which reduces the work function of the bare sample. For the Cs layer on the sample surface elevated sample temperatures can possibly also be beneficial, since the influence of co-adsorbed impurities is reduced.

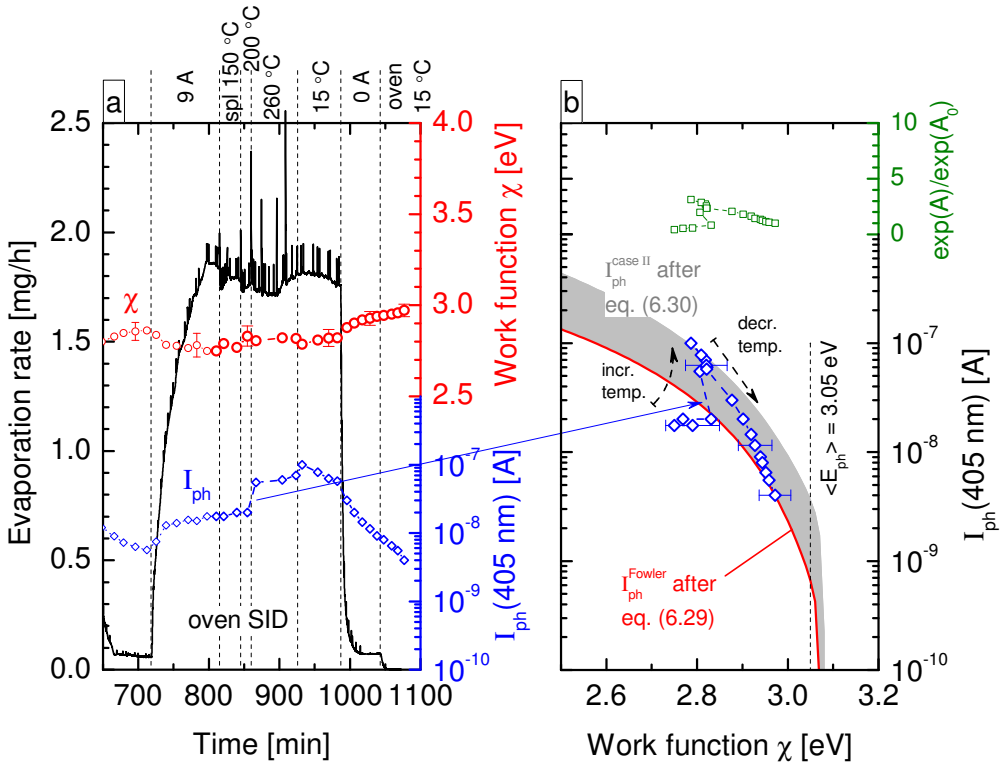

Figure 8.11: (a) *Influence of heating the stainless steel sample on its work function and on the photo current for the 405 nm filter during cesiation.* **(b)** *Analysis of the accuracy of the determined work functions after section 6.3.4.*

Heating during cesiation

Figure 8.11 (a) shows the influence of heating the sample while evaporating Cs. The measured work function is shown at the top while the photocurrent arising from the 405 nm filter ($\langle E_{\mathrm{ph}} \rangle = 3.05\,\mathrm{eV}$) is plotted at the bottom. The investigations here are performed just after the cesiation process described in the preceding section. Thus, the evaporation rate of about 1.8 mg/h leads to a work function of slightly below 2.8 eV at a sample temperature of about 80 °C.

Heating the sample to 150 °C and subsequently to 200 °C causes temporarily a rising background pressure (not shown) and an increasing SID signal (observable as additional peaks besides the recurring disturbance due to the WABS lamp). While the former is to be ascribed to the evaporation of adsorbed residual gases, the latter indicates the evaporation of caesium from the sample surface. Whether the evaporation occurs directly or out of caesium compounds cannot be distinguished. However, an influence on the work function or on the photocurrent cannot be observed. Increasing the temperature further to 260 °C again yields an increasing background pressure and temporary peaks in the SID sig-

nal. The measured work function is again unaffected whereas the photocurrent now increases significantly. Cooling the sample leads to slightly decreasing photocurrents whereas the work function is only affected when the Cs evaporation is stopped. One and a half hour after cesiation the work function has increased to about 3.0 eV.

The measured temporary evaporation of adsorbed particles from the sample surface upon heating is caused by a varied balance of adsorption and desorption fluxes for the residual gases as well as for the Cs vapor due to the elevated surface temperature. For Cs similar estimations as in section 8.2.2 can be conducted leading to a decreasing covering fraction from initially 0.86 monolayers at 80 °C down to 0.70 monolayers at 260 °C. In contrast to the previous discussion this decrease should result in a varied work function, if pure Cs layers were determinant. However, since Cs compounds are most likely involved, the actual influence of the surface temperature on the condition of the coating cannot be assessed from a theoretical point of view. The measurements, however, show a constant work function and, by contrast, significantly increased photocurrents. This deviation can indicate a wrongly evaluated work function which is addressed via the procedure described in section 6.3.4, that was already performed in figure 8.9.

Figure 8.11 (b) shows the measured photocurrents resulting from the filter for 405 nm ($\langle E_{\mathrm{ph}} \rangle = 3.05\,\mathrm{eV}$) plotted against the evaluated work functions and compared to the theoretical evolution after Fowler and after case II (see sections 6.3.4 and 8.2.2 for details). The '0' value is taken as the last measured work function of $\chi = 2.97\,\mathrm{eV}$ to fulfill $\langle E_{\mathrm{ph}} \rangle \approx \chi$ and the range of the Fermi energy is again assumed to be $E_{\mathrm{F}}^{\mathrm{Cs}} = 1.6\,\mathrm{eV} \leq E_{\mathrm{F}} \leq 11.1\,\mathrm{eV} = E_{\mathrm{F}}^{\mathrm{Fe}}$. The evolution of the values due to heating and cooling the sample is indicated by the dashed black arrows and the measured jump in the photocurrent due to the heating to 260 °C is denoted by the full blue arrow. The question arises whether or not the values corresponding to the high sample temperatures are actually to be ascribed to lower work functions.

A procedure for correcting work functions as performed in section 8.2.2 cannot be done here since no further interference filters were available and thus the actual uncertainty due to a possibly inappropriate set of filters cannot be assessed. However, as described in section 6.3.4, each measured value $I_{\mathrm{ph}}^{\mathrm{meas}}(\chi)$ within the gray shaded area can be explained by a variation of the Fermi energy within the stated range and no correction of work functions within this area is to be done. Applied to the present case, the evolution of the measured values due to the

decreasing sample temperature would be ascribed to an increasing Fermi energy from 1.6 eV for the highest photocurrent up to 11.1 eV for the lowest photocurrent. However, the values prior to heating the sample deviate from this behavior as they are below the gray shaded area. This indicates a Fermi energy larger than the '0' value, which in turn would imply, that the last value ('0') should be assigned a Fermi energy of below 11.1 eV. This would lead to a reduced upper boundary of the gray shaded area and thus, the uppermost values would have to be corrected. However, as pointed out in section 6.3.4, an assessment of the accuracy of values below the gray shaded area cannot be performed. Therefore, the reduced Fermi energy of the '0' value cannot be assessed and thus, no correction can be conducted. Moreover, if the errors of the evaluated work functions are considered additionally, the deviations from the gray shaded area reduce to a negligible amount and a possible correction would be very small. This is also indicated by the fitting constant A, which is plotted supplementally at the top of the figure relative to the initial value '0': compared to figure 8.9, where great deviations were to be observed and work functions had to be corrected, the increase in the constant A is rather negligible in the present case.

Therefore, the evaluated work functions in figure 8.11 (a) are not corrected keeping in mind the possible overestimation at elevated sample temperatures. The sudden increase in the photocurrent upon heating the sample to 260 °C is ascribed to a reduction of the Fermi energy while the work function is probably also reduced, which however cannot be measured with the applied set of interference filters.

The change in E_F and χ due to heating the sample while maintaining a constant flux of caesium onto the surface can be explained by a cleaning or 'healing' effect of the adsorbed layer, where impurities or defects within the layer are replenished. Cooling the sample and stopping the cesiation process leads to a degradation of the layer and thus to decreasing photocurrents and increasing work functions.

Furthermore, an interesting résumé can be drawn: The measured photocurrents are directly correlated to the probability for releasing an electron from the surface. This probability also determines the process of converting hydrogen particles to negative ions. Therefore, concerning the surface formation of negative hydrogen ions, the measured photocurrent can give valuable information on the condition of the converter surface and is moreover an easy to apply monitoring tool.

Cesiation onto a hot sample surface

Figure 8.12 shows the influence of heating a cesiated stainless steel sample without the presence of a Cs flux onto the sample surface and the influence of a subsequent cesiation process onto the hot sample surface. The work function is plotted at the top and at the bottom the photocurrent arising from the 405 nm filter is shown.

The initial cesiated stainless steel sample has a work function of slightly below 3.1 eV due to degradation of the Cs (compound) layer in vacuum (compare figure 8.11 (a) to the end) and only a very low photocurrent can be drawn. The slightly increasing photocurrent at the beginning can be ascribed to the increasing sample temperature due to the red-hot SID wires (turned on at 120 minutes). At 200 minutes the sample temperature intrinsically raised to about 60 °C. The measured influence on the work function is still negligible at this state.

Heating the sample to 100 °C causes a sudden evaporation of Cs from the sample surface. It is detected by the oven SID yielding a signal corresponding to an evaporation rate of about 0.2 mg/h, which is similar to the observations in figure 8.11 (a). Together with the accompanied evaporation of further adsorbates (observable at the increasing background pressure, not shown) an increase of the photocurrent of one order of magnitude and a slight decrease of the work function is achieved. Further heating the sample successively to 200 °C each time leads to a temporarily increased background pressure accompanied by further increasing photocurrents and the work function is decreased to 2.85 eV. In contrast to figure 8.11 (a) these subsequent temperature raises cause only negligible evaporation of further Cs from the sample surface, which can be explained by the absence of a steady flux of Cs onto the surface compared to figure 8.11 (a). However, the terminal temperature increase up to 260 °C in fact leads to a measurable Cs signal at the oven SID (although it is barely observable at this scale). The result is an increasing work function and a slightly decreasing photocurrent.

Neither the evaluated work functions nor the measured photocurrents indicate effects assignable to erroneous work functions. Therefore, an analysis as performed in figures 8.9 and 8.11 (b) is omitted here keeping in mind the possible overestimation of the evaluated work functions via the Fowler method.

The observed influences in figure 8.12 can be explained by a cleaning effect of the Cs (compound) layer on the sample surface. Since the sample is exposed to the residual gases within the vacuum vessel, these impurities are responsible for the degradation of the layer. Heating the sample evaporates the impurities and the work function enhances. However, too high surface temperatures of about

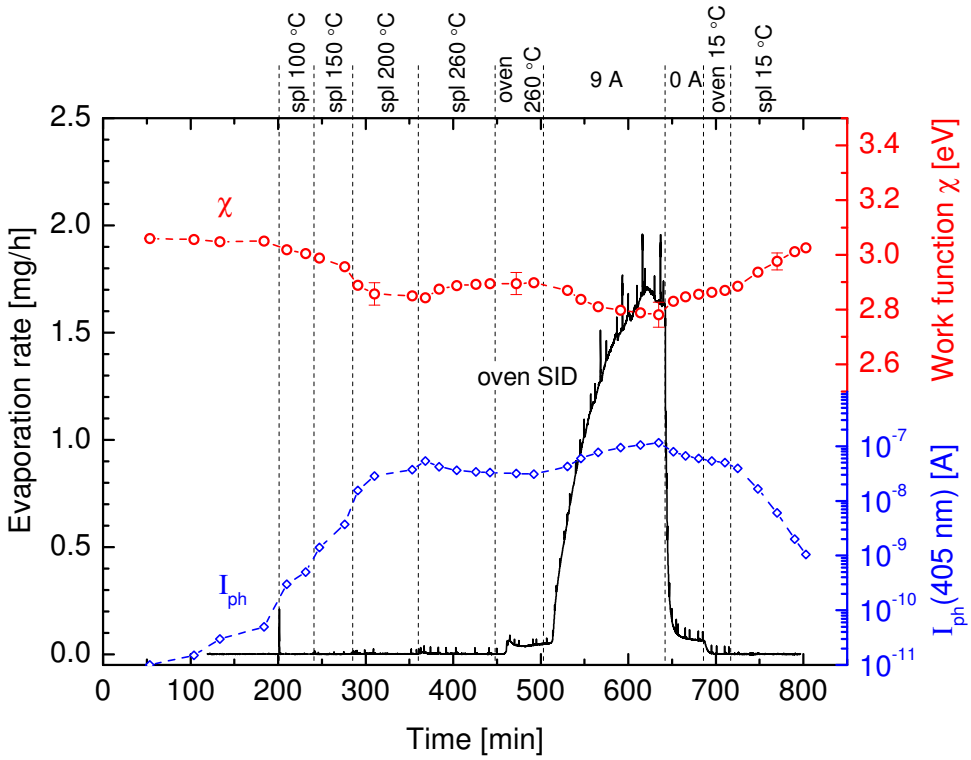

Figure 8.12: *Influence of heating a cesiated stainless steel sample in absence of a Cs flux onto the sample and the effect of cesiating the hot sample surface.*

260 °C can lead to an effective evaporation of Cs from the layer which leads to an increasing work function. This is in contrast to the observations in figure 8.11 (a), where a replenishment of the Cs layer is achieved by heating the sample to 260 °C. The main difference to the present case is the presence of a Cs flux which is required to compensate for the diminishing of the amount of Cs on the surface.

This can also be observed in the following in figure 8.12 by the impact of cesiating the hot sample surface. The sample temperature is set to 260 °C and the work function saturates at 2.9 eV. Engaging a Cs flux onto the surface via evaporation rates of up to 1.7 mg/h enhances the work function down to slightly below 2.8 eV. The photocurrent simultaneously also increases to values very similar to the observations in figure 8.11 (a). Stopping the Cs flux onto the sample yields increasing work functions and decreasing photo currents again. Furthermore it can be seen clearly, that cooling down the sample leads to an increased rate of degradation for both parameters.

These observations confirm the statement, that high surface temperatures in presence of a Cs flux onto the sample lead to the replenishment of the layer accompanied by decreasing work functions and increasing photocurrents. Furthermore,

an elevated surface temperature not only cleans the layer but is also beneficial against degradation of the layer after cesiation. Moreover it seems irrelevant if the surface is cesiated and afterwards heated or the other way round: in both cases the minimal work function is slightly below 2.8 eV and the maximal photocurrent for the 405 nm filter is at about 0.1 µA.

8.2.4 Summary

The performed investigations on the work function of a cesiated stainless steel surface are summarized in figure 8.13. The 3D-plot shows the work function on the z-axis depending on the surface temperature and on the evaporation rate from the oven. The corresponding single investigations are recognizable by the different colors of the trajectories. In summary the following conclusions can be drawn:

- The minimum obtainable work function for the stainless steel sample due to cesiation in vacuum is below 2.75 eV. An evaporation rate of 1 mg/h is sufficient for achieving and maintaining this value.
- Elevated surface temperatures are beneficial for cleaning and against degradation, where a temperature of about 200 °C seems optimal.
- The order of cesiation and heating is subordinate.
- The determined work functions are most likely overestimated, especially at high surface temperatures. The actual uncertainty is difficult to assess, but is typically of the order of 0.1 eV.
- Observation of the photocurrents gives valuable additional information of the surface condition, since the direct correlation between emitted electrons and measured current is much less subject to disturbances than the determination of a quantitative value with several intrinsic issues of the evaluation procedure.

For the evaluation of absolute work functions it would be very beneficial in future to use additional interference filters with longer transmission wavelengths for more reliable observations of low work functions. Another approach is to replace the light source consisting of a broadband emitting high pressure mercury lamp and a set of interference filters by lasers. Having several tunable diode lasers with complementary wavelength ranges, the threshold at $E_{\mathrm{ph}} \approx \chi$ can be determined very accurately and for $E_{\mathrm{ph}} > \chi$ the Fowler function could be traced directly.

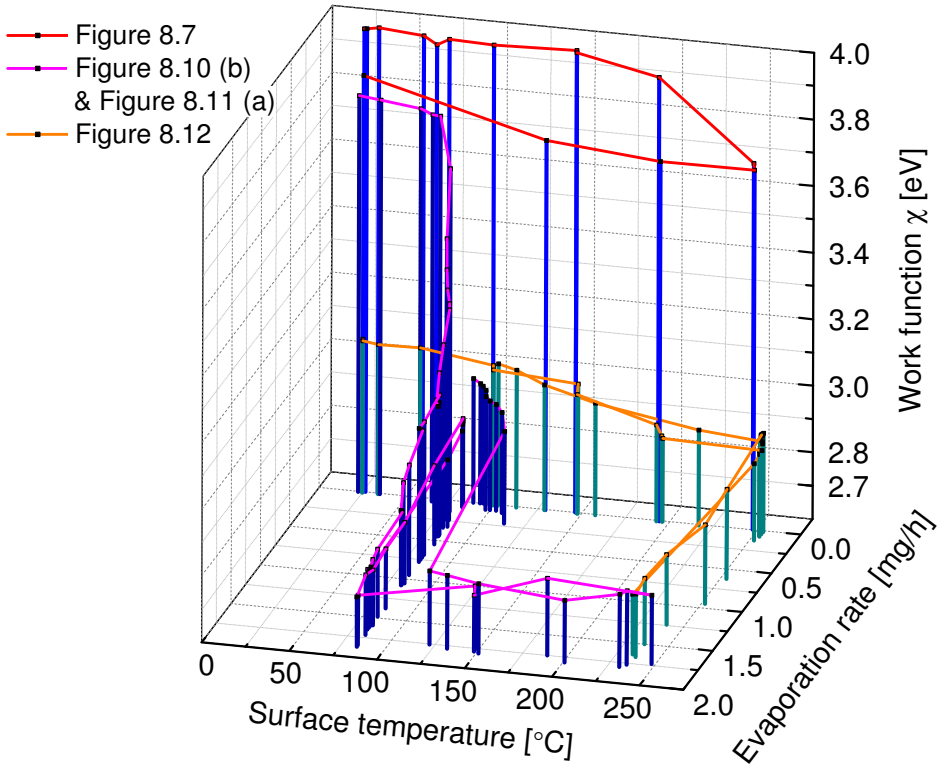

Figure 8.13: *Compilation of the progression of the work function of the stainless steel sample throughout the investigations regarding evaporation rate and sample temperature. Particular aspects can be found in the figures denoted in the legend.*

9 Investigation of the Cs dynamics in hydrogen plasmas

The investigations on the caesium dynamics in hydrogen plasmas are performed by evaporating caesium into hydrogen discharges operated at 10 Pa absolute pressure and 250 W RF power. Typical Cs densities are 10^{14}–$10^{16}\,\mathrm{m}^{-3}$ which are much lower than the gas density of the hydrogen discharge. Therefore, such plasmas are called *caesium seeded discharges*. In contrast to actual caesium plasmas, the dominating constituents in caesium *seeded* plasmas are the particles from the background plasma. In this case, caesium is regarded as disturbance to the main (hydrogen) plasma and variations of the plasma parameters due to the presence of caesium in the discharge are examined depending on the Cs density.

In order to distinguish between effects resulting from the high atomic mass of caesium and those from plasma and surface chemistry, investigations on the influence of the rare gas xenon (similar mass to Cs) are performed in a first step. However, the ionization energy of caesium (3.89 eV) is much lower than that of xenon (12.1 eV). Hence, the ionization rate coefficient of Cs is several orders of magnitude larger than the one for Xe (see figure 4.6 (b)), where the ratio steeply depends on T_e. Thus, for comparable influences on the plasma much higher xenon densities are required: Cs densities of $10^{16}\,\mathrm{m}^{-3}$ correspond to Xe partial pressures between 10^{-3} and 10 Pa depending on whether the electron temperature is close to 0.8 eV or 3 eV. Thus, the investigations are performed in the sense of *xenon admixtures* to the hydrogen plasma (typically some percent of the absolute pressure), where the xenon content is adjusted directly via the gas supply system.

The comparability of the influence of xenon and caesium admixtures is thus dependent on the actually occurring electron temperature in the hydrogen plasma and its variation due to the heavy atom. This has to be determined experimentally, and in order to cover a wide range of different T_e values the investigations

on Xe admixtures are performed for varying absolute pressures between 5 and 20 Pa, whereas the RF power is maintained constant at 250 W.

Plasma profiles

Owing to the heating mechanism of the planar inductively coupled plasma, the plasma parameters are dependent on the radial and axial position within the discharge vessel [LL05]. Measurements in an equivalent experimental setup (identical setup apart from the matching network) have shown, that the electron temperature is radially homogeneous (due to the high thermal conductivity of the electrons in the plasma), whereas the electron density is subject to a Bessel profile (attributable to the electron diffusion to the vessel walls) [SFAP01]. Langmuir probe measurements in the present setup are performed radially and axially centered. On the contrary, the line of sight for the spectroscopic diagnostics leads axially centered diagonally through the vessel. Hence, spectroscopic measurements average over the Bessel profile in n_e whereas probe measurements are taken at the maximum of the profile. Therefore, the density profile has to be taken into account, when results from these diagnostics are interchanged: commonly the measured electron density from probe measurements is divided by a so-called profile factor of about 1.6[1] [SFAP01].

However, within the scope of this work also a sample surface in proximity to the line of sight is applied. Such an additional plasma boundary can have a significant influence on the density profile (see [SFAP01] for instance). Unfortunately, in the present setup the impact of the sample surface cannot be determined. Hence, the density profile is unknown and cannot be considered if the sample holder is present and for consistency the profile is neither considered if the sample holder is not installed.

This means, that for the evaluation of OES measurements the required electron density is always taken directly from the probe measurements in the center of the discharge without installed sample holder. Since the profile would be considered by means of a profile factor, this approach should only have a slight influence on the absolute value of the determined parameters but not on relative variations.

[1] This factor is determined by the maximum of the Bessel function relative to the average value.

9.1 Xenon admixtures to H_2/D_2 plasmas

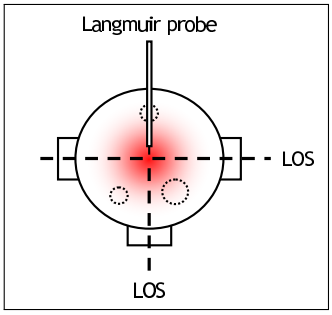

Figure 9.1 shows two exemplary spectra of the ICP discharge recorded with the survey spectrometer: a pure hydrogen plasma and a plasma with 5 % xenon admixture. Emission from molecular hydrogen is to be seen at the Fulcher system ($d\,^3\Pi_u \rightarrow a\,^3\Sigma_g^+$) and at some rotational lines from the transition $E\,^1\Sigma_g^+ \rightarrow B\,^1\Sigma_u^+$ (not denoted in the figure, basically 700–900 nm), whereas atomic hydrogen is represented by the Balmer lines H_α and H_β. For xenon much more transitions are observable even at only 5 % share of the absolute pressure. The transition systems are denoted in Paschen notation. Lines originating from up to the 5d state are detectable, whereas the $2p_x \rightarrow 1s_y$ lines are the most prominent, as usual for the rare gases. For the following investigations the transition at 828.0 nm ($2p_5 \rightarrow 1s_4$) is used to monitor the xenon emission representatively.

From this rough overview in figure 9.1 it can already be seen, that a xenon admixture of 5 % leads to decreasing Balmer emissions whereas emission from molecular hydrogen is almost no more observable. These trends can be recognized in fig-

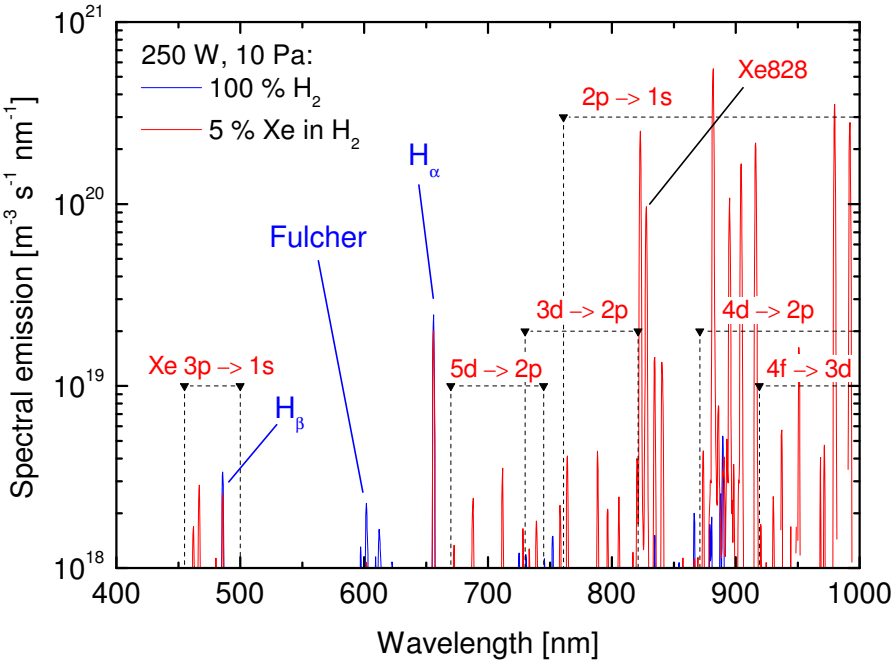

Figure 9.1: *Exemplary spectra of the ICP discharge for a pure hydrogen plasma and with 5 % admixture of xenon at an absolute pressure of 10 Pa and 250 W RF power. The dominant emission lines and systems are denoted.*

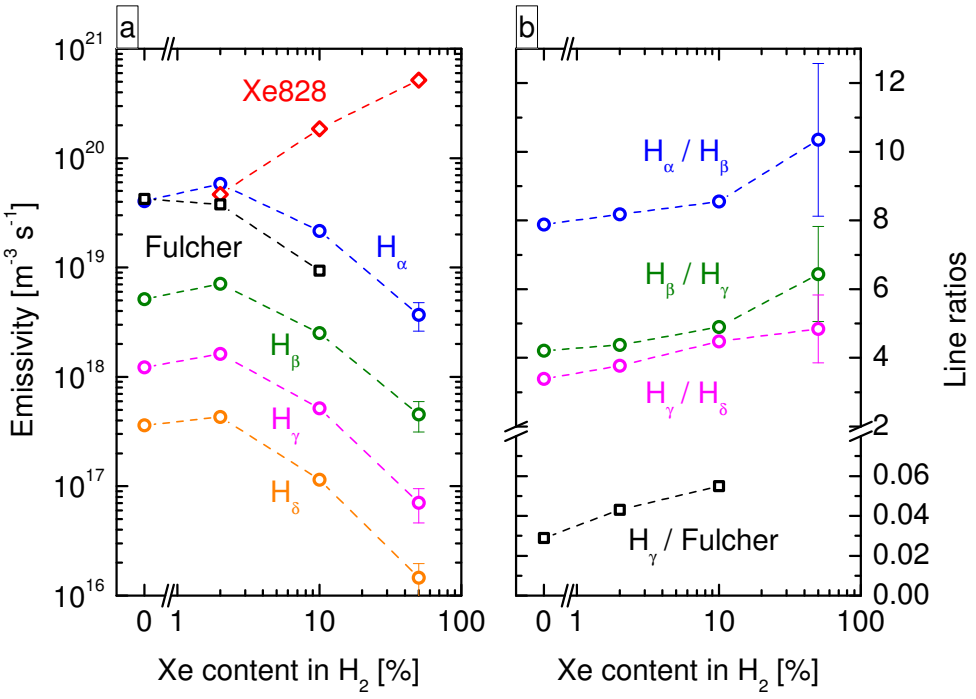

Figure 9.2: *Influence of the rising Xe content on the hydrogen plasma at 10 Pa and 250 W.* **(a)** *Representative emissivities for xenon and atomic and molecular hydrogen.* **(b)** *Line ratios of the Balmer lines and the ratio H_γ/Fulcher.*

ure 9.2 (a) where the emissivities of the first four Balmer lines, of the entire Fulcher system and of the xenon line at 828.0 nm are plotted with increasing Xe content. Besides the error of a single measurement, the denoted error bars further include the error for the reproducibility of the emission over several operational days.

It can be seen, that a very little content of 2 % xenon in the hydrogen discharge leads to an increase of the Balmer emissions whereas the Fulcher emission is slightly decreased. Further increasing the xenon content yields decreasing emissions from both atomic and molecular hydrogen, as already observed in figure 9.1, whereas the xenon emission increases. At 50 % Xe in H_2 the Fulcher emission is no longer evaluable since only very few rotational lines are still detectable. Figure 9.2 (b) shows the paired ratios of the Balmer lines and the ratio H_γ/Fulcher which is representative for the atom-to-molecule density ratio. An increasing Xe content leads to an increase of each line ratio.

While the increasing Xe emission could simply be explained by the increasing partial pressure of Xe, the observed progressions of the hydrogen emissions and the line ratios indicate varying plasma parameters.

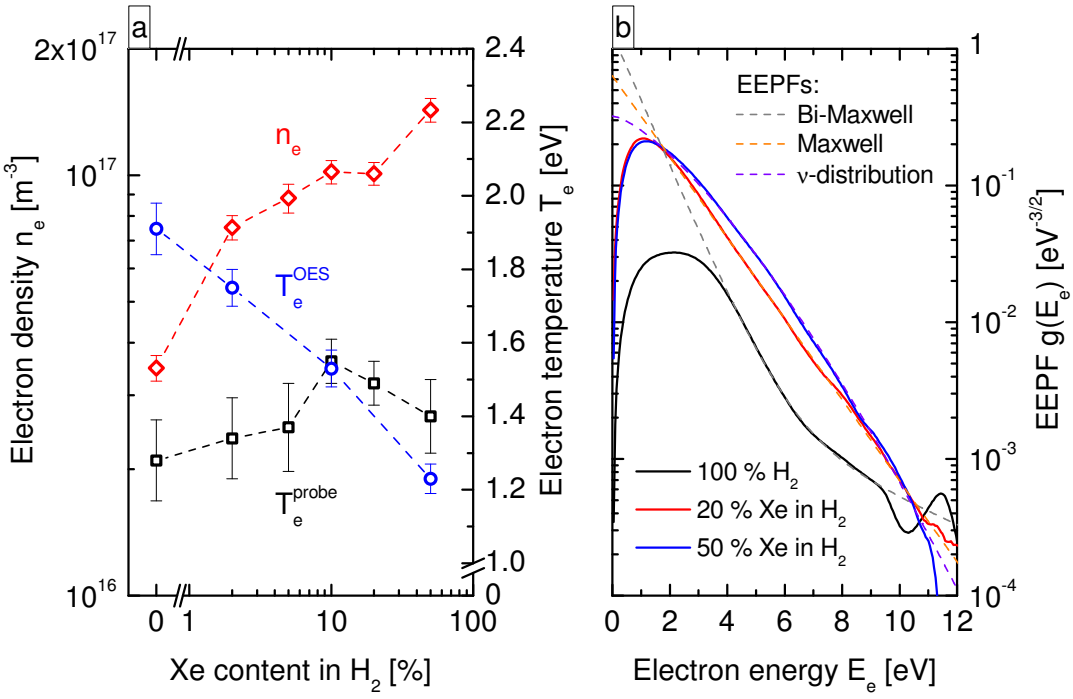

Figure 9.3: (a) *Electron density and electron temperature determined via probe measurements and OES depending on the plasma composition for 10 Pa absolute pressure and 250 W RF power.* **(b)** *Measured and fitted EEPFs for several plasma compositions. The fit parameters are:* $T_{\mathrm{e,low}} = 0.9\,eV$, $T_{\mathrm{e,high}} = 4.5\,eV$, $\beta = 0.04$ *for the Bi-Maxwellian distribution;* $T_{\mathrm{e}} = 1.47\,eV$ *for the Maxwellian distribution;* $\nu = 1.4$, $T_{\mathrm{e}} = 1.75\,eV$ *for the* ν*-distribution.*

Electron density and temperature

Figure 9.3 (a) shows the electron density n_{e} and the electron temperature T_{e} in dependence of the rising Xe content. The electron density is measured by the Langmuir probe whereas for T_{e} two different diagnostics exist: the probe measurements, $T_{\mathrm{e}}^{\mathrm{probe}}$, and the optical emission spectroscopy, $T_{\mathrm{e}}^{\mathrm{OES}}$. While the former is determined via the slope of the logarithm of the second derivative of the probe characteristic, the latter is evaluated by means of the collisional radiative model Yacora H using, among others, the Balmer lines H_α to H_δ (see section 6.7).

It can be seen that the electron density increases from about $3.5 \times 10^{16}\,\mathrm{m}^{-3}$ for a pure hydrogen plasma to about $1.5 \times 10^{17}\,\mathrm{m}^{-3}$ at 50 % Xe in H_2. This can be explained by the power balance of the plasma (see section 3.1.2): With decreasing content of the molecular gas H_2 within the discharge the power losses for vibrational excitation and dissociative processes is reduced. Since the input power of 250 W is maintained constant, consequently more power is available for

the ionization processes. Together with the larger ionization rate coefficient for Xe compared to hydrogen due to the lower ionization potential (see figure 4.6 (b)), n_e increases with increasing Xe content.

For the electron temperature, different evolutions can be observed depending on the diagnostic: while the OES gives a decreasing T_e from 1.9 eV in pure hydrogen down to 1.2 eV with 50 % Xe admixture, the probe measurements show an increasing T_e from initially 1.3 eV up to 1.55 eV at 10 % Xe in H_2 followed by a decrease to 1.4 eV at 50 % Xe content. This is directly correlated with the different evaluation methods. The OES uses the radiation from the plasma, which originates from electronically excited states with excitation energies of at least 12.1 eV (level $n = 3$, H_α line). On the contrary, the evaluation of electron temperatures by means of probe measurements is done via a linear fit to the low-energy part of the measured electron energy probability function (EEPF). This low-energy region typically ranges from 2 eV to 10 eV. Therefore, the evaluated electron temperatures from the two diagnostics correspond to different parts of the actual energy distribution function of the electrons in the plasma. Moreover, both diagnostics assume a Maxwellian distribution, which itself is not necessarily fulfilled.

In principle, the following implications can be drawn regarding the evaluated electron temperatures depending on the actually existing EEDF:

- If a **Maxwellian distribution** is present in the plasma, the slope of the EEPF is constant over the entire electron energy range. Thus, both diagnostics should yield the same value: $T_e^{\text{probe}} = T_e^{\text{OES}}$.

- If the EEPF is **Bi-Maxwellian**, then the slope of the EEPF is steeper for low electron energies and flatter at high energies. This yields $T_e^{\text{probe}} \leq T_e^{\text{OES}}$.

- A **Druyvesteyn distribution** (or more general a ν-distribution with $\nu > 1$) has a flatter low-energy part and a steeper high-energy part. If such an EEPF is present in the plasma, then $T_e^{\text{probe}} \geq T_e^{\text{OES}}$.

For the present investigations on increasing xenon admixtures to a hydrogen plasma, the measured EEPFs are shown in figure 9.3 (b) together with appropriate fits of theoretical EEPFs. For pure H_2 the EEPF is Bi-Maxwellian with $T_{e,\text{low}} = 0.9\,\text{eV}$, $T_{e,\text{high}} = 4.5\,\text{eV}$ and a share of the higher temperature of $\beta = 0.04$. This can be ascribed to the heating mechanism of the molecular RF discharge, which can lead to an efficient heating of a small amount of electrons yielding

higher temperatures for this ensemble ('stochastic heating', see [LL05] for instance). Therefore, these electrons dominate at higher electron energies and the Bi-Maxwellian character evolves. At electron energies below 4 eV the measured EEPF deviates from the theoretical Bi-Maxwellian evolution. In this region excitation of vibrational levels of the hydrogen molecule can occur which leads to the observed underpopulation ('molecular dip'). Together with the drop of the measured EEPF at lowest energies (see section 6.5.2 for explanatory approaches), a very broad low-energy region is obtained in discharges where the hydrogen molecule is the dominating species.

Decreasing the molecular influence on the EEPF via increasing the xenon content leads to the diminishing of the broad low-energy region. Additionally, the Bi-Maxwellian character vanishes and at 20 % Xe in H_2 the EEPF can be treated as Maxwellian. In the present case, the fitted electron temperature is 1.47 eV.

If the amount of the rare gas within the plasma is further increased the EEPF changes into a Druyvesteyn-like evolution, i. e. a faster decrease of the EEPF at higher electron energies due to the excitation of electronic states of xenon (at $E_e > 8\,\mathrm{eV}$). For 50 % Xe in H_2 the distribution can be described by a ν-distribution with $\nu = 1.4$ and $T_e = 1.75\,\mathrm{eV}$[2]. This behavior of the EEPF is often observed in atomic RF discharges [GPA92].

Using the measured EEPFs the deviating progression of the electron temperatures determined with the Langmuir probe and evaluated via OES in figure 9.3 (a) confirms the general implications drawn above: At low xenon contents, where the EEPF is Bi-Maxwellian, T_e^{probe} is smaller than T_e^{OES}. Around 10–20 % Xe in H_2 the EEPF is Maxwellian-like and both diagnostics yield similar values for T_e. For high xenon contents the EEPF converts to a ν-distribution yielding $T_e^{\mathrm{probe}} \geq T_e^{\mathrm{OES}}$. Thereby, the particular evolution of T_e^{probe} with increasing xenon content arises from the preformed linear fit to the measured EEPFs: the transition from a convex EEPF to a concave EEPF initially leads to increasing T_e^{probe} values, then to the maximum at 10–20 % Xe in H_2 for the Maxwellian EEPF with infinitesimal curvature and finally to decreasing values for further increasing xenon contents. Moreover, the corresponding measurement errors reflect the uncertainty of a linear fit performed to a non-linear EEPF. Finally, the decreasing high-energy region of the EEPFs explains the decreasing evolution of T_e^{OES}, since the optical emission spectroscopy gives only access to this region of the EEPF.

As the high-energy tail of the EEPF is also responsible for the ionization of

[2] It has to be kept in mind, that this T_e-value is not a thermodynamic temperature.

the plasma particles, the decreasing evolution of T_e^{OES} upon increasing xenon content can be explained by means of the ionization balance in low temperature plasmas (see section 3.1.2): $X_{ion}(T_e) \sim 1/\sqrt{m_{ion}}$, where X_{ion} is the ionization rate coefficient depending on T_e and m_{ion} is the ion mass. Thus, the higher mass of 131.3 u for Xe compared to 3.0 u for H_2 (mean ion mass) and the lower ionization energy of xenon leads to the observed decrease of T_e^{OES} in figure 9.3 (a).

Since the dominating ion within the plasma is a crucial parameter for the discharge dynamics, the ionization processes and thus the high-energy tail of the EEPF are most relevant. Therefore, only the electron temperature determined via the optical emission spectroscopy is considered in the following and $T_e \equiv T_e^{OES}$.

Plasma potential and atomic hydrogen density

Figure 9.4 (a) shows the influence of the increasing Xe content on the electrostatic potentials measured by the Langmuir probe. It can be seen that with rising Xe amount the plasma potential ϕ_{pl} decreases from 12.1 V in a pure hydrogen plasma down to 9.4 V at 50 % Xe in H_2. The potential drop to a floating surface $\phi_{pl} - \phi_{fl}$ in a pure hydrogen discharge is at 4.5 V, whereas the presence of xenon in the plasma leads to an increase of $\phi_{pl} - \phi_{fl}$ to 6.8 V followed by a steady decrease down to 6.4 V with increasing Xe content.

Since the Langmuir probe measures the electrostatic potentials against the vessel walls, the decrease in the plasma potential due to increasing Xe content indicates a varied charge flux balance to the vessel walls and thus, modified profiles of the densities and the potentials within the plasma can be expected: The introduction of the heavy particle xenon and its ion results in a hindrance of the diffusion of plasma particles (electrons, ions) to the vessel walls and thus to flatter profiles. The local measurement of the Langmuir probe in the center of the discharge would then yield lower values of ϕ_{pl}. An additional reasonable influence could be the decreasing electron temperature, which in turn is determined by the hindered diffusion of ions to the vessel walls via the ionization balance. A decrease in T_e leads to a decrease in the wall flux of negative charges which in turn leads to a lower potential drop between the main plasma and the vessel wall.

On the other hand, the difference of the plasma and the floating potential measured by the Langmuir probe is not subject to plasma profiles towards the vessel walls but reflects the local situation at the location of the probe tip, i. e. the potential drop between the plasma and a floating body at the location of the probe. Here the influence of the heavy xenon ion can directly be seen at the jump

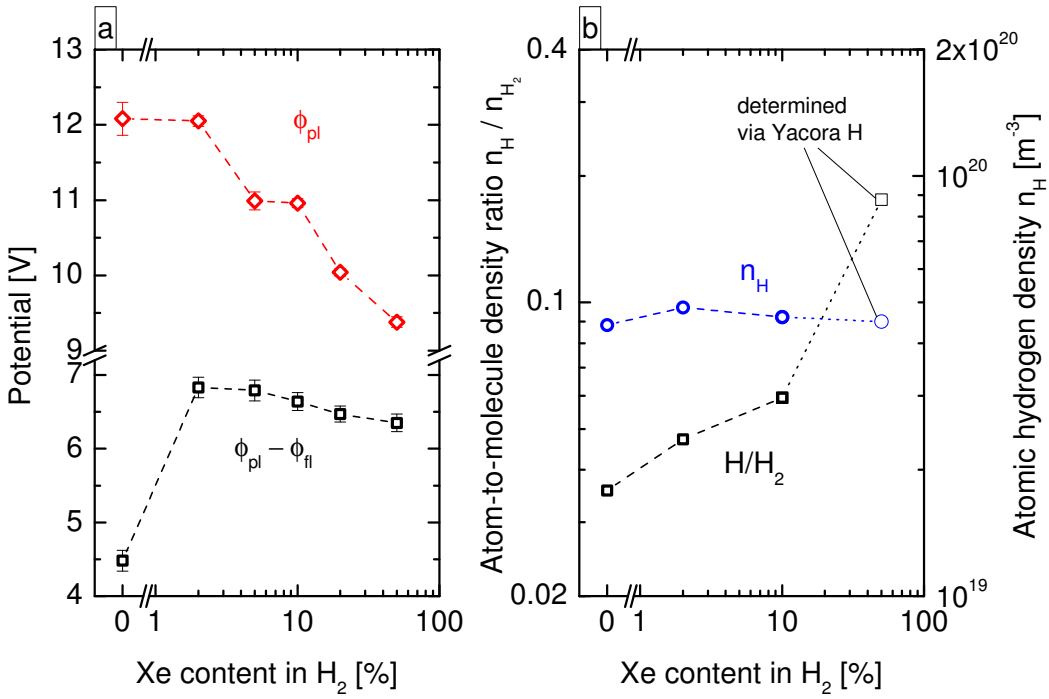

Figure 9.4: (a) *Plasma potential and potential drop to a floating body in a plasma at 10 Pa absolute pressure and 250 W RF power with varying content of xenon in hydrogen.* **(b)** *Atom-to-molecule density ratio and atomic hydrogen density for the same parameters as in part (a).*

in the progression of $\phi_{\mathrm{pl}} - \phi_{\mathrm{fl}}$ as soon as xenon is present in the plasma. As shown in equation (6.34), the potential drop depends on the (mean) ion mass. The mean ion mass can in turn roughly be estimated via the required quasineutrality within the plasma. Pursuing this approach, the ion density evaluated via the BRL theory can be fitted to the electron density by varying the mean ion mass. The required mean ion mass increases from 2.3 u for a pure hydrogen plasma to 44 u for 2 % Xe in H_2. Applying these values to equation (6.34) yields an increase of $\phi_{\mathrm{pl}} - \phi_{\mathrm{fl}}$ by 2.2 V, which is very close to the actually measured increase. The subsequent decrease of the potential drop can then be explained by a decreasing electron temperature as after equation (6.34) $\phi_{\mathrm{pl}} - \phi_{\mathrm{fl}}$ is directly proportional to T_{e}. Again, the temperature is just an approximation for the mean electron energy assuming a Maxwellian EEDF, which is not necessarily present as shown in figure 9.3 (b). Therefore, the temperature in equation (6.34) needs not to coincide with the temperatures determined in figure 9.3 (a).

In figure 9.4 (b) the atom-to-molecule density ratio (hereafter called atom-to-molecule ratio or H/H_2 for short) and the corresponding atomic hydrogen density are plotted against the Xe content in the plasma. Since for 50 % Xe content the

Fulcher emission cannot be determined and thus neither the ratio H_γ/Fulcher (see figure 9.2), the atom-to-molecule ratio is indeterminate. In this case, the atomic hydrogen density is solely determined by means of the CR model Yacora H using the measured emissions from the Balmer series. The evaluated value of n_H then leads to the plotted H/H_2 ratio.

An increasing amount of xenon in the discharge leads to an increasing atom-to-molecule ratio from initially 3.6 % for a pure hydrogen plasma up to 17.6 % at 50 % Xe in H_2. Since the absolute pressure is maintained constant, an increasing Xe content yields a decreasing H_2 content which together with the increasing H/H_2 ratio leads in conclusion to a constant atomic hydrogen density in the plasma of about $4.6 \times 10^{19}\,\mathrm{m}^{-3}$.

The evolution of H/H_2 can be ascribed to the dissociation process, which is based on the electron impact excitation of hydrogen molecules into the anti-bonding state $\mathrm{b}\,^3\Sigma_u^+$ (see section 3.3). Since for this process electron energies of below 8.6 eV are required, the low energy part of the EEPF is determinant. This region is in turn described by T_e^{probe} and, as can be seen in figure 9.3 (a), xenon has only a slight influence on T_e^{probe}. Therefore, the dissociation degree is determined by the linear dependency of the rate of electron impact dissociation on the electron density. Thus, the observed increase of n_e by a factor of 4.3 in total is responsible for the increased H/H_2 ratio.

Summary

The admixture of the heavy rare gas xenon to a hydrogen plasma leads to an increasing electron density, a transition from a Bi-Maxwellian EEDF to a Druyvesteyn-like EEDF, a decreasing plasma potential and an increased potential drop to a floating body within the plasma. The increased n_e further leads to an increasing atom-to-molecule density ratio which in turn leads to a constant density of atomic hydrogen despite the decreasing density of molecular hydrogen in the plasma. The observed transition of the EEDF is accompanied by a declining high-energy part of the EEDF, which leads to a decreasing electron temperature for that share of electron energies which is relevant to plasma processes like excitation or ionization from the ground state.

With these results, the observed evolutions of the emission and the line ratios in figure 9.2 can be explained: The decreasing molecular hydrogen density and the decreasing T_e lead to the diminishing of the Fulcher emission. The contrary trends of n_e and T_e together with the constant atomic hydrogen density result in

the initial increase of the Balmer emission followed by the receding emission due to the steep dependence on the electron temperature. While the ratio H_γ/Fulcher is directly correlated to the atom-to-molecule ratio, the line ratios of the Balmer lines reflect the specific impact of the decreasing electron temperature and the increasing electron density on the population of the particular upper Balmer levels.

9.1.1 Comparison of H_2 and D_2 plasmas

Figure 9.5 (a) shows the Fulcher emission, the D_γ line and the emission of the xenon line at 828.0 nm in deuterium discharges at an absolute pressure of 10 Pa and 250 W RF power depending on the Xe content and compared to the values obtained in H_2 plasmas. Besides the similar tendencies concerning the xenon admixture, the emissions in deuterium plasmas are each slightly higher. While for the Fulcher emission an increase of about 55 % can be observed, the Balmer emission is inceased by a factor of about 2.3, increasing to about 3.8 at 50 % Xe content. The xenon emission increases from initially equal values in hydrogen and deuterium to a factor of 2.7 higher emission at 50 % Xe in D_2 than in H_2.

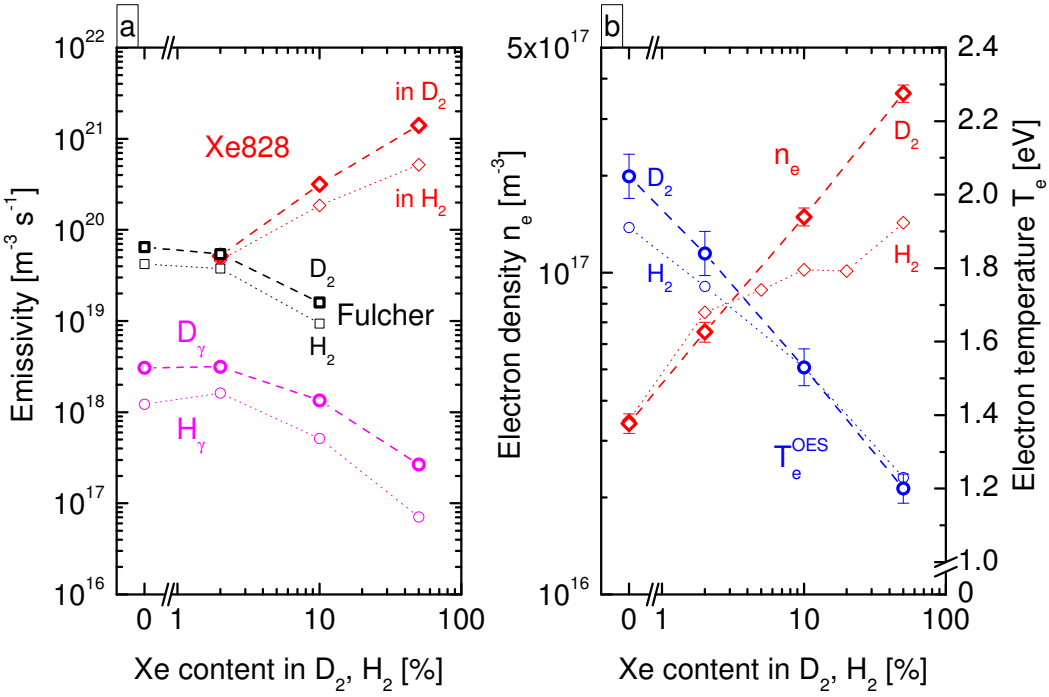

Figure 9.5: *Influence of xenon admixtures to a deuterium plasma at 10 Pa absolute pressure and 250 W RF power on* **(a)** *the plasma emission and on* **(b)** *the electron temperature and density. Results for H_2 from figures 9.2 (a) and 9.3 (a) are plotted for comparison.*

The line ratios for the Balmer lines in deuterium (not shown) are equal within some percent to the corresponding line ratios in hydrogen for each concentration of xenon in the plasma (see figure 9.2 (b)). However, due to the differently increased emission of atomic and molecular hydrogen (factor 2.3 vs. 1.55) the ratio D_γ/Fulcher is increased by about 50 % in D_2 compared to H_2 (not shown).

These tendencies of the emissions can be explained by means of the plasma parameters shown in figure 9.5 (b). It can be seen, that the electron temperature (determined via OES) is slightly higher in deuterium than in hydrogen (0.1 eV) for low Xe contents, whereas it is equal at higher xenon admixtures. The electron density behaves contrary: In pure hydrogen or deuterium plasmas n_e is equal, but with rising xenon content the deuterium plasma shows an increased electron density reaching a factor of 2.5 higher n_e in D_2 than in H_2 at 50 % xenon admixture: $n_{e,max} = 3.6 \times 10^{17}\,m^{-3}$.

The higher mass of deuterium should normally lead to a decreased electron temperature due to the hindered diffusion as described in section 3.1.2. On the other hand, the increased mass leads to a less efficient energy transfer from the RF heated electrons to the heavy particle gas. This is confirmed by a slightly decreased gas temperature in D_2 compared to hydrogen (-80 K on average, not shown). Therefore, the effect of the lessened energy loss due to elastic collisions with deuterium molecules seems to be determinant, resulting in an increased electron temperature. With increasing Xe content the influence of the molecular gas as collision partner decreases and the T_e values for D_2 and H_2 converge.

The increased electron density at high xenon contents in deuterium compared to hydrogen must arise from interactions between the molecule and the rare gas, since the ionization energies and the electron temperature are equal for each isotope and any impact resulting from the single molecules should also be observable without xenon. However, this xenon related effect was not investigated further within this framework.

However, the evolution of the emissions in figure 9.5 (a) can be deduced. The combined influence of a higher T_e at low Xe content and a higher n_e at higher Xe content leads to the almost constantly increased Fulcher emission in deuterium compared to hydrogen. The increased Balmer emission can partly also be ascribed to this behavior of T_e and n_e but is additionally influenced by the atomic hydrogen density, which will be shown in figure 9.7 (b). The increased ratio of D_γ/Fulcher already indicates an increased atomic density, which accounts for the additional increase of the emission. At 50 % xenon admixture the increased electron density

in D_2 leads to the further increased Balmer emission in deuterium by a factor of 3.8 compared to hydrogen. The effect of the increased electron density can also be observed at the xenon emission, where at 50 % Xe in D_2 the increase by a factor of 2.7 can be ascribed to the increased n_e by a factor of 2.5 compared to H_2.

Electron energy distribution

Figure 9.6 shows the comparison of the measured EEPFs in deuterium and hydrogen and the resultant impact on the electron temperature determined by the probe measurements. In part (a) it can be seen that T_e^{probe} in pure deuterium is much higher than in pure hydrogen. This can be ascribed to the EEPF, which is shown in part (b): in contrast to the Bi-Maxwellian EEPF in H_2, the EEPF in D_2 behaves very close to a Maxwellian distribution, which leads to an increased temperature of the low-energy part corresponding to T_e^{probe}. Furthermore, the

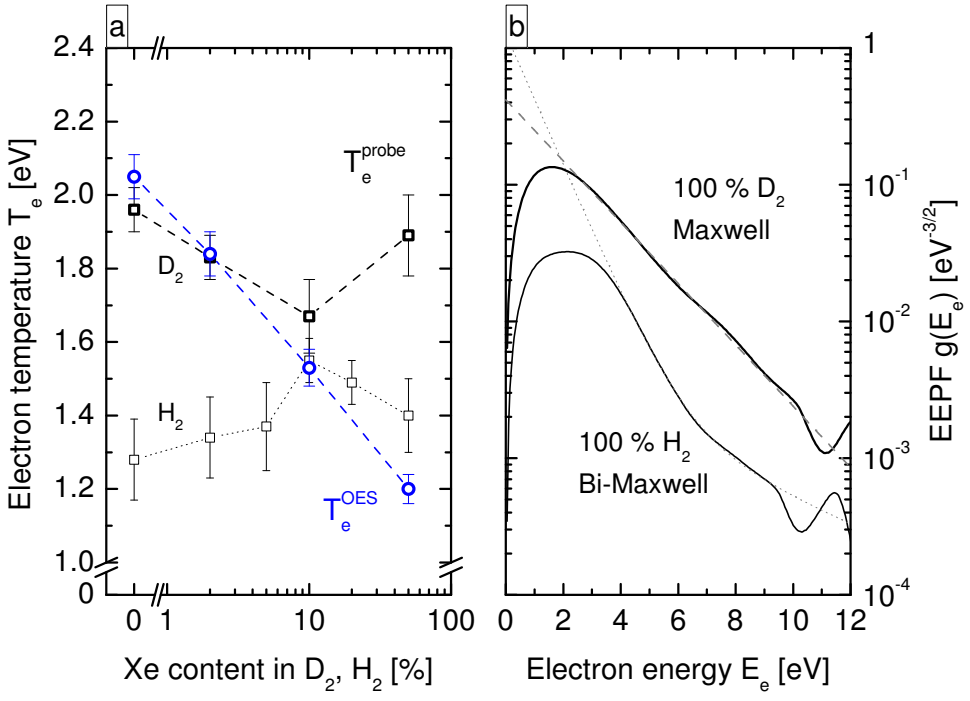

Figure 9.6: (a) *Electron temperatures of deuterium plasmas with different admixtures of xenon at an absolute pressure of 10 Pa and 250 W RF power determined via probe measurements and OES. Probe measurements for H_2 plasmas are shown for comparison from figure 9.3 (a).* **(b)** *EEPFs of pure H_2 and D_2 plasmas including appropriate fits with the following parameters: $T_{e,low} = 0.9\,eV$, $T_{e,high} = 4.5\,eV$, $\beta = 0.04$ for the Bi-Maxwellian distribution; $T_e = 1.94\,eV$ for the Maxwellian distribution.*

impact of vibrational excitations ('molecular dip') is restricted to lower electron energies, as the vibrational levels in D_2 lie closer than in H_2 due to the higher mass [FW06a]. Therefore, the deviation of the measured EEPF from the theoretical evolution starts at energies only below 2.5 eV in D_2 compared to 4 eV in H_2 (for comparison: in atomic discharges this threshold is at 1.5 eV as can be seen in figure 9.3 (b)).

In fact, the Maxwellian evolution of the EEPF in D_2 also leads to the virtual coincidence with the T_e values determined by means of the OES and the CR model Yacora H. This accordance between T_e^{probe} and T_e^{OES} is maintained as long as the EEPF behaves close to a Maxwellian distribution, which is up to 10 % Xe in D_2. As around 10 % Xe content the EEPF in H_2-Xe-mixtures is also Maxwellian-like (see figure 9.3 (b)), the electron temperature in the H_2 plasma is also very similar to the corresponding deuterium plasma within the error margins. At 50 % Xe admixture to the deuterium plasma the EEPF shows a very distinct Druyvesteyn-like evolution (not shown), which explains the overestimation of T_e^{probe} compared to T_e^{OES}.

Plasma potential and atomic hydrogen density

In figure 9.7 (a) the dependency of the plasma potential and of the potential drop to a floating surface is plotted against the xenon content in the D_2 plasma and compared to the corresponding values in hydrogen. The evolution of the potentials is very similar, whereas in deuterium the absolute plasma potential as well as the potential drop is higher. This can be ascribed to the higher ion mass in deuterium plasmas which leads to a reduced flux of positive charges. To ensure flux equality of positive and negative charges to the vessel walls or to a floating body within the plasma the plasma potential and the potential drop are increased. For $\phi_{pl} - \phi_{fl}$ it can additionally be observed, that the increase due to the presence of xenon ions in the discharge is less pronounced than in hydrogen, as expected from the lower difference in mass.

Part (b) of figure 9.7 shows the influence of xenon admixtures on the atom-to-molecule ratio and on the atomic density for deuterium discharges compared to hydrogen. As already expected from the ratio D_γ/Fulcher the atom-to-molecule ratio is increased in deuterium by 50 % in average, which directly leads to an increased atomic deuterium density of about $7.3 \times 10^{19}\,m^{-3}$ compared to $4.6 \times 10^{19}\,m^{-3}$ in H_2. The increased dissociation degree in deuterium discharges is directly correlated to the higher cross section for dissociative electron impact

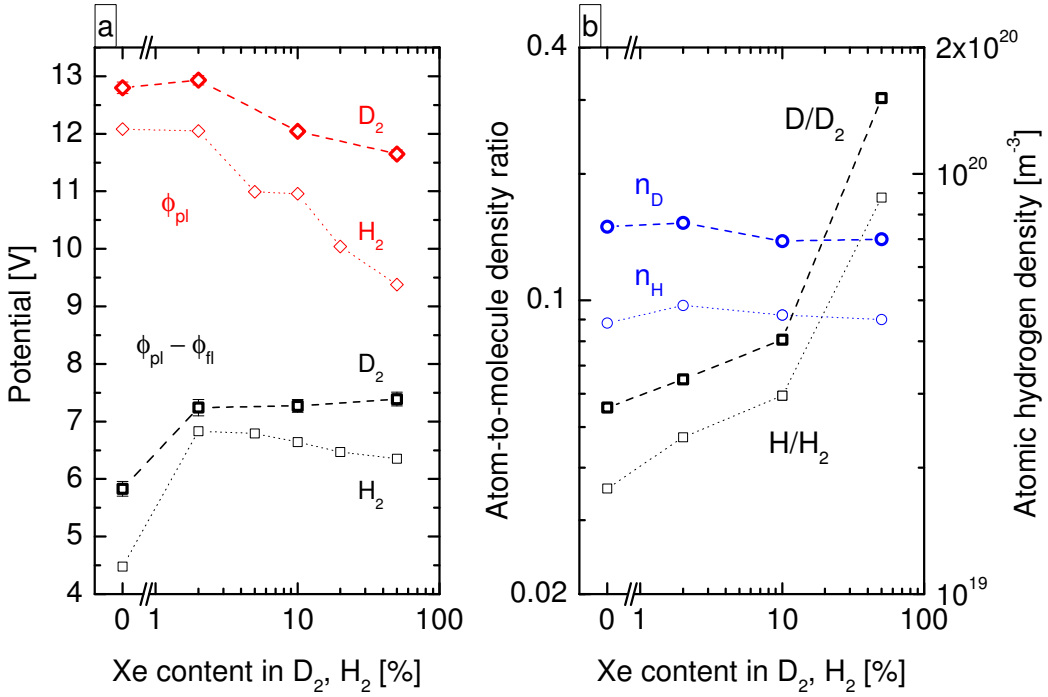

Figure 9.7: (a) *Electrostatic potentials and* **(b)** *atom-to-molecule ratio together with the atomic hydrogen density for deuterium and hydrogen plasmas (see figure 9.4) at an absolute pressure of 10 Pa and 250 W RF power with varying admixture of xenon.*

excitation via the anti-bonding state $b\,^3\Sigma_u^+$ for D_2 compared to H_2 (see figure 3.3). Furthermore, the higher temperature of the low-energy part of the EEPF in D_2 compared to H_2 is expected to have an additional influence.

Summary

The influence of xenon admixtures to a deuterium discharge is very similar to the influence on the hydrogen plasma. The observed differences are mostly connected to basic isotopic variances: The deuterium molecule is twice as heavy as the hydrogen molecule. This leads to a slightly increased electron temperature due to a reduced energy loss in elastic electron-deuterium collisions and to a less pronounced molecular dip in the EEPF due to the closer lying vibrational levels. The associated higher mass of the ionic species yields a larger plasma potential and a larger potential drop in deuterium plasmas and the larger dissociation cross section for D_2 results in a higher dissociation degree. Furthermore, the EEPF in pure deuterium is similar to a Maxwellian evolution, which leads to coinciding values of T_e from probe and OES measurements and the electron density is equal in pure deuterium and hydrogen discharges.

9.1.2 Influence of Xe at varied initial plasma parameters

The observed influence of the admixture of a heavy particle to the hydrogen plasma certainly depends on the plasma parameters of the initial discharge. Thus, the xenon-induced effects on the electron density and temperature are additionally investigated for a varying absolute pressure between 5 and 20 Pa.

Figure 9.8 (a) shows the progression of the electron density of hydrogen-xenon plasmas for different absolute pressures. The basic behavior at different absolute pressures is similar to the observations at 10 Pa (see figure 9.3 (a)): increasing Xe contents yield an increasing n_e due to the varied power balance. However, the absolute variation of n_e due to the admixture of Xe depends on the absolute pressure: For 5 Pa the evolution is steepest reaching an increase in n_e from initially $1.1 \times 10^{16}\,\mathrm{m}^{-3}$ up to $2.8 \times 10^{17}\,\mathrm{m}^{-3}$ for 50 % Xe in H_2, which is a factor of 25. At 10 Pa the influence of xenon is lessened leading to an increase by a factor of only four and at 20 Pa a Xe admixture of 2 % leads to an increase of n_e by a factor of two, whereas at higher admixtures the electron density remains constant within the error margins.

This behavior can be explained via part (b) of figure 9.8 where the same electron densities are now plotted against the absolute pressure for several xenon contents: for the molecular hydrogen plasma an increasing pressure leads to an increasing n_e, whereas a high amount of the heavy atomic rare gas xenon leads to decreasing electron densities upon increasing pressure. This contrary influence of the pressure on the atomic and the molecular gas leads to the apparently reduced influence of xenon in discharges with increased initial electron density observed in part (a).

In figure 9.9 the electron temperature determined by means of optical emission spectroscopy is plotted depending on the Xe content in hydrogen for different absolute pressures in part (a) and depending on the absolute pressure for different plasma compositions in part (b). In both diagrams it is clearly observable, that increasing the xenon content or increasing the absolute pressure leads to decreasing T_e values. Both dependencies are explainable by the increasingly hindered diffusion if the ion mass is increased or if the pressure is raised, whereas for increasing Xe content the increasing ionization rate coefficient is an additional influence (see section 3.1.2).

However, it can also be seen, that the influence of xenon increases with decreasing pressure: at 5 Pa the admixture of 50 % Xe to the H_2 discharge leads to a decrease of T_e from initially 2.8 eV down to 1.5 eV, whereas at 20 Pa the decrease

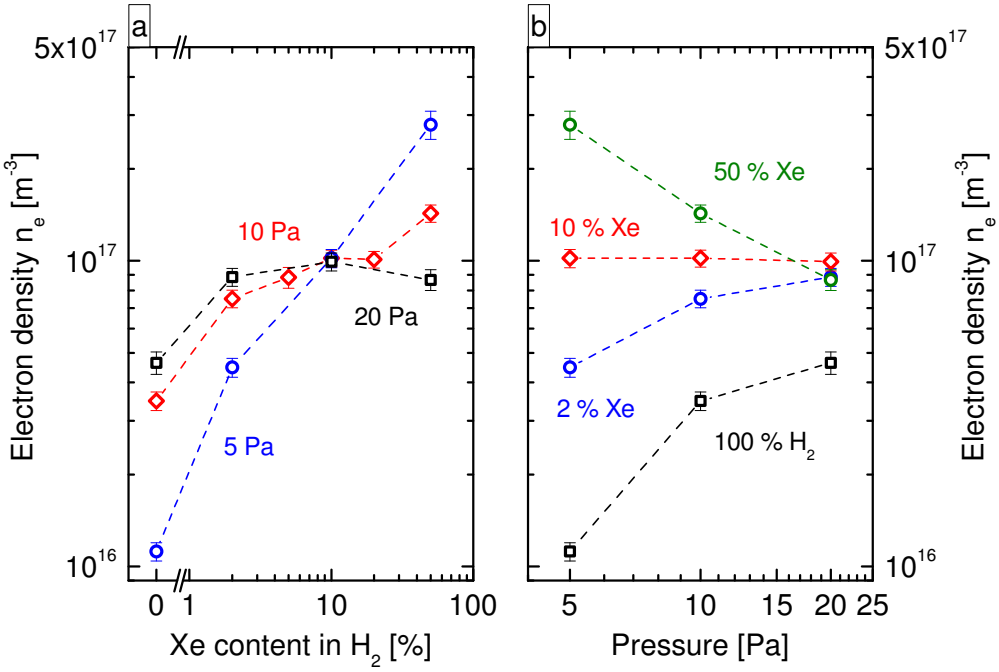

Figure 9.8: *Electron density depending on* **(a)** *the Xe content in a hydrogen plasma at differing absolute pressures and on* **(b)** *the absolute pressure for several Xe-H_2 mixtures. The RF power is maintained constant at 250 W.*

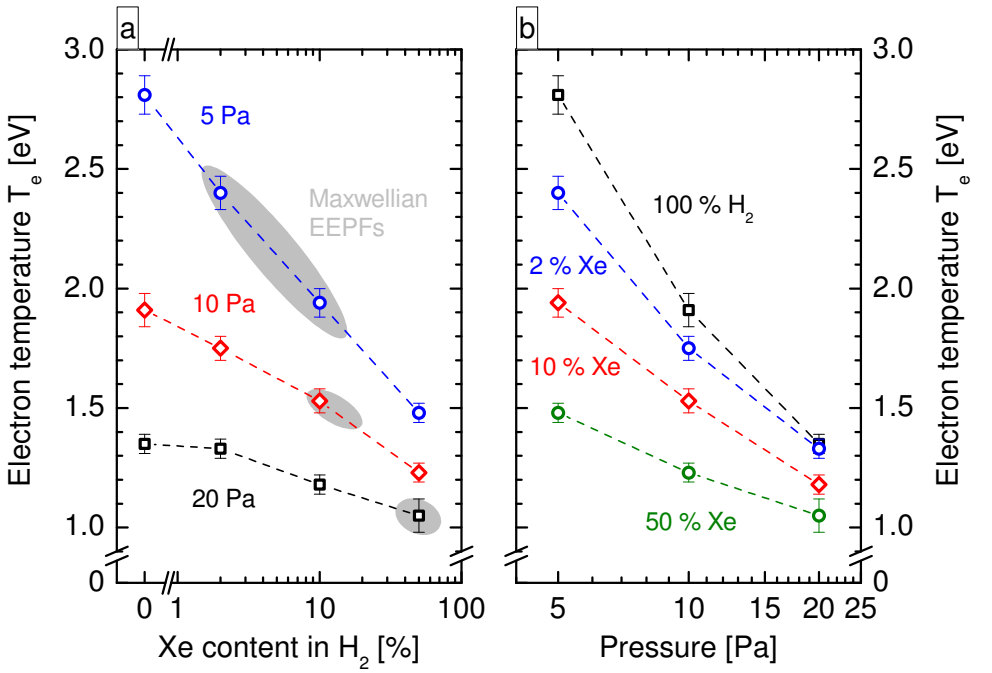

Figure 9.9: *Electron temperature determined via OES depending on* **(a)** *the Xe content in a hydrogen plasma at differing absolute pressures and on* **(b)** *the absolute pressure for several Xe-H_2 mixture ratios. The RF power is maintained constant at 250 W and in part (a) the discharges in which Maxwellian EEPFs are measured via the Langmuir probe are highlighted.*

from initially 1.35 eV is only 0.3 eV. Concluding, the influence of the heavy rare gas xenon increases with increasing initial electron temperature. This behavior arises from the temperature dependence of the ionization rate coefficient, which becomes steeper at lower T_e values. Thus, with decreasing T_e, smaller variations of T_e are sufficient for a comparable impact on the ionization rate. Hence, at higher pressures, where the electron temperature is lower, the influence of xenon on T_e is apparently reduced or even barely detectable.

Furthermore, the parameter ranges for which a Maxwellian EEPF is measured are illustrated by gray shaded areas in figure 9.9 (a). Thus, within these areas the electron temperatures determined via the probe measurements yield similar values ($T_e^{probe} \approx T_e^{OES}$). To the left of these areas the EEPFs are Bi-Maxwellian ($T_e^{probe} \leq T_e^{OES}$), to the right they are Druyvesteyn-like ($T_e^{probe} \geq T_e^{OES}$) (compare figure 9.3). Hence, at higher pressures larger amounts of the heavy rare gas are required to obtain a Maxwellian EEDF, since the Bi-Maxwellian character of the initial EEDF in the pure H_2 discharge is more pronounced with increased pressure.

Summary

In conclusion, the influence of the heavy rare gas xenon is stronger in discharges with higher electron temperature. The apparently observed stronger effect at lower electron densities is however to be ascribed to the performed approach to vary the plasma parameters: the impact of the pressure variation on n_e depends on the plasma composition and thus, the sole effect of the admixture of xenon on the electron density at varied initial n_e values cannot be assessed.

9.2 Caesium seeded H_2/D_2 plasmas

Recapitulating the investigations on the admixture of xenon to a hydrogen plasma, the following effects due to the higher mass of caesium and its lower ionization potential compared to molecular and atomic hydrogen can be expected:

- n_e increases due to the higher share of the input power for ionizing processes.
- T_e decreases due to the high mass and the higher ionization rate coefficient.
- The EEPF is modified at energies of about 1–4 eV due to the electronic levels and the ionization potential of Cs.

- ϕ_{pl} decreases due to the decreased T_{e}.
- The influence on $\phi_{\mathrm{pl}} - \phi_{\mathrm{fl}}$ depends on the interaction of the increasing $\overline{m}_{\mathrm{ion}}$ and the decreasing T_{e}.
- The influence on the H/H_2 ratio depends on the interaction of n_{e} and T_{e}.
- The influence of Cs on the plasma does not depend on the hydrogen isotope.

Since the ionization rate coefficient for Cs is much larger than for Xe, these effects occur at much lower admixtures of Cs to the plasma than the investigated Xe admixtures. On the other hand, the minimally required Cs density for these effects to be observable can be assessed via considering the ratio of the ionization rates of the corresponding plasma constituents:

$$\frac{n_j X_{\mathrm{ion},j}(T_{\mathrm{e}})}{n_{\mathrm{H_2}} X_{\mathrm{ion,H_2}}(T_{\mathrm{e}}) + n_{\mathrm{H}} X_{\mathrm{ion,H}}(T_{\mathrm{e}})} = \frac{n_j}{n_{\mathrm{H_2}}} \frac{X_{\mathrm{ion},j}(T_{\mathrm{e}})}{X_{\mathrm{ion,H_2}}(T_{\mathrm{e}}) + \frac{n_{\mathrm{H}}}{n_{\mathrm{H_2}}} X_{\mathrm{ion,H}}(T_{\mathrm{e}})} \quad \text{for } j = \mathrm{Xe}, \mathrm{Cs}\,, \tag{9.1}$$

where the ionization rate coefficients X_{ion} are taken from figure 4.6 (b) and the appropriate electron temperature should be that of the 'undisturbed' hydrogen plasma. If this *measure of influence* is of the order of unity, the ionization rate of the 'disturbing' particle j would be similar to the ionization rate of the 'background' particles, i. e. molecular and atomic hydrogen. Thus, a substantial influence on the plasma dynamics of the volume plasma can be expected.

Figure 9.10 (a) shows the ratio (9.1) for the performed investigations on Xe admixtures to the H_2 plasma at different absolute pressures. The initial electron temperatures and H/H_2 ratios of the pure hydrogen discharges at the particular pressures are taken for the calculations. It can be seen, that the measure of influence is greater than 0.2 as soon as 1 % Xe admixture is present in the H_2 plasma. The influence of the investigated 2 % admixture on the electron temperature is denoted confirming a measurable influence. Furthermore, it can be seen, that at higher initial T_{e} values (e. g. at 5 Pa absolute pressure) a significant influence on the plasma can be observed already at lower values of the measure of influence, i. e. at higher electron temperatures the relative observable influence is larger, which confirms the observations in section 9.1.2. However, considering the transferability of the present investigations to the plasma in front of the plasma grid in NNBI ion sources, the ICP discharge at an absolute pressure of 5 Pa shows too low n_{e} and too high T_{e} values.

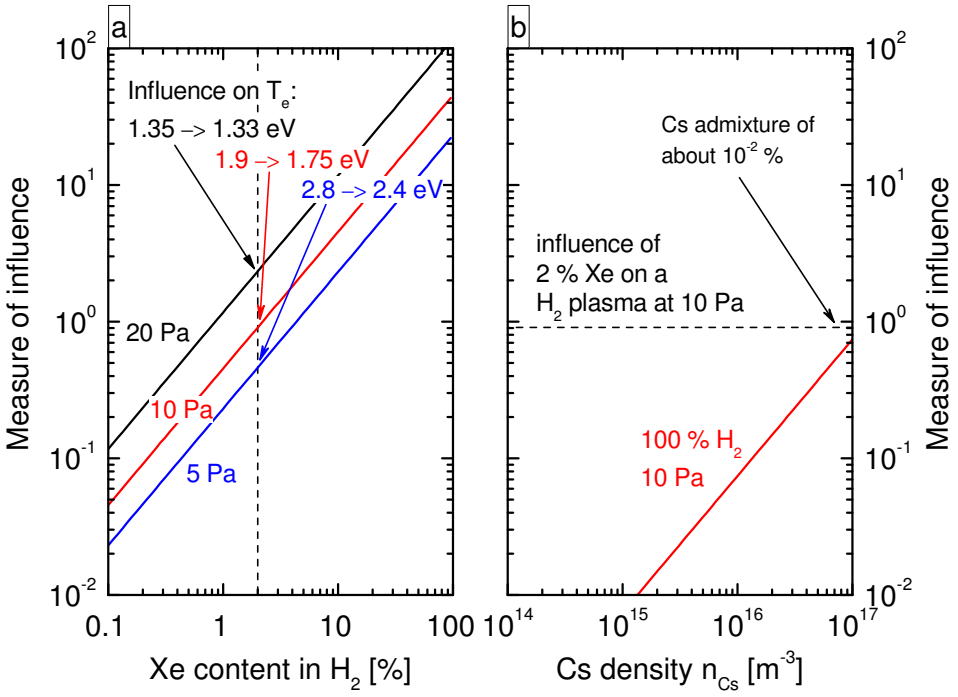

Figure 9.10: *Ratio of ionization rates after equation* (9.1) *as a measure of influence of* **(a)** *xenon admixtures to hydrogen plasmas at different absolute pressures and of* **(b)** *caesium admixtures to a 10 Pa H_2 plasma. The actual influence on T_e is additionally denoted in part (a) for 2 % Xe admixture and the corresponding measure of influence on a 10 Pa H_2 plasma is shown in part (b) as dashed line.*

Thus, hydrogen discharges at 10 Pa absolute pressure are investigated and part (b) of figure 9.10 shows the expected influence of Cs seeding after ratio (9.1). Additionally the measure of influence for a 2 % Xe admixture to this plasma is denoted. It can now be stated, that a comparable influence of Cs on the plasma is expected for Cs densities of $10^{17}\,\mathrm{m}^{-3}$ corresponding to an admixture of about 10^{-2} %, which is much lower than the 2 % Xe admixture constituting a density of $2 \times 10^{19}\,\mathrm{m}^{-3}$. This confirms the enhanced influence of Cs due to the lower ionization potential.

However, this leads further to the conclusion, that the influences of Cs on the volume plasma listed above are not expected until Cs densities of $10^{17}\,\mathrm{m}^{-3}$ are reached in the H_2 plasma. As usually n_{Cs} is below $10^{16}\,\mathrm{m}^{-3}$ a direct influence on the volume plasma is not expected for the following investigations. However, effects due to plasma and surface chemistry can occur already at much lower densities and subsequent influences of possible surface effects on the volume plasma can neither be excluded a priori.

9.2.1 Influence on the plasma emission

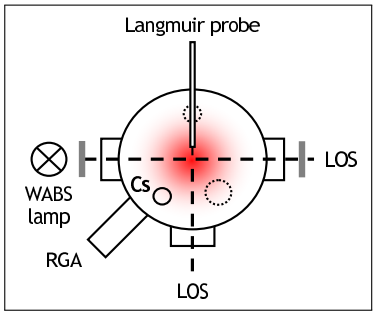

The investigations on the caesium dynamics in hydrogen and deuterium plasmas are performed by evaporating caesium into discharges operated at 10 Pa absolute pressure and 250 W RF power. To analyze the caesium-induced influences the full set of plasma diagnostics is applied: optical emission spectroscopy using two lines of sight for the survey spectrometer and the higher resolution spectrometer Acton, white light absorption spectroscopy, Langmuir probe measurements and the residual gas analyzer. The interplay of the diagnostics is illustrated in section 6.7. The neutral density filters are only applied during the recording of absorption spectra and the shutter in front of the absorption lamp is required for recording of emission signals with the Acton spectrometer. During the experiments, the plasma emission is constantly monitored via the survey spectrometer by means of time traces of the relevant emission lines. Moreover, as shown in figure 7.12, the Cs emission is also utilized to monitor the evaporation rate from the dispenser oven. Prior to the measurements it was verified, that the highly intense emission from the absorption lamp has no influence on the recording of survey spectra or the emission time traces via the perpendicular line of sight. Neither are the probe measurements influenced by the absorption lamp and in order to counteract the accumulation of Cs on the Langmuir probe, the probe tip is heated to red heat each time before an $I - V$ curve is recorded.

Spectra of Cs seeded H_2 discharges look very similar to those of pure hydrogen plasmas in figure 9.1, i. e. the Balmer lines of atomic hydrogen and the Fulcher system of molecular hydrogen are most prominent. Caesium can be observed at the resonance lines at 894.3 nm and 852.1 nm originating from the 6 P fine structure states. Resonance lines from the 7 P states are hardly detected as they are much less intense and are furthermore overlapped by emission from molecular hydrogen at the transitions $\mathrm{k}\,^3\Pi_\mathrm{u} \rightarrow \mathrm{a}\,^3\Sigma_\mathrm{g}^+$ and $\mathrm{I}\,^1\Pi_\mathrm{g} \rightarrow \mathrm{B}\,^1\Sigma_\mathrm{u}^+$. Introducing Cs into the discharge is observable by the emergence of the two Cs D lines and a decrease of the Balmer emission, while the Fulcher emission and other emission systems of molecular hydrogen are virtually unaffected. Hence, the overall structure of the survey spectra is not changed considerably, even at Cs densities of up to $10^{16}\,\mathrm{m}^{-3}$.

Figure 9.11 shows the influence of evaporating Cs into the hydrogen plasma monitored with optical emission and white light absorption spectroscopy. The

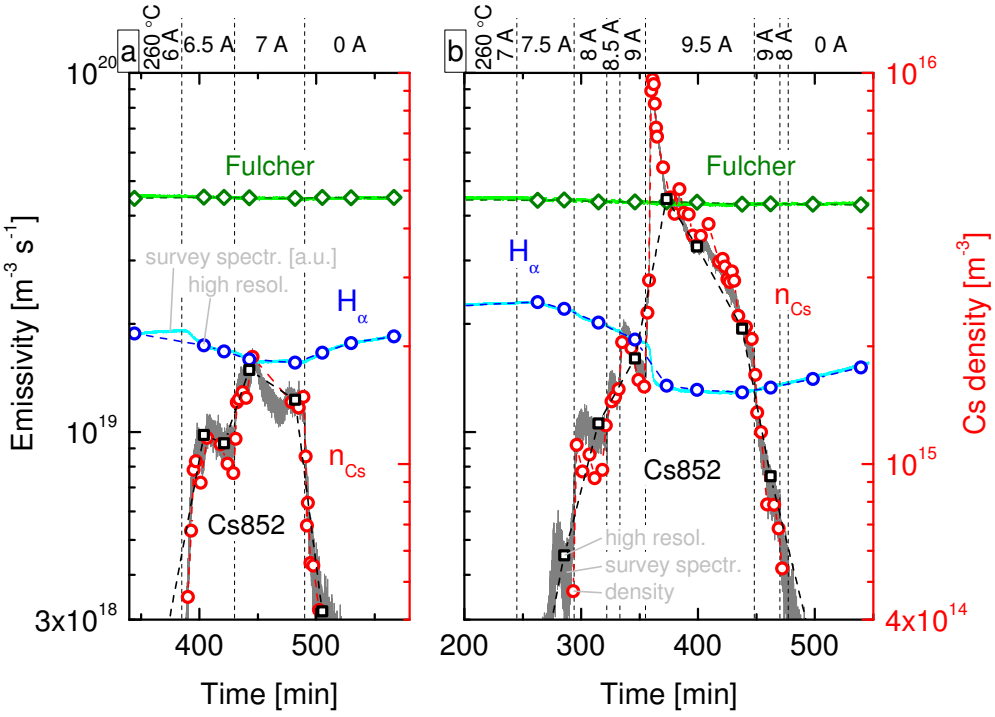

Figure 9.11: *Emission of molecular and atomic hydrogen together with emission and absorption signals of caesium with varying evaporation rate of Cs into a H_2 plasma at 10 Pa and 250 W. Emission signals from the survey spectrometer (lines) and the Acton spectrometer (symbols) are shown. The axis is only valid for the Acton spectrometer. Part* **(a)** *and* **(b)** *are two cases differing in the maximal Cs density.*

axis for the Cs density is scaled to follow the emission signals (the justification for this constant scaling is given in section 9.2.3). The oven is heated to working temperature and the dispenser current is increased incrementally. The two parts of the figure show two different cases for the behavior of the hydrogen plasma on the evaporation of Cs.

In part (a) the evaporation rate is moderate leading to Cs emission intensities of $1\text{–}2\times10^{19}\,\mathrm{m^{-3}s^{-1}}$ corresponding to Cs densities of $1\text{–}2\times10^{15}\,\mathrm{m^{-3}}$. It can be seen, that the increasing Cs amount within the discharge leads to a decrease of the Balmer emission of about 20 %. On the contrary, the Fulcher emission remains unaffected. Turning the dispenser heating current off leads to the rapid decay of the Cs density within the plasma accompanied by decreasing Cs emission and the recovery of the Balmer emission.

Part (b) of figure 9.11 shows a similar procedure, except the evaporation is increased further achieving about ten times higher Cs densities and emission: $n_{\mathrm{Cs,max}} \approx 1\times10^{16}\,\mathrm{m^{-3}}$, $\epsilon_{\mathrm{Cs,max}} \approx 1\times10^{20}\,\mathrm{m^{-3}s^{-1}}$. While the Fulcher emission is

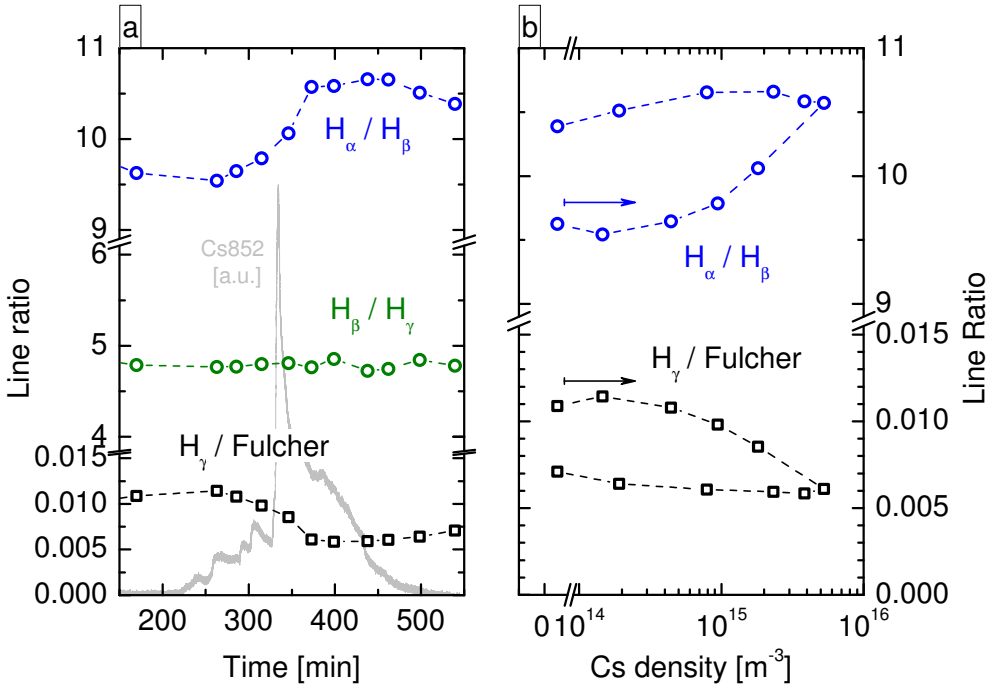

Figure 9.12: (a) *Line ratios of the procedure shown in figure 9.11 (b) and the Cs emission from the survey spectrometer in the background.* **(b)** *The same line ratios plotted against the corresponding Cs density. The starting point of the arrows denotes the beginning Cs evaporation.*

still unaffected the Balmer emission now decreases almost by half. Furthermore, although the Cs density and emission rapidly decrease upon shutting down the dispenser current, the Balmer emission recovers considerably delayed.

This hysteresis behavior can also be seen at certain line ratios, which is shown in figure 9.12 (a) for the case of high Cs evaporation (figure 9.11 (b)). For reasons of clarity the performed steps to increase the Cs density (increasing the dispenser current) are omitted here, but the evolution of the Cs emission is shown in the background. It can be seen that as soon as Cs is introduced into the plasma the line ratio H_α/H_β increases, the ratio H_γ/Fulcher decreases and H_β/H_γ as well as H_γ/H_δ (not shown) remain constant. After the Cs evaporation both modified ratios tend towards the initial values. However, like the Balmer emission, the reaction of the line ratios is also delayed. In part (b) the ratios H_α/H_β and H_γ/Fulcher are plotted against the corresponding caesium density illustrating the strong hysteresis of both parameters.

Furthermore, the investigations performed on the influence of Cs on deuterium discharges (not shown) yield equivalent results: The Fulcher emission is unaffected while the Balmer series decreases with increasing Cs density. The Balmer

series and the line ratios D_α/D_β and D_γ/Fulcher again show a distinct hysteresis. The fundamental differences between hydrogen and deuterium, which were already observed in section 9.1.1, still apply, where the significantly enhanced emission from the Balmer lines is again most noticeable.

The following conclusions can already be drawn from the emissions and the line ratios: The unaffected Fulcher emission together with the expected behavior of the plasma parameters arising from the comparison with the xenon investigations in figure 9.10 indicate, that the electron density and temperature are in fact not strongly affected by the presence of Cs with densities below $10^{16}\,\mathrm{m}^{-3}$. Further on, the constant Fulcher emission implies that the observed decrease in H_γ/Fulcher arises from the decrease in H_γ, which in turn is equally influenced by Cs as H_β, since the ratio H_β/H_γ is not affected. The increase in H_α/H_β then shows, that Cs has either less influence on H_α than on H_β or that additional processes occur for the state $n = 3$ of atomic hydrogen (from which H_α originates) which partly compensate the decreasing population due to Cs. The observed effects on the Balmer series are analyzed by means of the CR model Yacora H in the context of the evaluation of the plasma parameters.

9.2.2 Influence on the plasma parameters

Figure 9.13 (a) shows the electron density obtained from probe measurements at the top and the electron temperature evaluated by means of the OES using the CR model Yacora H at the bottom. It can be seen, that caesium densities up to nearly $10^{16}\,\mathrm{m}^{-3}$ within the discharge have virtually no influence on n_e or T_e: $n_\mathrm{e} \approx 3.5\times10^{16}\,\mathrm{m}^{-3}$, $T_\mathrm{e} \approx 2.0\,\mathrm{eV}$. Moreover, no difference between the isotopes can be observed and furthermore no influence of Cs on the corresponding EEDFs (see figure 9.6 (b)) is measured. Thus, the expected behavior is confirmed, according to which the typically relevant Cs densities are too low to have a measurable influence on the electron density or temperature of the volume plasma. Hence, the Fulcher emission remains unaffected upon Cs seeding and the observed influence of Cs on the Balmer series must be ascribed to other effects besides variations of n_e and T_e.

As presented in section 6.6.2, the emission of the Balmer series is determined by the coupling to the hydrogen species H, H_2, H^+, H_2^+ and H^-. Thereby, the coupling to molecular hydrogen H_2 via dissociative excitation ($H_2 + e \rightarrow H^* + H + e$) is not influenced by the presence of Cs, since besides n_e and T_e also n_{H_2} is unaffected: the absolute pressure is kept constant at 10 Pa and the gas temperature

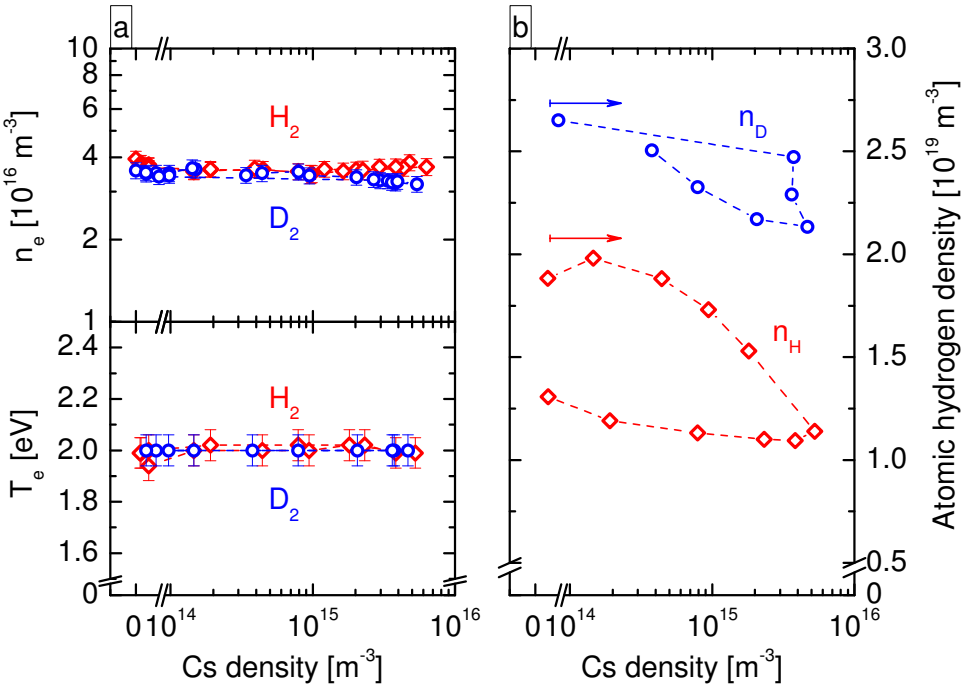

Figure 9.13: (a) *Electron density (probe) and temperature (OES) for H_2 and D_2 plasmas at 10 Pa and 250 W with varying Cs density.* **(b)** *Atomic hydrogen density within the corresponding discharges. The starting point of the arrows denotes the beginning Cs evaporation.*

at about 575 K for H_2 and 520 K for D_2 is independent of the Cs content.

For the coupling to atomic hydrogen ($H + e \rightarrow H^* + e$, more precisely reactions (1)–(5) in table 6.4) the crucial parameter is the atomic hydrogen density. It is evaluated from the ratio H_γ/Fulcher in combination with the CR model Yacora H and is shown in figure 9.13 (b) for both isotopes. It can be seen, that increasing the Cs density up to about $5 \times 10^{15}\,m^{-3}$ leads to a decrease of the atomic hydrogen density from $2 \times 10^{19}\,m^{-3}$ down to about $1 \times 10^{19}\,m^{-3}$, whereas n_D decreases by about 20 % in the present investigations. The higher absolute atomic density for D_2 can again be attributed to the higher cross section for dissociative electron impact excitation compared to H_2 (see figure 3.3). The densities also show the hysteresis effect, i. e. a delayed response to the decreasing Cs density. While in deuterium the initial atomic density can be recovered, the H density is still significantly decreased even at infinitesimal Cs density.

The smaller relative decrease of n_D compared to n_H despite similar Cs densities might be ascribed to the overall evaporated amount of caesium, which is determined by the time-integrated Cs density: in D_2 this value is 33 % smaller than in H_2. This might also be the cause for the faster increase of the density after Cs

evaporation, resulting in a less pronounced hysteresis in D_2. Furthermore it can be seen, that in hydrogen the atomic density decreases gradually with increasing Cs density, whereas in deuterium the Cs content within the discharge stays constant during the decrease of the atomic density. This behavior results from the faster increase of the Cs density during the investigations performed in the D_2 discharge (the maximum Cs density is achieved in about half the time).

Hence, the evolution of the atomic density explains the decreasing evolution of the Balmer emission. However, the clearly observable impact of Cs on the line ratio H_α/H_β in figure 9.12 cannot be assessed by the coupling to H or H_2. But the coupling to H_2^+ can indeed lead to a variation of the line ratio H_α/H_β while the ratios H_β/H_γ and H_γ/H_δ are virtually unaffected. This arises from the fact, that the dissociative recombination process ($H_2^+ + e \rightarrow H^* + H$) has more impact on the Balmer lines H_β, H_γ and H_δ than on H_α (see figure 6.16). Thus, the observed increasing line ratio H_α/H_β upon Cs seeding could indicate a decreasing molecular ion density $n_{H_2^+}$. However, for the present discharges the contribution of dissociative recombination to the total population of the upper Balmer levels is almost negligible, which leads to a very low sensitivity of the modeled emission on the density $n_{H_2^+}$. This means that the measured variation of H_α/H_β cannot be ascribed reliably to a variation of $n_{H_2^+}$, especially if the measurement errors of 10 % for the emissivities are taken into account. Furthermore, the influence of negative ions H^- on the Balmer emission via the mutual neutralization reactions ($H^- + H^+ \rightarrow H^* + H$ and $H^- + H_2^+ \rightarrow H^* + H_2$) cannot be assessed either, since the densities of H^+ and H_2^+ are undetermined.

In conclusion, for the present Cs seeded hydrogen discharges the behavior of the Balmer series upon Cs seeding is determined by the constant contribution of the coupling to molecular hydrogen and the varying contribution of the coupling to atomic hydrogen due to the decreasing H density within the discharge. The couplings to the molecular ion and to the negative ion have only very little contribution to the absolute Balmer emission and thus the behavior of these species is not accessible via OES.

The getter effect of Cs

The observations including the hysteresis effect and the dependencies on the 'application time' of Cs on the system imply the involvement of chemical processes at the vessel surfaces. Reactive processes within the plasma volume (as presented in section 4.4.2) should lead to a direct correlation to the measured Cs density

within the volume, which excludes effects like hysteresis etc. However, chemical surface processes can constitute an effective sink leading to the gettering of hydrogen particles at the vessel walls and a delayed release of the gettered particles. The getter effect can also be observed at the RGA signal for water (not shown) and is also to be seen in figure 7.9 at the background pressure, in figure 7.12 at the H_2O content and in figure 7.10, where the enhanced chemical gettering of Cs due to hydrogenation of the vessel walls is considered as a cause for the decreasing Cs density. Moreover, the investigations on the work function of a cesiated sample surface in section 8.2 are entirely based on surface effects: the Cs layers on the surface and thus the work function of the sample are also subject to hysteresis and the dependency on the evaporation time.

Therefore, it can be stated, that the cesiation of the vessel surfaces due to the evaporation of Cs causes the gettering of atomic hydrogen at the vessel walls. The influence of Cs on the atomic hydrogen density is of the order of $10^{19}\,\mathrm{m}^{-3}$, in contrast to the Cs volume density of the order of only $10^{15}\,\mathrm{m}^{-3}$. This illustrates, that the majority of the evaporated Cs covers the vessel walls leading to the getter effect and only a very small amount of the evaporated Cs actually remains gaseous in the vessel volume. A longer 'application time' of Cs, i. e. a higher value of the time-integrated Cs density, then leads to increased cesiation of the vessel walls and thus to enhanced gettering. This explains the apparent larger impact of Cs on the H_2 plasma than on the D_2 plasma, even if the Cs densities are comparable. Differing reaction kinetics between the two isotopes should be excludable, since chemical reactions are connected to the electronic properties of the particles, and not to the isotopic mass.

The getter effect of Cs can also be seen when comparing the atomic densities in the present investigations prior to Cs evaporation (figure 9.13 (b): 2.0 and $2.7 \times 10^{19}\,\mathrm{m}^{-3}$ for H and D, respectively) to those in pure hydrogen discharges among the investigations performed in section 9.1, more precisely in figure 9.7 (b) (4.6 and $7.3 \times 10^{19}\,\mathrm{m}^{-3}$ for H and D, respectively). The investigations on xenon admixtures are performed in a chemically cleaned discharge vessel. On the contrary, the present campaign on the Cs dynamics also involves several investigations in vacuum prior to the plasma investigations (see section 8). Therefore, large amounts of caesium were already evaporated prior to the first measurement of the atomic hydrogen density in plasma. Thus, the vessel surfaces are already coated with Cs or Cs compounds yielding enhanced gettering of H and D at the walls even if the Cs density is still negligible.

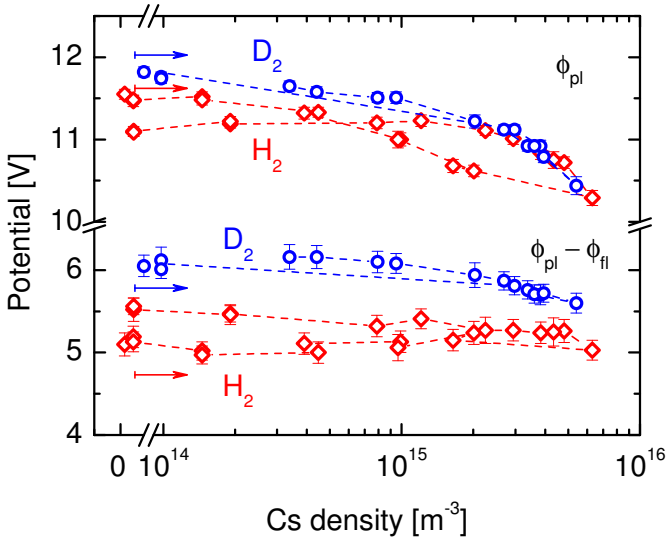

Figure 9.14: *Electrostatic potentials of H_2 and D_2 plasmas at 10 Pa and 250 W RF power with varying Cs density. The arrows denote the starting point for Cs evaporation.*

Influence on the plasma potential – indications for H^- ions

Figure 9.14 shows the influence of evaporating Cs into hydrogen or deuterium plasmas on the plasma potential and on the potential drop to a floating surface plotted against the corresponding Cs density within the discharge. It can be seen that for both isotopes an increasing Cs density of up to $6 \times 10^{15}\,\mathrm{m}^{-3}$ leads to a decreasing plasma potential by about 1.3 V. Decreasing the Cs density leads to increasing plasma potentials, where for H_2 the plasma potential at infinitesimal Cs density is lower than the initial one. On the other hand, the influence on the potential drop is not clearly perceived: while in H_2 $\phi_{\mathrm{pl}} - \phi_{\mathrm{fl}}$ does not vary with increasing Cs density, but increases with decreasing Cs content, a slight decrease of about 0.4 V can be observed in D_2. Nevertheless, the much lesser influence of Cs on $\phi_{\mathrm{pl}} - \phi_{\mathrm{fl}}$ than on ϕ_{pl} leads to a shift of the entire probe characteristic to lower voltages if Cs is present in the discharge.

The evaporation of Cs into the discharge leads to the cesiation of the vessel surfaces which in turn results in a lowering of the work function, as shown in section 8.2.2. The plasma within the vessel now additionally leads to increased vessel wall temperatures, impinging ions onto the walls due to the boundary potentials and the incidence of UV radiation from the hydrogen plasma onto the walls. These effects are supposed to induce a cleaning of the Cs layer and thus to a further decrease of the work function, as was shown in section 8.2.3

for the influence of an increased surface temperature. Consequently, at the low work function surfaces atomic and ionic hydrogen particles can be converted into negative ions and the UV radiation from the plasma can lead to the emission of photoelectrons. The resulting negative space charge leads to a decrease of the electron flux from the plasma onto the walls. Hence, a smaller potential barrier between the volume plasma and the grounded vessel walls is sufficient and thus ϕ_{pl} decreases. The larger evaporated amount of Cs for the H_2 plasma and the associated enhanced cesiation of the vessel walls again leads to the persistent effect after Cs evaporation.

However, for the potential drop $\phi_{\mathrm{pl}} - \phi_{\mathrm{fl}}$, measured at the location of the probe tip, no influence upon Cs seeding is expected: Since a high destruction rate of the negative hydrogen ions via associative and collisional detachment is expected within the hydrogen plasma at 10 Pa due to the high densities of atomic and molecular hydrogen (see section 2.2, processes (2.6) and (2.7)), the influence of negative ions produced at the vessel walls is very limited at the location of the probe tip. Moreover, no increase of the electron density is observed and thus photoemitted electrons from the vessel walls are at least not detectable in the plasma volume. Further, as the probe tip is heated to red-heat each time before an $I - V$ curve is recorded, the probe tip should not be covered with Cs or Cs compounds and thus production of negative ions or photoelectrons directly at the probe surface is also negligible. Finally, the production of negative ions via processes in the plasma volume contributes only to an infinitesimal extent to the ion balance and should not be dependent on the Cs density, as long as the plasma parameters are not influenced by Cs, which is presently not the case. Therefore, negative ions as well as photoelectrons should have only negligible influence on the charge flux balance at the location of the Langmuir probe. Further, the electron temperature is not influenced by Cs and a rough estimation of the ionization degree of Cs using equation (3.12) yields only some percent, which in turn implies that the mean ion mass is neither influenced significantly.

Hence, from a theoretical point of view, no influence of Cs on the potential drop $\phi_{\mathrm{pl}} - \phi_{\mathrm{fl}}$ is expected. The observed variations of the potential drop including the differing behavior in H_2 and D_2 can thus not be explained up to now. However, the measured effects remain within 0.5 V.

The increased potentials for the D_2 plasma are again attributable to the higher mass: the consequently smaller ion fluxes are compensated by higher potentials as already observed in section 9.1.1. Concerning the absolute values of the plasma

potentials, the continual evaporation of Cs in the present investigations in contrast to the clean vessel walls during the xenon investigations leads to the already decreased initial values for ϕ_{pl} in figure 9.14, as it was similarly already observed with the initial atomic hydrogen densities.

Summary

Cs seeding into H_2 and D_2 discharges with densities of up to $10^{16}\,\mathrm{m}^{-3}$ has no influence on the electron temperature or density, nor on the EEDF. However, the getter effect of Cs leads to a decreasing density of atomic hydrogen and the production of negative ions and photoelectrons at the vessel walls is suggested as reason for the decreased plasma potential.

9.2.3 Application of the extended corona model for Cs

It was commonly observed, that emission from the resonance lines of Cs was detectable well before Cs could be detected by the white light absorption spectroscopy. Hence, by means of the Cs emission the detection limit for Cs could be decreased drastically. The correlation of the emissivity of the resonance lines with the Cs density is described by an extended corona model, which is introduced in section 6.2.2.

Since the model incorporates only electron impact excitation from the ground state as well as cascades for the 6 P levels (inherently included in the applied cross section), it has to be verified, that further excitation channels for the upper states of the resonance transitions are negligible. This is performed by comparing calculated and measured emissions for the four resonance lines from the 6 P and the 7 P levels. The benchmark is shown in figure 9.15 for the Cs seeding procedure already presented in figure 9.11 (b). For the calculations via the extended corona model after equation (6.19) the electron density from probe measurements, the electron temperature evaluated from OES via the CR model Yacora H and the caesium density from white light absorption spectroscopy are used. Certainly, comparison can only be performed, when the Cs density exceeds the detection limit for the absorption spectroscopy, which is between 280 and 480 minutes. In contrast, emission from the lines at 852.1 nm and 894.3 nm is detectable from the beginning, which illustrates the increased sensitivity of the OES.

The error bars for the calculations arise from variations of the input parameters within the corresponding uncertainties. Hence, it can be seen, that the extended

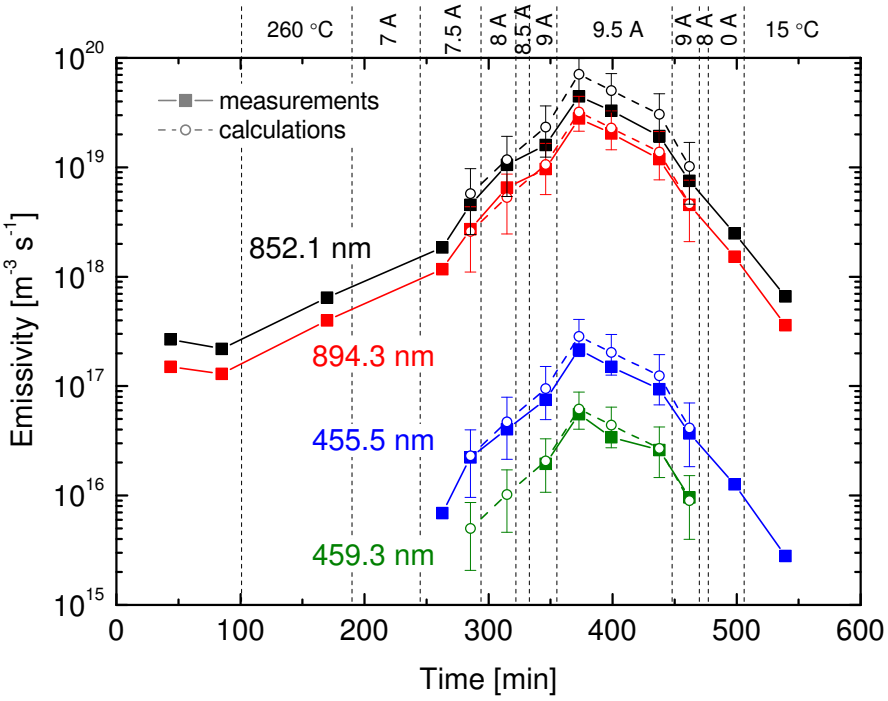

Figure 9.15: *Emission of the first four resonance lines of Cs due to evaporation into a H_2 plasma at 10 Pa and 250 W. Measurements and calculated values via the extended corona model for Cs are shown.*

corona model reproduces the measured emission within the errors of the input data. Thus, further population channels for the resonant levels of the Cs atom are negligible in the present ICP, and electron impact excitation from the Cs ground state is the main excitation process. More precisely, interaction of Cs with hydrogen particles in the plasma (see section 4.4.2) does not lead to a measurable population or depopulation of electronic levels of Cs. In particular, the mutual neutralization reaction of Cs ions and negative hydrogen ions (process (4.22)) has no influence due to the low densities of the two species.

In conclusion, the extended corona model for Cs can be used to monitor the caesium density via OES, if the electron density and temperature are known. However, n_e and T_e proved to be independent of the Cs content within the plasma and thus a constant correlation between emission and density is achieved:

$$\epsilon_{852} \overset{(6.19)}{=} n_e n_{Cs} X_{em,852}(T_e) \approx n_{Cs} \times 1.2 \times 10^4\,s^{-1}\,, \qquad (9.2)$$
$$\text{for} \quad n_e = 3.5 \times 10^{16}\,m^{-3}$$
$$\text{and} \quad T_e = 2\,eV\,.$$

Based on the detection limit of emission signals at the 852.1 nm line of $7 \times 10^{16}\,\mathrm{m^{-3}s^{-1}}$ the detection limit for the Cs density can be decreased down to $6 \times 10^{12}\,\mathrm{m^{-3}}$, which corresponds to an enhancement by about a factor of 60 compared to the white light absorption spectroscopy.

For the present investigations the Cs density below the detection limit of the absorption spectroscopy is determined via OES using the extended corona model, as e. g. already performed for figures 9.12 (b), 9.13 and 9.14.

9.3 Caesium seeded H_2 plasmas in proximity to a surface

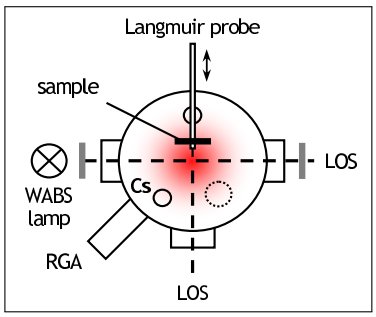

In section 9.2 it was pointed out that evaporating Cs into a hydrogen plasma at 10 Pa and 250 W RF power mainly leads to the cesiation of the vessel walls. The coating of the surfaces results in the gettering of hydrogen particles from the plasma and indications for the production of negative ions have been observed via the decreasing plasma potential. In order to confirm the expected formation of H^- at the vessel surfaces a dedicated stainless steel sample (same material as the vessel walls, $30\times30\,\mathrm{mm^2}$) is introduced near the center of the vessel and the Langmuir probe is fed through the sample surface.

In figure 9.16 the resulting geometrical constellations are shown. The sample holder is positioned in such a way, that the sample surface is located at 17 mm distance from the line of sight for the optical emission and white light absorption spectroscopy. As described in section 6.5.3, the position of the Langmuir probe can be varied, whereas for the present investigations two different configurations are applied: In case I the probe tip (length 8 mm) starts 3 mm above the surface leading to a maximal distance of 11 mm from the surface. In case II the Langmuir probe is steeped 3 mm in the sample holder. Owing to the 4 mm diameter of the hole the distance of the probe tip to the sample surface is minimal 2 mm and maximal 5 mm. The presented measurements from the Langmuir probe are consequently an average over the covered distances, whereas always the maximal distance is given in the graphs as reference.

The sample is floating within the plasma and the plasma parameters in proximity of the surface are certainly influenced by the presence of this additional

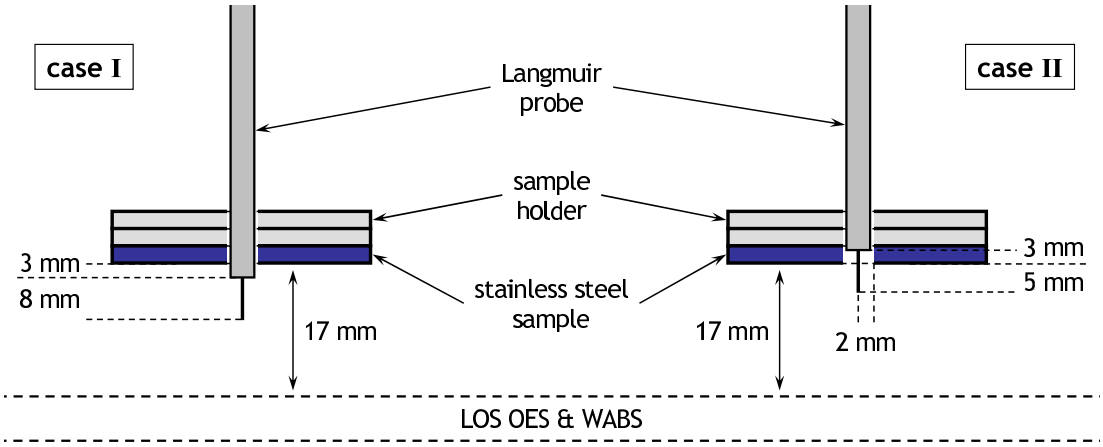

Figure 9.16: *Illustration of the configurations for the measurements in the vicinity of the stainless steel sample surface.*

plasma boundary. Therefore, the measured electron densities from the probe measurements cannot be used for the evaluation of OES signals. A constant electron density corresponding to the values without sample surface is used in the evaluations: $n_e = 3.5 \times 10^{16}\,\mathrm{m}^{-3}$.

Electron temperature and atomic hydrogen density within the LOS

Figure 9.17 shows the electron temperature (top) and the atomic hydrogen density (bottom) evaluated via OES using the CR model Yacora H for varying the Cs density in the H_2 plasma. Results with the stainless steel sample in 17 mm distance from the LOS are compared to the results without the sample surface from figure 9.13.

It can be seen that the surface has no influence on the electron temperature measured 17 mm away, which is in accordance with the observations of flat T_e profiles in ICP discharges (see [SFAP01] for instance). The high thermal conductivity of the electrons within the plasma leads to a homogeneous temperature distribution within the vessel which is modified only very close ($\ll$ mm) to the surfaces due to the plasma sheath. Furthermore, the independence of T_e from the Cs content within the discharge is confirmed.

However, the surface influences the atomic hydrogen density leading to a 40 % decrease prior to Cs evaporation. The nearby surface acts as additional sink for the H atoms which modifies the atomic hydrogen density profile and leads to a reduced density within the LOS even if electron density and temperature (and thus the dissociation rate) are left unaltered. This effect is already observed in

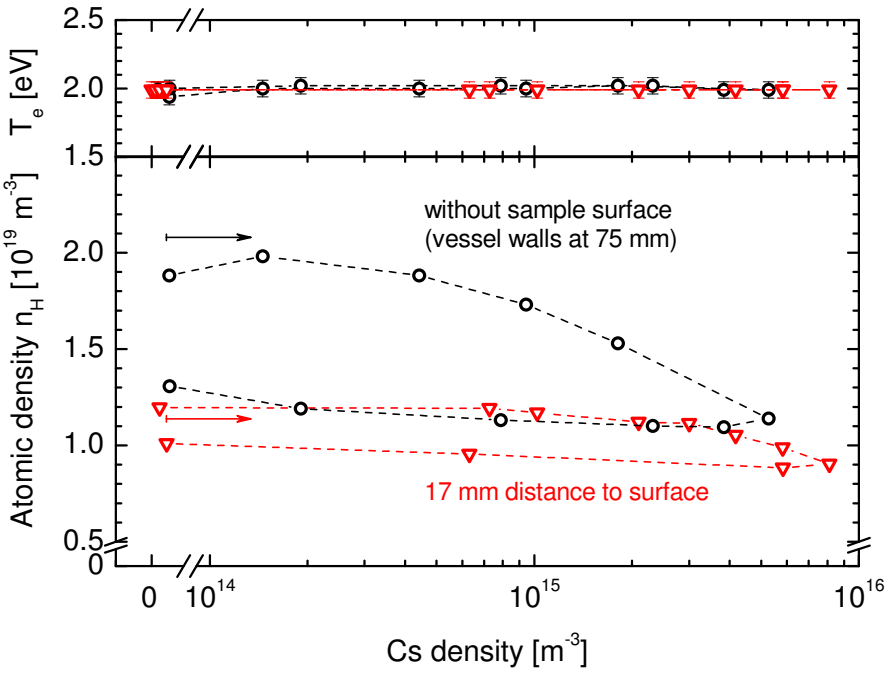

Figure 9.17: *Electron temperature and atomic hydrogen density depending on the Cs density in a H_2 plasma at 10 Pa and 250 W for two different distances to the closest surface. The starting point of beginning Cs evaporation is denoted by arrows.*

[Fan04] for instance, showing decreased atomic hydrogen densities above several surface materials up to 18 mm distance.

Introducing the Cs evaporation leads to the decrease of the atomic hydrogen density due to the getter effect of the cesiated vessel surfaces and the accompanied hysteresis due to the persistent Cs layers (see section 9.2.2). However, with the sample surface present, n_H is reduced by only about 25 % compared to 45 % without the sample surface. A rough estimation reveals (not shown here), that this can be explained by the already reduced initial atomic density due to the sample surface, which leads to a reduced relative influence of the cesiation, even if the efficiency of the gettering at the vessel walls is the same. Thereby, the additional getter surface of the sample can be neglected, as it constitutes only 2 % of the entire vessel surface area.

Hence, the sample surface does not affect the electron temperature measured in the LOS but slightly reduces the sensitivity for detecting the getter effect.

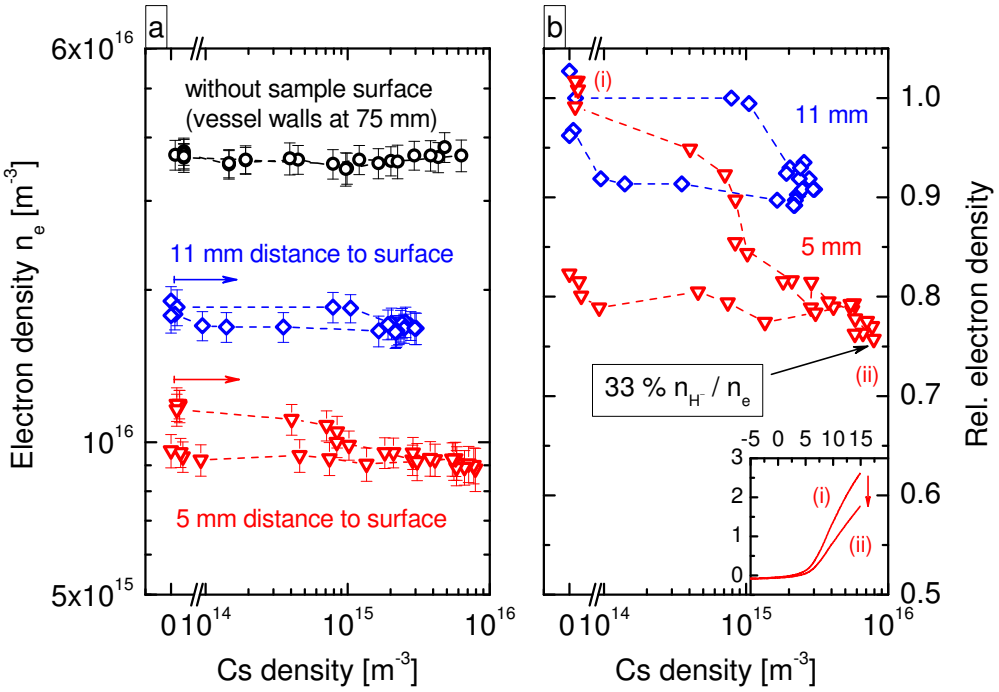

Figure 9.18: *Electron density depending on the Cs density in a H_2 plasma at 10 Pa and 250 W for different distances from a stainless steel surface (see figure 9.16).* **(a)** *Absolute values.* **(b)** *Relative values. The arrows in (a) denote the beginning Cs evaporation and the inlet in (b) shows two exemplary $I-V$ curves ([mA]–[V]) from the Langmuir probe at 5 mm distance for (i) infinitesimal and (ii) high Cs density.*

Electron density above the sample surface

In figure 9.18 (a) the electron densities measured above the surface are shown depending on the Cs density. The distance titled '11 mm' corresponds to case I in figure 9.16, '5 mm' to case II.

At the initial electron densities prior to the evaporation of caesium it can be seen, that n_e decreases approaching the surface: down to 50 % at 11 mm distance and down to about 30 % at 5 mm. This is attributable to the additional plasma boundary and the resulting plasma profile towards this boundary, comparable to the decrease of n_e from the plasma center towards the vessel walls according to the Bessel profile (see [SFAP01]).

Evaporating Cs into the H_2 plasma has no effect on the electron density of the volume plasma, as described in detail in section 9.2.2. However, in the vicinity of the surface the increasing Cs density leads to a decreasing electron density and the influence increases with decreasing distance to the surface. This behavior

is emphasized in figure 9.18 (b) where the electron densities are plotted relative to the initial densities. It can be seen, that at 11 mm distance the maximal Cs density of $3 \times 10^{15}\,\mathrm{m}^{-3}$ yields a decrease in n_e of about 10 %. At the same Cs content the electron density at 5 mm distance is already decreased by 20 %. Further increasing the Cs density up to $8 \times 10^{15}\,\mathrm{m}^{-3}$ decreases the electron density at 5 mm distance from the surface down to 75 % from the initial value. Decreasing the Cs density again reveals the often observed hysteresis.

As described in section 8.2, cesiation of the sample surface in vacuum leads to the decrease of the work function down to 2.75 eV. The elevated surface temperature of above 230 °C in plasma together with the impinging ions due to the boundary potentials and the UV radiation from the hydrogen plasma have an additional cleaning effect on the Cs layer and thus the work function should be further decreased in plasma operation compared to the observations in vacuum. This behavior is already confirmed in [GWF11]. Thus, negative hydrogen ions will be produced by surface conversion of particles from the H_2 plasma (atomic hydrogen H and the ions H^+, H_2^+ and H_3^+) at the low work function surface. These negative ions repress electrons from the sample surface and replace them in the charge balance equation to maintain quasineutrality. However, due to their high mass the charge flux of negative ions onto the probe is negligible compared to the remaining flux of electrons. Therefore, the branch of the $I - V$ curve corresponding to negative charges (i. e. the 'electron branch') decreases due to the repression of electrons upon the presence of negative hydrogen ions (see section 6.5.1, page 98). This can be seen at the inlet in figure 9.18 (b) where two probe characteristics are shown from 5 mm distance to the surface: the arrow illustrates the reduction of the electron branch from prior to Cs evaporation to the state of maximum Cs density within the discharge.

The decreasing electron branch directly leads to the evaluation of a lower electron density and from the discussion it is justified to directly associate this decrease to the negative hydrogen ion density. Thus, an amount of 33 % $n_{\mathrm{H}^-}/n_\mathrm{e}$ is measured at 5 mm distance from the stainless steel sample surface and a Cs density of $8 \times 10^{15}\,\mathrm{m}^{-3}$.

It is to mention, that a possible influence of photoelectrons emitted from the low work function sample surface due to the UV radiation from the plasma would not be detectable by means of the Langmuir probe, since the origin of the measured electron flux is indeterminate and it is not possible to distinguish between photoelectrons and plasma electrons.

With increasing distance to the surface the dominance of destructive collisions (see section 2.2) increases and thus the negative hydrogen ion density decreases, which is detected as a less pronounced influence on the measured electron density. At the distance of the LOS, 17 mm from the surface, the influence of negative ions is already reduced to a level at which no impact on the Balmer emission via the mutual neutralization reactions can be observed, as pointed out in section 9.2.2.

Potential drop $\phi_{\mathrm{pl}} - \phi_{\mathrm{fl}}$ above the sample surface

Figure 9.19 (a) shows the potential drop $\phi_{\mathrm{pl}} - \phi_{\mathrm{fl}}$ measured at different distances from the sample surface (bottom) depending on the Cs density together with the sample temperature (top). For the measurements without the sample surface (figure 9.14) only the part for increasing Cs density is shown for reasons of clarity.

Approaching the surface the measured potential drop increases. After equation (6.34) $\phi_{\mathrm{pl}} - \phi_{\mathrm{fl}}$ depends on the electron temperature and on the ion mass, whereas the latter should not be dependent on the distance to the surface. However, an increasing T_{e} is actually measured via the Langmuir probe approaching the surface (not shown). This arises from the increasing potential barrier for the electrons by which the amount of low energy electrons is subsequently reduced.

Evaporating Cs into the discharge has virtually no influence on the potential drop within the plasma volume if the measurement error is considered. However, with decreasing distance to the sample surface, the influence of Cs increases resulting in a decreasing potential drop with increasing Cs density. At 11 mm distance to the surface the maximum Cs density of $3 \times 10^{15}\,\mathrm{m}^{-3}$ leads to a decrease in $\phi_{\mathrm{pl}} - \phi_{\mathrm{fl}}$ of 0.45 V. At 5 mm distance from the surface the same Cs density results in a decrease of 0.7 V and increasing the Cs density further to $8 \times 10^{15}\,\mathrm{m}^{-3}$ yields a decrease of the potential drop of 0.9 V. Decreasing the Cs density shows the well-known hysteresis effect.

The behavior of $\phi_{\mathrm{pl}} - \phi_{\mathrm{fl}}$ at the particular distances is very similar to the corresponding progression of the electron density in figure 9.18. This suggests, that the formation of negative hydrogen ions at the low work function surface is also the cause for the present observations. As already described, the produced negative ions from the surface repress the electrons and alter the charge balance in front of the sample surface. Therefore, a lessened potential barrier for the negative charges (electrons and negative ions) is sufficient to obtain flux equilibrium. The increasing negative hydrogen ion density with increasing cesiation of the sample (see figure 9.18) thus leads to a decreasing value of $\phi_{\mathrm{pl}} - \phi_{\mathrm{fl}}$. However, a possible

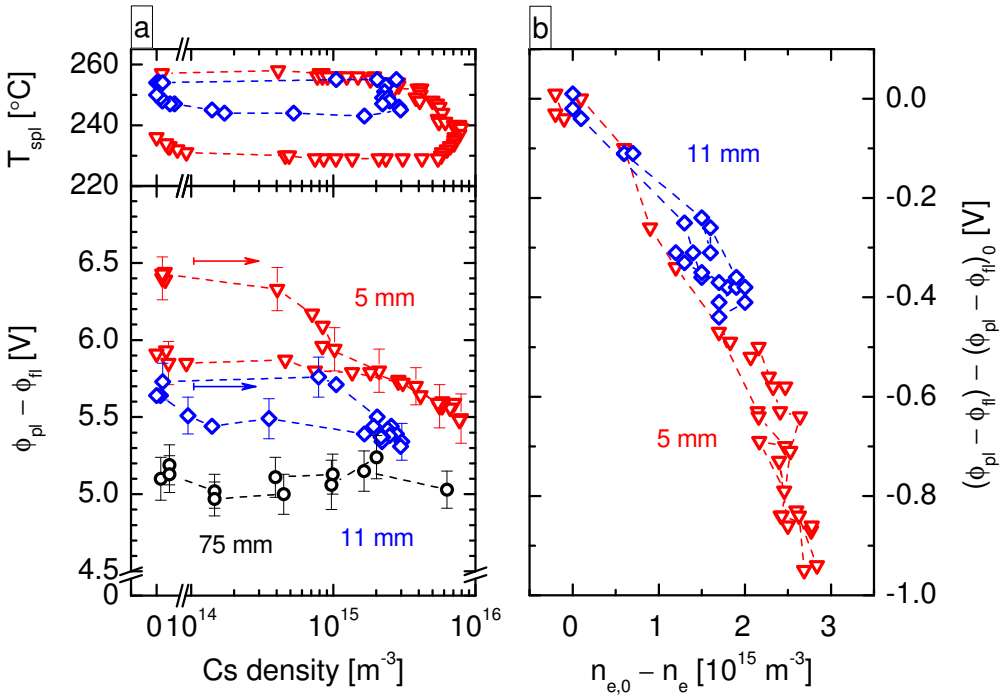

Figure 9.19: (a) *Potential drop $\phi_{\mathrm{pl}} - \phi_{\mathrm{fl}}$ depending on the Cs density in a H_2 plasma at 10 Pa and 250 W at different distances from a stainless steel sample and the corresponding sample temperature. The arrows denote beginning Cs evaporation.* **(b)** *Reduction of the potential drop against the corresponding reduction of the electron density.*

influence on the potential drop due to a decreasing electron temperature upon Cs seeding cannot be excluded and, in fact, a slight decrease in T_{e} determined via the Langmuir probe is observed at 5 mm distance and high Cs densities (not shown).

Further, as the negative hydrogen ion density decreases with increasing distance from the surface the influence of Cs on $\phi_{\mathrm{pl}} - \phi_{\mathrm{fl}}$ decreases apparently. However, the resultant influence of the negative ions should in principle not depend on the actual position but only on the H^- density. This is confirmed in figure 9.19 (b) where the decrease in the potential drop is plotted against the corresponding decrease of the electron density, which is very likely to be associated with the negative hydrogen ion density. The correlation is clearly observable: the lessened decrease of $\phi_{\mathrm{pl}} - \phi_{\mathrm{fl}}$ with increasing distance is attributed to the decreasing density of negative hydrogen ions.

The above described influence on $\phi_{\mathrm{pl}} - \phi_{\mathrm{fl}}$ is still always restricted to the conditions at the actual position of the probe tip. However, the formation of negative ions at the surface will also cause a decrease of the total potential drop from the

plasma towards the sample surface. This can be observed at the sample temperature T_{spl} on top of figure 9.19 (a). The temperature of the floating sample within the plasma is determined by the energy input of the positive ions from the plasma which are accelerated due to the boundary potential. Since this potential decreases due to the cesiation of the sample surface, the temperature of the sample decreases. Certainly, the sample temperature does not depend on the distance of the Langmuir probe: the larger impact on T_{spl} for 5 mm distance from the surface arises solely from the enhanced cesiation due to the higher Cs densities during this investigation. In maximum the temperature of the sample decreases by 30 °C and a hysteresis due to the persistent Cs layer on the surface is also observable.

9.4 Summary: influence of Cs on the hydrogen plasma

The investigations have shown, that Cs densities up to $10^{16}\,\mathrm{m}^{-3}$ within a 10 Pa H_2 discharge have no influence on the electron density, the electron temperature or the EEDF of the volume plasma. This is in accordance with the expected influence arising from the observed effects of xenon admixtures to the H_2 plasma, according to which Cs densities of about $10^{17}\,\mathrm{m}^{-3}$ would be necessary to reveal the consequences of the high atomic mass and the low ionization energy of Cs (decreasing T_{e}, increasing n_{e}).

The main impact of the evaporation of Cs into the H_2 discharge is the covering of the vessel surfaces. Due to the high reactivity of caesium the resultant Cs layers act as effective sink for atomic hydrogen from the plasma. Here, Cs densities of only $4 \times 10^{14}\,\mathrm{m}^{-3}$ are sufficient to induce observable effects. However, this limit is not strictly fixed since actually the characteristics of the Cs layer are decisive, which are subject to hysteresis effects. At Cs densities of $5 \times 10^{15}\,\mathrm{m}^{-3}$ in the volume the atomic hydrogen density is reduced by about 50 %. The consequently decreasing dissociation degree can be monitored at the decreasing ratio H_γ/Fulcher and the decreasing Balmer emissions. The accompanied increasing line ratio H_α/H_β may indicate a decreasing density of the molecular ion H_2^+, but the variation is too small to make a reliable statement. Furthermore, from the Balmer emission no indications for the existence of negative ions within the volume plasma were found.

However, at the vessel surfaces the lowering of the work function due to cesiation indeed leads to the formation of negative hydrogen ions. At 5 mm distance to a stainless steel sample surface a density ratio of 33 % n_{H^-}/n_e is achieved for a Cs density of $8 \times 10^{15}\,m^{-3}$ above the surface. The H^- ions produced at the vessel walls together with possibly photoemitted electrons due to the UV radiation from the hydrogen plasma induce a decreasing potential of the volume plasma relative to the grounded vessel walls (up to -1.3 V). Furthermore, the potential drop towards a floating surface within the plasma is decreased yielding lower surface temperatures (up to -30 °C).

The investigations showed no differences between H_2 and D_2 concerning the influence of Cs seeding. The basic isotopic differences observed in section 9.1.1 are however confirmed: D_2 plasmas show a larger dissociation degree, a higher plasma potential and potential drop and a slightly decreased gas temperature, while electron density and temperature are almost identical.

The benchmark of the established extended corona model for the Cs atom showed, that the resonance levels are predominantly populated by electron impact excitation from the ground state. Hence, the model can be applied to determine the Cs density via OES, if electron density and temperature are known. This results in a 60-fold enhanced detection limit compared to the white light absorption spectroscopy if the Cs transition at 852.1 nm is used as diagnostic line.

10 Implications of the results for NNBI ion sources

As described in section 2.3 the present laboratory experiment has vacuum conditions and plasma parameters close to those in NNBI ion sources. Therefore, the presented investigations on the Cs dynamics in vacuum and plasma are directly applicable to NNBI ion sources like the ITER reference ion source at the Max-Planck-Institut für Plasmaphysik (IPP) in Garching.

Caesium consumption

An assessment of the Cs consumption for the ITER NNBI ion source yields about 40 g per year based on the evaporation rates presently required at the IPP prototype ion source in order to achieve the ITER requirements [HDG$^+$09]. Furthermore, the penetration of the evaporated Cs through the extraction apertures of the converter surface into the acceleration system has to be prevented to maintain the high voltage stability. Hence, in order to prolong the periods for the exchange of the Cs reservoir and to avoid contamination of the accelerator by Cs as effectively as possible, a reduction of the required Cs evaporation and thus of the Cs consumption is very desirable. The investigations performed within this work give two starting points for a possible reduction: an alternative Cs source and the reduction of the influence of impurities.

Alternative Cs source: Cs dispenser oven

The Cs source developed within the scope of this work can provide a stable, controllable and reliable Cs source for negative ion sources with the opportunity for reduced Cs consumption, as will be shown in the following paragraphs. The device comprises a dispenser with variable Cs content as Cs reservoir, an all-metal valve to separate the Cs reservoir from the ion source vessel during maintenance phases and a surface ionization detector (SID) to measure the evaporation rate. Furthermore, the all-metal construction together with several feedback controlled heating circuits allows for a homogeneous temperature profile at oven tempera-

tures of up to 300 °C, which is essential against the formation of cold spots and thus for the reliable operation of the Cs source.

It was shown, that using the **dispenser as Cs reservoir**, the evaporation rate of the entire system can be adjusted independently of the oven temperature. Thus, the Cs flux can be controlled with short response times by varying the electric heating current of the dispenser. This can moreover be beneficial for the high voltage high power RF environment at ion sources since basically only the electrical circuit for the dispenser has to be adjusted to adapt the evaporation rate. The Cs content within the dispenser is chemically stable under ambient conditions, as long as the dispenser is not activated. Thus, the Cs handling and safety is facilitated compared to the presently used liquid Cs reservoirs at the ion sources. Furthermore, the presented investigations have shown, that the dispenser itself is not degenerated due to the presence of an increased partial pressure of impurities. Accordingly, the evaporation rate recovers after the impurity content is diminished or it can be recovered manually via increasing the dispenser heating current. Due to this lessened susceptibility to impurities compared to liquid Cs reservoirs the overall Cs consumption could be reduced.

The integrated **valve** proved to maintain the conditioning of the vessel, if the dispenser has to be exchanged and, on the other hand, it protects the activated dispenser from ambient air, if the main vessel needs to be vented. These advantages can directly be transfered to the ion source. Hence, the Cs reservoir and the conditioning of the source vessel, respectively, can be protected and thus the Cs consumption can again be reduced.

The **SID mounted at the oven nozzle** proved to be an excellent tool for monitoring the evaporation of the oven with a very high sensitivity (2 µg/h) and a dynamic range of more than four orders of magnitude. This gives the opportunity for a feedback controlled evaporation via the dispenser heating current, which is in turn finely tunable. Thus, the Cs evaporation can be controlled accurately which again gives a possibility for reducing the overall Cs consumption. Furthermore, due to the quantification of the evaporation rate the evaporated amount of Cs can be assessed and the run out of the reservoir can be predicted.

The **comprehensive Cs oven** shows a reliable evaporation of Cs with adjustable evaporation rates between 50 µg/h and more than 10 mg/h which can be maintained stable for several hours. Furthermore, the present investigations have shown, that in the laboratory setup a stable low work function of a sample surface is achieved at evaporation rates slightly above 1 mg/h in vacuum. Consid-

ering the increased inner vessel surface area of NNBI ion sources, it is expected that correspondingly higher evaporation rates are required. This can easily be achieved via increasing the dispenser heating current and for ITER, in particular, not only one Cs oven will be applied [IAE02]. The increased evaporation rate in turn leads to a faster depletion of the dispenser, which can however be addressed by using dispensers with larger amounts of Cs. Dispensers with Cs contents of the order of several grams are commercially available [Alv10], which are expected to have basically the same behavior as the 100 mg dispensers used for the present investigations and can thus readily be applied.

In conclusion, the design of the Cs source applied within the scope of this work represents a real alternative to the presently used liquid Cs ovens at NNBI ion sources with the opportunity to significantly reduce the Cs consumption.

Influence of impurities on the Cs content

Caesium reacts rapidly with the residual gases in negative ion sources and is thus no longer available for the required coating of the converter surface. This has to be compensated and consequently leads to an increased Cs consumption. Thus, information on the influence of the particular constituents of the residual gas on the Cs content can provide indications for the reduction of the Cs consumption.

The performed investigations in the laboratory setup have revealed, that nitrogen can be neglected as reactive impurity for Cs compared to oxygen and water. Embedding of N_2 in the Cs layers at the inner surfaces of the dispenser oven was only observed after several days at ambient air. For the Cs chemistry at relevant time scales and partial pressures however, O_2 and H_2O are the decisive reaction partners. Already very low partial pressures of the order of 10^{-5} mbar have a significant impact: the evaporation rate from the dispenser oven and the Cs content within the vessel decrease instantaneously due to the aggravated chemical binding of Cs in compounds.

In presence of H_2O each Cs compound will react to the stable crystalline caesium hydroxide CsOH. Since the water partial pressure is the main constituent of the background pressure in high vacuum environments, reducing the background pressure will have a crucial impact on the Cs content: the dominance of Cs compounds is reduced and this in turn leads to a reduced Cs consumption and a shortened conditioning time of the source. This was already observed in [FFW12] and is confirmed by the present dedicated investigations on water admixtures.

On the other hand, the presently observed 'H_2 effect', i. e. a drastic increase of the Cs content within the vessel due to the presence of several pascals of hydrogen gas and red-hot filaments, is not expected for NNBI RF ion sources since the hydrogen pressure is typically below 1 Pa and no permanently heated filaments are present.

Work function of the converter surface

The work function of the converter surface in negative ion sources is the key parameter for the formation of negative ions. However, in ion sources commonly no diagnostic is present to measure the work function and the inherent involvement of Cs compounds implies that data from the literature about the work function of cesiated substrates cannot be applied. Thus, systematic investigations are performed in the laboratory experiment.

The present investigations on cesiating a stainless steel sample in vacuum have confirmed, that a flux of Cs onto the sample decreases its work function. However, the work function decrease is not determined by the growth of a pure Cs layer since the minimally achievable work function is slightly below 2.8 eV (possibly overestimated by some 0.1 eV due to the evaluation method), whereas pure Cs has a work function of 2.14 eV. Thus, as already mentioned, Cs compounds are very likely to be involved, which increase the work function due to their non-metallic character. In ion sources the impact of impurities is comparable to the present ICP and thus, a comparable decrease of the work function is to be expected for cesiation of the converter surface in vacuum.

Furthermore, it was shown that elevated temperatures are beneficial for cleaning of the Cs layer and against its degradation. Investigations on surface temperatures of up to 250 °C revealed, that 200 °C are optimal for an effective cleaning of the Cs layer and the accompanied reduction of the work function even if no Cs flux onto the surface is present. At higher temperatures the absence of a compensating Cs flux however can lead to a diminishing of the Cs occupancy and thus to an increase of the work function. Hence, for an effective replenishment of the Cs layer at surface temperatures of 250 °C or above a constant Cs flux onto the surface is indispensable. For negative ion sources it was observed, that a temperature of 150 °C is already sufficient for a significant increase of the source performance [SFF+06]. Here the impact of the plasma surface interaction with the hydrogen/deuterium plasma in front of the converter surface can be crucial: the energy input due to impinging ions from the plasma and high energetic pho-

tons from optical transitions within the discharge assist the thermally induced cleaning of the surface layer. Preliminary investigations on this effect were already performed [GWF11] and detailed studies will be conducted in forthcoming campaigns at the laboratory setup.

Impact of Cs on the plasma in front of the converter surface

Evaporating Cs into the ion source basically affects two aspects of the source performance: the negative ion current is increased and simultaneously the co-extracted electron current is decreased, as presented in [SFF+06, SMF+11] for instance. The former is clearly explained by the enhanced production of negative ions at the converter surface due to Cs coating and the accompanied reduced work function. For the latter however, two causes can be thought of: a direct influence of caesium on the plasma parameters in front of the plasma grid ('direct influence' of Cs) or the repression of electrons from the plasma grid due to the production of negative hydrogen/deuterium ions ('indirect influence' of Cs). Since the co-extracted electrons produce high heat loads in the extraction system and thus often limit the achievable performance of the ion source, understanding the processes that lead to the reduction of the co-extracted electron current is a crucial issue for the optimization of the ion source.

Using the rare gas xenon as a substitute (similar mass to caesium), the present investigations have shown that the presence of a heavy particle with low ionization energy within the hydrogen/deuterium plasma leads to increasing electron density and decreasing electron temperature, as expected from the physics of low temperature plasmas. However, for Cs these effects can be excluded in the laboratory ICP for densities below $10^{17}\,\mathrm{m}^{-3}$ as shown by an assessment using the ratio of ionization rate coefficients of the plasma constituents. The estimations are confirmed by the measurements: up to densities of $10^{16}\,\mathrm{m}^{-3}$ no influence on n_e or T_e could be measured in the plasma volume. In NNBI ion sources an analogous assessment yields a Cs density of minimally $6 \times 10^{15}\,\mathrm{m}^{-3}$ to reveal the direct influence due to the lower absolute pressure. Typically this density is rarely achieved in ion sources [FW11, WFN13] and thus for the majority of cases a **direct influence** of Cs on the plasma parameters in front of the plasma grid can be excluded. Furthermore, the direct influence would lead to an increase of the electron density in contrast to the observed decrease.

On the other hand, the **indirect influence** of Cs was confirmed by the present investigations: The electron density 5 mm above a sample surface is decreased by

25 % due to the presence of Cs densities of $8 \times 10^{15}\,\mathrm{m}^{-3}$. Furthermore, the potential drop $\phi_{\mathrm{pl}} - \phi_{\mathrm{fl}}$ is decreased by 0.9 V. Both reductions are interpreted by the formation of negative hydrogen ions produced at the low work function surface. Departing from the surface their influence diminishes due to the increasing dominance of destructive processes.

However, the **Cs chemistry** at the vessel surfaces still has an influence on the main plasma. The Cs coating of the vessel walls reduces the work function and leads to the enhanced formation of negative ions as well as the emission of photoelectrons induced by the UV radiation from the hydrogen plasma. Consequently, the potential of the plasma relative to the vessel walls is reduced: ϕ_{pl} decreases by about 1.3 V due to Cs densities of $6 \times 10^{15}\,\mathrm{m}^{-3}$. Furthermore, the getter effect of Cs at the vessel surfaces leads to the diminishing of the density of atomic hydrogen/deuterium: in the laboratory setup the atomic hydrogen density was reduced by about 50 % due to Cs densities of $5 \times 10^{15}\,\mathrm{m}^{-3}$.

Especially the unaffected electron temperature and the reduced plasma potential upon Cs seeding are frequently observed in negative ion sources like the ITER reference ion source at IPP [SMF+11, FSWN13]. For the electron density distinct three-dimensional plasma profiles complicate the interpretation of the bare influence of Cs. The present investigations have however proven, that n_{e} is not directly influenced in the plasma volume at Cs densities commonly achieved in ion sources. But close to the converter surface a significant impact is yet to be expected due to the formation of negative ions.

Therefore, it can be stated that the reduction of the co-extracted electron current in NNBI ion sources upon Cs seeding cannot be attributed to a direct influence of Cs on the plasma parameters of the bulk plasma, but is predominantly caused by the repression of electrons from the extraction system.

Furthermore, the present investigations have shown, that effects induced by Cs are mostly subject to a hysteresis. This again arises from the surface chemistry, which persists even if the density of the Cs vapor is already diminished. Thus, the correlation between the measured Cs density above the converter surface and the source parameters like the extracted negative ion current density is disturbed. This is observed in [WFN13] for instance and can now be confirmed by the presented remaining influence of Cs even at negligible Cs density: the condition of the Cs layer on the converter surface, and thus its work function is the determinant parameter for the source performance.

Excessive caesium contents From the present investigations two negative impacts on the performance of a negative ion source can be cited, if the evaporation rate of caesium into the source gets too high: Firstly, at high Cs densities the direct effect of Cs on the volume plasma can evolve, i. e. the electron density increases due to the low ionization potential of caesium. This directly leads to an increasing co-extracted electron current. Secondly, the getter effect of Cs will result in the diminishing of the atomic hydrogen/deuterium density. Since negative ions are predominantly converted from the atom flux onto the converter surface [WSM+12], the extracted negative ion current decreases consequently. Thus, excessive Cs contents within the ion source have to be prevented and the optimum Cs amount should be determined by the correlation to the actual work function of the converter surface, which however cannot be determined up to now.

Differences of H_2 and D_2

It is commonly observed in negative ion sources, that the amount of co-extracted electrons is higher in deuterium operation than in hydrogen, as presented in [FSWN13] for instance. The reason behind this discrepancy between the two isotopes is not understood up to now. Explanatory approaches include differences in the transport of the plasma particles across the filter field, which separates the driver region from the extraction region and is actually used to cool the electrons. The differing filter field transport can lead to differing plasma profiles within the ion source resulting in a higher electron density in front of the converter surface in deuterium operation. The question remains, if fundamental isotopic differences exist which can contribute to the higher co-extracted electron current in D_2 and if the presence of caesium in the plasma has an impact.

The laboratory experiment showed, that the electron density in the volume is equal for both isotopes, and that the electron temperature determined via optical emission spectroscopy (T_e^{OES}), is also very similar. However, the EEDF measured by Langmuir probe is Maxwellian like in D_2 plasmas compared to a Bi-Maxwellian EEDF in hydrogen. Thus, especially the low energy part of the EEDF differs strongly and in deuterium a higher temperature T_e^{probe} can be assigned to this region. Furthermore, the dissociation degree is higher in deuterium due to a higher dissociation cross section and the plasma potential is higher due to the higher mass of deuterium ions. However, no difference in the influence of Cs on the bulk plasma could be observed.

An increased plasma potential and atomic density in deuterium compared to hydrogen are also measured in the plasma volume of the ITER reference negative ion source [FSWN13]. The increased atomic density increases the atom flux onto the converter surface and thus enhances the negative ion production. However, this advantageous effect of D_2 is accompanied by an increased amount of co-extracted electrons, as mentioned above. Here, neither the atomic density nor the plasma potential should have an influence. Moreover, probe measurements in the ion source have shown that here also the low-energy part of the EEDF has very similar evolutions in D_2 and H_2 yielding equal electron temperatures T_e^{probe} for both isotopes. Together with the measured equality of n_e and T_e^{OES} for both isotopes in the ICP, **it can be stated, that the present investigations give no indication for an increased co-extracted electron current in deuterium, as long as effects in the plasma volume are considered.**

However, it is to be expected, that the higher mass of D_2 results in a varied diffusion and thus in varied plasma profiles compared to hydrogen, as it was already presented for the ITER reference ion source in [FSWN13]. Therefore, it cannot be ruled out that isotopic effects with or without caesium occur at the plasma boundary. Thus, the investigations performed in proximity of a sample surface within this work are also to be performed in D_2 discharges.

Outlook

It was shown, that the presented laboratory setup is capable of reproducing a variety of effects observed at the ITER reference ion source at IPP. Several implications could already be deduced and thus the opportunity is given for dedicated investigations of further particular issues:

- The work function of the cesiated converter surface is the key issue for the source performance. Additionally, impurities within the source can have a major impact on the Cs content. Thus, the impact of impurities on the work function of a cesiated sample surface is to be investigated by dedicated admixtures of impurity gases.

- The converter surface in NNBI ion sources is permanently heated, which yields reduced amounts of adsorbed impurities on the surface. Fresh cesiation onto such a heated surface could possibly yield lower work functions than the performed coating of a cold surface due to the reduced contribution of Cs compounds. Thus, the cesiation of a bare sample surface at elevated

temperatures is to be examined, whereas the present investigations indicate, that a temperature of about 200 °C should be most promising.

- Due to the pulsed operation of NNBI ion sources the cesiated converter surface is periodically in contact with the hydrogen/deuterium plasma. Hence, the influence of plasma surface interaction on the work function is a crucial issue to be investigated: hydrogenation due to atomic hydrogen, energy input due to hydrogen and caesium ions as well as the intrinsic UV radiation of the hydrogen plasma can have an impact on the Cs coating. An extended setup for work function measurements during plasma operation using a triggered pulsed plasma system is already available [GWF11].

- Biasing the surface against the plasma can attract or repel ions from the plasma. Thus, the influence of the energy input of impinging ions on the work function can be investigated particularly. It can be thought of an additional cleaning effect and/or an effective erosion of Cs from the surface depending on the bias potential.

- The converter surface in negative ion sources is typically made of molybdenum. Thus, the dependency of the work function of cesiated surfaces on the substrate material under ion source conditions needs to be investigated.

- The isotope effect in negative ion sources is to be approached by investigating the plasma parameters in front of a sample surface in Cs seeded D_2 plasmas and comparing them to the already obtained results for H_2 plasmas.

- Evaluation of work functions is currently performed by means of the Fowler method. Due to necessary assumptions in the evaluation method in combination with the used light source, the determined work function values are always upper limits, where the deviation to the actual values increases with decreasing work function and can reach up to 0.5 eV in a very unfavorable case. Therefore, an enhancement of the accuracy would be most desirable. An approach to this issue is envisaged by using tunable diode lasers with appropriate wavelength ranges as alternative light sources.

- In the long term it is planned to equip the laboratory setup with another diagnostic: Using cavity ringdown spectroscopy (CRDS) the negative ion density within the bulk plasma and above the sample surface can be determined [OD88, WFN13]. Thus, the drawn implications about the existence

of H^- ions in vicinity to the sample surface can be examined. Furthermore, the combination with work function measurements during plasma can give a direct insight into the correlation between the surface work function and the corresponding formation of negative hydrogen/deuterium ions. In the final analysis this can yield the optimal evaporation rate which is required to achieve a stable Cs layer with low work function on the surface.

11 Conclusions

For the ITER HNB and DNB systems powerful ion sources for negative hydrogen and deuterium ions are required. The achievement of the ambitious target parameters is approached by utilizing the surface production of H^-/D^- at a low work function converter surface, which is therefore coated with caesium. The reliability and stability of a high negative ion current and a low co-extracted electron current thus drastically depends on the Cs dynamics within the source in vacuum phases as well as in the hydrogen/deuterium plasma.

Therefore, fundamental studies on the Cs dynamics under ion source relevant vacuum and plasma conditions were performed in a dedicated flexible laboratory experiment. The driving questions are the reasons behind the reduction of the co-extracted electron current due to an increasing Cs content as well as the higher co-extracted electron current for deuterium discharges compared to hydrogen. Hence, investigations on the influence of Cs on the plasma parameters of H_2 and D_2 plasmas were conducted, supported by the usage of xenon as a substitute for caesium: the rare gas can be used to analyze the effects of a heavy atomic particle within the discharge without the additional effects of plasma and surface chemistry inherent to Cs admixtures. Furthermore, the high chemical reactivity of caesium and the resultant susceptibility to impurities from the background gases leads to the involvement of Cs compounds in the Cs dynamics, which can have significantly differing characteristics compared to pure Cs. Hence, studies were performed aiming at the influence of increased partial pressures of impurity gases on the Cs evaporation and the Cs content within the vessel and at the evolution of the work function of a sample surface due to cesiation under ion source relevant background pressures depending on the surface temperature.

For these purposes the laboratory ICP setup (15 cm in diameter, 10 cm in height, max. 600 W RF power, 27.12 MHz) was equipped with multiple diagnostics for Cs and its environment: Surface ionization detectors measure local Cs fluxes within the vessel (local SID) as well as the evaporation rate of the Cs source (oven SID), white light absorption spectroscopy and optical emission spec-

troscopy are applied to determine the line-of-sight integrated Cs density, the work function of a dedicated sample surface is determined by means of the photoelectric effect using the Fowler method, a residual gas analyzer monitors the impurity content, a Langmuir probe is used to determine local plasma parameters and optical emission spectroscopy (OES) is moreover applied to evaluate global plasma parameters via two lines of sight. Since the Cs dynamics are subject to a short- and long-term behavior, the diagnostics were arranged in a way, that simultaneous operation is possible, which is indispensable to relate parameters from different diagnostics to the same experimental condition. The dedicated sample surface (stainless steel) is introduced into the experiment mounted on a sample holder which enables feedback controlled heating of the sample and biasing the sample against the vessel wall. Like this, the temperature dependent work function of the sample can be analyzed and in plasma operation conditions near the converter surface of negative ion sources can be simulated. Due to a feed-through for the Langmuir probe, measurements close to the sample surface are possible.

As Cs source for the investigations the commonly used Cs ovens at IPP cannot be applied, since they are not suitable for the desired dynamic range of evaporation rates. Furthermore, they are based on Cs reservoirs with a content of 1 g of liquid Cs, which require laborious handling and are very susceptible to contaminations. Therefore, a new Cs source is designed, based on a Cs dispenser filled with 100 mg of chemically bound caesium, which is mounted in an oven equipped with a blocking valve and the oven SID to monitor the Cs evaporation.

The developed caesium dispenser oven proved to be capable of a stable and controllable evaporation of pure caesium in vacuum and into hydrogen/deuterium plasmas generating adjustable caesium densities of up to more than $10^{16}\,\mathrm{m}^{-3}$ for both conditions, which is the proper range for ion source relevant conditions. The 100 mg dispenser showed no degeneration due to the presence of an increased impurity partial pressure and the evaporation rate of the oven can be controlled with short response times due to the adjustability via the dispenser heating current. The valve proved full functionality, i. e. the activated dispenser can be protected from contamination if the main vessel needs to be vented and the conditioning of the vessel is maintained if the dispenser needs to be exchanged. The oven SID is an excellent tool for monitoring the evaporation of the oven with a very high sensitivity (2 µg/h) and a dynamic range of more than four orders of magnitude. The Cs dispenser oven showed reliable and adjustable evaporation rates between 50 µg/h and more than 10 mg/h which can be maintained stable for several hours.

The investigations on the influence of particular background gases on the Cs content showed that N_2 can be neglected as harmful impurity under ion source conditions. Like for the inert rare gases, an influence is not expected until partial pressures of several Pa are reached, leading to effects like gas conductive cooling, hindered expansion of Cs out of the oven and hindered diffusion of Cs to the vessel walls. O_2 and H_2O however can have a crucial impact already at very low partial pressures of the order of 10^{-5} mbar, severely diminishing the Cs content due to the formation of crystalline Cs compounds at the vessel surfaces. The working gas H_2 showed to induce the termed 'H_2 effect', i. e. a drastic increase of the Cs content within the vessel due to the presence of red-hot filaments and hydrogen gas, whereas this behavior does not occur in plasma. The effect was observed for the first time and clarification is required through subsequent investigations.

The inherent co-adsorption of Cs compounds besides pure Cs on surfaces is expected to have a significant impact on the resultant surface work function, which was investigated systematically. At the laboratory setup work functions are determined by analyzing photocurrents after the Fowler method. Due to the applied light source and the assumptions required for the evaluation technique, the determined values are an upper limit for the actual work functions. Thorough analyses of the evaluation method were performed and a procedure for recognizing and correcting overestimated work function values is introduced. The consequently observed overestimation is typically of the order of 0.1 eV. The application to a stainless steel sample in vacuum environment showed, that cesiation leads to the expected decrease of the surface work function. However, the minimally achieved value of about 2.75 eV (upper limit) instead of 2.14 eV for a pure Cs layer confirms, that the Cs coating dominantly consists of Cs compounds. This leads to effects of cleaning, healing and degradation of the surface coating depending on the surface temperature and to a considerable hysteresis of the work function regarding the Cs density above the surface. The investigations showed an optimal surface temperature of 200 °C and an optimal evaporation rate of slightly above 1 mg/h for achieving and maintaining a stable low work function of 2.75 eV in vacuum. In hydrogen discharges the plasma surface interaction can have a significant impact on the Cs layer and thus on the work function, which is going to be investigated in forthcoming campaigns.

The investigations on the admixture of xenon to hydrogen/deuterium plasmas (250 W, 10 Pa, 0–50 % Xe content) showed an increasing electron density and a decreasing electron temperature with increasing Xe content. The plasma poten-

tial decreases as well, whereas the potential drop to a floating surface increases. The EEDF changes from a Bi-Maxwellian evolution for pure H_2 plasmas via a Maxwellian distribution to a Druyvesteyn like EEDF at high Xe contents. The influence of xenon at varied initial plasma parameters was analyzed by varying the absolute pressure (5–20 Pa), revealing enhanced influence at higher initial electron temperatures. The dominant isotopic variations are an enhanced dissociation degree in D_2 independently of the xenon admixture and a Maxwellian like EEDF in pure deuterium.

Comparing the ionization rate coefficients of xenon and caesium indicates, that similar effects for Cs admixtures to hydrogen/deuterium plasmas are not expected until Cs densities of $10^{17}\,\mathrm{m}^{-3}$ are reached. This is confirmed by the investigations on Cs seeded H_2 and D_2 plasmas (250 W, 10 Pa) revealing unaffected electron density and temperature in the plasma volume for Cs densities of up to $10^{16}\,\mathrm{m}^{-3}$ independently of the isotope. However, effects related to surface chemistry are already observable at Cs densities of about $4 \times 10^{14}\,\mathrm{m}^{-3}$. The production of negative hydrogen ions at the low work function sample surface leads to a decrease of the electron density in proximity to the surface by up to 25 %. The negative ions moreover lead to the reduction of the plasma potential due to a varied flux balance to the vessel walls. Furthermore, the getter effect of Cs at the vessel surfaces leads to a significant diminishing of the atomic hydrogen/deuterium density by up to 50 % accompanied by a distinct hysteresis concerning the Cs density in the plasma volume. Besides the already observed general isotopic differences between H_2 and D_2 plasmas, no difference in the influence of caesium on the bulk plasma was observed.

The established extended corona model for Cs was benchmarked using the electron temperature from OES, the electron density from probe measurements and the Cs density from white light absorption spectroscopy. It was shown that modeled and measured emissions agree within experimental errors, which proves that the resonant levels of Cs are predominantly populated via electron impact excitation from the ground state. Thus, if electron density and temperature are known, the model can now be applied to monitor the caesium density via OES, which has the advantage of a significantly enhanced detection limit compared to the commonly applied white light absorption spectroscopy.

The underlying similarity of vacuum and plasma conditions of the laboratory setup and negative ion sources allows for an application of the achieved results to the ion sources. Owing to the relevance of this transfer the detailed analysis

is presented in the preceding chapter 10 and only a short summary is given here:

The work function of the converter surface is determined by Cs compound layers instead of pure Cs and depends on the surface temperature and the interaction with the hydrogen/deuterium plasma. The commonly observed reduction of the co-extracted electron current due to Cs seeding does not arise from a direct influence of Cs on the plasma parameters of the bulk plasma, but rather from the repression of electrons from the extraction system due to the formation of negative ions. Furthermore, within the present investigations on the bulk plasma no indications for the higher co-extracted electron current in deuterium operation compared to hydrogen were observed. Finally, it can be stated, that excessive amounts of caesium in the ion source can lead to a diminished negative ion production due to the gettering of atomic hydrogen/deuterium, which are consequently missing for the conversion to H^-/D^-, as well as to an increased co-extracted electron current due to an increasing electron density.

In conclusion, a laboratory experiment for fundamental investigations on the Cs dynamics under ion source conditions has been established, equipped with a reliable Cs source and a comprehensive set of diagnostics. The investigations have shown, that the Cs dynamics are determined by the surface chemistry of caesium compounds leading to increased work functions compared to pure Cs layers and to effects of gettering and hysteresis. The bulk plasma of the hydrogen discharge is not influenced by the presence of typical amounts of caesium regardless of the hydrogen isotope, whereas the surface effects of Cs particularly lead to the formation of negative ions and the gettering of atomic hydrogen and deuterium.

Appendix

A Data on the hyperfine structure of the Cs D lines

The total angular momentum J of the electron shell of the Cs atom couples with the nuclear spin $I = 7/2$ [Lid05] to the total angular momentum of the Cs atom F and the resulting energetic splitting of the electronic states constitutes the hyperfine structure of the Cs atom. Table A.1 shows the energies of the hyperfine structure levels of the ground state and the 6 P states of caesium after [Ste10] relative to the energies of the corresponding fine structure states. In table A.2 the corresponding hyperfine transitions can be found together with their relative intensities after [WE33].

Table A.1: *Level energies of the fine structure and the hyperfine structure of the Cs atom [Ste10].*

Level	Fine structure energy [eV]	Hyperfine structure energy [µeV]	
$6\,^2\mathrm{P}_{3/2}$	1.45	$F = 5$	+1.09
		$F = 4$	+0.05
		$F = 3$	−0.78
		$F = 2$	−1.40
$6\,^2\mathrm{P}_{1/2}$	1.39	$F = 4$	+2.11
		$F = 3$	−2.72
$6\,^2\mathrm{S}_{1/2}$	0	$F = 4$	+16.6
		$F = 3$	−21.4

Table A.2: *Hyperfine transitions of the Cs D_1 and D_2 line including relative line intensities [Ste10, WE33].*

Transition		Wavelength [nm]	Relative intensity
D_2: $6\,^2P_{3/2} \rightarrow 6\,^2S_{1/2}$		852.12	1.000
$F \rightarrow F'$	$5 \rightarrow 4$	852.1296	0.344
	$4 \rightarrow 4$	852.1302	0.164
	$3 \rightarrow 4$	852.1307	0.055
	$4 \rightarrow 3$	852.1080	0.117
	$3 \rightarrow 3$	852.1085	0.164
	$2 \rightarrow 3$	852.1088	0.156
D_1: $6\,^2P_{1/2} \rightarrow 6\,^2S_{1/2}$		894.36	1.000
$F \rightarrow F'$	$4 \rightarrow 4$	894.3645	0.235
	$3 \rightarrow 4$	894.3676	0.328
	$4 \rightarrow 3$	894.3400	0.328
	$3 \rightarrow 3$	894.3431	0.110

Table B.1: *Molecular constants of hydrogen and deuterium [HH13].*

	Hydrogen			Deuterium		
$[cm^{-1}]$	$X\,^1\Sigma_g^+$	$d\,^3\Pi_u$	$B^X_{\nu=0}/B^d_\nu$	$X\,^1\Sigma_g^+$	$d\,^3\Pi_u$	$B^X_{\nu=0}/B^d_\nu$
B_e	60.853	30.364		30.443	15.2	
α	3.062	1.545		1.0786	0.552	
$B_{\nu=0}$	59.322	29.592	2.00	29.9037	14.924	2.00
$B_{\nu=1}$		28.047	2.12		14.372	2.08
$B_{\nu=2}$		26.502	2.24		13.820	2.16
$B_{\nu=3}$		24.957	2.38		13.268	2.25

B Data for OES on molecular hydrogen and deuterium

B.1 Rotational constants for H_2 and D_2

In the first approximation, the energy of the rotational level J' relative to the vibrational level ν of an electronic state is given by $B_\nu\, J'(J'+1)$ [Her50]. B_ν is the corresponding rotational constant, for which applies

$$B_\nu = B_\mathrm{e} - \alpha(\nu + 1/2) + \dots \ ,$$

where B_e and α are molecular constants which are specific for each electronic state [Her50]. For H_2 and D_2 these constants are summarized in table B.1 after [HH13] for the ground state and the upper state of the Fulcher transition, together with the ratio of particular rotational constants which are required for the determination of the gas temperature after equation (6.43).

B.2 Data for the emissivity of rotational lines

The emissivity $\epsilon_{\mathrm{d\,a}}^{\nu'\nu''J'J''}$ of a single rotational line of the Fulcher system of molecular hydrogen or deuterium $(\mathrm{d}\,^3\Pi_\mathrm{u}, \nu', J') \rightarrow (\mathrm{a}\,^3\Sigma_\mathrm{g}^+, \nu'', J'')$ is determined after equation (6.42). Besides the energies $\Delta E_\mathrm{rot}(J')$ of the rotational level J' relative to the state $J' = 1$, which can be found in [Cro72, LU08], the values for the statistical factors $g_I(J')$ and the Hönl-London factors (HLF) $S_\mathrm{P,Q,R}(J')$ are required.

The statistical factor $g_I(J')$ [Her50]

The nuclear spins of the protons of the H_2 molecule couple to a total spin of the nuclei of either $I = 0$ or $I = 1$. The former configuration is called *parahydrogen*, the second *orthohydrogen*. Owing to the statistical weight of angular momenta, $(2I + 1)$, orthohydrogen occurs three times more likely than parahydrogen. Since the total wave function of the molecule needs to be antisymmetric, rotational states with odd quantum numbers can only exist for orthohydrogen and vice versa. Hence, odd rotational quantum numbers occur three times more likely

than even quantum numbers:

$$g_I(J') = \begin{cases} 3, & \text{for } J' \text{ odd} , \\ 1, & \text{for } J' \text{ even} . \end{cases}$$

Accordingly, the emissivity of the rotational lines alternates.
For atomic deuterium the nuclear spin is 1 [Lid05] and thus, the total spin of the D_2 nuclei can be $I = 0, 1, 2$. Analogously, the emissivity of the rotational lines in D_2 alternate according to

$$g_I(J') = \begin{cases} 3, & \text{for } J' \text{ odd} , \\ 6, & \text{for } J' \text{ even} . \end{cases}$$

Hönl-London factors

Formulas for the calculation of the Hönl-London factors $S_{\mathrm{P,Q,R}}(J')$ can be found in [Her50, Kov69] depending on the actual electronic transition. For the Fulcher transition in hydrogen and deuterium applies likewise

$$\begin{aligned} S_{\mathrm{P}}(J') &= \frac{J'}{4} , \\ S_{\mathrm{Q}}(J') &= \frac{2J'+1}{4} , \\ S_{\mathrm{R}}(J') &= \frac{J'+1}{4} . \end{aligned}$$

B.3 Scaling factors for the entire Fulcher emission

The emissivity ϵ_{Ful} of the entire Fulcher emission is determined by extrapolating the summed emissivities $\epsilon_{\mathrm{d\,a}}^{\nu'\nu''}$ of the first four diagonal bands $\nu' = 0, 1, 2, 3 \rightarrow \nu'' = \nu'$ of the Fulcher system using a scaling factor $f_{\mathrm{Ful}}(T_{\mathrm{vib}})$ (see equation (6.46). The values of $f_{\mathrm{Ful}}(T_{\mathrm{vib}})$ are given in table B.2 after [Die10] depending on the vibrational temperature T_{vib} of the molecular ground state.

Table B.2: *Scaling factors for the determination of the Fulcher emission after equation* (6.46) *depending on the vibrational temperature* T_{vib} *of the ground state [Die10].*

	f_{Ful} for	
T_{vib} [K]	H_2	D_2
0	1.97	3.47
1000	1.97	3.44
2000	1.95	3.22
3000	1.92	2.97
4000	1.89	2.79
5000	1.87	2.67
6000	1.86	2.60
7000	1.86	2.59
8000	1.88	2.61
9000	1.92	2.67

C Transmission spectra of the filters for the work function lamp

Different photon energies for the evaluation of work functions after the Fowler method are obtained by using interference filters for a broadband emitting UV light source, a high pressure mercury lamp. In figure C.1 the spectra of the work function lamp transmitted through these filters as well as through the required lenses and the quartz window of the experiment vessel are presented, normalized to the integral of the spectrum of the 280 nm filter. The actual filter transmission is additionally shown in gray. Since it is obtained solely using the work function lamp, large interferences emerge for wavelengths, where the work function lamp has no emission.

For each filter, the relative intensity $F(h\nu)$ of the light, which incides onto the surface under investigation, is thus determined by the integral of the shown transmission spectrum and the mean photon energy $\langle E_{\mathrm{ph}} \rangle$ is determined by the mathematical expectation of the spectrum using the top axis. The values of $F(h\nu)$ are plotted in figure 6.10 and the corresponding values of $\langle E_{\mathrm{ph}} \rangle$, which are used as '$h\nu$' within the evaluation procedure after Fowler, are shown as vertical lines in figure C.1 and are furthermore given in table 6.2.

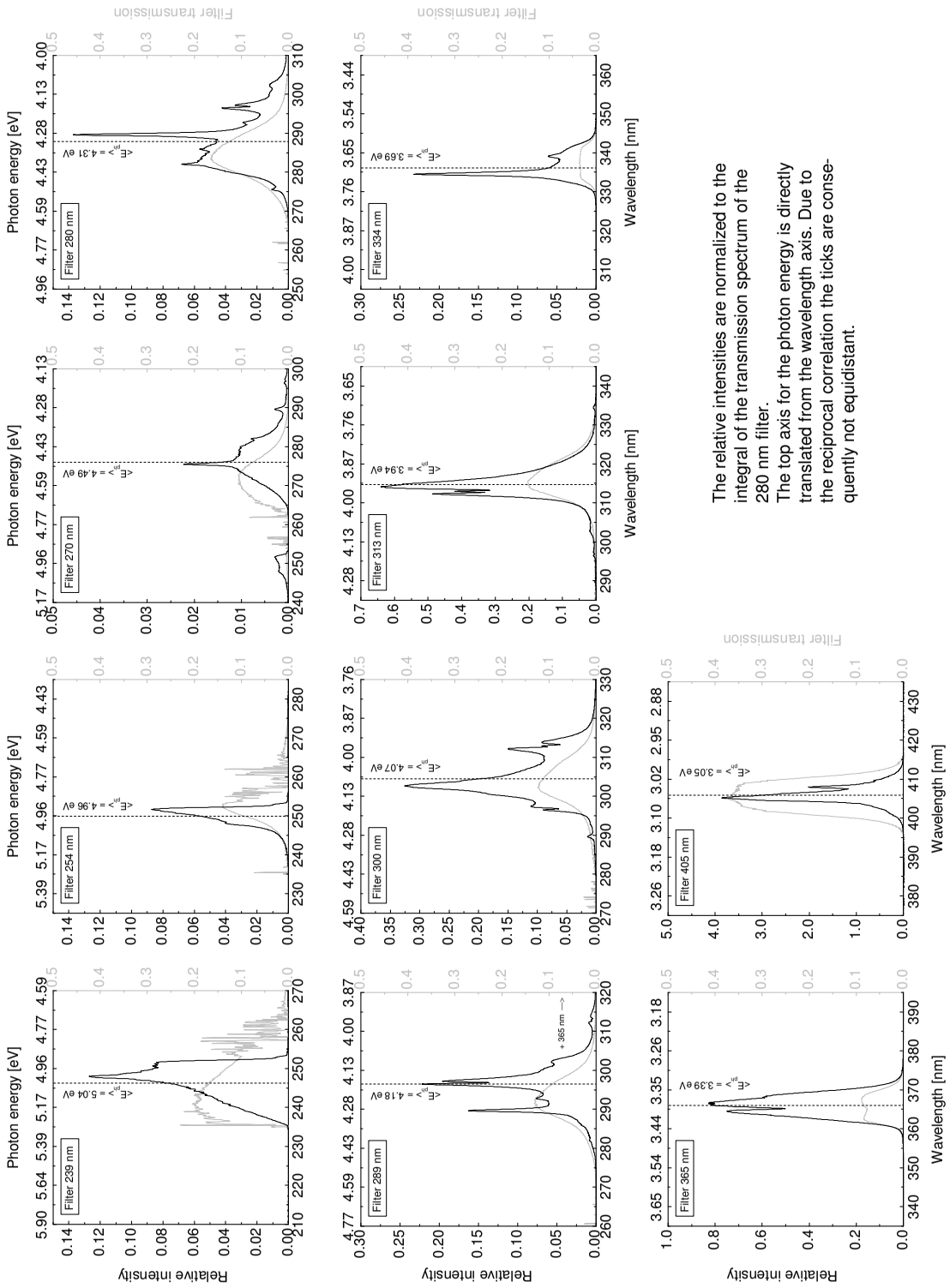

Figure C.1: *Transmission spectra of the work function filters and the corresponding filter transmission.*

Bibliography

[ABR57] J. E. Allen, R. L. F. Boyd, and P. Reynolds, *The Collection of Positive Ions by a Probe Immersed in a Plasma*, Proc. Phys. Soc. B **70** (1957), 297–304.

[Alv10] Alvatec GmbH, Austria, 2010, `http://www.alvatec.com`.

[ATG85] P. W. van Amersfoort, Y. C. Tong, and E. H. A. Granneman, *A model for the stationary cesium coverage on a converter surface in a cesium seeded hydrogen discharge*, J. Appl. Phys. **58** (1985), 2317–2325.

[Bac06] M. Bacal, *Physics aspects of negative ion sources*, Nucl. Fusion **46** (2006), S250–S259.

[BCP85] Y. K. Bae, M. J. Coggiola, and J. R. Peterson, *Charge transfer of 50-eV–4-keV H^+, H_2^+, H_3^+, N^+, and N_2^+ in Cs: Absolute cross sections*, Phys. Rev. A **31** (1985), 3627–3632.

[BDD74] Y. I. Belchenko, G. I. Dimov, and V. G. Dudnikov, *A powerful injector of neutrals with a surface-plasma source of negative ions*, Nucl. Fusion **14** (1974), 113–114.

[Beh91] K. Behringer, *Diagnostics and modelling of ECRH microwave discharges*, Plasma Phys. Control. Fusion **33** (1991), 997–1028.

[Ber05] P. F. Bernath, *Spectra of Atoms and Molecules*, 2nd ed., Oxford University Press, New York, NY, 2005.

[BF94] K. Behringer and U. Fantz, *Spectroscopic diagnostics of glow discharge plasmas with non-Maxwellian electron energy distributions*, J. Phys. D: Appl. Phys. **27** (1994), 2128–2135.

[BF00] ———, *The influence of opacity on hydrogen excited-state population and applications to low-temperature plasmas*, New J. Phys. **2** (2000), 23 (19pp).

[BPS75] K. H. Berkner, R. V. Pyle, and J. W. Stearns, *Intense, mixed-energy hydrogen beams for CTR injection*, Nucl. Fusion **15** (1975), 249–254.

[BR59] I. B. Bernstein and I. N. Rabinowitz, *Theory of Electrostatic Probes in a Low-Density Plasma*, Physics of Fluids **2** (1959), 112–121.

[Bri11] S. Briefi, *Spectroscopic Investigation of Indium Halides as Substitutes of Mercury in Low Pressure Discharges for Lighting Applications*, Ph.D. thesis, University of Augsburg, 2011.

[BWF12] S. Briefi, C. Wimmer, and U. Fantz, *Correction factors for saturation effects in white light and laser absorption spectroscopy for application to low pressure plasmas*, Physics of Plasmas **19** (2012), 053501 (10pp).

[CEA02] F. F. Chen, J. D. Evans, and D. Arnush, *A floating potential method for measuring ion density*, Physics of Plasmas **9** (2002), 1449–1455.

[CF72] R. P. Clow and J. H. Futrell, *Ion-molecule reactions in isotopic hydrogen by ion cyclotron resonance*, International Journal of Mass Spectrometry and Ion Physics **8** (1972), 119–142.

[CG78] S. T. Chen and A. C. Gallagher, *Electron excitation of the resonance lines of the alkali-metal atoms*, Phys. Rev. A **17** (1978), 551–560.

[Che65] F. F. Chen, *Numerical computations for ion probe characteristics in a collisionless plasma*, J. Nucl. Energy, Part C Plasma Phys. **7** (1965), 47–67.

[Che03] ———, *Lecture Notes on Langmuir Probe Diagnostics*, Mini-Course on Plasma Diagnostics, IEEE-ICOPS meeting (Jeju), 2003.

[Chi11] C. D. Child, *Discharge From Hot CaO*, Phys. Rev. (Series I) **32** (1911), 492–511.

[CJL+01] R. Celiberto, R. K. Janev, A. Laricchiuta, M. Capitelli, J. M. Wadehra, and D. E. Atems, *Cross section data for electron-impact*

inelastic processes of vibrationally excited molecules of hydrogen and its isotopes, Atomic Data and Nuclear Data Tables **77** (2001), 161–213.

[Cro72] H. M. Crosswhite, *The hydrogen molecule wavelength tables of Gerhard Heinrich Dieke*, Wiley-Interscience, New York, NY, 1972.

[Die58] G. H. Dieke, *The molecular spectrum of hydrogen and its isotopes*, Journal of Molecular Spectroscopy **2** (1958), 494–517.

[Die10] S. Dietrich, *Verifikation von optischen Diagnostikmethoden an H_2/D_2–Plasmen*, Ph.D. thesis, University of Augsburg, 2010.

[DP40] M. J. Druyvesteyn and F. M. Penning, *The Mechanism of Electrical Discharges in Gases of Low Pressure*, Rev. Mod. Phys. **12** (1940), 87–174.

[DP41] ———, *Errata: Mechanism of Electrical Discharges in Gases of Low Pressure*, Rev. Mod. Phys. **13** (1941), 72–73.

[Dru30] M. J. Druyvesteyn, *Der Niedervoltbogen*, Zeitschrift für Physik **64** (1930), 781–798.

[Ert10] D. Ertle, *Teilchendichten in HF-angeregten Wasserstoff- und Deuteriumplasmen*, Diploma thesis, Ulm University in cooperation with University of Augsburg, 2010.

[ESOS95] M. J. J. Eerden, M. C. M. van de Sanden, D. K. Otorbaev, and D. C. Schram, *Cross section for the mutual neutralization reaction $H_2^+ + H^-$, calculated in a multiple-crossing Landau-Zener approximation*, Phys. Rev. A **51** (1995), 3362–3365.

[Fan04] U. Fantz, *Emission Spectroscopy of Molecular Low Pressure Plasmas*, Contrib. Plasma Phys. **44** (2004), 508–515.

[FFF+06a] U. Fantz, H. Falter, P. Franzen, D. Wünderlich, M. Berger, A. Lorenz, W. Kraus, P. McNeely, R. Riedl, and E. Speth, *Spectroscopy – a powerful diagnostic tool in source development*, Nucl. Fusion **46** (2006), S297–S306.

[FFF+06b] U. Fantz, H. D. Falter, P. Franzen, E. Speth, R. Hemsworth, D. Boilson, and A. Krylov, *Plasma diagnostic tools for optimizing negative hydrogen ion sources*, Rev. Sci. Instrum. **77** (2006), 03A516 (4pp).

[FFF12] U. Fantz, R. Friedl, and M. Fröschle, *Controllable evaporation of cesium from a dispenser oven*, Rev. Sci. Instrum. **83** (2012), 123305 (5pp).

[FFK+07] U. Fantz, P. Franzen, W. Kraus, M. Berger, S. Christ-Koch, M. Fröschle, R. Gutser, B. Heinemann, C. Martens, P. McNeely, et al., *Negative ion RF sources for ITER NBI: status of the development and recent achievements*, Plasma Phys. Control. Fusion **49** (2007), B563–B580.

[FFW12] U. Fantz, P. Franzen, and D. Wünderlich, *Development of negative hydrogen ion sources for fusion: Experiments and modelling*, Chemical Physics **398** (2012), 7–16.

[FGW10] U. Fantz, R. Gutser, and C. Wimmer, *Fundamental experiments on evaporation of cesium in ion sources*, Rev. Sci. Instrum. **81** (2010), 02B102 (4pp).

[FH98] U. Fantz and B. Heger, *Spectroscopic diagnostics of the vibrational population in the ground state of H_2 and D_2 molecules*, Plasma Phys. Control. Fusion **40** (1998), 2023–2032.

[Fow31] R. H. Fowler, *The Analysis of Photoelectric Sensitivity Curves for Clean Metals at Various Temperatures*, Phys. Rev. **38** (1931), 45–56.

[FSC85] R. S. Freund, J. A. Schiavone, and H. M. Crosswhite, *The Electronic Spectrum and Energy Levels of the Deuterium Molecule*, J. Phys. Chem. Ref. Data **14** (1985), 235–383.

[FSWN13] U. Fantz, L. Schiesko, D. Wünderlich, and NNBI Team, *A comparison of hydrogen and deuterium plasmas in the IPP prototype ion source for fusion*, AIP Conf. Proc. **1515** (2013), 187–196.

[FW06a] U. Fantz and D. Wünderlich, *Franck-Condon factors, transition probabilities, and radiative lifetimes for hydrogen molecules and their isotopomeres*, Atomic Data and Nuclear Data Tables **92** (2006), 853–973.

[FW06b] ———, *A novel diagnostic technique for H^- (D^-) densities in negative hydrogen ion sources*, New J. Phys. **8** (2006), 301 (23pp).

[FW11] U. Fantz and C. Wimmer, *Optimizing the laser absorption technique for quantification of caesium densities in negative hydrogen ion sources*, J. Phys. D: Appl. Phys. **44** (2011), 335202 (12pp).

[Gan82] P. S. Ganas, *Excitation of cesium atoms by electron impact*, J. Chem. Phys. **76** (1982), 2103–2105.

[GMS95] V. A. Godyak, V. P. Meytlis, and H. R. Strauss, *Tonks-Langmuir problem for a Bi-Maxwellian plasma*, IEEE Transactions on Plasma Science **23** (1995), 728–734.

[GPA92] V. A. Godyak, R. B. Piejak, and B. M. Alexandrovich, *Measurement of electron energy distribution in low-pressure RF discharges*, Plasma Sources Sci. Technol. **1** (1992), 36–58.

[GWF11] R. Gutser, C. Wimmer, and U. Fantz, *Work function measurements during plasma exposition at conditions relevant in negative ion sources for the ITER neutral beam injection*, Rev. Sci. Instrum. **82** (2011), 023506 (7pp).

[GWFN09] R. Gutser, D. Wünderlich, U. Fantz, and the NNBI-Team, *Negative hydrogen ion transport in RF-driven ion sources for ITER NBI*, Plasma Phys. Control. Fusion **51** (2009), 045005 (14pp).

[GWFN11] R. Gutser, D. Wünderlich, U. Fantz, and the N-NBI Team, *Dynamics of the transport of ionic and atomic cesium in radio frequency-driven ion sources for ITER neutral beam injection*, Plasma Phys. Control. Fusion **53** (2011), 105014 (18pp).

[HDG+09] R. Hemsworth, H. Decamps, J. Graceffa, B. Schunke, M. Tanaka, M. Dremel, A. Tanga, H. P. L. De Esch, F. Geli, J. Milnes, et al., *Status of the ITER heating neutral beam system*, Nucl. Fusion **49** (2009), 045006 (15pp).

[Her50] G. Herzberg, *Molecular spectra and molecular structure, I. Spectra of diatomic molecules*, 2nd ed., D. van Nostrand Company, New York, NY, 1950.

[Her89] N. Hershkowitz, *How Langmuir probes work*, in: Plasma Diagnostics: Volume 1, Discharge Parameters and Chemistry (O. Auciello and D. L. Flamm, eds.), Academic Press, San Diego, CA, 1989.

[HFF+11] B. Heinemann, H.-D. Falter, U. Fantz, P. Franzen, M. Froeschle, W. Kraus, C. Martens, R. Nocentini, R. Riedl, E. Speth, and A. Staebler, *The negative ion source test facility ELISE*, Fusion Engineering and Design **86** (2011), 768–771.

[HH13] K. P. Huber and G. Herzberg, *Constants of Diatomic Molecules (data prepared by J. W. Gallagher and R. D. Johnson, III)*, NIST Chemistry WebBook, NIST Standard Reference Database Number 69 (P. J. Linstrom and W. G. Mallard, eds.), National Institute of Standards and Technology, Gaithersburg, MD, 2013, available online: `http://webbook.nist.gov`.

[IAE02] IAEA, *ITER technical basis*, ITER EDA documentation series 24, International Atomic Energy Agency, Vienna, 2002.

[IKS92] J. D. Isenberg, H. J. Kwon, and M. Seidl, *Surface production of H^- ions by backscattering of H^+ and H_2^+ ions in the 3–50 eV ion energy range*, AIP Conf. Proc. **287** (1992), 38–47.

[JR78] R. K. Janev and Z. M. Radulović, *Ion-ion recombination and ion-pair formation processes in alkali-hydrogen diatomic systems*, Phys. Rev. A **17** (1978), 889–896.

[JRS03] R. K. Janev, D. Reiter, and U. Samm, *Collision Processes in Low-Temperature Hydrogen Plasmas*, Berichte des Forschungszentrums Jülich JUEL-4105, Forschungszentrum Jülich, 2003.

[KFF+12] W. Kraus, U. Fantz, P. Franzen, M. Fröschle, B. Heinemann, R. Riedl, and D. Wünderlich, *The development of the radio frequency driven negative ion source for neutral beam injectors (invited)*, Rev. Sci. Instrum. **83** (2012), 02B104 (5pp).

[Kov69] I. Kovács, *Rotational structure in the spectra of diatomic molecules*, Adam Hilger, London, 1969.

[KRRN13] A. Kramida, Y. Ralchenko, J. Reader, and NIST ASD Team, *NIST Atomic Spectra Database* (ver. 5.0), National Institute of Standards and Technology, Gaithersburg, MD, 2013, available online: `http://physics.nist.gov/asd`.

[Laf66] J. G. Laframboise, *Theory of spherical and cylindrical Langmuir probes in a collisionless, Maxwellian plasma at rest*, UTIAS report 100, University of Toronto, 1966.

[Lid05] D. R. Lide (ed.), *CRC Handbook of Chemistry and Physics*, CRC Press, Boca Raton, FL, 2005.

[LL05] M. A. Lieberman and A. J. Lichtenberg, *Principles of Plasma Discharges and Materials Processing*, 2nd ed., John Wiley & Sons, Hoboken, NJ, 2005.

[LRV91] J.-M. L'Hermite, G. Rahmat, and R. Vetter, *The $Cs(7P) + H_2 \rightarrow CsH + H$ reaction. II. Rotationally resolved total cross sections*, J. Chem. Phys. **95** (1991), 3347–3360.

[LS92] B. S. Lee and M. Seidl, *Surface production of H^- ions by hyperthermal hydrogen atoms*, Appl. Phys. Lett. **61** (1992), 2857–2859.

[LU08] B. P. Lavrov and I. S. Umrikhin, *Optimal values of rovibronic energy levels for triplet electronic states of molecular deuterium*, J. Phys. B: At. Mol. Opt. Phys. **41** (2008), 105103 (25pp).

[MDCK+09] P. McNeely, S. V. Dudin, S. Christ-Koch, U. Fantz, and the NNBI Team, *A Langmuir probe system for high power RF-driven negative ion sources on high potential*, Plasma Sources Sci. Technol. **18** (2009), 014011 (17pp).

[MGVHT06] I. Méndez, F. J. Gordillo-Vázquez, V. J. Herrero, and I. Tanarro, *Atom and Ion Chemistry in Low Pressure Hydrogen DC Plasmas*, J. Phys. Chem. A **110** (2006), 6060–6066.

[MHL77] G. R. Möhlmann, F. J. de Heer, and J. Los, *Emission cross sections of Balmer-α,β,γ radiation for electrons (0–2000 eV) on H_2 and D_2*, Chemical Physics **25** (1977), 103–116.

[Mic77] H. B. Michaelson, *The work function of the elements and its periodicity*, J. Appl. Phys. **48** (1977), 4729–4733.

[Möl93] W. Möller, *Plasma and surface modeling of the deposition of hydrogenated carbon films from low-pressure methane plasmas*, Appl. Phys. A **56** (1993), 527–546.

[MOSG85] T. J. Morgan, R. E. Olson, A. S. Schlachter, and J. W. Gallagher, *Charge Transfer of Hydrogen Ions and Atoms in Metal Vapors*, J. Phys. Chem. Ref. Data **14** (1985), 971–1040.

[MS10] P. McNeely and L. Schiesko, *Investigation of fringe plasma parameters on a high power rf driven ion source*, Rev. Sci. Instrum. **81** (2010), 02B111 (3pp).

[MSL26] H. M. Mott-Smith and I. Langmuir, *The Theory of Collectors in Gaseous Discharges*, Phys. Rev. **28** (1926), 727–763.

[NGH+11] R. Nocentini, R. Gutser, B. Heinemann, M. Fröschle, and R. Riedl, *Optimization of the cooling circuit and thermo-mechanical analysis for the extraction grid of ELISE*, Fusion Engineering and Design **86** (2011), 916–919.

[NK07] S. Nunomura and M. Kondo, *Characterization of high-pressure capacitively coupled hydrogen plasmas*, J. Appl. Phys. **102** (2007), 093306 (7pp).

[NTN87] K. Nakashima, H. Takagi, and H. Nakamura, *Dissociative recombination of H_2^+, HD^+, and D_2^+ by collisions with slow electrons*, J. Chem. Phys. **86** (1987), 726–737.

[Nyg68] K. J. Nygaard, *Electron-Impact Ionization Cross Section in Cesium*, J. Chem. Phys. **49** (1968), 1995–2002.

[OD88] A. O'Keefe and D. A. G. Deacon, *Cavity ring-down optical spectrometer for absorption measurements using pulsed laser sources*, Rev. Sci. Instrum. **59** (1988), 2544–2551.

[OM92] T. Okuyama and Y. Mori, *Cesium catalysis effect of H^- ion production in volume production type of H^- ion source*, Rev. Sci. Instrum. **63** (1992), 2711–2713.

[OOR+89] D. K. Otorbaev, V. N. Ochkin, P. L. Rubin, S. Y. Savinov, N. N. Sobolev, and S. N. Tskhai, *Electron-impact excitation levels of the rotational levels of molecular electron states in gas discharges*, in: Electron-excited Molecules in Nonequilibrium Plasma (N. N. Sobolev, ed.), Nova Science Publishers, Commack, NY, 1989.

[Pas19] F. Paschen, *Das Spektrum des Neon*, Annalen der Physik **365** (1919), 405–453.

[PCI+01] E. Di Pietro, A. Costley, T. Inoue, A. Krylov, A. Panasenkov, Y. Utin, G. Vayakis, M. von Hellerman, and M. Yamada, *Conceptual design and integration of a diagnostic neutral beam in ITER*, Fusion Engineering and Design **56–57** (2001), 929–934.

[PFP10] G. A. Pitz, C. D. Fox, and G. P. Perram, *Pressure broadening and shift of the cesium D_2 transition by the noble gases and N_2, H_2, HD, D_2, CH_4, C_2H_6, CF_4, and ^3He with comparison to the D_1 transition*, Phys. Rev. A **82** (2010), 042502 (9pp).

[PTVZ09] G. Peters, I. Thede, V. Vill, and R. Zenczykowski, *Landolt-Börnstein Substance / Property Index*, Hamburg, 2009, available online: `http://lb.chemie.uni-hamburg.de/`.

[RWL82] B. Rasser, J. N. M. van Wunnik, and J. Los, *Theoretical models of the negative ionization of hydrogen on clean tungsten, cesiated tungsten and cesium surfaces at low energies*, Surface Science **118** (1982), 697–710.

[SAE10] SAES Getters S.p.A., Italy, 2010, `http://www.saesgetters.com`.

[SCM+07] M. Shimada, D. J. Campbell, V. Mukhovatov, M. Fujiwara, N. Kirneva, K. Lackner, M. Nagami, V. D. Pustovitov, N. Uckan, J. Wesley, et al., *Progress in the ITER physics basis – Chapter 1: Overview and summary*, Nucl. Fusion **47** (2007), S1–S17.

[SFAP01] P. Scheubert, U. Fantz, P. Awakowicz, and H. Paulin, *Experimental and theoretical characterization of an inductively coupled plasma source*, J. Appl. Phys. **90** (2001), 587–598.

[SFF+06] E. Speth, H. D. Falter, P. Franzen, U. Fantz, M. Bandyopadhyay, S. Christ, A. Encheva, M. Fröschle, D. Holtum, B. Heinemann, et al.,

Overview of the RF source development programme at IPP Garching, Nucl. Fusion **46** (2006), S220–S238.

[SFLB81] B. Sayer, M. Ferray, J. Lozingot, and J. Berlande, *Experimental investigation of cesium hydride formation by reactive interaction between Cs(7P) and H_2 molecules*, J. Chem. Phys. **75** (1981), 3894–3903.

[Sha70] T. E. Sharp, *Potential-energy curves for molecular hydrogen and its ions*, Atomic Data and Nuclear Data Tables **2** (1970), 119–169.

[Sha71] ———, *Erratum: Potential-energy curves for molecular hydrogen and its ions*, Atomic Data and Nuclear Data Tables **3** (1971), 299.

[SMF+11] L. Schiesko, P. McNeely, U. Fantz, P. Franzen, and NNBI Team, *Caesium influence on plasma parameters and source performance during conditioning of the prototype ITER neutral beam injector negative ion source*, Plasma Phys. Control. Fusion **53** (2011), 085029 (12pp).

[Sob92] I. I. Sobelman, *Atomic Spectra and Radiative Transitions*, 2nd ed., Springer Series on Atoms and Plasmas, vol. 12, Springer-Verlag, Berlin Heidelberg, 1992.

[SP94] J. Songster and A. D. Pelton, *The H–Cs (hydrogen–cesium) system*, Journal of Phase Equilibria **15** (1994), 84–86.

[Spe89] E. Speth, *Neutral beam heating of fusion plasmas*, Reports on Progress in Physics **52** (1989), 57–121.

[SS68] L. W. Swanson and R. W. Strayer, *Field-Electron-Microscopy Studies of Cesium Layers on Various Refractory Metals: Work Function Change*, J. Chem. Phys. **48** (1968), 2421–2442.

[Ste10] D. A. Steck, *Cesium D Line Data*, available online at `http://steck.us/alkalidata` (revision 2.1.4, 23 December 2010), 2010.

[SVY81] I. I. Sobelman, L. A. Vainshtein, and E. A. Yukov, *Excitation of Atoms and Broadening of Spectral Lines*, Springer Series in Chemical Physics, vol. 7, Springer-Verlag, Berlin Heidelberg, 1981.

[SZY91] W. C. Stwalley, W. T. Zemke, and S. C. Yang, *Spectroscopy and Structure of the Alkali Hydride Diatomic Molecules and their Ions*, J. Phys. Chem. Ref. Data **20** (1991), 153–187.

[Tak02] H. Takagi, *Dissociative Recombination and Excitation of H_2^+, HD^+, and D_2^+ with Electrons for Various Vibrational States*, Physica Scripta **T96** (2002), 52–60.

[Tay29] J. B. Taylor, *Eine Methode zur direkten Messung der Intensitätsverteilung in Molekularstrahlen*, Zeitschrift für Physik **57** (1929), 242–248.

[TL33] J. B. Taylor and I. Langmuir, *The Evaporation of Atoms, Ions and Electrons from Caesium Films on Tungsten*, Phys. Rev. **44** (1933), 423–458.

[TL37] ———, *Vapor Pressure of Caesium by the Positive Ion Method*, Phys. Rev. **51** (1937), 753–760.

[TLJ99] A. Thorne, U. Litzén, and S. Johansson, *Spectrophysics: Principles and Applications*, Springer-Verlag, Berlin Heidelberg, 1999.

[TMH75] A. Tam, G. Moe, and W. Happer, *Particle Formation by Resonant Laser Light in Alkali-Metal Vapor*, Phys. Rev. Lett. **35** (1975), 1630–1633.

[TNK+12] K. Tsumori, H. Nakano, M. Kisaki, K. Ikeda, K. Nagaoka, M. Osakabe, Y. Takeiri, O. Kaneko, M. Shibuya, E. Asano, et al., *Spatial distribution of the charged particles and potentials during beam extraction in a negative-ion source*, Rev. Sci. Instrum. **83** (2012), 02B116 (5pp).

[VFDS86] J. P. Visticot, M. Ferray, P. D'Oliveira, and B. Sayer, *Processes involved in the $Cs(7P) + H_2 \rightarrow CsH$ reaction and nascent rotational distribution*, J. Chem. Phys. **84** (1986), 1482–1486.

[VFLS83] J. P. Visticot, M. Ferray, J. Lozingot, and B. Sayer, *Investigation of various ways of forming CsH by irradiating a $Cs + H_2$ mixture with laser light*, J. Chem. Phys. **79** (1983), 2839–2847.

[VSSB02] A. A. Vasilyev, I. M. Savukov, M. S. Safronova, and H. G. Berry, *Measurement of the 6s–7p transition probabilities in atomic cesium and a revised value for the weak charge Q_W*, Phys. Rev. A **66** (2002), 020101 (4pp).

[War68] B. Warner, *Atomic oscillator strengths–III. Alkali-like spectra*, Monthly Notices of the Royal Astronomical Society **139** (1968), 115–128.

[WBHF87] R. C. Wetzel, F. A. Baiocchi, T. R. Hayes, and R. S. Freund, *Absolute cross sections for electron-impact ionization of the rare-gas atoms by the fast-neutral-beam method*, Phys. Rev. A **35** (1987), 559–577.

[WCD87] Y. Wang, R. L. Champion, and L. D. Doverspike, *Slow collisions of H^- and D^- with Cs*, Phys. Rev. A **36** (1987), 381–383.

[WDF09] D. Wünderlich, S. Dietrich, and U. Fantz, *Application of a collisional radiative model to atomic hydrogen for diagnostic purposes*, Journal of Quantitative Spectroscopy and Radiative Transfer **110** (2009), 62–71.

[WE33] H. E. White and A. Y. Eliason, *Relative Intensity Tables for Spectrum Lines*, Phys. Rev. **44** (1933), 753–756.

[WFN13] C. Wimmer, U. Fantz, and NNBI-Team, *Cesium dynamics and H^- density in the extended boundary layer of negative hydrogen ion sources for fusion*, AIP Conf. Proc. **1515** (2013), 246–254.

[Wil66a] R. G. Wilson, *Electron and Ion Emission from Polycrystalline surfaces of Be, Ti, Cr, Ni, Cu, Pt, and Type-304 Stainless Steel in Cesium Vapor*, J. Appl. Phys. **37** (1966), 3161–3169.

[Wil66b] ———, *Electron and Ion Emission from Polycrystalline surfaces of Nb, Mo, Ta, W, Re, Os, and Ir in Cesium Vapor*, J. Appl. Phys. **37** (1966), 4125–4131.

[WMA75] A. Y. Wong, D. L. Mamas, and D. Arnush, *Negative ion plasmas*, Physics of Fluids **18** (1975), 1489–1493.

[Wün04] D. Wünderlich, *Berechnung von Teilchendichten für die Diagnostik an Niedertemperaturplasmen*, Ph.D. thesis, University of Augsburg, 2004.

[WN11] D. Wünderlich and the NNBI Team, *Influence of photoelectron emission on the plasma sheath in cesiated sources for negative hydrogen ions*, Proc. 30th ICPIG (Belfast), 2011.

[Wün12] D. Wünderlich, *Private communication*, Max-Planck-Institut für Plasmaphysik (IPP), Garching, 2012.

[WPL73] G. A. Woolsey, I. C. Plumb, and D. B. Lewis, *Langmuir probe characteristics in a positive-ion/negative-ion plasma*, J. Phys. D: Appl. Phys. **6** (1973), 1883–1890.

[WSM+12] D. Wünderlich, L. Schiesko, P. McNeely, U. Fantz, P. Franzen, and the NNBI-Team, *On the proton flux toward the plasma grid in a RF-driven negative hydrogen ion source for ITER NBI*, Plasma Phys. Control. Fusion **54** (2012), 125002 (9pp).

Acknowledgements

An dieser Stelle möchte ich mich bei allen bedanken, die zur Entstehung dieser Arbeit beigetragen haben. Insbesondere gilt mein Dank:

- **Prof. Dr.-Ing. Ursel Fantz** für die Möglichkeit, die interessante Aufgabenstellung im Rahmen einer Doktorarbeit in der AG Experimentelle Plasmaphysik zu bearbeiten, die durchgehend hervorragende Betreuung und Unterstützung während der Arbeit sowie für das stets gute Arbeitsklima.
- **Prof. Dr. Achim Wixforth** für die Übernahme des Zweitgutachtens.
- **Dr. Stefan Briefi, Dipl.-Phys. Uwe Kurutz und Dipl.-Phys. David Ertle** für die exzellente und freundschaftliche Zusammenarbeit in der AG, die Hilfsbereitschaft bei jeglichen Problemen, der Vielzahl an wertvollen wissenschaftlichen Diskussionen und nicht zuletzt für das Korrekturlesen der Arbeit.
  ...Jungs, es war und ist mir eine Ehre!
- **Dr. Dirk Wünderlich** für die Bereitstellung des Stoß-Strahlungsmodells Yacora, für die Unterstützung bei dessen Anwendung sowie für die diesbezüglichen wissenschaftlichen Diskussionen.
- **Markus Fröschle** für die Zusammenarbeit beim Design der neuen Cs-Quelle sowie für die Konstruktion und die Unterstützung bei der Inbetriebnahme.
- **Martin Kammerloher und Peter Turba** für die Hilfsbereitschaft und die kompetente Beratung bei jeglichen Fragestellungen hinsichtlich elektrotechnischer Angelegenheiten sowie für die umgehende Reparatur etwaiger Geräte.
- **der feinmechanischen Werkstatt** und **der Elektronikwerkstatt** des Physik-Instituts für die Unterstützung und die Herstellung zahlreicher Komponenten für den Versuchsaufbau.
- **Dipl.-Phys. Florian Vogel, M.Sc. Sinan Kalafat, Dr. Raphael Gutser, Dipl.-Phys. Christian Wimmer, B.Sc. Patrick Gutmann, B.Sc. David Rauner und B.Sc. Johannes Doerfler** für die gute Zusammenarbeit, die interessanten Diskussionen und die tatkräftige Unterstützung. *...weiter so!*

Zuletzt, jedoch nicht minder wichtig, möchte ich mich bei meiner Familie, meiner Freundin und meinem gesamten Freundeskreis für ihr Verständnis, die Geduld sowie den Rückhalt während der gesamten Doktorarbeit bedanken.

Curriculum vitae

Name:	Roland Friedl
Date of birth:	July 27th, 1982 in Munich, Germany
Nationality:	German
Marital status:	single

09/1989 – 07/1992	Primary school Altdorf
09/1992 – 07/1993	Primary school Ostendschule Neuburg/Do.
09/1993 – 06/2002	Grammar school Descartes-Gymnasium Neuburg/Do. High-school graduation: A levels
07/2002 – 03/2003	Basic military service at JG 74 'Mölders' Neuburg/Do.
04/2003 – 10/2009	Physics studies at University of Augsburg Graduation: Diploma in physics
10/2009 – 10/2012	PhD student at the Max-Planck-Institut für Plasmaphysik (IPP) Garching, workplace and laboratory at the AG Experimentelle Plasmaphysik at University of Augsburg

Augsburg, August 22nd, 2013